Sedimentology and stratigraphy of the Ktawa Group: the record of a shallow marine siliciclastic platform of Late Ordovician age in the Anti-Atlas, Morocco.

Inaugural dissertation
of the Faculty of Science,
University of Bern

presented by

Déborah Harlet

from Eaubonne, France

Supervisors of the doctoral thesis:
Prof. Dr. Fritz Schlunegger
Dr. Guilhem Amin Douillet
Dr. Jean-François Ghienne

Institute of Geological Sciences

source: https://doi.org/10.48549/5756 | downloaded: 31.1.2025

WISSEN
SCHAFFT
WERT.

Sedimentology and stratigraphy of the Ktawa Group: the record of a shallow marine siliciclastic platform of Late Ordovician age in the Anti-Atlas, Morocco.

Inaugural dissertation
of the Faculty of Science,
University of Bern

presented by

Déborah Harlet

from Eaubonne, France

Supervisors of the doctoral thesis:
Prof. Dr. Fritz Schlunegger
Dr. Guilhem Amin Douillet
Dr. Jean-François Ghienne

Institute of Geological Sciences

Accepted by the Faculty of Science.

Bern,

The Dean
Prof. Dr. Marco Herwegh

WISSEN
SCHAFFT
WERT.

This work is licensed under a Creative Commons Attribution 4.0 International License
https://creativecommons.org/licenses/by/4.0/

Abstract

Detailed facies association observations are crucial for interpretations and calibrations of depositional environments of shallow marine deposits, which in turn, are fundamental for reconstruction of a relative sea level curve. An important aspect of basin evolution is flexural isostasy, which affects the accommodation space available in the basin, which therefore can have feedback on the relative sea level curve reconstructed. To investigate these processes, the Ktawa Group of Late Ordovician age in the Central Anti-Atlas (South Morocco) was studied. The group is composed of shallow marine siliciclastic sediments dominated by storm-wave action. Detailed sedimentology, stratigraphy and subsidence analysis were conducted through this field-based study. Two possible depositional models were reconstructed for the Lower Ktawa Formation (older formation in the Ktawa Group) based on two different hypotheses on facies associations. These hypotheses are either a ramp-like setting deposited during a regression, or a bimodal setting composed of a ramp deposited during a forced regression followed by a barrier-lagoon system formed during the transgression. Furthermore, the Lower Ktawa lowstands could be deposited as megalobe geometries prograding toward the North (+/-45°). Each megalobe may have been emplaced in the depression and accommodation space created by the deposition and isostatic adjustment of the previous megalobe. This emplacement progressively shifted toward the East, until the deposition of the Rouïd-Aïssa Formation (overlying the Lower Ktawa Formation). The Rouïd-Aïssa Formation deposits would show a proximal-to-distal trend from the West to the East relatively. A ca. 90° shift in the proximal-to-distal trend between the Lower Ktawa and Rouïd-Aïssa Formations is observed. This shift might be induced by tectonic influence. Finally, the Ktawa Group (Sandbian-Katian) was deposited prior to the Late Ordovician glaciation maximum (Hirnantian). Lowstands observed in the field of the Ktawa Group were interpreted as likely driven by allocylic glacio-eustasy with autocyclicity in the emplacement of megalobes. This thesis combines the above data to gain a new understanding of the sedimentology and stratigraphy of the Ktawa Group in the Central Anti-Atlas.

Acknowledgments

My firsts thank you go to my main supervisors, Dr. Guilhem Amin Douillet and Prof. Dr. Fritz Schlunegger. Guilhem, thank you for your mentorship, all of those field seasons with the weirdest things happening to us, for challenging me and helping me to grow scientifically. Thank you Fritz for the discussions we had and constant support.

I would also to thank Dr. Jean-François Ghienne and Dr. Pierre Dietrich for the many, fruitful, full of information, discussions we had over the past 4 years. Thank you both for your guidance and help throughout this thesis. Thank you to Dr. Chloé Bouscary and Prof. Dr. Philippe Razin for your help in the first field season and showing us these incredible outcrops.

Thank you to Prof. Dr. Nestor Cardozo and Dr. Eun Young Lee for your help and patience with the modelling part.

I would like to thank my new supervisors in Dublin, iCRAG, Dr. Koen Torremans and Dr. Simon Jones for giving me the time to finish this Ph.D. thesis. Thank you both for your support. The same thank you goes to the team of Sandfire in Botswana.

I could not have done without the people at the institute of geology of Bern. Thank you all for your tremendous support during the many ups and downs. Thank you all for the nice coffee breaks, lunches or drinks. A special one goes to Renée. I don't even think I can thank you enough for being here for me throughout all of this. I will never forget the laughs, tears, the beers (of course), to set the world to rights, the many plans we had over the past few years to make the world a better place, or even just our world. Thank you also to my wonderful offices mates, Siro and Bennet. Best office ever. Thank you for your help (especially Siro for your "assistance" at the end) and the many discussions we had putting the world to rights. I would also like to thank Prof. Dr. Pierre Lanari and Camille. Thank you both for your wise advices, especially to Pierre. I also made it because you were there for me toward the end and thank you for listening to me when I needed it.

Thank you to my family, *maman, papa, Alexis, et Eléonore*. Thank you so much for your tremendous support throughout those 4 years. I haven't been really easy with you but that's how family is I guess. I hope all of you are proud and beyond.

Thank you to all of my friends in Eaubonne, Paris, Grenoble. You are the best, never forget it. Thank you for your support, for always being keen to see each other and catch up as much as we can in the little time we have together. Friendships that last for more than 20 years

are special, especially since we are quite young and fresh still. Thank you Yann for being here for me when I needed it, for visiting from across France and travelling for so long. Thank you for all the laughs you made me had. The Bachelor was much better with you by my side. To all of this, me annoying you badly, us almost getting expelled of the class because I was laughing too much, to this amazing friendship.

Thank you all. I don’t think I could have done it without all of you.

Contents

Abstract 5

Acknowledgments 7

Chapter one. Introduction and thesis outline

1.1. Introduction 16

1.2. Outline of the thesis 18

Chapter two. Sedimentary facies and shelf morphology of the Late Ordovician Ktawa Group (Morocco): shoreface or barrier-lagoon within a siliciclastic storm-dominated platform? 25

Abstract 26

2.1. Introduction 27

2.1.1. Storm-wave imprint 27

2.1.2. Bioturbation imprint 29

2.2. Geological setting 30

2.3. Methods 32

2.4. Facies associations 35

2.4.1. Mudstones 35

2.4.2. Ferruginous horizons 35

2.4.3. Silts and sandstones with ripple marks 36

2.4.4. Siltstones and isolated HCS-bearing sandstones 37

2.4.5. Stacked HCS sandstones 40

2.4.6. Quartzose amalgamated sandstones 42

2.4.7. Coarse-grained cross-bedded sandstones 43

2.4.8. Intensely bioturbated muddy sandstones 47

2.5. Stratigraphic architecture 49

2.5.1. Typical sequential architecture 49

2.5.2. Isolated coarse-grained sandstone lenses 51

2.5.3 Progradation direction 56

2.6. Discussion 58

2.6.1. Bioturbated sandstones: lower shoreface or lagoon? *58*

2.6.1.a. Regressive lower shoreface 58

2.6.1.b. Low vs. high energy ramp 59

2.6.1.c Transgressive barrier-lagoon system 59

2.6.2. Implications for sequence stratigraphy 60

2.6.3. Progradation direction 63

2.7. Conclusion and Outlook 63

Chapter three. Sedimentology, stratigraphy of the pre-glacial deposits of the Rouïd-Aïssa Formation of Late Ordovician time (Morocco)……..83

3.1. Introduction 84

3.2. Geological setting 84

3.3. Methods 86

3.4. Facies associations 87

3.4.1. Isolated sandstones bearing HCS sandstones and shell concentrations, with silts and sand ripple-marked interbeds 87

3.4.2. Stacked to amalgamated HCS sandstones bearing shell concentrations 92

3.4.3. Coarse cross-bedded sandstones bearing rip-up and shell clasts in concentrations ... 94

3.4.4. Silty and medium-grained intensely bioturbated sandstones 96

3.4.5. Lag deposits bearing pebble and shell clasts 97

3.4.6. Highly deformed sandstones 99

3.5. Architecture 99

3.6. Regional paleogeography 105

3.6.1. Progradation direction 106

3.6.2. Isopachs 106

3.6.3. Tectonic influence 107

3.6.4. Morphology 108

3.7. Summary 108

Chapter four. Depositional facies and stratigraphic architecture recording relative sea level variations (Ktawa Group, Morocco): the onset of the Early Paleozoic glaciation……117

Abstract **118**

4.1. Introduction **119**

4.2. Geological setting **121**

4.3. Methods **124**

4.4. Stratigraphic signals in the study area **127**

4.4.1. Age constrains 129
4.4.2. The Lower Ktawa Formation 129
4.4.3. The Rouïd-Aïssa Formation 134

4.5. Correlations **135**

4.5.1. Correlation of members within the study area 135
4.5.2. Correlations at the global scale 138
4.5.3. Correlations across the northern Gondwana platform 143
4.5.4. Correlations within the Ktawa Group 145

4.6. Conclusion **149**

Chapter five. Isostatic adjustment due to sediment loading of the Lower Ktawa Formation in the Anti-Atlas (Morocco) **159**

Abstract **160**

5.1. Introduction **161**

5.2. Geological setting **162**

5.2.1 The Lower Ktawa Formation 162
5.2.2 The Tagounite trough 163
5.2.3. Orientation of the system 164
5.2.4. Paleo-markers for the orientation of progradation 165

5.3. Methods **169**

5.3.1. Geological dataset 169
5.3.2. Extrapolation of lobe shapes in 3D 169
5.3.3. Subsidence model 170
5.3.4. Input parameters 171

5.4. Results 172

5.5. Discussion.....183

5.5.1. Autocyclic location process through lateral deflection 184
5.5.2. Eastward shift in the stacking architecture.....185
5.5.3. Artifacts in loads are transferred to artifacts in deflection 185
5.5.4. Bathymetry vs type of sediment.....185
5.5.5. Symmetry of lobe shapes 186
5.5.6. Scale, flexural isostasy and timing of adjustment of subaqueous megalobe system187
5.5.6.a. Scale of megalobes 187
5.5.6.b. Effective elastic thickness 187
5.5.6.c. Timing for isostatic adjustment.....187
5.5.7. The effect of lateral deflection in other modelling tools.....188

5.6. Conclusion.....189

Chapter six. Conclusion and outlooks ……..197

Appendix A. Detailed stratigraphic profiles of the Lower Ktawa Formation in the western Central Anti-Atlas ……201

Appendix B. 3D photogrammetric reconstruction of stratigraphic profiles ……..235

Appendix C. Detailed stratigraphic profiles of the Rouïd-Aïssa Formation in the western Central Anti-Atlas ……245

List of figures……...251

List of tables……....254

Curriculum vitae……256

Declaration of consent……...….260

CHAPTER ONE

Introduction and thesis outline

1.1. Introduction

The depositional environments interpreted from ancient facies associations of shallow marine siliciclastic deposits, for example those formed on passive margins, are critical for the reconstruction of a relative sea level curve. This sea level curve is useful for regional to global correlations with other basins, and gives information on the paleoclimate, such as ice sheet formation, paleogeography and emergence of the continents, and possible habitable environments for life. Detailed facies association recognition is essential for the calibration of the paleo-bathymetry of basins, i.e., the depositional environment at that time. The interpretation and stacking pattern of facies associations also has implications the sequence stratigraphy of that particular environment, but also in correlations with the larger basin structure, and furthermore other coeval basins in marine settings (Catuneanu et al., 2009).

Here, the Ktawa Group was investigated in detail through a field-based study on sedimentology, stratigraphy and subsidence analysis in the Anti-Atlas (Jbel Bani cliff, South Morocco, Fig. 1.1A and B). Sediments composing the group were deposited in a shallow marine siliciclastic environment, dominated by storm-wave action (Álvaro et al., 2022, Cocco et al., 2023, Dabard et al., 2009, Destombes, 1985, Dietrich et al., 2019, Ghienne et al., 2007, Loi et al., 2010, Marante, 2008, Meddour, 2016, Vidal et al., 2011, Videt et al., 2010).

Storm-wave-dominated environment shape deltas in large features (ca. 100s of km, Lin and Bhattacharya, 2021, Patruno and Helland-Hansen, 2018, Proust et al., 2018), where constant reworking shapes the shoreline and enables transport offshore (Driscoll and Karner, 1994, Hampson and Premwichein, 2017, Mitchell et al., 2012). Hummocky-Cross Stratifications (HCS) sedimentary structures are characteristics of storm reworking (e.g. Jelby et al., 2020). Storm-wave reworking can build barrier systems and protect the back-barrier from storm-wave action. A protected to restricted environment is then important for the thrive of bioturbation (Dashtgard et al., 2021, Dillenburg et al., 2009).

The Ktawa Group was deposited close to the South Pole in the Late Ordovician times during Sandbian to Katian (ca. 459 to 446 Ma, Fig. 1.1.C, Cocks and Torsvik, 2021, Destombes, 1985, Loi et al., 2010, Torsvik and Cocks, 2013), prior to the Late Ordovician glaciation (Hirnantian, ca. 445.2 Ma). The onset of the Early Paleozoic glaciation was as early as Middle Ordovician (Pohl et al., 2016). The glaciation and changes in volumes of ice masses

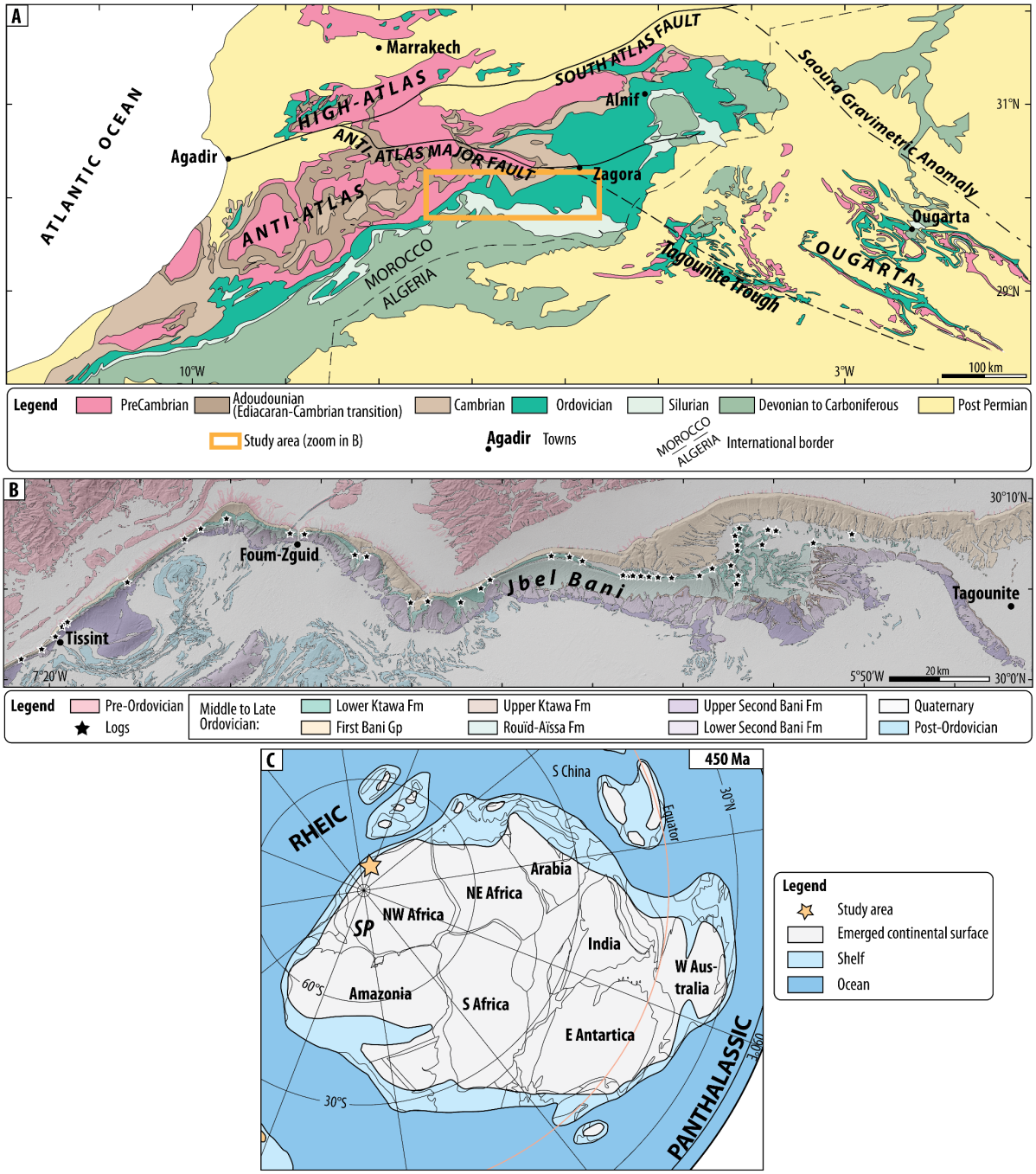

***Figure 1.1**: Geological context of the Ktawa Group in the Anti-Atlas, South Morocco. (A) Simplified geological map with characteristics features of southern Morocco and western Algeria (modified from Ghienne et al., 2007, Hollard et al., 1985, Ennih and Liégeois, 2001), with zoom in (B) Detailed geological map of the Jbel Bani cliff in the Central Anti-Atlas, including field-based stratigraphic profiles location (modified from Choubert et al., 1970, Choubert et al., 1989, Ennadifi, 1971). Background Digital Elevation Model: NASA (2019). (C) Paleogeographic reconstruction of Gondwana during Late Ordovician (450 Ma, Katian, modified from Cocks and Torsvik, 2021)*

inland influenced the global relative sea level as well as sediment transport (Sømme et al., 2009).

Furthermore, the Ktawa Group was deposited on the northern giant platform of North Gondwana (Fig. 1.1.C). As sediments deposit on a platform, several factors control the accommodation space available in the basin. These include local subsidence, global sea level variations and sediment supply, but also the compaction of sediments, isostatic adjustment due to a sedimentary load, river avulsion or piracy (Jankowski et al., 2017, Milliman et al., 1989, Polanco et al., 2024, Steckler et al., 2022, Syvitski et al., 2022). Megalobe of subaqueous deltas prograding and depositing sediments in shallow marine environments would create depression, i.e. accommodation space, on the side of the load after isostatic adjustment (Reynolds et al., 1991).

1.2. Outline of the thesis

The aim of this thesis is to investigate the deposits from a shallow marine siliciclastic platform in order to unravel the depositional environments, sediment dynamics, flexural to subsidence isostasy due to a sedimentary load, and to correlate these data and observations to other studies along a large and wide platform. We investigated the Lower Ktawa and Rouïd-Aïssa deposits, siliciclastic shallow marine sediments deposited on the northern passive margin of Gondwana during Early Sandbian to Katian (ca. 459 to 446 Ma). The deposits encompass offshore to storm-wave-dominated shoreface and tidal to river mouth environments. Depositional models were extrapolated from the stacking patterns, which lead to the reconstruction of relative sea level (RSL) curves. A composite RSL curve was extrapolated for the Lower Ktawa and Rouïd-Aïssa Formations to enable correlations to local, regional, and global studies. These were used to unravel the onset of the Late Ordovician glaciation prior to the Hirnantian maximum (ca. 445.2 Ma) in the study area. Finally, a study on the subsidence of the Lower Ktawa is used to investigate the isostatic adjustment of a sedimentary and how accommodation space created can control the emplacement and location of the next sedimentary load.

Chapter 2 is under submission in *Sedimentology*. This chapter focuses on the Lower Ktawa Formation, previously described in the literature as mudstone-dominated (Destombes, 1985). Detailed stratigraphic profiles were logged in the field, where seven sandstone-dominated packages were recognized outcropping in the mudstone-dominated background, which were defined as *members*. Grain-size, sedimentary structures, and ichnology were compiled in order to interpret facies associations. From the stacking pattern (i.e. genetic units), a typical sequence was interpreted for the Lower Ktawa deposits. Facies associations were

interpreted as depositional environments in order to reconstruct a depositional model for these deposits. However, two facies associations (out of eight) can be interpreted as two depositional environments (lower shoreface or lagoonal, shoals or barrier). This leads to two depositional models: a ramp-like setting and a bimodal setting including a barrier-lagoon system. Depending on the depositional model, the locality of the MRS will change and to some extent, change the reconstructed RSL curve. Finally, this chapter highlights the South-to-North prograding trend of the Lower Ktawa deposits, where sediments are deposited as megalobes shapes prograding toward the North.

Chapter 3 focuses on the sedimentology of the Rouïd-Aïssa Formation, which is sandstone-dominated, and overlies the Lower Ktawa Formation. Focus is put on the description of the facies associations recognized in the field. Proximal-to-distal trend of the deposits was interpreted as West to East, from changes in facies associations, thinning and fining trends of sandstones bodies. Regional tectonics is discussed in regard of whether tectonics might have an influence and control on the change of the proximal-to-distal trend between the Lower Ktawa and Rouïd-Aïssa Formations.

Chapter 4 investigates correlations from local to regional and global scales. From the seven sandstone members recognized, six 3rd order RSL cycles were interpreted after biostratigraphic calibrations and correlations of members. RSL curves were reconstructed for the Lower Ktawa and Rouïd-Aïssa Formations, extrapolated from depositional environments interpreted from facies associations. A composite RSL curve was reconstructed for the Ktawa Group. The curve was compared to the global RSL curve, geochemical proxies ($\delta^{18}O$ and $\delta^{13}C$), and regional studies (i.e. Ougarta, Hoggar, Armorican Massif, and Sardinia) to investigate the recognition of glacially induced events in the study area (e.g. Guttenberg Isotopic Carbon Excursion, Kope, Waynesville, and Whitewater). The deposition of the Ktawa Group lowstands (i.e. sandstone members) was likely driven by allocyclic, glacially related, eustasy.

Chapter 5 investigates the isostatic adjustment of sedimentary loads and resulted seabed morphology. The Lower Ktawa deposits are taken as the sedimentary load. Each member embedded in a RSL cycle was extrapolated as a megalobe shape (or a channel-complex) prograding toward the North. The Flex3D Matlab code was used to unravel the flexural isostasy due to deposition of each megalobe. After isostatic adjustment of each megalobe, accommodation space and depressions of the seabed are created on each side laterally of the megalobe. These are compared to the emplacement of the subsequence megalobe. The

accommodation space created on the sides of the megalobes after isostatic adjustment would control the emplacement of the subsequent megalobe. Furthermore, after deposition of the second member, the South-to-North prograding megalobes shift toward the East of the studied region. Hence, the deposition of the Lower Ktawa megalobe was likely driven by allocyclic eustasy related to glacial events, where the locality of the sediment and megalobe emplacement was likely influenced by autocyclicity of accommodation space created by flexural isostatic adjustment.

Chapter 6 outlines the main conclusions and outlook of this study.

References

Álvaro, J. J., Benharref, M., Destombes, J., Gutiérrez-Marco, J. C., Hunter, A. W., Lefebvre, B., Van Roy, P. & Zamora, S. 2022. Ordovician stratigraphy and benthic community replacements in the eastern Anti-Atlas, Morocco.

Catuneanu, O., Abreu, V., Bhattacharya, J., Blum, M., Dalrymple, R., Eriksson, P., Fielding, C. R., Fisher, W., Galloway, W. & Gibling, M. 2009. Towards the standardization of sequence stratigraphy. *Earth-Science Reviews,* 92**,** 1-33.

Choubert, G., Destombes, J., Faure-Muret, A., Gauthier, H., Hindermeyer, J., Hollard, H. & Jouravsky, G. 1970. Carte géologique de l'Anti-Atlas central et de la zone synclinale de Ouarzazate: feuilles Ouarzazate-Alougoum et Telouet sud. *Notes et Mém. Serv. Géol. Maroc,* 138.

Choubert, G., Faure-Muret, A. & Destombes, J 1989. Carte géologique du Maroc, Zagora-Coude du Dra-Hamada du Dra (pp). Echelle 1/200 000. *Notes Mém. Serv. Mines Carte géol. Maroc*.

Cocco, F., Loi, A., Funedda, A., Casini, L., Ghienne, J.-F., Pillola, G. L., Vidal, M., Meloni, M. A. & Oggiano, G. 2023. Ordovician tectonics of the South European Variscan Realm: new insights from Sardinia. *International Journal of Earth Sciences,* 112**,** 321-344.

Cocks, L. R. M. & Torsvik, T. H. 2021. Ordovician palaeogeography and climate change. *Gondwana Research,* 100**,** 53-72.

Dabard, M.-P., Guillocheau, F., Loi, A., Paris, F. & Ballèvre, M. 2009. Evolution de la plate-forme paléozoïque centre-armoricaine de l'Ordovicien au Dévonien. *12ème Congrès Français de Sédimentologie,* 65**,** 5-102.

Dashtgard, S. E., Vaucher, R., Yang, B. & Dalrymple, R. W. 2021. Hutchison medallist 1. Wave-dominated to tide-dominated coastal systems: a unifying model for tidal shorefaces and refinement of the coastal-environments classification scheme. *Geoscience Canada,* 48**,** 5-22.

Destombes, J. 1985. Lower palaeozoic rocks of Morocco. *Lower Palaeozoic of north-western and west-central Africa***,** 91-336.

Dietrich, P., Ghienne, J.-F., Lajeunesse, P., Normandeau, A., Deschamps, R. & Razin, P. 2019. Deglacial sequences and glacio-isostatic adjustment: Quaternary compared with Ordovician glaciations. *Geological Society, London, Special Publications,* 475**,** 149-179.

Dillenburg, S. R., Hesp, P. A., Angulo, R. J., Souza, M. C. D. & Lessa, G. C. 2009. The Holocene barrier systems of Paranaguá and northern Santa Catarina coasts, southern Brazil. *Geology and geomorphology of Holocene coastal barriers of Brazil***,** 135-176.

Driscoll, N. W. & Karner, G. D. 1994. Flexural deformation due to Amazon Fan loading: A feedback mechanism affecting sediment delivery to margins. *Geology,* 22**,** 1015-1018.

Ennih, N. & Liégeois, J.-P. 2001. The Moroccan Anti-Atlas: the West African craton passive margin with limited Pan-African activity. Implications for the northern limit of the craton. *Precambrian Research,* 112**,** 289-302.

Ghienne, J. F., Le Heron, D. P., Moreau, J., Denis, M. & Deynoux, M. 2007. The Late Ordovician glacial sedimentary system of the North Gondwana platform. *Glacial sedimentary processes and products***,** 295-319.

Hampson, G. J. & Premwichein, K. 2017. Sedimentologic character of ancient muddy subaqueous-deltaic clinoforms: Down Cliff Clay Member, Bridport Sand Formation, Wessex Basin, UK. *Journal of Sedimentary Research,* 87**,** 951-966.

Hollard, H., Choubert, G., Bronner, G., Marchand, J. & Sougy, J. 1985. Carte géologique du Maroc, scale 1: 1,000,000. *Serv. Carte géol. Maroc,* 260.

Jankowski, K. L., Törnqvist, T. E. & Fernandes, A. M. 2017. Vulnerability of Louisiana's coastal wetlands to present-day rates of relative sea-level rise. *Nature Communications,* 8**,** 14792.

Jelby, M. E., Grundvåg, S. A., Helland-Hansen, W., Olaussen, S. & Stemmerik, L. 2020. Tempestite facies variability and storm-depositional processes across a wide ramp: Towards a polygenetic model for hummocky cross-stratification. *Sedimentology,* 67**,** 742-781.

Lin, W. & Bhattacharya, J. P. 2021. Storm-flood-dominated delta: a new type of delta in stormy oceans. *Sedimentology,* 68**,** 1109-1136.

Loi, A., Ghienne, J.-F., Dabard, M.-P., Paris, F., Botquelen, A., Christ, N., Elaouad-Debbaj, Z., Gorini, A., Vidal, M. & Videt, B. 2010. The Late Ordovician glacio-eustatic record from a high-latitude storm-dominated shelf succession: The Bou Ingarf section (Anti-Atlas, Southern Morocco). *Palaeogeography, Palaeoclimatology, Palaeoecology,* 296**,** 332-358.

Marante, A. 2008. *Architecture et dynamique des systèmes sédimentaires silico-clastiques sur la" plate-forme géante" nord-gondwanienne: l'Ordivicien moyen de l'Anti-Atlas marocain.* Bordeaux 3.

Meddour, A. 2016. *Les séries de l'Ordovicien moyen et supérieur de l'Anti-Atlas oriental (Maroc): stratigraphie, sédimentologie et paléogeographie des systèmes de plate-forme silico-clastique.* Bordeaux 3.

Milliman, J. D., Broadus, J. M. & Gable, F. 1989. Environmental and economic implications of rising sea level and subsiding deltas: the Nile and Bengal examples. *Ambio***,** 340-345.

Mitchell, N. C., Masselink, G., Huthnance, J. M., Fernandez-Salas, L. M. & Lobo, F. J. 2012. Depths of modern coastal sand clinoforms. *Journal of Sedimentary Research,* 82**,** 469-481.

NASA/METI/AIST/Japan Spacesystems and U.S./Japan ASTER Science Team (2019). *ASTER Global Digital Elevation Model V003* [Data set]. NASA EOSDIS Land Processes Distributed Active Archive Center. https://doi.org/10.5067/ASTER/ASTGTM.003

Patruno, S. & Helland-Hansen, W. 2018. Clinoforms and clinoform systems: Review and dynamic classification scheme for shorelines, subaqueous deltas, shelf edges and continental margins. *Earth-Science Reviews,* 185**,** 202-233.

Pohl, A., Donnadieu, Y., Le Hir, G., Ladant, J. B., Dumas, C., Alvarez-Solas, J. & Vandenbroucke, T. R. 2016. Glacial onset predated Late Ordovician climate cooling. *Paleoceanography,* 31**,** 800-821.

Polanco, S., Blum, M., Salles, T., Frederick, B. C., Farrington, R., Ding, X., Mather, B., Mallard, C. & Moresi, L. 2024. Flexural isostatic response of continental-scale deltas to climatically driven sea level changes. *Earth Surface Dynamics,* 12**,** 301-320.

Proust, J.-N., Pouderoux, H., Ando, H., Hesselbo, S. P., Hodgson, D. M., Lofi, J., Rabineau, M. & Sugarman, P. J. 2018. Facies architecture of Miocene subaqueous clinothems of

the New Jersey passive margin: Results from IODP-ICDP Expedition 313. *Geosphere,* 14**,** 1564-1591.

Reynolds, D. J., Steckler, M. S. & Coakley, B. J. 1991. The role of the sediment load in sequence stratigraphy: The influence of flexural isostasy and compaction. *Journal of Geophysical Research: Solid Earth,* 96**,** 6931-6949.

Sømme, T. O., Helland-Hansen, W. & Granjeon, D. 2009. Impact of eustatic amplitude variations on shelf morphology, sediment dispersal, and sequence stratigraphic interpretation: Icehouse versus greenhouse systems. *Geology,* 37**,** 587-590.

Steckler, M. S., Oryan, B., Wilson, C. A., Grall, C., Nooner, S. L., Mondal, D. R., Akhter, S. H., Dewolf, S. & Goodbred, S. L. 2022. Synthesis of the distribution of subsidence of the lower Ganges-Brahmaputra Delta, Bangladesh. *Earth-Science Reviews,* 224**,** 103887.

Syvitski, J., Anthony, E., Saito, Y., Zăinescu, F., Day, J., Bhattacharya, J. P. & Giosan, L. 2022. Large deltas, small deltas: Toward a more rigorous understanding of coastal marine deltas. *Global and Planetary Change,* 218**,** 103958.

Torsvik, T. H. & Cocks, L. R. M. 2013. Gondwana from top to base in space and time. *Gondwana Research,* 24**,** 999-1030.

Vidal, M., Loi, A., Dabard, M.-P. & Botquelen, A. 2011. A Palaeozoic open shelf benthic assemblage in a protected marine environment. *Palaeogeography, Palaeoclimatology, Palaeoecology,* 306**,** 27-40.

Videt, B., Paris, F., Rubino, J.-L., Boumendjel, K., Dabard, M.-P., Loi, A., Ghienne, J.-F., Marante, A. & Gorini, A. 2010. Biostratigraphical calibration of third order Ordovician sequences on the northern Gondwana platform. *Palaeogeography, Palaeoclimatology, Palaeoecology,* 296**,** 359-375.

CHAPTER TWO

Sedimentary facies and shelf morphology of the Late Ordovician Ktawa Group (Morocco): shoreface or barrier-lagoon within a siliciclastic storm-dominated platform?

Déborah Caroline Stella Harlet [1,2], Guilhem Amin Douillet [1], Chloé Bouscary [3,4], Pierre Dietrich [5], Jean-François Ghienne [6], Philippe Razin [7], Fritz Schlunegger [1]

[1] Institut für Geologie, Universität Bern, Bern, Switzerland

[2] iCRAG, University College Dublin, Dublin, Ireland

[3] GFZ Potsdam, Helmholtz-Zentrum Potsdam, Potsdam, Germany

[4] Liebniz Institute for Applied Geophysics - LIAG, Hannover, Germany

[5] CNRS, Géosciences Rennes, Université de Rennes 1, Rennes, France

[6] CNRS, ITES, Université de Strasbourg, Strasbourg, France

[7] ENSEGID, Université Bordeaux Montaigne, EA 4592, Pessac, France

Abstract

The Lower Ktawa Formation in the Central Anti-Atlas (Morocco) exhibits Late Ordovician deposits from the northern rim of the Tindouf basin. They record a series of regression-transgression cycles within a shallow marine, storm-dominated, siliciclastic platform. These cycles exhibit variations from offshore to tidal/river mouth environments, which are related to glacial events during the early phases of the Late Ordovician glaciation. Up to 7 sequences spanning ca. 10 Myr have been recognized in the form of sandstone-rich units defined as "members".

Most members record thick coarsening-upward and thin fining-upward trends. They contain a variety of event-related beds and hummocky-cross-stratification emphasizing the influence of storm-wave action. The coarsening upward sequences are often interrupted by packages of intensely bioturbated material, which are usually topped by amalgamated HCS sandstones. This configuration is thought to record a bimodal coast, with the passage from an open-coast, storm-wave-dominated environment during sea level fall, to a lagoon-barrier system during lowstand and sea level rise. Alternatively, these horizons of bioturbated sandstones might develop within a purely open-coast system, whereby particular conditions would allow bioturbation rates to overtake the sediment input and preservation rates, in a lower shoreface environment. The two contrasted interpretations for the bioturbated sandstones imply a position of the Maximum Regressive Surface at the base of the bioturbated sandstones for a barrier-lagoon system, or within the base of amalgamated sandstones in an open-coast setting.

Two members differ significantly in terms of facies association, preserving coarse-grained, bioturbated, cross-bedded and rhythmically bedded sandstones. They are understood as tidal to river-mouth deposits deposited within channel belt systems reflecting major drops in relative sea level.

The progradation direction is interpreted as roughly South to North, based on the symmetry of facies associations and architecture along the semi-3D West-East transect, as well as lateral thinning trends of members.

2.1. Introduction

Siliciclastic coasts dominated by waves and storm processes represent about 20 to 30% of the worldwide modern coastlines (Davidson-Arnott, 2011). These sandy coasts display a large variety of morphologies, such as beach ridges in the open coast and strand plains, barriers and lagoons, spits, longshore bars etc. Their occurrence, formation and evolution through time and space are controlled by a combination of sediment supply and availability, transport energy of waves, and variations of relative sea level (RSL) (Anderson et al., 2016, Dillenburg et al., 2009, Dominguez and Da Silva Pinto Bittencourt, 1996, Fraser et al., 2005, Hein et al., 2013, Otvos, 2012, Otvos and Carter, 2013, Tamura, 2012). The morphology and evolution of modern coasts is largely influenced by glacio-eustatic and glacio-isostatic RSL changes linked to the Last-Glacial-Maximum (Meijer, 2002). Whereas the impacts of these variations on the coastal morphologies can be quantified for short timescales (Lerma et al., 2019, Masselink et al., 2022), the stratigraphic architectures and sediment-facies changes that arise from RSL fluctuations over millions of years can only be accessed from the sedimentary record. In order to better understand the long-term evolution of siliciclastic storm dominated platforms, one must therefore combine information from the large-scale architecture, with detailed sedimentary facies analysis.

Here, we take advantage of a large-scale outcrop (100s km in length, 100s m in thickness) in the Central Anti-Atlas in southern Morocco that offers a continuous exposure on a wave- and storm-dominated siliciclastic succession (Fig. 2.1). The deposits of the Ktawa Group (also "Ktaoua" in e.g. Choubert, 1942, Colmenar et al., 2022, Destombes, 1985, Gutiérrez-Marco et al., 2022, Loi et al., 2010, Meddour, 2016), early Late Ordovician in age, and deposited on the northern passive margin of Gondwana (Cocks and Torsvik, 2021, Destombes, 1985) were investigated. The goal is to determine in detail the lateral variations of facies associations, which are combined with data about the large-scale stratigraphic architecture, and the long-term evolution through time, yielding new information that will challenge commonly accepted depositional models.

2.1.1. Storm-wave imprint

Siliciclastic, storm-dominated environments have been described and documented at a high level of details from the Ordovician in Morocco and over the entire northern Gondwana platform (Chacrone et al., 2004, Destombes, 1985, Loi et al., 2010, Razin et al. 2020). Such

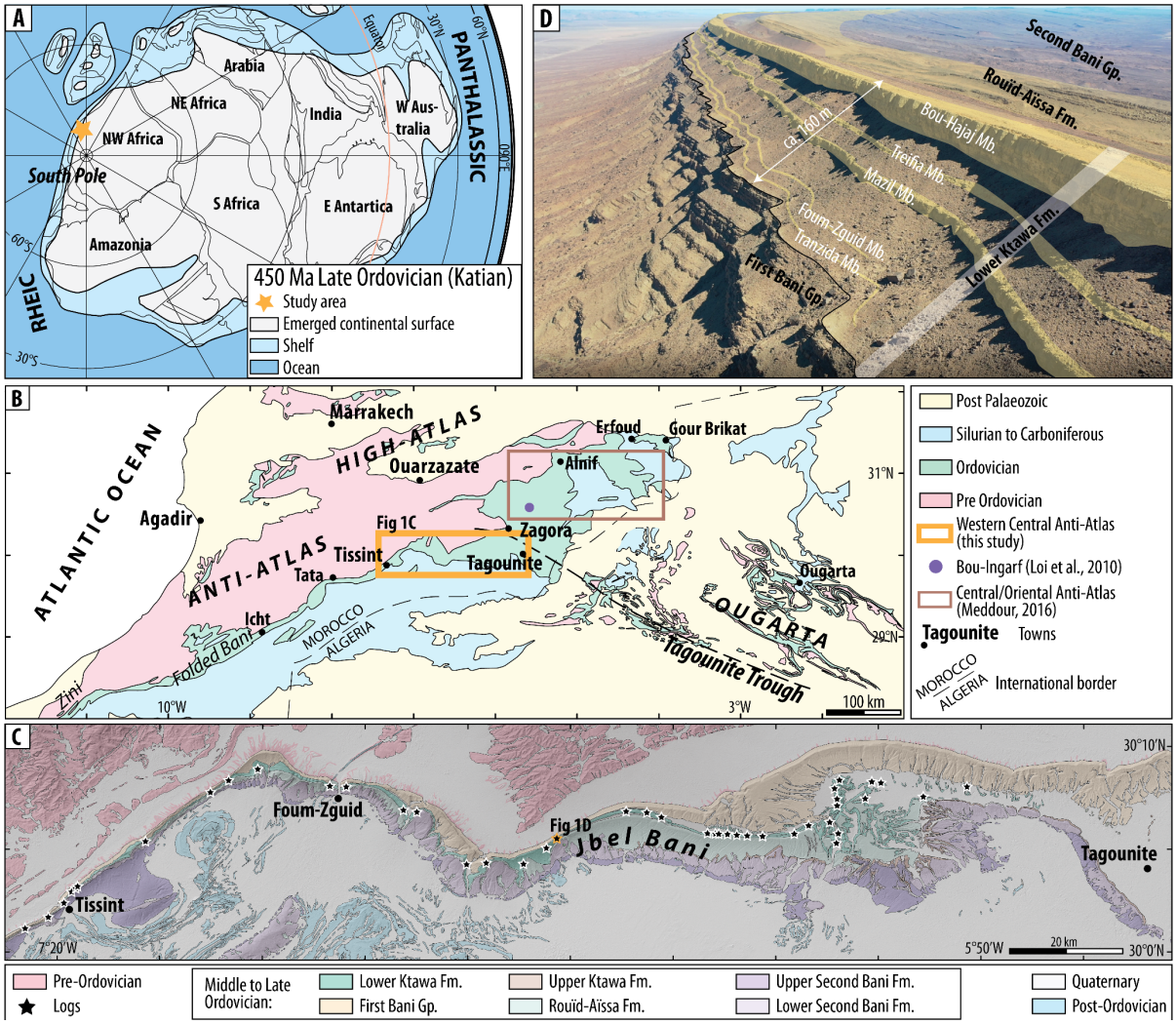

***Figure 2.1**: Location of the studied area. (A) Paleogeographic reconstruction of Gondwana during the Late Ordovician (Katian, 450 Ma, modified from Cocks and Torsvik, 2021). (B) Simplified geological map of southern Morocco and western Algeria, highlighting the Late Ordovician deposits South of the Atlas Mountain Range (modified from Ghienne et al., 2007, Hollard et al., 1985). (C) Detailed geological map of the Jbel Bani cliff between the localities of Tissint and Tagounite, including location of profiles (Choubert et al., 1970, Choubert et al., 1989, Ennadifi, 1971). Background Digital Elevation Model: NASA (2019). (D) Aerial photograph of the Jbel Bani with emphasis on the Lower Ktawa Members (location: orange star on map C).*

sedimentary successions have characteristic organizations of mudstones and intercalated sandstone beds (e.g. Dashtgard et al., 2021, Ghienne et al., 2007, Hampson, and Storms, 2003, Keen et al., 2012), the latter exhibiting distinctive sedimentary structures known as Hummocky and Swaley Cross Stratifications -HCS and SCS- (Cheel et al., 1993, Dott Jr and Bourgeois, 1982, Harms et al., 1975, Jelby et al., 2020, Myrow and Southard, 1996). HCS/SCS are traditionally interpreted as sedimentary structures built from sand reworked from the shoreface by

storm waves and deposited farther distally by a combination of long wavelength storm wave oscillations and density currents (e.g. Dumas and Arnott, 2006, Greenwood and Sherman, 1986, Tinterri, 2011). They reflect a continuum spectrum of surface waves that impacted the seabed from offshore to shoreface environments (e.g. Basilici et al., 2012, Ito et al., 2001, Peters and Loss, 2012).

2.1.2. Bioturbation imprint

Within storm-wave-dominated sedimentary facies associations, it is common to encounter sandstone intervals that are highly bioturbated (Baniak et al., 2014, Gil-Ortiz et al., 2022, Hampson, 2010, La Croix and Gingras, 2021). These contrast with storm-wave-dominated facies associations suggesting a calmer depositional environment, and they appear out of sequence on a wave-dominated depositional succession. They are generally interpreted as representing the zone where wave action is low enough to minimize reworking, yet with important inputs of nutrients and thus intense colonization by biota. Data from modern storms suggest that there is a minimal bed thickness and recurrence interval for storm-derived beds to be preserved from bioturbation reworking (e.g. Bentley et al., 2006, Keen et al., 2006). Alternatively, it has been suggested that bioturbated sandstones within storm-dominated successions could be emplaced within a locally protected to restricted marine environment (e.g. Dabard et al. 2015, Loi et al. 2010).

Whereas the vertical stack of storm-influenced beds over geological time has been commonly described, and the short-term evolution of shoreline morphologies during the Holocene transgression is relatively well understood, the spatial evolution of storm-dominated coasts remains blurry for geological timescales (e.g. Gao and Collins, 2014, Grundvåg et al., 2021, Hampson and Storms, 2003). This subject is addressed here, with special attention given to the dichotomy of storm sequences between a regressive and transgressive context. Indeed, storm successions are essentially deposited within a regressive falling sea level stage context, whereas transgressive settings preserve limited and concentrated stratasets. It will be argued that the morphology of the shore and shallow water ramp shows bimodal characteristics with distinct regressive and transgressive morphologies. In particular, the significance of intensely bioturbated sandstones intercalated in successions otherwise dominated by a storm signature will be discussed. It is suggested that a regressive open marine environment would switch to a barrier lagoon system during the

early transgression phase. Such a bimodal ramp setting would be characterized by two distinct systems of facies associations, sedimentary systems and ramp morphology occurring subsequently during the regressive and transgressive phases.

2.2. Geological setting

The Anti-Atlas range of Morocco exposes the northern rim of the Tindouf intracratonic sedimentary basin (Fig. 1). The latter consists of an up to 10-km thick succession spanning the time interval between the Latest Neoproterozoic and the Late Carboniferous (Boote et al., 1998, Michard et al., 2008). This sedimentary basin was inverted in the Late Carboniferous and Permian during the Variscan orogeny, exposing the sedimentary succession (Fig. 2.1, Burkhard et al., 2006, Hoepffner et al., 2005). The Neoproterozoic to Mid Ordovician suite consists of an up to 1.6 km-thick pile of sediments recording the response to a large-scale and polyphased flooding (Álvaro et al., 2007, 2022, Beuf et al., 1971, Bourahrouh et al., 2004, Colmenar and Alvaro, 2015, Craig et al., 2008, Destombes, 1985, Ghienne et al., 2007, 2023, Hamoumi, 1999, Lefebvre et al., 2016, Lefebvre et al., 2018, Marante, 2008, Martin et al., 2016, Meddour, 2016, Vaucher et al., 2016, 2017, Videt et al., 2010, Villas et al., 2006). During the Late Ordovician, the Tindouf Basin was located at a high paleolatitude between 80°S (ca. 450 Ma) and 70°S (ca. 445 Ma) (Fig. 2.1A, Cocks and Torsvik, 2021). During this time interval, siliciclastic sedimentation prevailed and was marked by fluvial, shallow-marine and offshore environments (Fig. 2.2A, Destombes, 1985, Loi et al., 2010). The end-Ordovician glacial episode is archived by glacigenic material and glacial erosion surfaces. The related deposits filled in 50-250 m-deep troughs that are incised into the underlying sedimentary succession (Figs 2.2A-B, and 3, Loi et al., 2010, Clerc et al., 2013, Ravier et al., 2015, Dietrich et al., 2019, Ghienne et al., 2014, Le Heron, 2007).

The study area is located in the western Anti-Atlas, between the towns of Tissint to the West and Zagora to the East

***Figure 2.2**: Nomenclature. (A) Lithostratigraphic units in the Anti Atlas as defined by Destombes (1985), including localities for Loi et al. (2010) and Meddour (2016). (B) Correlations of the Ktawa and Second Bani Group along the Jbel Bani cliff between the towns of Tissint and Alnif including the 7 members defined in this study compiled with neighboring localities investigated in Loi et al. (2010) (and modified after Álvaro et al., 2022) and Meddour (2016). glacigenic deposits modified from Dietrich et al. (2019). See Fig. 2.1B for location. (C) Chronostratigraphic correlations with respect to chitinozoan biozones.*

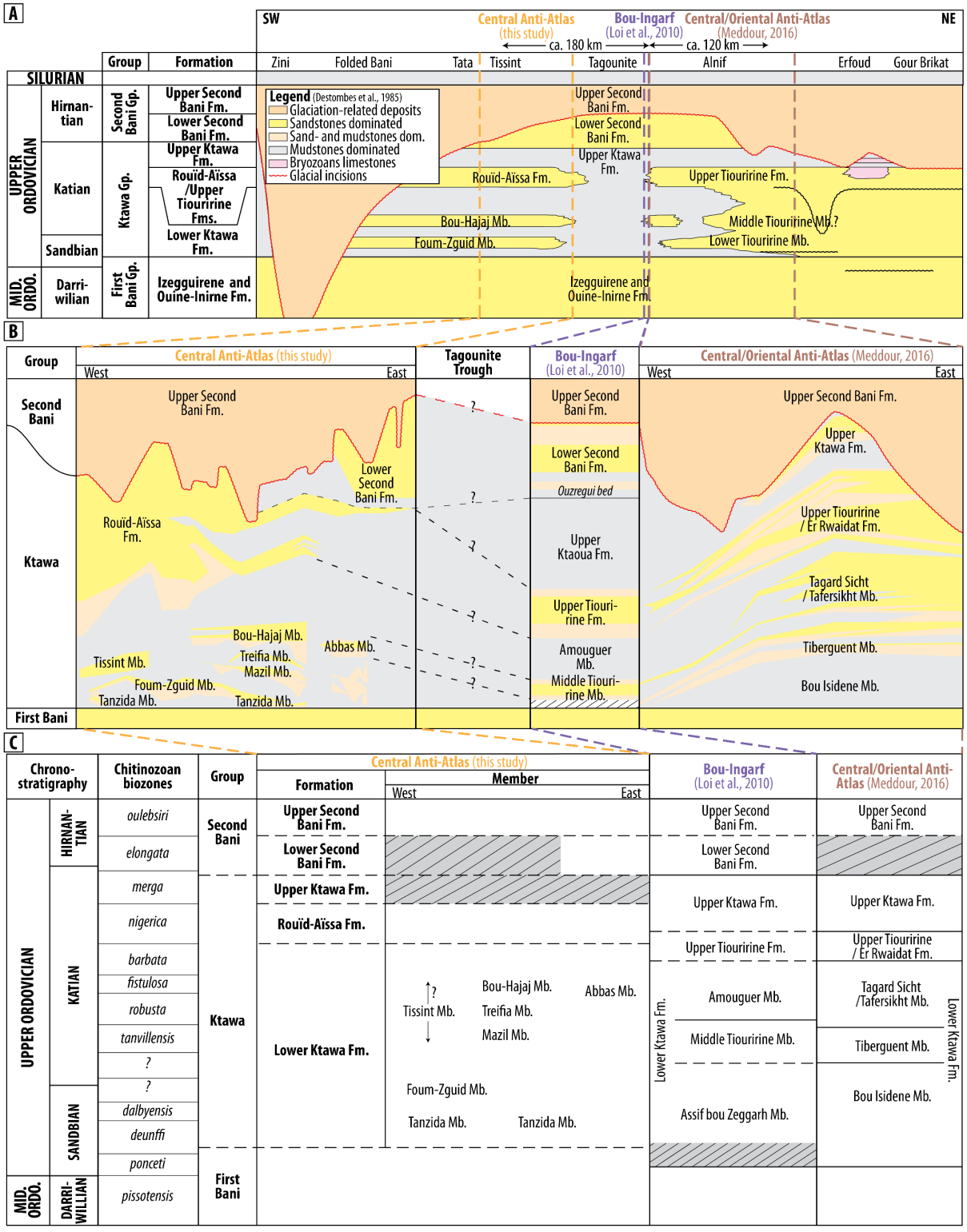

(Fig. 2.1B and C). Here, the Middle to Late Ordovician sedimentary successions outcrop as up to 1400 m high prominent cuestas, called the Jbel Bani (Bani Range). The Jbel Bani is organized in multiple cuestas formed by resistant sandstone lithologies, which themselves are intercalated in recessive foothills or badlands made up of muddier, less-resistant material. The sedimentary succession is

divided into three lithostratigraphic groups (Destombes, 1985; Videt et al., 2010) that are from base to top: (i) the First Bani Group of late Middle to early Late Ordovician age (Darriwilian to Early Sandbian, Marante, 2008); (ii) the Ktawa Group, mid-Sandbian to Katian in age (Fig. 1D); and (iii) the Second Bani Group, Hirnantian in age, including glacigenic deposits in its upper part (Fig. 2.2).

The age of the Ktawa Group is biostratigraphically constrained, and the unit contains a rich fauna including brachiopods, trilobites, echinoderms, gastropods, bivalves, ostracods and palynomorphs (Fig. 2.2C, Álvaro et al., 2007, Colmenar et al., 2022, Destombes, 1985, Elaouad-Debbaj, 1984, Fortey and Edgecombe, 2017, Gutiérrez-Marco and Vinn, 2018, Gutiérrez-Marco et al., 2021, Videt et al., 2010,). The Ktawa Group is itself subdivided into three formations: (a) the Lower Ktawa Formation (ca. 250 m thick, mid-Sandbian to mid-Katian), mostly consisting in the area of fine-grained sediments with interstratified sandstone lenses; (b) the Rouïd-Aïssa Formation (ca. 200 m thick, Middle-Late Katian), mainly composed of sandstone beds; and (c) the Upper Ktawa Formation, dominated by mudstones (Late Katian). From the West to the East of the study area, the Upper Ktawa Formation has been progressively eroded beneath the glaciation-related succession of the Upper Second Bani Group (Fig. 2.2B and C). The Lower Ktawa Formation, the focus of this study, encompasses a sedimentary succession deposited in shallow marine environments ranging from offshore to coastal through wave and storm-dominated depositional environments (Fig. 2.2B and C, Loi et al., 2010, Meddour, 2016). Here, focus is put on the analysis of the sedimentary facies associations within the Lower Ktawa Formation, their spatial extension and significance in terms of paleoenvironments. A separate contribution is dedicated to the Rouïd-Aïssa Formation (Chapter 3).

2.3. Methods

A field-based dataset consisting of 42 sedimentary profiles was acquired along a continuous, ca. 150 km-long transect oriented in a general E-W direction along the Jbel Bani cliff (Figs 2.1C and 2.3). The profiles were measured at a scale of 1:100 and analyzed through facies description (grain size, sedimentary structures, fossiliferous and ichnology content, Appendix A) and interpreted in terms of depositional environments. Thicknesses were re-calibrated from 3D photogrammetric reconstructions acquired with an Unmanned Aerial Vehicle (UAV) for 17 logs (Appendix B). From the 42

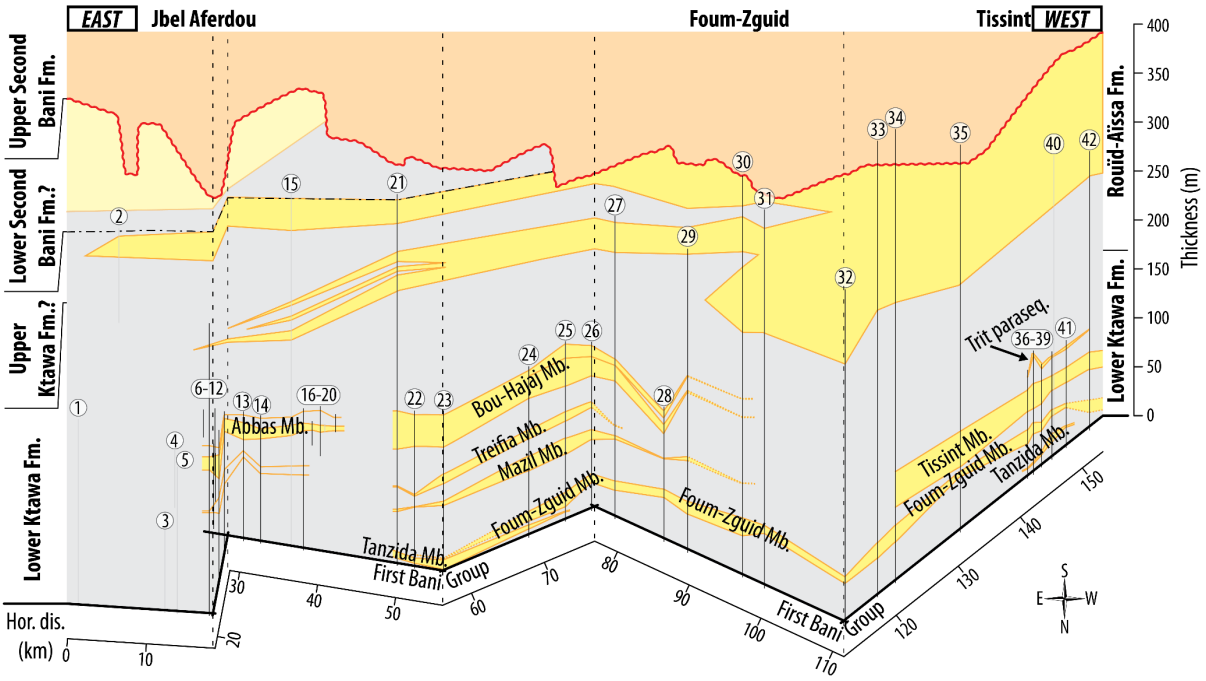

***Figure 2.3**: Overview of the entire investigated transect between the towns of Tissint and Zagora in semi-3D with location and heights of the individual log profiles. The figure is oriented E-W in order to match the orientation of the Jbel Bani cliff outcrop that faces North. The base line follows the 2D path of the Jbel Bani cliff with logs pointing up vertically. Gray vertical lines: stratigraphic profiles. Black vertical lines: stratigraphic profiles shown in Figs 2.14 to 2.18. Identified sandstone members are correlated from satellite and UAV images.*

profiles encompassing the Lower Ktawa Formation, 12 sections were further extended into the overlying Rouïd-Aïssa Formation, thereby reaching the base of the glacigenic deposits in locations where the Lower Second Bani Formation and uppermost part of Upper Ktawa have been eroded.

Members: The sedimentary analysis revealed the existence of individual sand-dominated packages, thereafter referred informally to as 'member' (Fig. 2.2B and C). Sandstone members were named after nearby type localities whereas the mudstone-dominated intercalations have not been considered as members. Physical correlations of these members between the profiles were performed from aerial images from the UAV and Google Earth engine (Fig. 2.3). Seven individual members physically disconnected from each other have been defined, from base to top: Tanzida, Foum-Zguid, Tissint, Mazil, Treifia, Abbas, Bou-Hajaj. The Foum-Zguid and Bou-Hajaj Mbs were individualized in the original lithostratigraphic scheme of Destombes et al. (1985) (Fig. 2A), yet they actually correspond to several members and their extension was overestimated in the original

scheme. The 5 other members correspond to newly described units. In addition, taking advantage of the zigzagging patterns of the Jbel Bani cliffs, semi-3D representations of the transects and logs are presented as fence diagrams, i.e. the datum-height of the topmost beds of the First Bani Group (underlying the base of the Ktawa Group) are plotted on a 2D localization pathway, from which vertical logs emanate (Figs 2.3, 2.14-18). Whereas physical discontinuity was established, the possible affiliation of several members to the same RSL cycles, their timing and correlation to regional and global scale signals will be discussed in a companion contribution (Chapter 4).

Datum: Considerations on the geometry and correlation of members rely on a fixed reference datum. Here, the reference bed is defined as the composite limit formed by the topmost sandstone beds of the underlying First Bani Group. Whereas these beds are a good geomorphic marker in the field at the scale of the study area, they might not have represented a flat geometry during deposition of the Ktawa sediments. Indeed, the First Bani sandstones appear to record more proximal depositional environments in the eastern part of the study area than on the western end (close to the Tissint area). However, we are currently not able to fully solve this problem with the available dataset and thus employed the topmost beds of the First Bani Group for the sake of simplicity.

Dietrich et al. (2019) represented the geometry of the Late Ordovician glacial incisions and those of the underlying Ktawa Group and top of First Bani Group using the base of the Silurian flooding as datum. This resulted in a W-E impression for the orientation of the distalization of the Lower Ktawa Fm. This choice, relevant for the study of the Late Ordovician glacigenics directly preceding the Silurian flooding, may however not apply for the entire Ktawa Group, and especially for the Lower Ktawa Fm, as the platform may well have evolved in ca. 13 Myr separating these deposits. All in all, given that the initial bathymetric profile is unknown and that isostatic subsidence due to sediment loading may have been acting during deposition (Pratson et al., 2007), it is not possible to rely on a unique reference for the ca. 13 Myr time interval corresponding to the Ktawa Group deposition. Only iterative processes can give an insight of the actual bathymetric profiles for each member. This aspect will be developed in a companion contribution (Chapter 5). Here, for simplicity, the reference is kept at the closest stratigraphic marker, i.e. the topmost beds of the First Bani Group.

2.4. Facies associations

The different sedimentary facies observed along the 42 sedimentary profiles were grouped into 8 facies associations (FAs). They represent a plethora of depositional environments reflecting the diversity of depositional conditions in a storm-influenced context through time and space, hereafter described and interpreted from distal to proximal.

2.4.1. Mudstones

Description: The mudstone facies association mainly consists of clayed to silty mudstones (Fig. 2.4A and B). These mudstones outcrop as finely laminated, mm-thick fissile shales to siltstones. Intercalations of planar or rippled silt layers up to a few cm in thickness, occasionally intensely bioturbated, are frequent. Alternation between mudstones and silts define highly asymmetric m-thick cycles in bed thickness, predominantly coarsening-upward.

Interpretation: The mudstones facies association is interpreted as deposited in a calm, subaqueous setting, dominated by decantation of a suspended load (Macquaker and Gawthorpe, 1993). The sediment input may come from diffuse suspension distributed within the water column or the distal signal of turbid plumes, as suggested by rippled silty layers indicating a tractive component (Talling et al., 2012). An offshore depositional environment is thus interpreted. The m-thick cyclic coarsening-upward trends may indicate the distal expression of a fluctuating sea level (Loi et al., 2010, Macquaker and Gawthorpe, 1993).

2.4.2. Ferruginous horizons

Description: Dark brown and highly competent horizons, up to 1.5 meters in thickness, consist of highly ferruginous beds encompassing abundant concretions (Fig. 2.4B to F). They often include phosphate and/or manganese pebbles as well as ferruginous to phosphatic oolites (Fig. 2.4C and D). These horizons overprint and bleach various other facies associations described below, sometimes with intense bioturbation (Fig. 2.4E). They occur either as isolated layers, as stacks of several layers either separated by dm-thick mudstones or fully amalgamated on each other.

Interpretation: Ferruginous horizons are interpreted as resulting from the dominance of chemical precipitation over detrital sedimentation and hence as a marker of low sedimentation rates (Mattern et al., 2022). They are therefore interpreted as condensed levels that develop on previously deposited material, most likely during the retrogradation phase (Dabard et al., 2015,

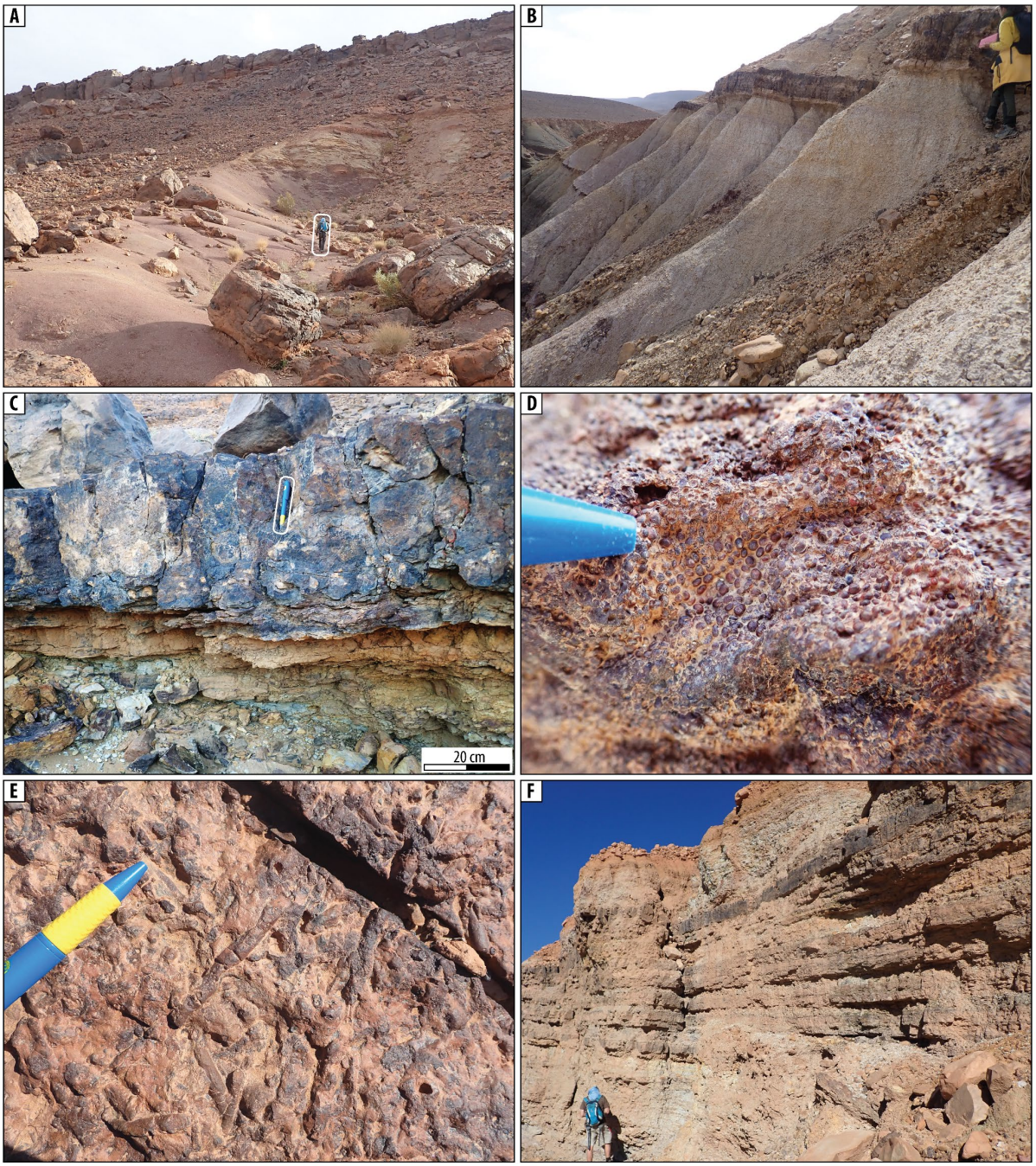

***Figure 2.4**: Offshore facies associations. (A) and (B): Mudstones. (B)-(F) Ferruginous levels. (B): Ferruginous horizon within shale. (C): Phosphate pebbles distributed within ferruginous level have light colors. (D): Ferruginous oolitic clasts. (E): Bioturbation within ferruginous level. (F): Stacked ferruginous levels within shales to silts and sand ripples. (A), (B) and (F): Geologist for scale 172 cm (C)-(E): Pen for scale 13.7 cm.*

Pistis et al., 2016), and as a marker of a time span during which the transgression occurred at the highest rates (McLaughlin et al., 2008).

2.4.3. Silts and sandstones with ripple marks

Description: Two lithologies characterize this heterogeneous facies, dominated by

laminated silts with subordinate intercalations of rippled sandstones (Fig. 2.5). Sandstone layers are a few cm thick and laterally continuous over at least 10-100s m. They are characterized by the occurrence of starved to climbing uni- to bidirectional ripples sometimes grading into plane lamination (Jobe et al., 2012). Hummocky-like ripples are common, characterized by sigmoidal and aggrading laminae forming pinch-and-swell bundles with reversing progradation direction (Fig. 2.5B). These beds laterally evolve from erosive-based to conformable. The organization resembles an heterolithic facies in places. Horizontal bioturbation is common, and presents variations in intensity, from anecdotic traces up to intensive overprint of the primary sediment structures at a plurimeter scale.

Interpretation: Laminated silts are interpreted as deposited in a calm environment from settling of material, likely in an offshore environment, although coarser and therefore more proximal than the previously described mudstones FA. Ripples result from tractive currents and their intercalation within the laminated silts indicate the occurrence of intermittent tractive events such as low-density sediment gravity flows (Talling et al., 2012). The recurrence of these sandstone layers points to recurrent trigger processes such as flood or storms (Mutti, 2019, Talling et al., 2015). Bidirectional and hummocky-like ripples suggest oscillatory flows and a wave influence and are equivalent to the "micro-Hummocky Cross-Stratification" of Jelby et al. (2020). The coexistence of beds containing unidirectional ripples and bidirectional ripples (hummocky-like ripples) suggests that only some of the parental gravity currents were subjected to an oscillatory component during deposition. As a consequence, the depositional depth must be shallower than the effective storm wave-base for oscillatory structures, yet slightly deeper when unidirectional ripples were emplaced. This facies association is thus interpreted to represent the upper offshore zone. Variations in the intensity of bioturbation may be related to a change in the balance between sediment aggradation rate and bioturbation rate. These may be either linked with availability of nutrient, high frequency sea level fluctuations, or intensity and frequency of storms.

2.4.4. Siltstones and isolated HCS-bearing sandstones

Description: The distinctive feature of this facies association is isolated sandstone beds containing well-defined HCS interstratified within a succession of sediments similar to the "silt and sand ripples" facies association

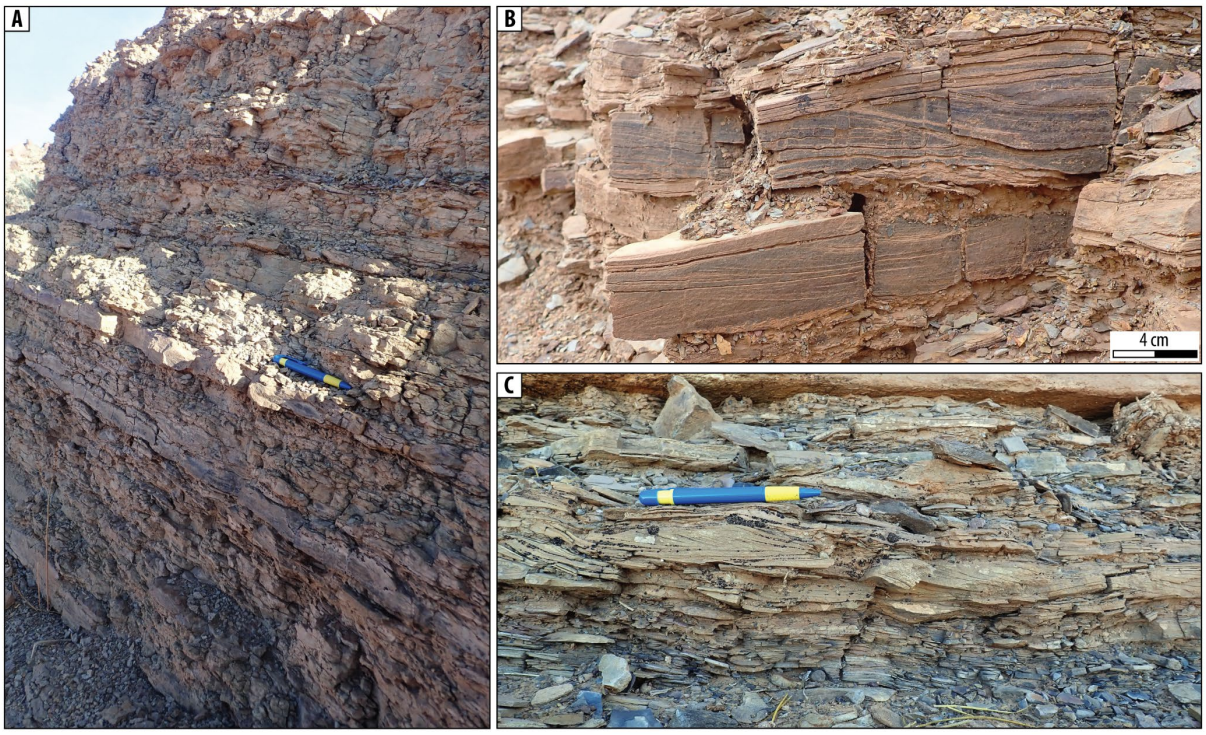

***Figure 2.5**: Silts and sandstone ripples facies association. (A) Isolated and continuous sandstone ripple beds within silt dominated ripple bedsets. (B) Hummocky-like ripples within isolated sandstone beds. (C) Coarsening- and thickening-upward heterolithic bedsets with unidirectional sandstone ripples. (A) and (C) Pen for scale 13.7 cm.*

(Fig. 2.6). The HCS-bearing sandstones are up to a few dm-thick and extend laterally either as lenses or continuously at least over the outcrop scale (>100 m). They are separated by dm- to several m-thick intervals of mudstones to heterolithics. The HCS-bearing sandstones commonly show a typical grading: 1) a flat and sharp base, without clear evidence of sole marks, which is overlain by 2) a massive basal zone evolving into 3) low-angle laminasets including truncations and hummocks that ultimately grade into 4) ripples, sometimes climbing ripples. The laminated parts of HCS often characteristically spall in platy pieces along sandstone laminae, rendering a slaty texture, possibly indicating clay/micaceous interlaminae. The upper part of HCS-bearing beds commonly displays horizontal traces (*Cruziana*) and rare vertical ichnofacies (*Skolithos*). In plan view, the shape of HCS bedforms vary from smooth hummocks to sharp brinkpoint (*sensu* Dumas et al., 2005). They have crestlines that are straight to linguoid, and irregular meter-scale pseudo-wavelengths.

Interpretation: As for 'silts and sand ripples', the finer intervals are interpreted as representing a calm, offshore environment dominated by the settling of buoyant material regularly disrupted by distal, low-density sediment gravity flows

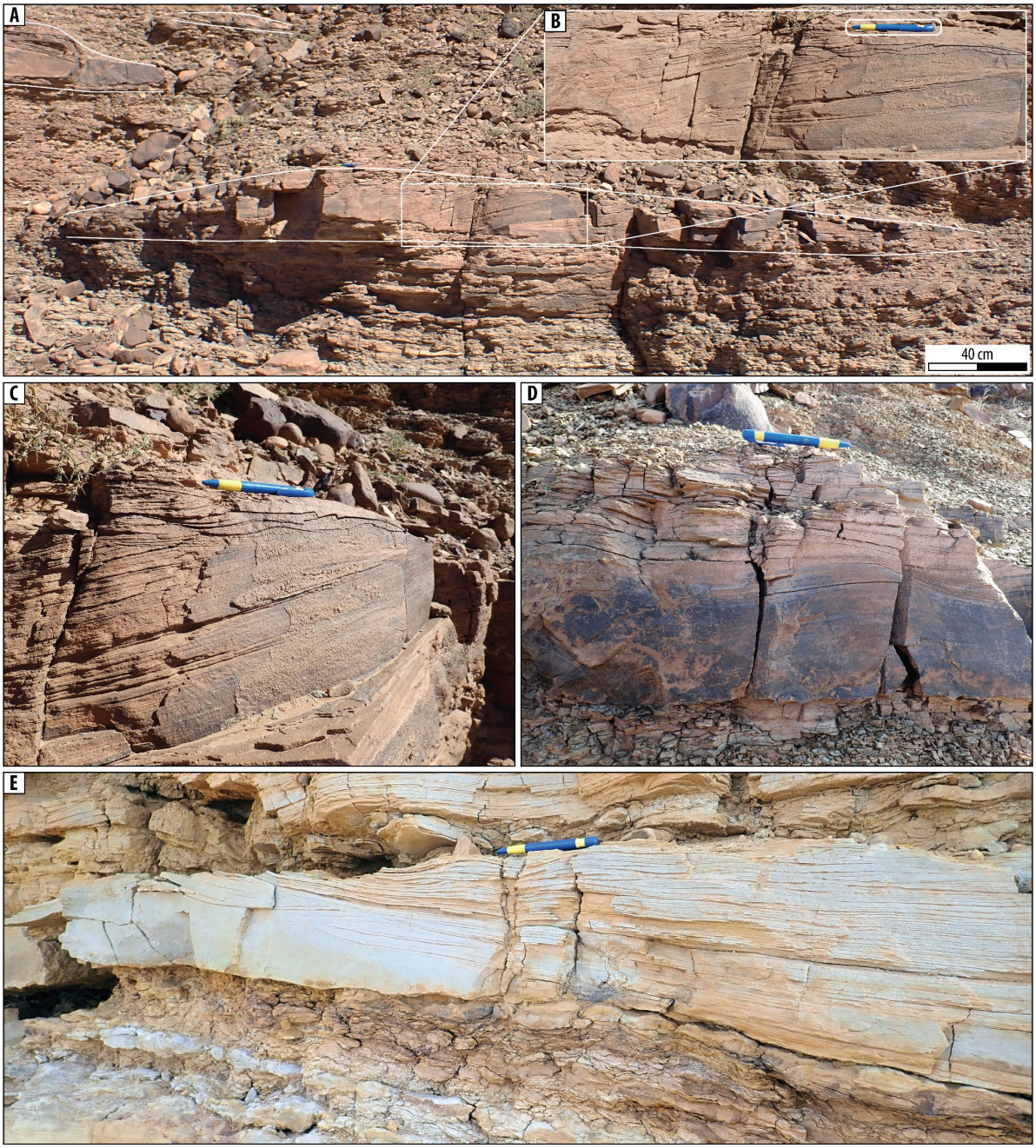

***Figure 2.6**: Silts and isolated HCS facies association. (A) Isolated HCS sandstone lens in silts and sand ripples with zoom in (B): Low-angle laminae with unidirectional climbing ripples at the top of the HCS. (C) Low-angle HCS laminasets evolving upward into unidirectional climbing ripples, with platy spalling. (D) Sharp-based HCS sandstone within shales, evolving from massive to low-angle. Two sandstone beds are possibly amalgamated. (E) Sharp-based isolated HCS sandstone with platy spalling within bioturbated silt and sandstone ripples. The lower left of the HCS is massive and evolves into low-angle truncations and into fully aggrading climbing ripples toward the top. (B)-(E) Pen for scale 13.7 cm.*

represented by sandstone beds. These sandstone beds indicate the occurrence of more energetic events. Within sandstone beds, the grading from massive sand to low-

angle laminasets to HCS and ultimately ripples resemble Bouma-type sequences and indicates deposition from waning flows (e.g. Lamb et al., 2008). HCS structures suggest that these events relate to an oscillatory component pointing toward combined oscillatory flows, i.e. an oscillation by waves superimposed on an unidirectional density current carrying the sediment load (Myrow, 2005, Myrow and Southard, 1996). Alternatively, the occurrence of truncating, low-angle laminasets might also be explained by the aggradation of Froude-supercritical flow antidunes and cyclic steps (Mulder et al., 2011, Rust and Gibling, 1990, Vaucher et al., 2018, Yagishita, 1994). HCS bearing sandstones can therefore be interpreted as representing emplacement from a spectrum of storm-derived or flood-derived events including turbidity currents and hyperpycnal flows (Jelby et al., 2020). The platy spalling of individual laminae suggests a bimodal grain size, with finer material and/or mica settling in between each sand lamina. In that sense, this would imply the occurrence of less energetic periods, during which the fine material would settle between the emplacement of successive sandstone laminae. In that view, the platy spalling might be a diagnosis feature for long period oscillations. This latter explanation further calls for an origin related to long-wavelength waves, such as deep storm- or swell-waves. The abundant "mudstones", and "silts and sand ripples" FAs in which HCS-bearing sandstone beds are intercalated, are interpreted as offshore or upper offshore limit. Therefore, the presence of HCS bearing beds, interpreted as deposited by recurrent event-currents likely related to powerful storm processes, indicate a depositional environment in the lower zone of the storm wave base within the upper offshore transition.

2.4.5. Stacked HCS sandstones

Description: In this FA, HCS-bearing sandstone beds similar to those described for the previous FA are stacked on each other with no or very little intercalation of 'silts and sand ripples' FA (Fig. 2.7). The HCS bedsets are 10-50 cm-thick and exhibit pronounced pinch and swell laminasets, as well as a well-developed platy spalling with parting lineations. Along the sandstone laminae, sand grains are well-sorted and range from fine- to medium-grained. Climbing ripple laminations are common in the upper part of beds. These HCS beds are stacked on each other often conformably or with local and limited truncations resembling SCS yet individual beds are tangled over large distances. This facies association occasionally contains pluricentimetric-

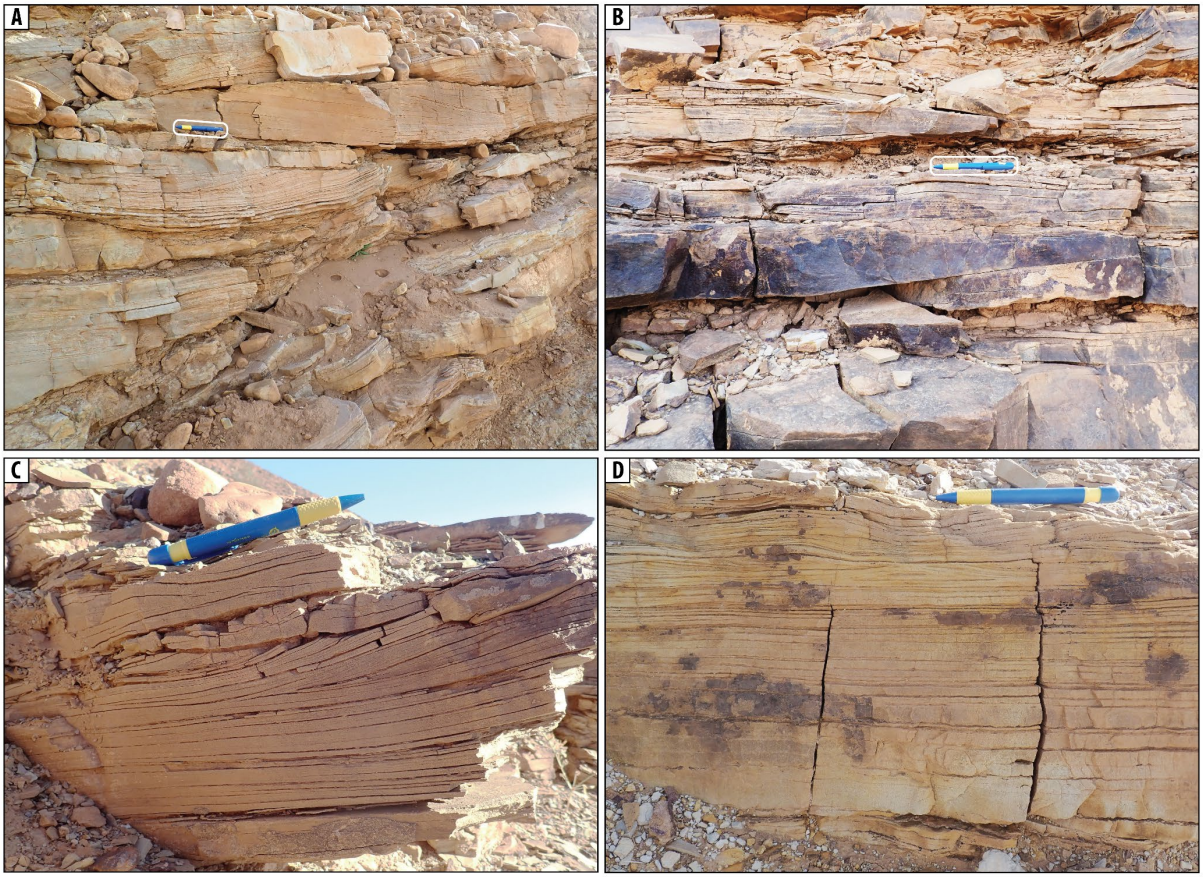

***Figure 2.7**: Stacked HCS sandstones facies association. (A) Low-angle slaty laminations and local truncations without preferential orientation. (B) Sharp-based HCS sandstones including massive based beds, slaty low-angle to sub-planar laminated beds and local truncations. (C) Slaty HCS with sub-horizontal laminations evolving into low-angle laminasets and truncation. (D) Thick planar laminae evolve into thin slaty laminasets of unidirectional to aggrading climbing ripples. Pen for scale 13.7 cm.*

thick lenses without lateral continuity made of matrix-supported coquina of centimetric biogenic/shells clasts.

Interpretation: HCS beds are interpreted as emplaced by storm-derived processes. The absence of interbedded heterolithics suggests that frequent storm-derived currents reached the depositional area, without allowing consequent calm enough periods for the settling of fines. The platy spalling between individual laminae suggests a pulsating current including waning phases in between each sand lamina for fines or mica to deposit. It may also result from the intense parting lineation that would refer to the alignment of particles in an upper flow regime (i.e. Froude supercritival currents; Amy et al., 2016, Fielding, 2006, Paola et al., 1989). In order to preserve such deposits, reworking must remain minor and thus emplacement cannot have occurred above an effective fair-weather wave base where constant remobilization prone to homogenization

usually occurs. Additionally, the stacking with few occurrences of swales further implies that the depositional zone is largely aggradational with only minor erosion. The presence of coquina lenses is envisioned as representing local hyperconcentration of these clasts due to reworking by mechanical sorting (winnowing) related to some specific flow dynamics and the atypical drag of the bioclasts (Álvaro et al., 2022, Bayet-Goll et al., 2015, Cattaneo and Steel, 2003, Ichaso and Dalrymple, 2009, Loi et al., 2010, Li et al., 2011, Vaucher et al., 2017). This facies association is thus understood as representing an environment shallower than the previous 'silts and isolated HCS', yet below the effective fair-weather base. It thus represents the transition zone from offshore to shoreface environment.

2.4.6. Quartzose amalgamated sandstones

Description: Quartzose amalgamated sandstones consist of well-sorted fine- to medium-grained thick sandstone packages organized as individual beds 0.2-1.5 m thick. The latter are fully amalgamated and occur in crosscutting relationships (Fig. 2.8A to C). Erosive bases are the norm and occur as sub-horizontal undulations, decimetric gullies and plurimetric troughs. Individual beds tend to display a massive aspect, yet lamination is sometimes observed. The latter include mainly HCS and more rarely sub-horizontal, low-angle, sigmoidal, tangential and trough cross-lamination. Rarely, shell bioclasts, rip-up clasts and coarse sand or granules are incorporated along lamination and aligned within the lamination (Fig. 2.8D).

Interpretation: The quartzose nature of this FA is interpreted here as a token for good sorting of the material and a virtual absence of fines and micas. Together with the amalgamation and cross-cutting relationships between beds, this suggests that the material was regularly and repeatedly reworked. The presence of a variety of sedimentary structures typical for tractive currents and absence of fines further call for a dynamic environment. In addition, the dominance of low angle and HCS-like features suggest a wave-influenced environment (Dott Jr and Bourgeois, 1982, Dumas and Arnott, 2006, Li et al., 2015, MacEachern et al., 2005). Possibly, some of the low angle laminasets and HCS-like features could also be explained by Froude-supercritical flows, potentially wave-induced currents (Vaucher et al., 2018). Sub-horizontal laminations resembling "doublets" rhythmites, high-angle laminations (e.g. sigmoidal, tangential and trough) and presence of rip-up clasts point toward a

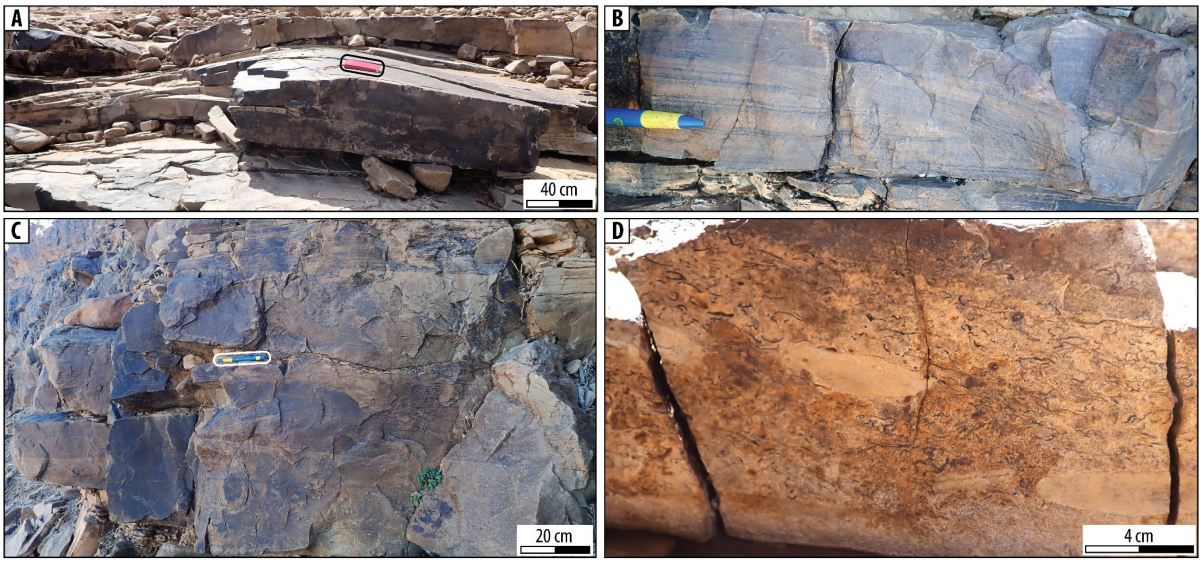

***Figure 2.8**: Quartzose amalgamated HCS sandstones facies association. (A) Hummock shaped HCS several meters in wavelength with a massive texture. (B) Low-angle truncations and sub-horizontal to low-angle laminations. (C) Fully amalgamated HCS sandstones with a massive texture to sub-horizontal and low-angle laminasets. Cross-cutting relationship with a gutter-like shape. (D) Coquina beds within HCS with aligned shells and isolated mud clasts. Pen for scale 13.7 cm.*

tidal environment, but are rarer than the storm-wave influenced HCS structures (Dashtgard et al., 2021, Vaucher et al., 2017, 2018). All these indications suggest that the quartzose amalgamated facies association was formed in a storm-wave-influenced tidal modulated shoreface environment.

2.4.7. Coarse-grained cross-bedded sandstones

Description: This facies association is characterized by alternations of dm to m-thick beds of cross-laminated sandstones ranging from medium- to very coarse-grained (Figs 2.9 to 2.11). Mud chips, shell lags and granule layers are sometimes aligned along laminae (Figs 2.9C and 2.11D). Erosive-based lenses up to 5-10 m in width and up to 2 m deep are common and filled with cross-bedded sandstones (Figs 2.9A and B, 2.11A and B). Four subfacies are recognized in the coarse-grained sandstones, which outcrop in distinctive locations within the Tissint and Bou-Hajaj Members exclusively.

Dune-bedded subfacies: The sandstones are often organized as dune bedsets up to 0.5 m thick, with planar, tabular, tangential, and sigmoidal cross-beds formed by individual beds that are up to 10 cm in thickness (Fig. 2.9A to C). They commonly have a quartzose texture. Individual beds can exhibit rippled surfaces. Up to 5 cm-thick mudstone

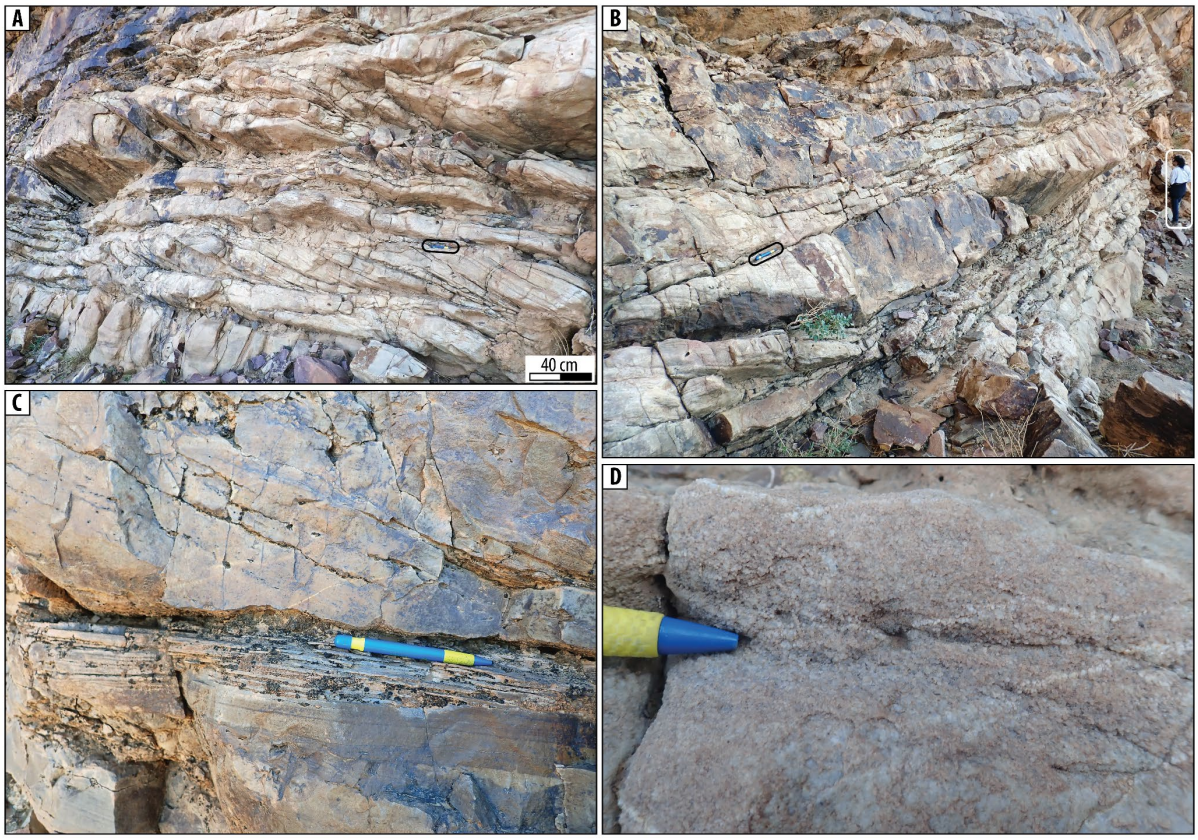

***Figure 2.9**: Coarse-grained cross-bedded sandstones facies association. Dune-bedded subfacies. (A) Tabular to tangential cross-bedding of quartzose sandstones and multiple erosive bases of beds. (B) Channel-like structures, possibly scroll bar with a progradation toward the right. The scroll-bars in B are located ca. 1 m above the cross-beds in A. Cross-bedded laminations and truncations are observed below and above the dunes. (C) Details within tabular cross-bedding, with imprints of mud to shell clasts aligned along cross-laminations. (D) Detail on texture and particle-size distribution within locally well-sorted lens. (B)-(D) Pen for scale 13.7 cm. (B) Geologist for scale ca. 174 cm.*

interbeds are commonly intercalated in-between and drape individual beds of dune stratifications. The bedsets have a rhythmic organization with periodic thickening-thinning of laminae and have common reactivation surfaces. Rare vertical and horizontal bioturbation were recognized. This dune-bedded subfacies is dominant in the Tissint Member.

Cross-bedded bioturbated subfacies: Sedimentary structures include cross-, trough and subplanar lamination as well as rare ripple formsets (Fig. 10A and B). Trough-cross laminations are dominant, occasionally forming herringbone cross-strata, and beds are often confined within erosive-based lenses (Fig. 2.10B). Bioturbation is abundant and includes dominantly *Diplocraterion* isp. and *Skolithos*, but also “oblique” and horizontal ichnofacies (Fig. 2.10C and D).

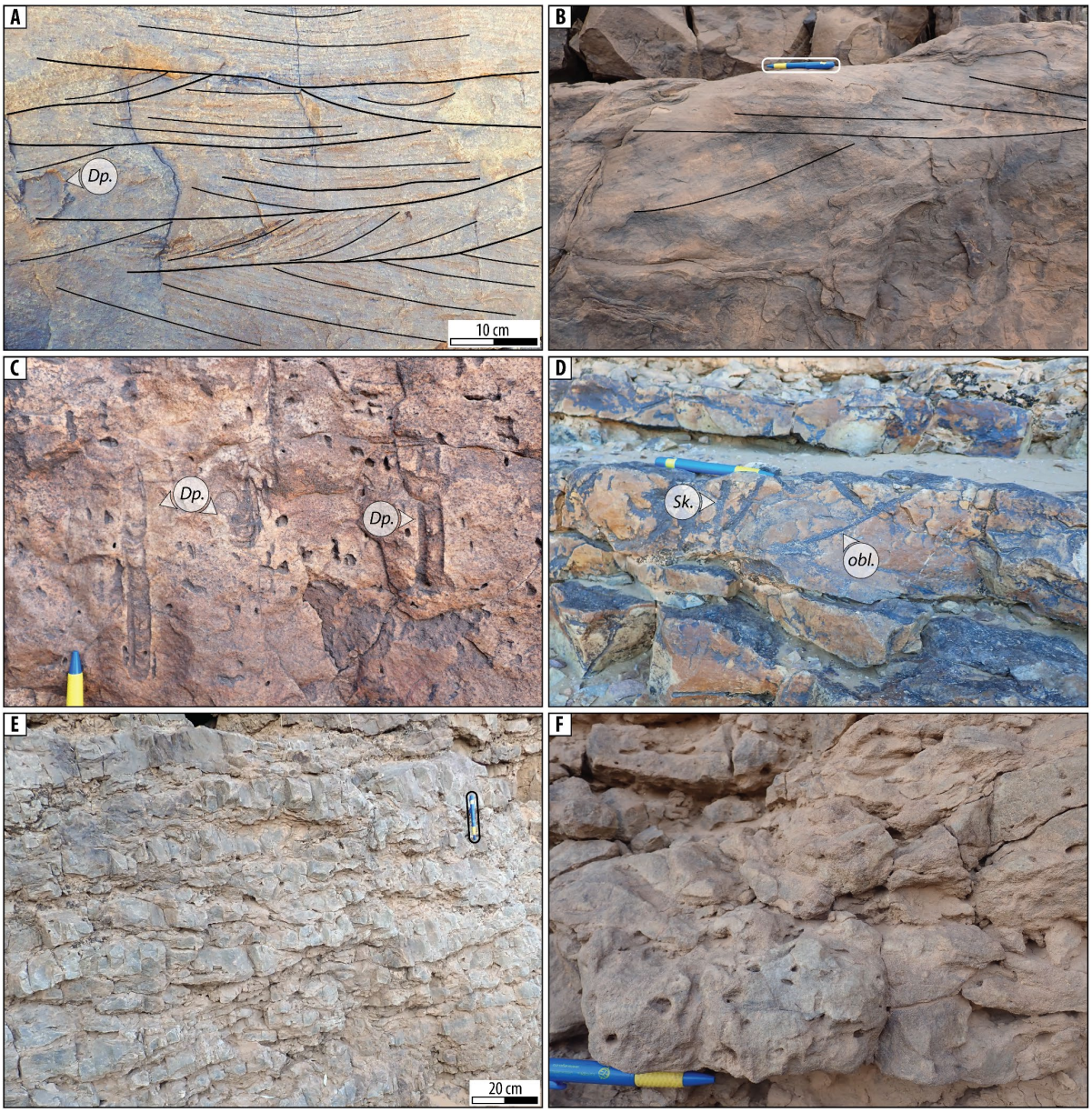

***Figure 2.10**: Coarse-grained cross-bedded sandstones facies association. (A)-(D) Cross-bedded bioturbated subfacies and (E)-(F) fully bioturbated subfacies. (A) Herringbone to trough-cross lamination in lower part and sub-planar laminations in upper part. Truncation: thick line. Lamination: fine line. Diplocraterion isp. (Dp.) to the left. (B) Cross- to trough-cross-laminated sandstone. (C) Abundant Diplocraterion isp. and Cruziana ichnofacies within cross-bedded sandstone. (D) Moderately bioturbated sandstones bearing Skolithos (Sk.) and "oblique" (obl.) ichnofacies. (E) Fully bioturbated sandstones, decimetricthick beds in cross-cutting relationships. (F) Close-up view on fully bioturbated sandstones with traces of Cruziana and Skolithos ichnofacies. Low-angle to cross-laminations to the bottom left. (B)-(F) Pen for scale 13.7cm.*

Fully-bioturbated subfacies: Medium- to coarse-grained strata are organized in undulating dm-thick layers (Fig. 2.10E and F). Bioturbation is intense (91-99%, Bioturbation Index -BI: 5 *sensu* Taylor and Goldring, 1993) and reworked

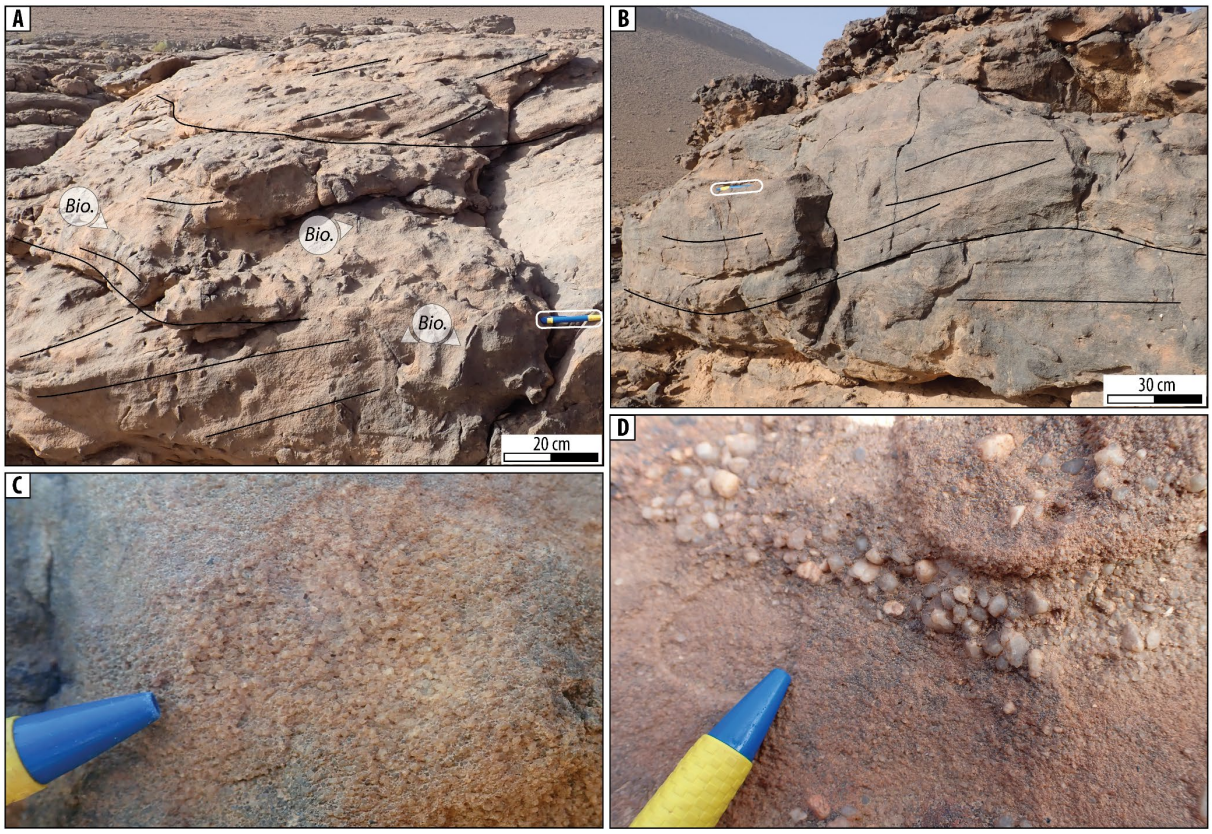

***Figure 2.11**: Coarse-grained cross-bedded sandstones facies association. Well-sorted subfacies. (A)-(B) Cross- to trough-cross- to sub-horizontal laminated sandstones with consistent orientation and moderate bioturbation (Bio.). Moderately to highly ferruginous. (C) Well-sorted particle-size distribution and rounded to angular grain shape of the subfacies. (D) Granules rich horizon, note sub-angular coarse-sand and granule grains with a dull and frosted texture.*

entirely the primary sedimentary structures, and only rare ripples on top of beds are sometimes identified.

Well-sorted subfacies: This subfacies consists of reddish-purple, well-sorted, medium to very coarse-grained sandstones (Fig. 2.11). Individual grains commonly exhibit a dull, frosted texture (Fig. 2.11C-D). Pluricentimetric-thick horizons of quartz granules that are rounded to angular sporadically occur, as well as rare shell beds (Fig. 2.11D). The material is exclusively organized as meter-thick trough cross-laminated bedsets (Fig. 2.11A-B). Bioturbation is moderate (31-60%; BI: 3, *sensu* Taylor and Goldring, 1993) with horizontal, vertical and oblique traces (Fig. 2.11A). This subfacies exclusively outcrops as a single package, few meter in thickness, and topping the Bou-Hajaj Member.

Interpretation: The large variety of grain sizes and coarseness indicates a proximity to the sediment delivery system. The variety in tractive sedimentary structures is characteristic of vigorous currents and frequent and rapid changes in flow

conditions. Periodic thickening-thinning of laminae, together with reactivation surfaces and herringbone stratifications are generally taken as a diagnostic feature for tidal processes (neap-spring cycles and flood-ebb tides respectively; Davis and Dalrymple, 2012, Kvale, 2006, Peng et al., 2018). In this context, the mud chips likely represent ripped-up fragments from desiccated mud that indicate nearby emersion (Davis and Dalrymple, 2012). In that frame, the dune-bedded subfacies could represent sand dunes and bars that were moving during tidal currents whereas mud layers would be deposited during slack waters (Davis and Dalrymple, 2012, FitzGerald and Miner, 2013, Vaucher et al., 2018). The bioturbated and cross-bedded lenses would be formed in tidal channels, whereas the fully bioturbated subfacies represent zones protected from currents, possibly marshes (FitzGerald and Miner, 2013, MacEachern et al., 2005). Combined with the reddish, i.e. oxidized colors, and cross-bedding, this subfacies could correspond to a fluvial-influenced environment, such as a river mouth system and/or inner estuary (Allen and Posamentier, 1993, Dashtgard et al., 2021. Gil-Ortiz et al., 2022, Van Yperen et al., 2020). Together, these features depict a shallow environment, tidal-dominated with a possible fluvial influence, including tidal-flats and/or flood-ebb delta, and river-mouths.

2.4.8. Intensely bioturbated muddy sandstones

Description: The sedimentary environment linked to this facies association will be treated in detail in the discussion. It consists of a mixture of unsorted muddy and very fine- to medium-grained sandstones forming several m-thick units (Fig. 2.12). The most characteristic feature is the intense to complete bioturbation (i.e. 60-99% corresponding to BI 4-5 in the sense of Taylor and Goldring, 1993, Taylor et al., 2003). Bioturbation generally hinders identification of primary sedimentary structures or ichnofossils yet individual vertical to horizontal burrows can sometimes be recognized (Fig. 2.12 C to E). Diffuse corrugated, undulating bedding boundaries are sometimes preserved and highlight beds of up to 20 cm in thickness. Sedimentary structures, although rare, include sporadically distributed low-angle cross-stratification (possibly HCS), climbing ripples, and muddy interbeds.

Interpretation: Bioturbation is indicative of brackish or marine environments during the Ordovician (e.g. Buatois and Mángano, 2007). The presence of sandy material with sedimentary structures indicates a sediment input and distribution by tractive and/or

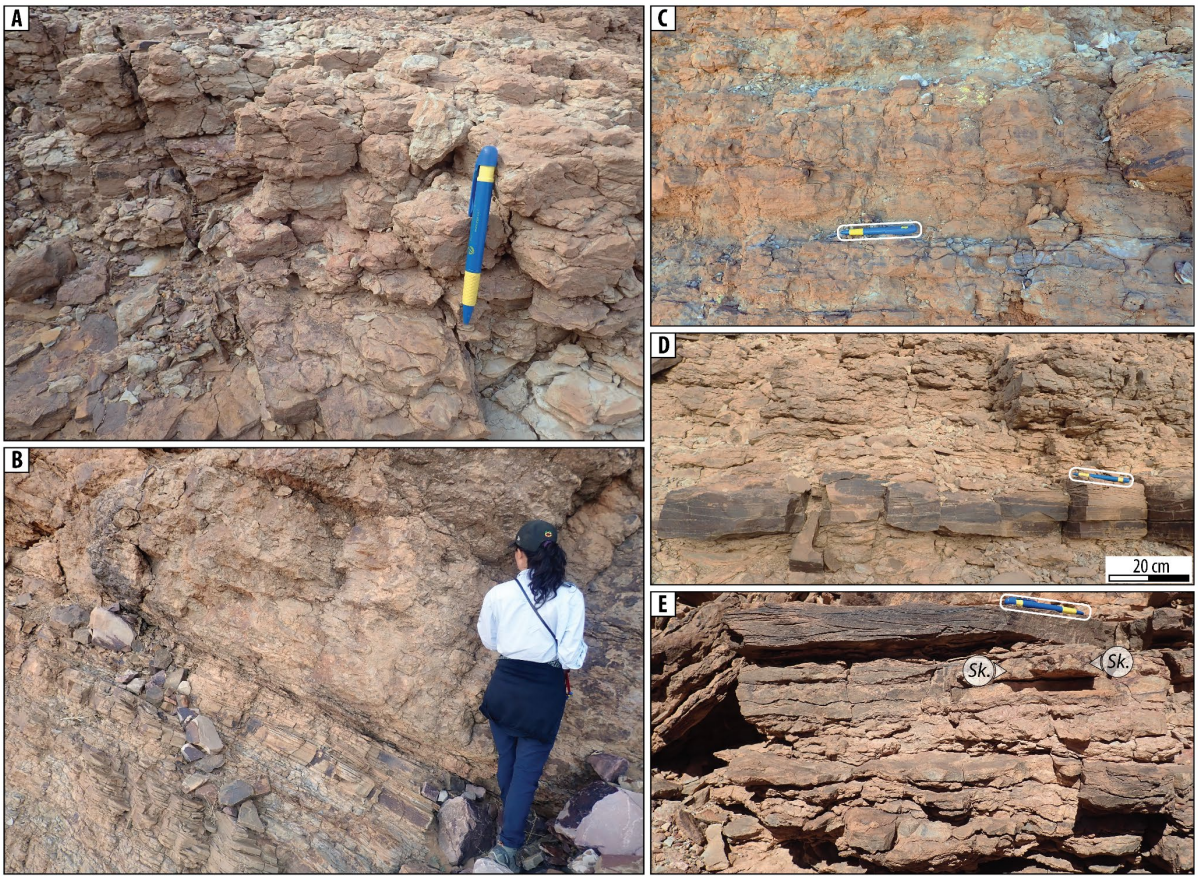

***Figure 2.12**: Intensely bioturbated muddy-sandstones facies association. (A) Muddy-sandstones intensively bioturbated (BI 5-6) hindering sedimentary structure. Diffuse undulating bedding boundaries. (B) Sharp contact between silts and isolated HCS facies association and intensely bioturbated sandstones. Diffuse bedding in bioturbated sandstones. (C) Muddy-sandstones highly bioturbated with diffuse HCS sandstones. (D) Isolated, low-angle laminated HCS/SCS sandstones in intensely bioturbated sandstones. (E) Intensely bioturbated sandstones interbedded with sandstone ripples, containing burrows. (A), (C)-(E) Pen for scale 13.7 cm. (B) Geologist for scale ca. 174 cm.*

oscillatory currents. The intense bioturbation implies rates of biogenic reworking supplanting the primary deposition rate, either because of intense biogenic activity, or due to low rates of sedimentation and reworking (Gowland, 1996, Keen et al., 2012). The possible but rare presence of HCS suggests intermittent material input transported by storm-derived processes. The preserved sedimentary structures could indicate a lower shoreface environment, as is often suggested for similar facies associations (Baniak et al., 2014, Hampson, 2010, La Croix and Gingras, 2021). Alternatively, this facies association may represent a calm environment with intense biogenic activity, i.e. a protected-restricted marine environment or lagoon (Bayet-Goll, 2022, Gil-Ortiz et al., 2022, Hein et al., 2013, Loi et al., 2010, Vidal et al., 2011). The interfingering of bioturbated sandstones

with HCS-beds suggests that the barrier was sporadically disturbed by storm events resulting in imported beds in the form of overwash/washover deposits, in particular during retrogradation / backstepping (Rodriguez et al., 2020, Sedgwick and Davis Jr, 2003, Switzer and Jones, 2008, Vidal et al., 2011). These two contrasted interpreted environments will be further discussed in the light of their stratigraphic context (see 2.6.1.-6.2).

2.5. Stratigraphic architecture

The continuous exposure of the Jbel Bani cliff allowed for direct correlation of sandstone members between individual logs over almost the entire transect. Lateral variations of facies associations were then used to interpret the stratigraphical context in regard to sequences, RSL variations, the evolution of the morphology of the platform, and the orientation of the system during deposition of the Lower Ktawa Formation.

2.5.1. Typical sequential architecture

In each member of the Lower Ktawa Formation (except the Bou-Hajaj and Tissint Members, see 2.5.2), the vertical succession of facies associations follows a typical organization that is characterized by a two-fold asymmetric stacking pattern (Fig. 2.13). Consistently, each individual member is underlaid by a thick coarsening-upward sequence from mudstones with gradual transition into the sandy member, which itself is topped by a much thinner (<5 m in thickness) fining-upward pile. These paired patterns, spanning thicknesses of ca. 15-80 meters, are interpreted as shallowing- and deepening-upward series. The exact position of the trend reversal depends on the interpretation of the paleoenvironment, as discussed below (see 2.6.1 & 2.6.2). In addition to this signal, metric to plurimetric-thick parasequences of lesser amplitude are commonly superimposed and understood to represent the response to higher-order fluctuations of environmental conditions.

The lower coarsening-upward succession comprises an offshore series and is generally ca. 10-60 m-thick. It includes, from the base to the top, mudstones, silts and sand ripples, and then isolated HCS-bearing sandstones. This offshore series is commonly overlain by a pile of bioturbated sandstones that are up to 10 m thick, yet this pattern is not systematically observed (Fig. 2.13A-B). Indeed, this succession can be halted by a package of amalgamated HCS that are up to ca. 15 m thick. They interrupt the underlying stacking trend within bioturbated sandstones or isolated HCS-

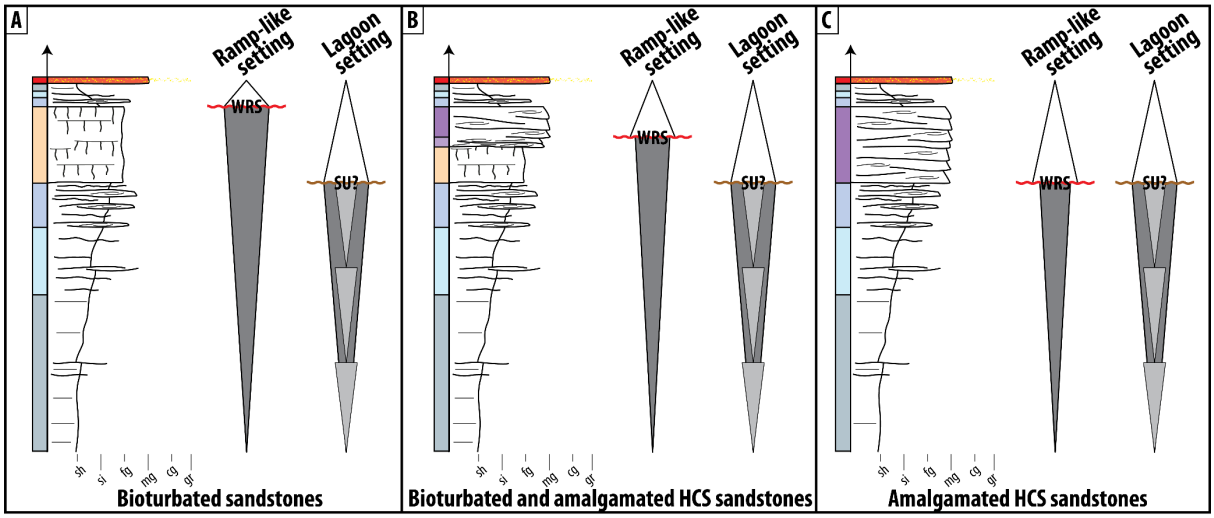

***Figure 2.13**: (A-B-C) Three typical stacking patterns of facies associations, as observed in the field, together with sequence key surfaces in both interpretation schemes developed in discussion. In the case of a ramp-like setting, the regressive parasequence entails bioturbated sandstones and is interrupted by a Wave-Ravinement Surface (WRS) and might be overlaid by amalgamated HCS sandstones. This limit marks the onset of the transgression. In a lagoon setting, the base of the bioturbated sandstones are taken as the onset of the transgression. The sequences end with a thin fining upward sequence. Facies associations color: see Fig. 2.14.*

bearing sandstones (Fig. 2.13B-C). In some sections, the amalgamated HCS sandstones are absent. The passage to amalgamated HCS sandstones is generally abrupt but can include a thin transition zone of a few meters containing stacked HCS, or an alternation of bioturbated sandstones and HCS-bearing sandstones. The base of amalgamated HCS sandstones is understood as an undulating, erosional unconformity that generally truncates the underlying deposits, sometimes with intermingling.

The thinner fining upward pile (<5 m) is generally overlaying the coarsening upward package, following either directly on top of the bioturbated sandstones or above the amalgamated HCS sandstones. It starts with a few beds of HCS-bearing sandstones and transitions into silt and sand ripples or mudstones, interpreted as representing a response to a RSL rise. Thick ferruginous horizons, laterally continuous over several kilometers, can occur within the mudstones, within the fining upward part of the sequence, or slightly above the top of low magnitude parasequences. These horizons are taken as condensed levels recording the maximum rates of transgression (McLaughlin et al., 2008; Loi et al., 2010). This general stacking trend is observed in most members, including Foum-Zguid, Mazil, Treifia, Abbas and the lower part of Bou-Hajaj (Figs 2.14 to 2.18).

2.5.2. Isolated coarse-grained sandstone lenses

The Tissint and Bou-Hajaj Members (Figs 2.15 & 2.17) differ significantly from the above-described stratigraphic stacking arrangement. Both these members contain an up to 40 m thick package of coarse-grained cross-bedded sandstones, this facies association being absent from the typical trend described above.

The Tissint Member almost exclusively consists of a thick (<35 m) package of dune-bedded sandstones and fully-bioturbated sandstones (Fig. 2.15). The Tissint Member is exposed as a prominent cliff lying above a debris talus, the latter hindering any observation but precluding less competent fine-grained material below. The Tissint sandstones occur exclusively on the SW part of the transect, and abruptly pinch out toward the NE: the Tissint cuesta which is followed over >35 km and reach 25 m in thickness on log 34 is laterally congruent to a few ferruginous horizons on log 33, just 3 km northeastward (Fig. 2.15).

The Bou-Hajaj Member has a two-fold stratigraphic architecture and can be divided in a lower and upper part (Fig. 2.17). The "lower Bou-Hajaj sequence" exhibits the typical sequence arrangement of the other members (as in 2.4.1). It outcrops on the western part of the member (logs 27-30) and lower parts of the central logs (logs 24-26). Toward the West, it splits in two parts, as observed from logs correlated by satellite images (logs 28-29), eventually grading laterally into condensed levels (log 30).

This lower Bou-Hajaj sequence is partly or fully interrupted or replaced toward the east by a composite body containing thick packages of cross-bedded sandstones of the cross-bedded bioturbated, and fully bioturbated subfacies, hereafter referred to as the "upper Bou-Hajaj sequence". The upper Bou-Hajaj sequence outcrops over >30 km-length in the Hassi Taska area (logs 21-26). The deposits are organized as individual sandstone packages

Figure 2.14*: Semi-3D transect with precise logs and correlations, Tanzida and Foum-Zguid Members. (A) Detailed logs. (B) Semi-3D transect of facies associations correlations. (C) Location of the semi-3D transect on the overview of the entire investigated transect in Fig. 3. (D) Legend of facies associations and sedimentary structures for Figs 2.14 to 2.18: Colored columns next to logs reflect interpreted facies associations. On all Figs 2.14-18: the connecting lines between logs indicate that physical correlations of members were verified by satellite and UAV images. Numbers at the top of each log refer to locations in Fig. 2.3.*

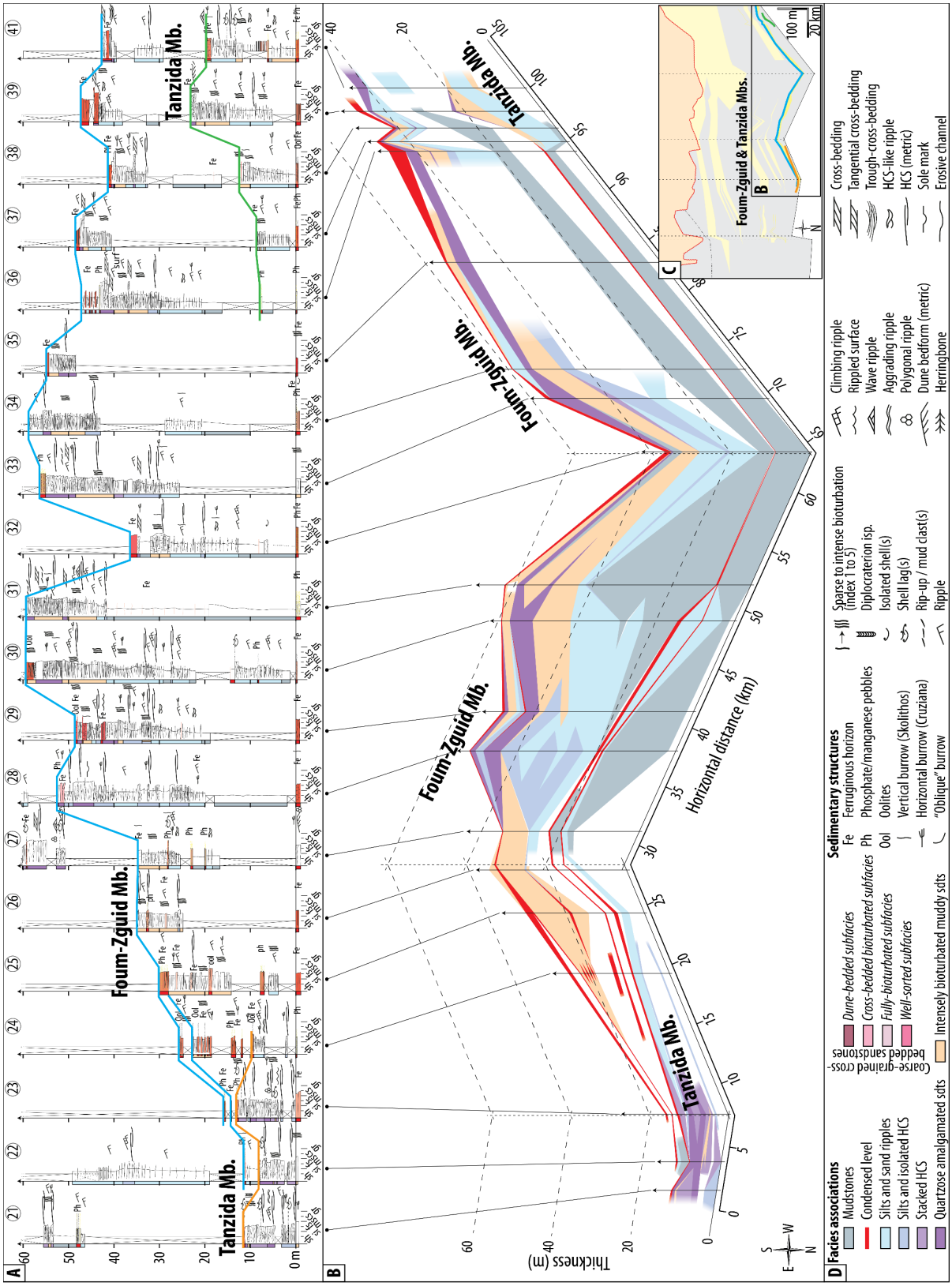

that can reach up to 15 m in thickness and several kilometers in length. At least 4-5 packages of these coarse-grained sandstones with limited lateral extension occur with finer grained intercalations (Fig. 2.17). The topmost beds of the upper Bou-Hajaj sequence consist of a few meters of well-sorted sandstones. This flat unit

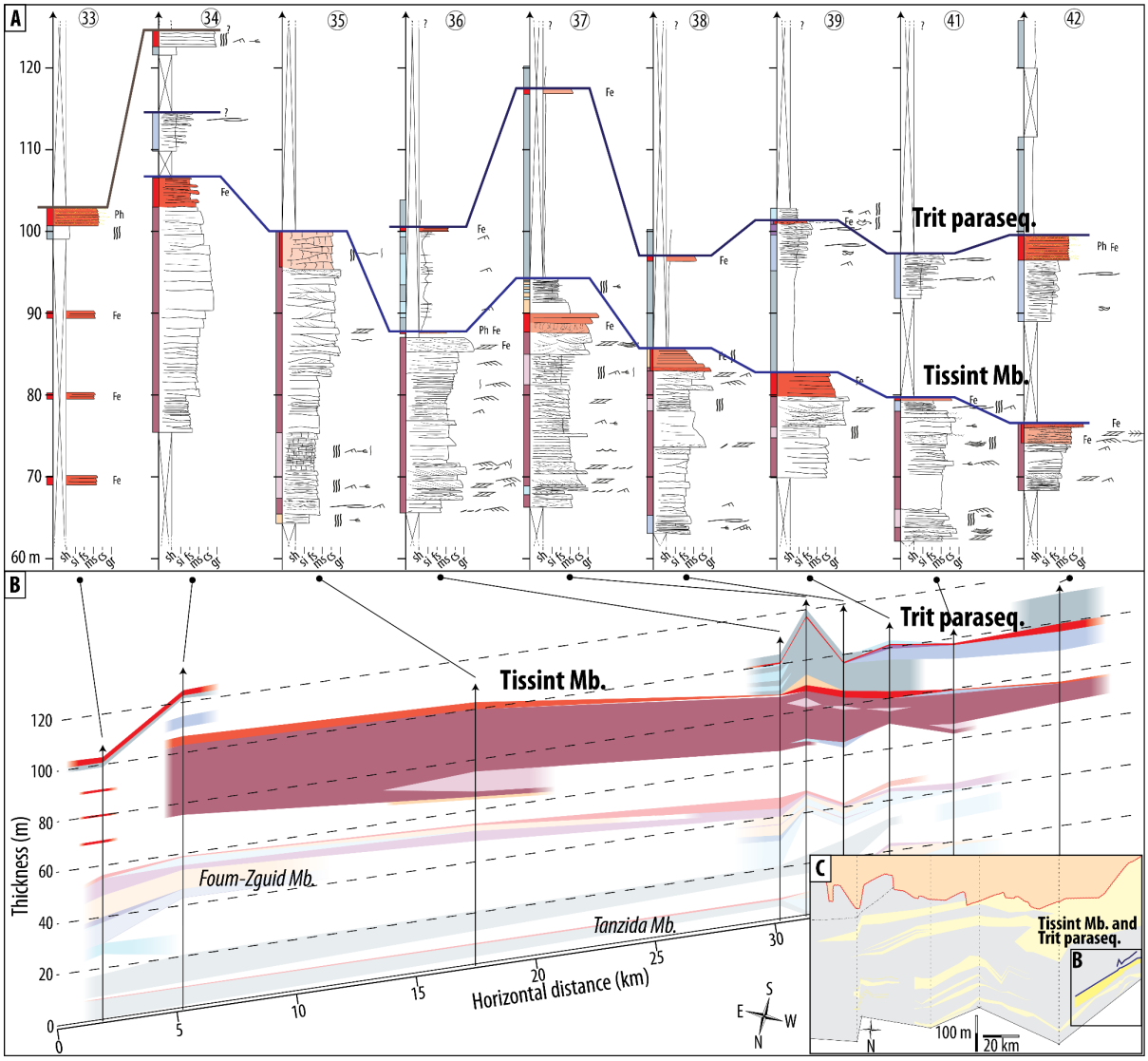

***Figure 2.15**: Semi-3D transect with logs correlations, Tissint Member. Legend see Fig. 2.14.*

topping the upper Bou-Hajaj sequence outcrops with a constant thickness over >25 km, between logs 21-25. The upper Bou-Hajaj sequence truncates the lower Bou-Hajaj sequence down to silts and isolated sand ripples in some areas (logs 21-23). Laterally, the upper Bou-Hajaj sequence seems to pinch out on the western part of the transect (logs 26-27). The eastern part is not exposed, covered by a debris talus over 6 km between logs 20-21. It can be tentatively interpreted that the Abbas Member could correspond to the eastern lateral continuation of the lower Bou-Hajaj sequence, based on the correlation of sediment thickness above the First Bani Group, and the fact that the Abbas Mb is the only prominent sandstone unit eastward from Bou-Hajaj.

The cross-, dune-bedded, rhythmic, bioturbated and coarse-grained nature of the sandstones in the Tissint and Bou-Hajaj Members are interpreted as recording a tidal influence and as representing the most

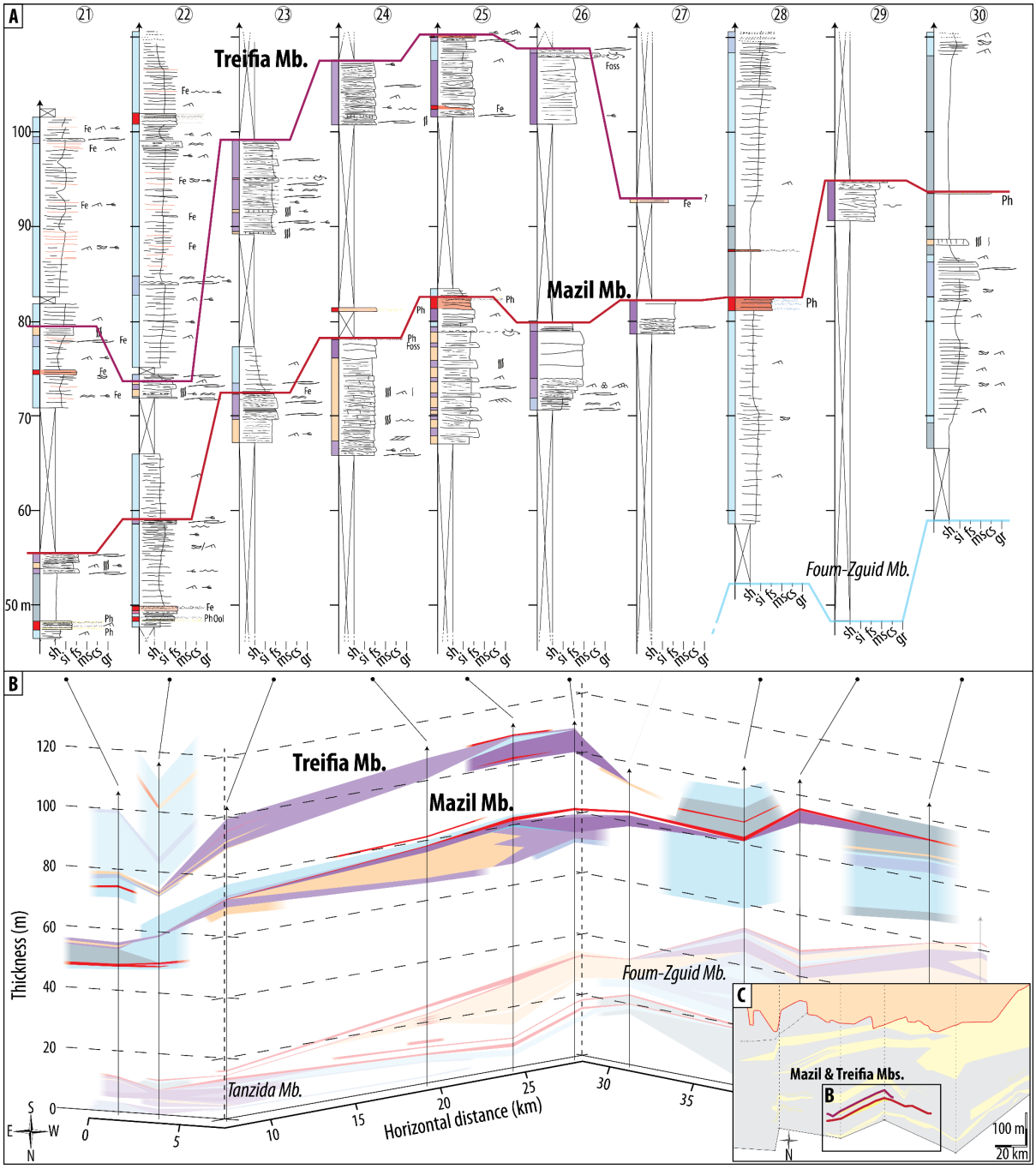

***Figure 2.16**: Semi-3D transect with logs correlations, Mazil and Treifia Members. Legend see Fig. 2.14.*

proximal deposits within the entire transect, in proximity of a feeder system (Figs 2.15 & 2.17). They are both laterally confined (over tens of kilometers) with abrupt termination, which may indicate the occurrence of channelized systems or embayments. Finally, both have irregular sharp bases that are taken as erosive bases. Accordingly, both members are interpreted as a fill of channel belt system of proximal tidal channels or as tidally influenced river mouth deposits. Altogether, these two

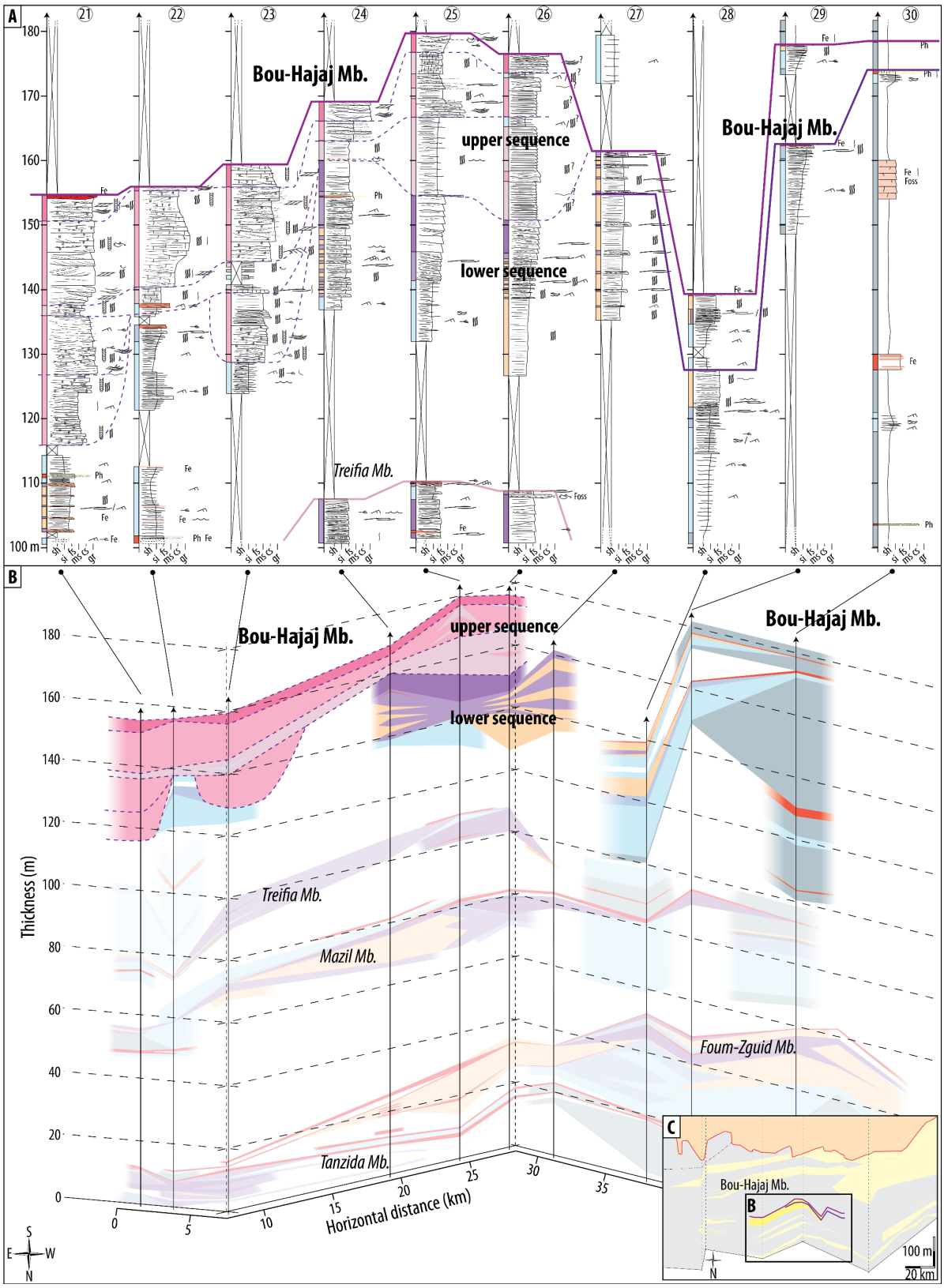

***Figure 2.17**: Semi-3D transect with logs correlations, Bou-Hajaj Member. Legend see Fig. 2.14.*

systems are thus understood as representing the fill of incised valleys corresponding to the most important drops in RSL (Blum et al., 2013).

variations of the orientation over 10s of km

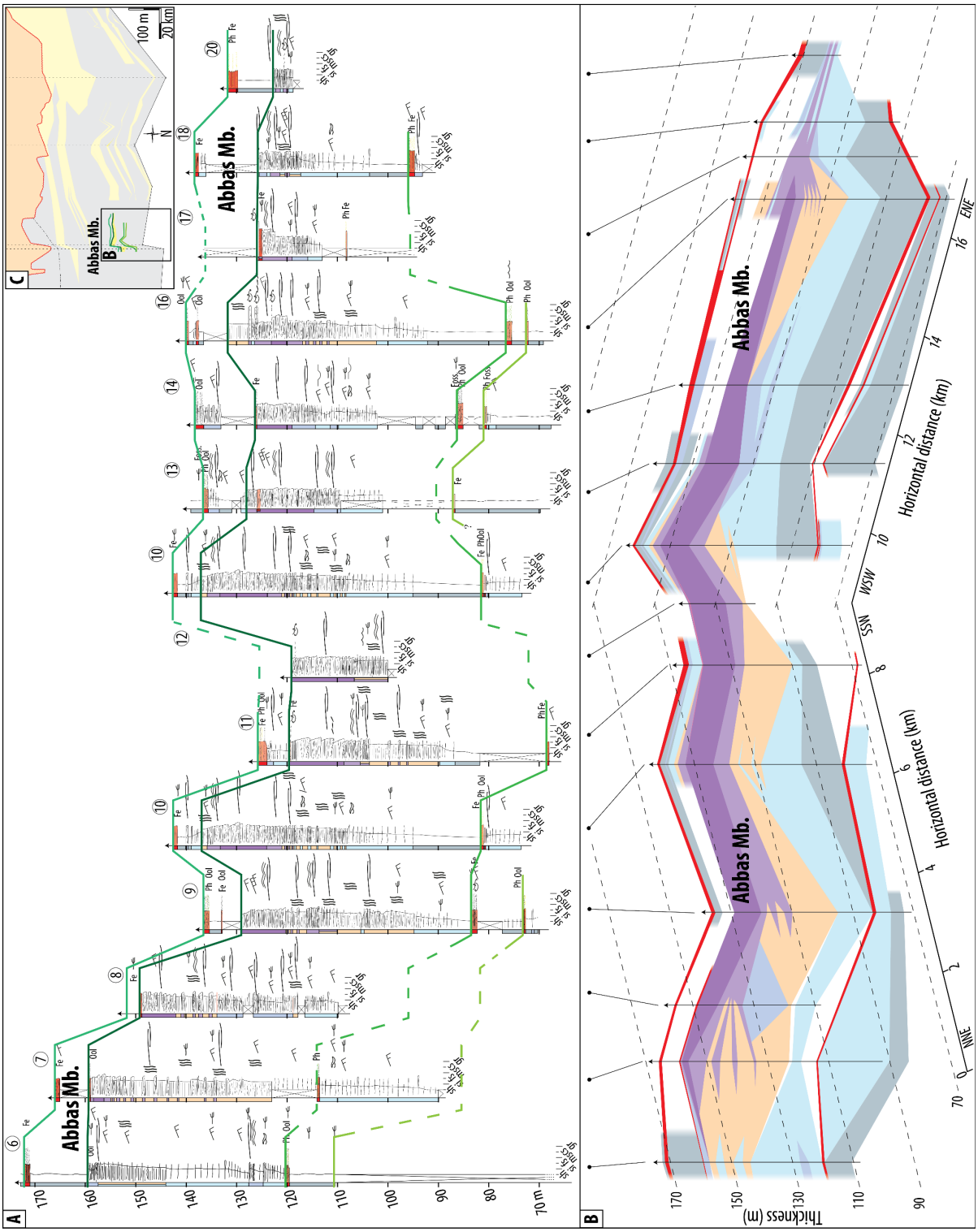

***Figure 2.18**: Semi-3D transect with logs correlations, Abbas Member. Legend see Fig. 2.14.*

2.5.3 Progradation direction

The Jbel Bani outcrops are globally oriented W-E in the study area, with serrate that give insights onto a semi-3D geometry (Figs 2.14 to 2.18). Nevertheless, some proximal-distal trends were encountered:

-In the western part of the study area, the thickness of the lowermost unit (i.e. Tanzida Member, Fig. 2.14, logs 36-41) decreases toward the NE. Its entire thickness measured from the datum (First Bani Group top) decreases from 23 m in the SW part down to ca. 7 m just 5 km further to the NE. This thinning coincides with a lateral variation of the FAs, with a transition from silts and sand ripples facies overlaid by bioturbated sandstones and topped by amalgamated HCS sandstones in the SW to mudstones and condensed levels in the NE. Hence, this member seems to dip and become more distal toward the NE, displaying a maximum apparent stratal dip of 0.2° relative to the datum.

- The Foum-Zguid Member appears relatively symmetrical on a W-E profile (Fig. 2.14). It is thickest in its central part (logs 30-31 and 33-35), and thins toward the W and E. Both the western and eastern parts, which also represent the southernmost outcrops, appear to record bioturbated sandstones grading into a suite of condensed levels (logs 36-39, 22-25). The central parts are instead dominated by amalgamated HCS (logs 28-30, 33-35). This symmetry suggests that the W-E transect is essentially oriented parallel to the shoreline (Gani et al., 2015).

- Above the Tissint Member, the Trit parasequence (Fig. 2.15, logs 36-42) outcrops toward the SW and is topped by a clear ferruginous marker bed. Although the thickness of the parasequence remains almost constant from the SW to the NE, thereby resulting in an apparent dip less than 0.048°, a clear SW-NE evolution of facies associations is observed. Toward the SW, the top of the parasequence (log 42) is composed of a stack of silts and isolated HCS sandstones, which disappear toward the NE, giving place to mudstones with few ripples within ca. 12 km of lateral distance (log 36).

- The Abbas Member (Fig. 2.18) appears more proximal in the southern outcrops (logs 10-13) with an evolution towards more distal FAs to the N and W (logs 6-8 and 17-20). This is associated with a decrease in thickness of sandstone units from ca. 30 to 5 m. The southernmost outcrop (log 12) consists of a ca. 20 m thick sand package made up by amalgamated sandstones and alternation of stacked HCS and bioturbated sandstones. It thins toward the north over ca. 10 km to <15 m, where bioturbated silts and sand ripples intercalated with thin bioturbated sandstones beds become more abundant (log 6). Similarly, a trend toward thinner and more distal deposits is also observed over ca. 10 km in a westward direction, where only 5 to 10 m of stacked HCS and

silts and sand ripples are observed (logs 17-20).

Notably, the overlying Rouïd-Aïssa Formation exhibits a different trend, with a clear proximal to distal polarization from the West to the East (Fig. 2.3): a decrease in thickness combines with the pinch out of parasequences, and coincides with finer-grained and lower-energy deposits to the East.

2.6. Discussion

2.6.1. Bioturbated sandstones: lower shoreface or lagoon?

Overall, the intensely bioturbated sandstones characterized by an unsorted mixture of mud and sand (Fig. 2.12) strongly contrast with the well-sorted, wave-dominated facies associations (HCS-bearing facies, Figs 2.6-8). The bioturbated sandstones suggest a calmer depositional environment and appear out of sequence in a depositional environment dominated by storm waves. Although the bioturbated sandstones in the Lower Ktawa are intensely bioturbated, identification of ichnofacies could not be effectuated confidently. Hereafter, three interpretations can be put forward to explain the coexistence of bioturbated sandstones within a wave-dominated setting.

2.6.1.a. Regressive lower shoreface

Bioturbated sandstones are most generally interpreted as deposited in lower shoreface environments (Baniak et al., 2014, Hampson, 2010, La Croix and Gingras, 2021). Considering the hypothesis of a lower shoreface environment, it is envisioned that the deposition and remobilization of sand by storm processes was intermittent enough, in a photic zone sufficiently supplied in nutrients, in order to allow episodic deposits to be intensely reworked by biogenic activity. Such an interpretation may explain the presence of unsorted, highly bioturbated sandstones above and below a suite of environments otherwise dominated by storm waves. Lower down along the depositional profile, in the upper offshore zone, intermittent HCS deposits should not be reworked. Therefore, it is hypothesized that insufficient nutrient reach these deeper zones for colonization (Baniak et al., 2014, Hampson, 2010, Isla et al., 2018). In more proximal zones, traces from biogenic activity would be supplanted by sedimentation and reworking by waves. In this setting, the HCS sandstones lying above the bioturbated sandstones would represent a more proximal shoreface environment than the bioturbated sandstones. It is hypothesized that the

stacked HCS facies, less sorted than the amalgamated HCS/sandstones, would have been subjected to less reworking than the well-sorted, fairly reworked amalgamated and quartzose sandstones. As such, the stacked HCS may represent a shoreface environment in a regression phase, whereas the amalgamated HCS would correspond to the same environment, yet during a transgressive phase. In such a setting, the nearshore bathymetric profile could correspond to a monotonically deepening ramp, recording a suite of nearshore facies submitted to a spectrum of waves (e.g. Dashtgard et al., 2021, Peters and Loss, 2012, Zecchin, 2007).

2.6.1.b. Low vs. high energy ramp

A similar dichotomy in bioturbated- vs. wave-dominated imprint within the First Bani Group, underlying the Ktawa Group, was explained with an alternative interpretation (Marante, 2008, Razin et al., 2020). A twofold system was hypothesized with an underlying "low energy ramp" that would occur during regression phases where bioturbation would be dominant, and it would be followed by a "high energy ramp" setting dominated by storm waves during transgressions.

2.6.1.c Transgressive barrier-lagoon system

Here, a new interpretation is suggested. It requires the development of a barrier-lagoon system, where a barrier made up of sand would protect the lagoon from the energy of the offshore waves.

Marine deposits associated to such morphologies are divided in open shelf and protected marine ones (Heward, 1981). Open marine deposits undergo the influence of waves and storms, displaying characteristic sedimentary features such as HCS, wave ripples, etc (Plint, 1988). The protected marine deposits, in a more proximal position than the storm-wave-dominated barrier, remain shielded to wave shoaling by the barrier and are often referred to as "back-barrier" or lagoonal deposits (Otvos, 2018, Rodriguez et al., 2020, Sedgwick and Davis Jr, 2003, Switzer and Jones, 2008, Vidal et al., 2011). In such a configuration, the barrier itself would be represented by the amalgamated HCS sandstones in term of facies association and would correspond to an upper shoreface environment submitted to intense wave action. The bioturbated sandstones would be the deposits emplaced in the lagoon. Indeed, it was proposed that bioturbated sandstones could be deposited in a protected, restricted- marine depositional zone (e.g. Dabard et al., 2015,

Hein et al., 2013, Loi et al., 2010, Vidal et al., 2011). Interestingly, an interfingering of open and protected marine deposits, such as observed in many members (e.g. Mazil, "lower" Bou-Hajaj and Abbas, Figs 2.16 to 2.18), can occur in response to a breach of the barrier during a storm event, which will deposit washover sediments into the back-barrier (Bayet-Goll, 2022, Rodriguez et al., 2020).

The barrier-lagoon system would be emplaced during the early transgression phase. In that sense, an open-ramp setting during regression would allow the emplacement of sediments with a storm-wave-dominated imprint, and the couplets bioturbated sandstones and amalgamated sandstones would represent the transgressive barrier-lagoon system. Indeed, deltaic environments situated on storm-dominated ramps have been documented and associated with barrier-lagoon systems that are related to transgressive deglaciation events (Armon, and McCann, 1979, Brenner et al., 2015, Gao, and Collins, 2014, Goff et al., 2010, Hein et al., 2014, Pellegrini et al., 2015, Raff et al., 2018). Although some studies suggest that barrier-lagoon systems may occur during high-stand system tracts (Angulo et al., 2006, Billy et al., 2015, de Souza et al., 2012), they are generally associated to transgressive events (Moore et al., 2010, Wolinsky and Murray, 2009).

2.6.2. Implications for sequence stratigraphy

The three possible interpretations of the bioturbated sandstones imply distinct morphologies of the shallow-marine depositional systems. This in turn has implications for the interpretation of system tracts and sequence stratigraphic interpretation within each sequence. Two depositional models emerge from the interpretation of the bioturbated sandstones: an open marine ramp-like geometry, and a barrier-lagoon system (Fig. 19).

In a "ramp-like" setting, the bioturbated sandstones would be sedimented in an open marine, lower shoreface environment (Fig. 2.19A to E). The lack of some FAs compared to the expected typical stacking pattern suggests an unconformity occurring before emplacement of the amalgamated HCS sandstones. Within a wave-dominated environment such unconformities are often understood as wave ravinement surfaces (WRS) forming during transgression (Fig. 2.19B to C; Mellere et al., 2005, Zecchin et al., 2019). Although no unconformity is visible at the outcrop scale, the sharp base of amalgamated HCS is a distinctive

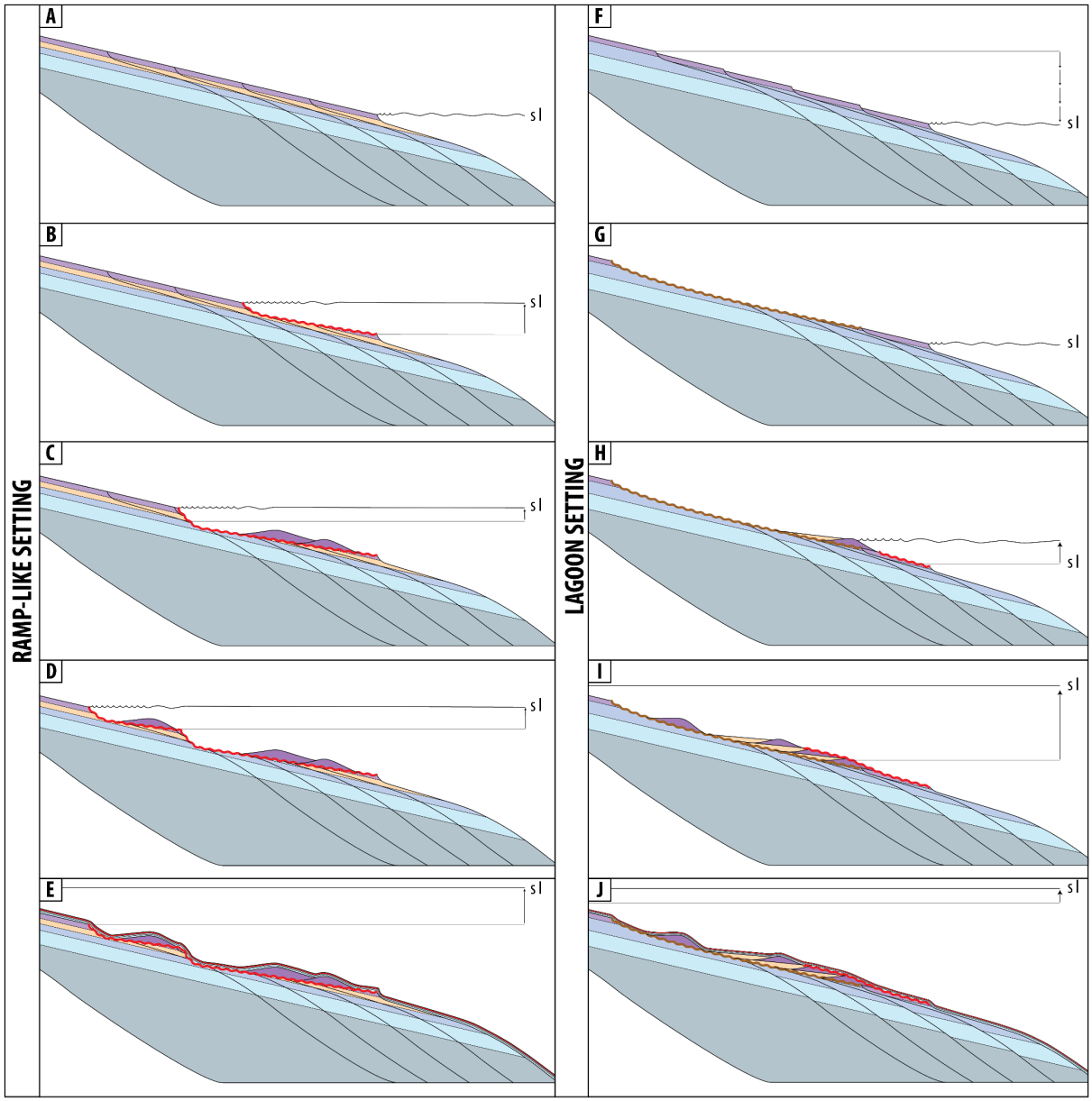

***Figure 2.19**: Depositional models, (A)-(E): in a ramp-like setting with bioturbated sandstones emplaced during regression, and (F)-(J): in lagoon setting with bioturbated sandstones emplaced during transgression. (A&F) Highstand to falling-stage clinothems deposited during regressions. (B&G) Partial ravinement, either in transgression, i.e. WRS (in B) or as a subaerial unconformity (SU) during falling stage (in G). (C&H) Amalgamated sandstones emplaced as shoreface deposits during transgression, as shoals/sand ridges (in C) or as a barrier (in H). (D&I) Backstepping of transgression and extension of the WRS where amalgamated HCS sandstones would be deposited as shoals/sand ridges. (E&J) Late stage of transgression with deepening upward sequence and condensed horizons. Red wavy line: WRS. Brown wavy line: SU. sl: sea level. Facies associations colors: see Fig. 2.14.*

marker horizon in the landscape. The inferred occurrence of a WRS would be in line with the subsequent deposition of the amalgamated HCS, and the latter would be deposited as offshore shoals or sand ridges (Fig. 2.19C-D; Cattaneo and Steel, 2003,

Sanders and Kumar, 1975, Zecchin and Catuneanu, 2015, Zecchin et al., 2019). This view implies that the base of the amalgamated HCS FA corresponds to the onset of transgression. The transgressive system tract would thus be composed of a succession of amalgamated sandstones, followed by silts and isolated HCS to sand ripples, and condensed horizons (Fig. 2.19E). The condensed levels would form during the maximum rates of sea level rise, when the supplied sediment is stored in the shoreface and the maximum flooding surface would occur somewhere above within mudstones (Dabard et al., 2015, Loi and Dabard, 2002, Loi et al., 2010, McLaughlin et al., 2008).

In a lagoon setting, a two-fold sediment system is envisioned, with an open marine regressive system fully dominated by waves, subsequently replaced by a transgressive system typified by the establishment of a barrier and lagoon system (Swift, 1975), and thus the emergence of new sedimentary facies distributions (Fig. 2.19F to J). Indeed, barrier and lagoon settings are generally understood as features restricted to transgressions (Armon and McCann, 1979, Brenner et al., 2015, Hein et al., 2013, Moore et al., 2010, Pellegrini et al., 2015, Raff et al., 2018). In a barrier-lagoon setting, bioturbated sandstones represent lagoonal / back-barrier sedimentation, whereas amalgamated HCS dominated by wave action are deposited within the transgressive barrier.

In the latter barrier-lagoon interpretation, highstand to falling stage clinothems should include from deep to shallow: mudstones, silts and sand ripples, silts and isolated HCS and stacked HCS around the topsets (Fig. 2.19F). However, bioturbated sandstones or amalgamated HCS sometimes lie abruptly on silt and isolated ripples. There is thus a gap in the FA series where HCS-bearing sandstones are missing. Either the latter were not deposited, thus implying a basinward shift related to an abrupt drop in RSL (Patruno et al., 2015, Proust et al., 2018), or a subaerial erosion unconformity would make the base for the deposition of the barrier lagoon system, i.e. the bioturbated sandstones and/or amalgamated HCS (Fig. 2.19G; Hunt and Tucker, 1992, Posamentier and Allen, 1993, Zecchin and Catuneanu, 2020, Zecchin et al., 2019). Erosion could also occur during the trangression, where a WRS of small anplitude may truncate the previously deposited sediments below/offshore of the barrier (Fig. 2.19H-I; Zecchin et al., 2019).

Notably, the Maximum Regressive Surface (MRS) and the onset of the transgression would lie at the base of the

bioturbated sandstones in a bimodal setting with a transgressive barrier-lagoon. Instead, in the ramp-like setting, it is the top of the bioturbated sandstones that would mark the onset of the transgression (Fig. 2.13).

2.6.3. Progradation direction

Overall, the 250-350 m-thick series of Lower Ktawa Fm extends over tens of kilometers with only minor lateral variations in facies associations. Lateral variations in thickness of each member/sequence are on the order of 10s of m over 50 km, representing an average dip of less than 0.1º (Fig. 2.3). No geometries were recognized that could preclude the existence of prograding clinoforms within these members along the exposures. The Lower Ktawa deposits are thus understood as a flat system. A flat geometry must correspond to a low ratio between the rates of sediment input from river mouths and the rates at which sediment is transferred offshore. Accordingly, the sediment transfer and spreading by wave action (and possibly tides) must have been very efficient in order to maintain flat to low angle geometries and to prevent the formation of clinoforms. Nevertheless, the few insights on the proximal-distal orientations and along-strike symmetries (see 2.5.3) coherently suggest a South to North progradation direction. This is supported by the interpretations of the underlying First Bani Group and lateral continuation of the Ktawa Group to the East. Indeed, the First Bani Group was interpreted as a system polarized from S to N (Marante, 2008). Similarly, Meddour (2016) suggested a broad S-N to E-W proximal-to-distal trend of the Ktawa Group approximately ca. 250 km northeast from the study area (Fig. 2.2). Additionally, it is noted that the Lower Ktawa exposures along the Jbel Bani record almost exclusively shallow marine sediments, with a notable absence of any insight for fluvial or emerged environments. In the case of a S-N progradation direction, the proximal part of the sediment signature would thus be located southward from the exposures. Finally, given the laterally constrained nature of each member, such a S-N interpretation with a relatively symmetrical signal further suggests the occurrence of megalobe-shape morphologies.

2.7. Conclusion and Outlook

The Lower Ktawa Formation was deposited during Late Ordovician time on the northern sedimentary platform of North Gondwana. In the region of Tissint-Zagora in Morocco, the sediments from the Lower Ktawa Formation record a siliciclastic system dominated by storm waves from offshore to shoreface as well as nearshore

tidal and river mouth environments. Seven prominent sandstone members were defined, representing deposition during shallow phases of relative sea level fluctuations. Two depositional models are envisioned based on the interpretation of intensely bioturbated sandstones. A bimodal model is suggested whereby an open shore is subjected to wave action during sea level fall, whereas a barrier-lagoon system develops during lowstand and transgression. In this case, the bioturbated sandstones would be deposited within the lagoon. As an alternative model, a zone of high biogenic activity and low wave reworking action within the lower shoreface. These sediments were deposited in between an otherwise wave-dominated facies, where intensely bioturbated sandstones were emplaced. In that frame, the bioturbated sandstones are part of regressive sequences that are cut by a wave ravinement surface during the transgression phase, ensuing deposition of shoals. Two members (Tissint and upper Bou-Hajaj sequence) record major sea level drops, recorded by the occurrence of tidal and river mouth deposits. The progradation direction of the Lower Ktawa Fm deposits is tentatively oriented from South to North. This is based on trends of thinning of sandstone members, as well as the along-strike symmetry of sedimentary facies exposed on West-East transects. However, the Lower Ktawa deposits are organized in very flat geometries along the investigated ca. 150 km long West-East zigzagging exposures.

The apparent flatness of the seven identified sandstone members is at odd with their limited spatial extension, and the difficulty to connect members to nearby investigated sections. Indeed, large variations in relative sea level are interpreted from the sedimentary signal. Such variations are expected to be recorded at least on a regional scale, which contrasts with the limited spatial extension observed for sandstone members. Thus, whereas the deposition of the different sandstone members may be correlated to allochthonous sea level variations, their occurrence at a particular place may be related to an autochthonous organization of the sediment delivery system. In that sense, it may be envisioned that each sandstone member was deposited as a megalobe-shaped unit with a limited extent. The deposition of a lobe would create a depression around the lobe due to the deflection created by isostatic subsidence driven by the sediment loading, and in consequence, influence the localization of the subsequent advance. As such, each sandstone member may result from an eustatic driving force linked to glacial

advances, and on average, would correspond to 1.7 Myr/sequence, representing third order fluctuations. As such the two major sea level drops recorded by the Tissint and Bou-Hajaj Members may represent the response to global-scale glaciation events from the early phase of the Late Ordovician glaciation.

References

Allen, G. P. & Posamentier, H. W. 1993. Sequence stratigraphy and facies model of an incised valley fill; the Gironde Estuary, France. *Journal of Sedimentary Research,* 63**,** 378-391.

Álvaro, J. J., Benharref, M., Destombes, J., Gutiérrez-Marco, J. C., Hunter, A. W., Lefebvre, B., Van Roy, P. & Zamora, S. 2022. Ordovician stratigraphy and benthic community replacements in the eastern Anti-Atlas, Morocco.

Álvaro, J. J., Vennin, E., Villas, E., Destombes, J. & Vizcaïno, D. 2007. Pre-Hirnantian (latest Ordovician) benthic community assemblages: controls and replacements in a siliciclastic-dominated platform of the eastern Anti-Atlas, Morocco. *Palaeogeography, Palaeoclimatology, Palaeoecology,* 245**,** 20-36.

Amy, L. A., Talling, P. J., Sumner, E. J. & Malgesini, G. 2016. Current-aligned dewatering sheets and 'enhanced'primary current lineation in turbidite sandstones of the Marnoso-arenacea Formation. *Sedimentology,* 63**,** 1260-1279.

Anderson, J. B., Wallace, D. J., Simms, A. R., Rodriguez, A. B., Weight, R. W. & Taha, Z. P. 2016. Recycling sediments between source and sink during a eustatic cycle: Systems of late Quaternary northwestern Gulf of Mexico Basin. *Earth-Science Reviews,* 153**,** 111-138.

Angulo, R. J., Lessa, G. C. & De Souza, M. C. 2006. A critical review of mid-to late-Holocene sea-level fluctuations on the eastern Brazilian coastline. *Quaternary science reviews,* 25**,** 486-506.

Armon, J. & Mccann, S. 1979. Morphology and landward sediment transfer in a transgressive barrier island system, southern Gulf of St. Lawrence, Canada. *Marine Geology,* 31**,** 333-344.

Baniak, G. M., Gingras, M. K., Burns, B. A. & George Pemberton, S. 2014. An example of a highly bioturbated, storm-influenced shoreface deposit: Upper Jurassic Ula Formation,

Norwegian North Sea. *Sedimentology,* 61**,** 1261-1285.

Basilici, G., De Luca, P. H. V. & Oliveira, E. P. 2012. A depositional model for a wave-dominated open-coast tidal flat, based on analyses of the Cambrian–Ordovician Lagarto and Palmares formations, north-eastern Brazil. *Sedimentology,* 59**,** 1613-1639.

Bayet-Goll, A. 2022. Ordovician matground and mixground ecosystems in shoreface–offshore and barrier-island environments from Central Iran, northern Gondwana. *Geological Magazine,* 159**,** 925-953.

Bayet-Goll, A., De Carvalho, C. N., Mahmudy-Gharaei, M. H. & Nadaf, R. 2015. Ichnology and sedimentology of a shallow marine Upper Cretaceous depositional system (Neyzar Formation, Kopet-Dagh, Iran): Palaeoceanographic influence on ichnodiversity. *Cretaceous Research,* 56**,** 628-646.

Bentley, S. J., Sheremet, A. & Jaeger, J. M. 2006. Event sedimentation, bioturbation, and preserved sedimentary fabric: Field and model comparisons in three contrasting marine settings. *Continental Shelf Research,* 26**,** 2108-2124.

Beuf, S. 1971. *Grès du Paléozoïque inférieur au Sahara*, Editions technip.

Billy, J., Robin, N., Hein, C. J., Certain, R. & Fitzgerald, D. M. 2015. Insight into the late Holocene sea-level changes in the NW Atlantic from a paraglacial beach-ridge plain south of Newfoundland. *Geomorphology,* 248**,** 134-146.

Blum, M., Martin, J., Milliken, K. & Garvin, M. 2013. Paleovalley systems: insights from Quaternary analogs and experiments. *Earth-Science Reviews,* 116**,** 128-169.

Boote, D. R., Clark-Lowes, D. D. & Traut, M. W. 1998. Palaeozoic petroleum systems of North Africa. *Geological Society, London, Special Publications,* 132**,** 7-68.

Bourahrouh, A., Paris, F. & Elaouad-Debbaj, Z. 2004. Biostratigraphy, biodiversity and palaeoenvironments of the chitinozoans and associated palynomorphs from the Upper Ordovician of the Central Anti-Atlas, Morocco. *Review of Palaeobotany and Palynology,* 130**,** 17-40.

Brenner, O. T., Moore, L. J. & Murray, A. B. 2015. The complex influences of back-barrier deposition, substrate

slope and underlying stratigraphy in barrier island response to sea-level rise: Insights from the Virginia Barrier Islands, Mid-Atlantic Bight, USA. *Geomorphology,* 246**,** 334-350.

Buatois, L. A. & Mángano, M. G. 2007. Invertebrate ichnology of continental freshwater environments. *Trace Fossils.* Elsevier.

Burkhard, M., Caritg, S., Helg, U., Robert-Charrue, C. & Soulaimani, A. 2006. Tectonics of the anti-Atlas of Morocco. *Comptes Rendus Geoscience,* 338**,** 11-24.

Cattaneo, A. & Steel, R. J. 2003. Transgressive deposits: a review of their variability. *Earth-Science Reviews,* 62**,** 187-228.

Chacrone, C., Hamoumi, N. & Attou, A. 2004. Climatic and tectonic control of Ordovician sedimentation in the western and central High Atlas (Morocco). *Journal of African Earth Sciences,* 39**,** 329-336.

Cheel, R. J., Leckie, D. A. & Wright, V. 1993. Hummocky cross-stratification. *Sedimentology review,* 1**,** 103-122.

Choubert, G. 1942. Constitution et puissance de la série primaire de l'Anti-Atlas. *CR Acad. Sci. Paris,* 215**,** 445-447.

Choubert, G., Destombes, J., Faure-Muret, A., Gauthier, H., Hindermeyer, J., Hollard, H. & Jouravsky, G. 1970. Carte géologique de l'Anti-Atlas central et de la zone synclinale de Ouarzazate: feuilles Ouarzazate-Alougoum et Telouet sud. *Notes et Mém. Serv. Géol. Maroc,* 138.

Choubert, G., Faure-Muret, A. & Destombes, J 1989. Carte géologique du Maroc, Zagora-Coude du Dra-Hamada du Dra (pp). Echelle 1/200 000. *Notes Mém. Serv. Mines Carte géol. Maroc*.

Clerc, S., Buoncristiani, J.-F., Guiraud, M., Vennin, E., Desaubliaux, G. & Portier, E. 2013. Subglacial to proglacial depositional environments in an Ordovician glacial tunnel valley, Alnif, Morocco. *Palaeogeography, Palaeoclimatology, Palaeoecology,* 370**,** 127-144.

Cocks, L. R. M. & Torsvik, T. H. 2021. Ordovician palaeogeography and climate change. *Gondwana Research,* 100**,** 53-72.

Colmenar, J., Villas, E. & Rasmussen, C. Ø. 2022. A synopsis of Late Ordovician brachiopod diversity in the Anti-Atlas, Morocco.

Colmenar, J. & Alvaro, J. J. 2015. Integrated brachiopod-based bioevents and sequence-stratigraphic framework for a Late Ordovician subpolar platform, eastern Anti-Atlas, Morocco. *Geological Magazine,* 152**,** 603-620.

Craig, J., Rizzi, C., Said, F., Thusu, B., Luning, S., Asbali, A., Keeley, M., Bell, J., Durham, M. & Eales, M. 2008. Structural styles and prospectivity in the Precambrian and Palaeozoic hydrocarbon systems of North Africa. *The Geology of East Libya,* 4**,** 51-122.

Dabard, M.-P., Loi, A., Paris, F., Ghienne, J.-F., Pistis, M. & Vidal, M. 2015. Sea-level curve for the Middle to early Late Ordovician in the Armorican Massif (western France): Icehouse third-order glacio-eustatic cycles. *Palaeogeography, Palaeoclimatology, Palaeoecology,* 436**,** 96-111.

Dashtgard, S. E., Vaucher, R., Yang, B. & Dalrymple, R. W. 2021. Hutchison medallist 1. Wave-dominated to tide-dominated coastal systems: a unifying model for tidal shorefaces and refinement of the coastal-environments classification scheme. *Geoscience Canada,* 48**,** 5-22.

Davidson-Arnott, R. 2011. Wave-Dominated Coasts. *Treatise on Estuarine and Coastal Science,* 3**,** 73-116.

Davis, R. A. & Dalrymple, R. W. 2012. *Principles of tidal sedimentology*, Springer.

De Souza, M. C., Angulo, R. J., Assine, M. L. & De Castro, D. L. 2012. Sequence of facies at a Holocene storm-dominated regressive barrier at Praia de Leste, southern Brazil. *Marine Geology,* 291**,** 49-62.

Destombes, J. 1985. Lower palaeozoic rocks of Morocco. *Lower Palaeozoic of north-western and west-central Africa***,** 91-336.

Dietrich, P., Ghienne, J.-F., Lajeunesse, P., Normandeau, A., Deschamps, R. & Razin, P. 2019. Deglacial sequences and glacio-isostatic adjustment: Quaternary compared with Ordovician glaciations. *Geological Society, London, Special Publications,* 475**,** 149-179.

Dillenburg, S. R., Hesp, P. A., Angulo, R. J., Souza, M. C. D. & Lessa, G. C. 2009. The Holocene barrier systems of Paranaguá and northern Santa Catarina coasts, southern Brazil. *Geology and geomorphology of*

Holocene coastal barriers of Brazil, 135-176.

Dominguez, J. M. L. & Da Silva Pinto Bittencourt, A. C. 1996. Regional assessment of long-term trends of coastal erosion in northeastern Brazil. *Anais da Academia Brasileira de Ciências,* 68**,** 355-372.

Dott Jr, R. & Bourgeois, J. 1982. Hummocky stratification: significance of its variable bedding sequences. *Geological Society of America Bulletin,* 93**,** 663-680.

Dumas, S. & Arnott, R. 2006. Origin of hummocky and swaley cross-stratification—The controlling influence of unidirectional current strength and aggradation rate. *Geology,* 34**,** 1073-1076.

Dumas, S., Arnott, R. & Southard, J. B. 2005. Experiments on oscillatory-flow and combined-flow bed forms: implications for interpreting parts of the shallow-marine sedimentary record. *Journal of Sedimentary research,* 75**,** 501-513.

Elaouad-Debbaj, Z. 1984. Chitinozoaires ashgilliens de l'Anti-Atlas (Maroc). *Geobios,* 17**,** 45-75.

Ennadifi, Y. 1971. Carte géologique des Plaines du Dra au sud de l'Anti-Atlas central. Agadir-Tissint-Oued Zemoul. 1: 200.000. *Notes Mém. Serv. Mines Carte géol. Maroc,* 219.

Fielding, C. R. 2006. Upper flow regime sheets, lenses and scour fills: extending the range of architectural elements for fluvial sediment bodies. *Sedimentary Geology,* 190**,** 227-240.

Fitzgerald, D. & Miner, M. 2013. 10.7 Tidal Inlets and Lagoons along Siliciclastic Barrier Coasts. *Treatise on Geomorphology,* 10**,** 149-165.

Fortey, R. A. & Edgecombe, G. D. 2017. An Upper Ordovician (Katian) trilobite fauna from the Lower Ktaoua Formation, Morocco. *Bulletin of Geosciences,* 92**,** 1-12.

Fraser, C., Hill, P. R. & Allard, M. 2005. Morphology and facies architecture of a falling sea level strandplain, Umiujaq, Hudson Bay, Canada. *Sedimentology,* 52**,** 141-160.

Gani, M. R., Ranson, A., Cross, D. B., Hampson, G. J., Gani, N. D. & Sahoo, H. 2015. Along-strike sequence stratigraphy across the Cretaceous shallow marine to coastal-plain transition, Wasatch Plateau, Utah, USA. *Sedimentary Geology,* 325**,** 59-70.

Gao, S. & Collins, M. 2014. Holocene sedimentary systems on continental

shelves. *Marine Geology,* 352**,** 268-294.

Ghienne, J.-F., Abdallah, H., Deschamps, R., Guiraud, M., Gutiérrez-Marco, J. C., Konaté, M., Meinhold, G., Moussa, A. & Rubino, J.-L. 2023. The Ordovician record of North and West Africa: unravelling sea-level variations, Gondwana tectonics, and the glacial impact. *Geological Society, London, Special Publications,* 533**,** 199-252.

Ghienne, J. F., Le Heron, D. P., Moreau, J., Denis, M. & Deynoux, M. 2007. The Late Ordovician glacial sedimentary system of the North Gondwana platform. *Glacial sedimentary processes and products***,** 295-319.

Gil-Ortiz, M., Mcdougall, N. D., Cabello, P., Marzo, M. & Ramos, E. 2022. Sedimentary architecture of a Middle Ordovician embayment in the Murzuq Basin (Libya). *Marine and Petroleum Geology,* 135**,** 105339.

Goff, J. A., Allison, M. A. & Gulick, S. P. 2010. Offshore transport of sediment during cyclonic storms: Hurricane Ike (2008), Texas Gulf Coast, USA. *Geology,* 38**,** 351-354.

Gowland, S. 1996. Facies characteristics and depositional models of highly bioturbated shallow marine siliciclastic strata: an example from the Fulmar Formation (Late Jurassic), UK Central Graben. *Geological Society, London, Special Publications,* 114**,** 185-214.

Greenwood, B. & Sherman, D. J. 1986. Hummocky cross-stratification in the surf zone: flow parameters and bedding genesis. *Sedimentology,* 33**,** 33-45.

Grundvåg, S. A., Jelby, M. E., Olaussen, S. & Śliwińska, K. K. 2021. The role of shelf morphology on storm-bed variability and stratigraphic architecture, Lower Cretaceous, Svalbard. *Sedimentology,* 68**,** 196-237.

Gutiérrez-Marco, J. C., Muir, L. A. & Mitchell, C. E. 2022. Upper Ordovician planktic and benthic graptolites and a possible hydroid from the Tafilalt Biota, southeastern Morocco.

Gutiérrez-Marco, J. C. & Vinn, O. 2018. Cornulitids (tubeworms) from the Late Ordovician Hirnantia fauna of Morocco. *Journal of African Earth Sciences,* 137**,** 61-68.

Hamblin, A., Duke, W. & Walker, R. 1979. Hummocky Cross-Stratification--Indicator of Storm-Dominated

Shallow-Marine Environments. *AAPG Bulletin,* 63**,** 460-461.

Hamblin, A. P. & Walker, R. G. 1979. Storm-dominated shallow marine deposits: the Fernie–Kootenay (Jurassic) transition, southern Rocky Mountains. *Canadian Journal of Earth Sciences,* 16**,** 1673-1690.

Hamoumi, N. 1999. Tidally influenced sedimentation during Upper Ordovician glaciation in the central Anti-Atlas, Morocco. *Acta Universitatis Carolinae-Geologica,* 43.

Hampson, G. J. 2010. Sediment dispersal and quantitative stratigraphic architecture across an ancient shelf. *Sedimentology,* 57**,** 96-141.

Hampson, G. J. & Storms, J. E. 2003. Geomorphological and sequence stratigraphic variability in wave-dominated, shoreface-shelf parasequences. *Sedimentology,* 50**,** 667-701.

Harms, J. C., Southard, J. B., Spearing, D. R. & Walker, R. G. 1975. *Depositional environments as interpreted from primary sedimentary structures and stratification sequences*, SEPM Society for Sedimentary Geology.

Hein, C. J., Fitzgerald, D. M., Cleary, W. J., Albernaz, M. B., De Menezes, J. T. & Klein, A. H. D. F. 2013. Evidence for a transgressive barrier within a regressive strandplain system: Implications for complex coastal response to environmental change. *Sedimentology,* 60**,** 469-502.

Hein, C. J., Fitzgerald, D., Buynevich, I., Van Heteren, S. & Kelley, J. 2014. Evolution of paraglacial coasts in response to changes in fluvial sediment supply. *Geological Society, London, Special Publications,* 388**,** 247-280.

Heward, A. P. 1981. A review of wave-dominated clastic shoreline deposits. *Earth-Science Reviews,* 17**,** 223-276.

Hoepffner, C., Soulaimani, A. & Piqué, A. 2005. The moroccan hercynides. *Journal of African Earth Sciences,* 43**,** 144-165.

Hollard, H., Choubert, G., Bronner, G., Marchand, J. & Sougy, J. 1985. Carte géologique du Maroc, scale 1: 1,000,000. *Serv. Carte géol. Maroc,* 260.

Hunt, D. & Tucker, M. E. 1992. Stranded parasequences and the forced regressive wedge systems tract: deposition during base-level'fall. *Sedimentary Geology,* 81**,** 1-9.

Ichaso, A. A. & Dalrymple, R. W. 2009. Tide-and wave-generated fluid mud deposits in the Tilje Formation (Jurassic), offshore Norway. *Geology,* 37**,** 539-542.

Isla, M. F., Schwarz, E. & Veiga, G. D. 2018. Bedset characterization within a wave-dominated shallow-marine succession: an evolutionary model related to sediment imbalances. *Sedimentary Geology,* 374**,** 36-52.

Ito, M., Ishigaki, A., Nishikawa, T. & Saito, T. 2001. Temporal variation in the wavelength of hummocky cross-stratification: Implications for storm intensity through Mesozoic and Cenozoic. *Geology,* 29**,** 87-89.

Jelby, M. E., Grundvåg, S. A., Helland-Hansen, W., Olaussen, S. & Stemmerik, L. 2020. Tempestite facies variability and storm-depositional processes across a wide ramp: Towards a polygenetic model for hummocky cross-stratification. *Sedimentology,* 67**,** 742-781.

Jobe, Z. R., Lowe, D. R. & Morris, W. R. 2012. Climbing-ripple successions in turbidite systems: depositional environments, sedimentation rates and accumulation times. *Sedimentology,* 59**,** 867-898.

Keen, T., Furukawa, Y., Bentley, S., Slingerland, R., Teague, W., Dykes, J. & Rowley, C. 2006. Geological and oceanographic perspectives on event bed formation during Hurricane Katrina. *Geophysical Research Letters,* 33.

Keen, T. R., Slingerland, R., Bentley, S. J., Furukawa, Y., Teague, W. J. & Dykes, J. D. 2012. Sediment transport on continental shelves: storm bed formation and preservation in heterogeneous sediments. *Sediments, Morphology and Sedimentary Processes on Continental Shelves: Advances in Technologies, Research, and Applications***,** 295-310.

Kvale, E. P. 2006. The origin of neap–spring tidal cycles. *Marine geology,* 235**,** 5-18.

La Croix, A. D. & Gingras, M. K. 2021. Facies characteristics and stratigraphy of an Upper Cretaceous mud-dominated subaqueous delta: Medicine Hat Member (Niobrara Formation), Alberta, Canada. *Sedimentology,* 68**,** 2820-2853.

Lamb, M., Myrow, P., Lukens, C., Houck, K. & Strauss, J. 2008. Deposits from wave-influenced turbidity currents: Pennsylvanian Minturn Formation, Colorado, USA. *Journal*

of Sedimentary Research, 78**,** 480-498.

Le Heron, D. P. 2007. Late Ordovician glacial record of the Anti-Atlas, Morocco. *Sedimentary Geology,* 201**,** 93-110.

Lefebvre, B., Gutiérrez-Marco, J. C., Lehnert, O., Martin, E. L., Nowak, H., Akodad, M., El Hariri, K. & Servais, T. 2018. Age calibration of the Lower Ordovician Fezouata Lagerstätte, Morocco. *Lethaia,* 51**,** 296-311.

Lefebvre, B., El Hariri, K., Lerosey-Aubril, R., Servais, T. & Van Roy, P. 2016. The Fezouata Shale (Lower Ordovician, Anti-Atlas, Morocco): a historical review. *Palaeogeography, Palaeoclimatology, Palaeoecology,* 460**,** 7-23.

Lerma, A. N., Ayache, B., Ulvoas, B., Paris, F., Bernon, N., Bulteau, T. & Mallet, C. 2019. Pluriannual beach-dune evolutions at regional scale: Erosion and recovery sequences analysis along the aquitaine coast based on airborne LiDAR data. *Continental Shelf Research,* 189**,** 103974.

Li, W., Bhattacharya, J. & Zhu, Y. 2011. Architecture of a forced regressive systems tract in the Turonian Ferron "Notom Delta", southern Utah, USA. *Marine and Petroleum Geology,* 28**,** 1517-1529.

Li, Z., Bhattacharya, J. & Schieber, J. 2015. Evaluating along-strike variation using thin-bedded facies analysis, Upper Cretaceous Ferron Notom Delta, Utah. *Sedimentology,* 62**,** 2060-2089.

Loi, A. & Dabard, M.-P. 2002. Controls of sea level fluctuations on the formation of Ordovician siliceous nodules in terrigenous offshore environments. *Sedimentary Geology,* 153**,** 65-84.

Loi, A., Ghienne, J.-F., Dabard, M.-P., Paris, F., Botquelen, A., Christ, N., Elaouad-Debbaj, Z., Gorini, A., Vidal, M. & Videt, B. 2010. The Late Ordovician glacio-eustatic record from a high-latitude storm-dominated shelf succession: The Bou Ingarf section (Anti-Atlas, Southern Morocco). *Palaeogeography, Palaeoclimatology, Palaeoecology,* 296**,** 332-358.

Maceachern, J. A., Bann, K. L., Bhattacharya, J. P. & Howell, C. D. 2005. Ichnology of deltas: organism responses to the dynamic interplay of rivers, waves, storms, and tides.

Macquaker, J. & Gawthorpe, R. 1993. Mudstone lithofacies in the Kimmeridge Clay Formation, Wessex Basin, southern England; implications for the origin and controls of the distribution of mudstones. *Journal of Sedimentary Research,* 63**,** 1129-1143.

Marante, A. 2008. *Architecture et dynamique des systèmes sédimentaires silico-clastiques sur la" plate-forme géante" nord-gondwanienne: l'Ordivicien moyen de l'Anti-Atlas marocain.* Bordeaux 3.

Martin, E. L., Vidal, M., Vizcaïno, D., Vaucher, R., Sansjofre, P., Lefebvre, B. & Destombes, J. 2016. Biostratigraphic and palaeoenvironmental controls on the trilobite associations from the Lower Ordovician Fezouata Shale of the central Anti-Atlas, Morocco. *Palaeogeography, Palaeoclimatology, Palaeoecology,* 460**,** 142-154.

Masselink, G., Brooks, S., Poate, T., Stokes, C. & Scott, T. 2022. Coastal dune dynamics in embayed settings with sea-level rise–Examples from the exposed and macrotidal north coast of SW England. *Marine Geology,* 450**,** 106853.

Mattern, F., Pracejus, B., Scharf, A., Frijia, G. & Al-Salmani, M. 2022. Microfacies and composition of ferruginous beds at the platform-foreland basin transition (Late Albian to Turonian Natih Formation, Oman Mountains): Forebulge dynamics and regional to global tectono-geochemical framework. *Sedimentary Geology,* 429**,** 106074.

Mclaughlin, P. I., Brett, C. E., Wilson, M. A., Pratt, B. & Holmden, C. 2008. Hierarchy of sedimentary discontinuity surfaces and condensed beds from the middle Paleozoic of eastern North America: implications for cratonic sequence stratigraphy. *Geological Association of Canada Special Paper,* 48**,** 175-200.

Meddour, A. 2016. *Les séries de l'Ordovicien moyen et supérieur de l'Anti-Atlas oriental (Maroc): stratigraphie, sédimentologie et paléogeographie des systèmes de plate-forme silico-clastique.* Bordeaux 3.

Meijer, X. 2002. Modelling the drainage evolution of a river–shelf system forced by Quaternary glacio-eustasy. *Basin Research,* 14**,** 361-377.

Mellere, D., Zecchin, M. & Perale, C. 2005. Stratigraphy and sedimentology of fault-controlled backstepping shorefaces, middle Pliocene of Crotone Basin, Southern Italy. *Sedimentary Geology,* 176**,** 281-303.

Michard, A., Hœpffner, C., Soulaimani, A. & Baidder, L. 2008. The variscan belt. *Continental Evolution: The Geology of Morocco: Structure, Stratigraphy, and Tectonics of the Africa-Atlantic-Mediterranean Triple Junction.* Springer.

Moore, L. J., List, J. H., Williams, S. J. & Stolper, D. 2010. Complexities in barrier island response to sea level rise: Insights from numerical model experiments, North Carolina Outer Banks. *Journal of Geophysical Research: Earth Surface,* 115.

Mount, J. F. 1982. Storm-surge-ebb origin of hummocky cross-stratified units of the Andrews Mountain Member, Campito Formation (Lower Cambrian), White-Inyo Mountains, eastern California. *Journal of Sedimentary Research,* 52**,** 941-958.

Mulder, T., Philippe, R., Faugères, J.-C. & Gérard, J. 2011. Reply to the Discussion by Roger Higgs on 'Hummocky cross stratification-like structures in deep-sea turbidites: Upper Cretaceous Basque basins (Western Pyrenees, France)'by Mulder et al. *Sedimentology,* 56**,** 997-1015.

Mutti, E. 2019. Thin-bedded plumites: an overlooked deep-water deposit. *Journal of Mediterranean Earth Sciences,* 11**,** 61-80.

Myrow, P. 2005. Storms and Storm Deposits. Sedimentary Environments.

Myrow, P. M. & Southard, J. B. 1996. Tempestite deposition. *Journal of Sedimentary Research,* 66**,** 875-887.

NASA/METI/AIST/Japan Spacesystems and U.S./Japan ASTER Science Team (2019). *ASTER Global Digital Elevation Model V003* [Data set]. NASA EOSDIS Land Processes Distributed Active Archive Center. https://doi.org/10.5067/ASTER/ASTGTM.003

Otvos, E. G. 2012. Coastal barriers—Nomenclature, processes, and classification issues. *Geomorphology,* 139**,** 39-52.

Otvos, E. G. 2018. Coastal barriers, northern Gulf-Last Eustatic Cycle; genetic categories and development

contrasts. A review. *Quaternary Science Reviews,* 193**,** 212-243.

Otvos, E. G. & Carter, G. A. 2013. Regressive and transgressive barrier islands on the North-Central Gulf Coast—Contrasts in evolution, sediment delivery, and island vulnerability. *Geomorphology,* 198**,** 1-19.

Paola, C., Wiele, S. M. & Reinhart, M. A. 1989. Upper-regime parallel lamination as the result of turbulent sediment transport and low-amplitude bed forms. *Sedimentology,* 36**,** 47-59.

Patruno, S., Hampson, G. J., Jackson, C. a. L. & Dreyer, T. 2015. Clinoform geometry, geomorphology, facies character and stratigraphic architecture of a sand-rich subaqueous delta: Jurassic Sognefjord Formation, offshore Norway. *Sedimentology,* 62**,** 350-388.

Pellegrini, C., Maselli, V., Cattaneo, A., Piva, A., Ceregato, A. & Trincardi, F. 2015. Anatomy of a compound delta from the post-glacial transgressive record in the Adriatic Sea. *Marine Geology,* 362**,** 43-59.

Peng, Y., Steel, R. J., Rossi, V. M. & Olariu, C. 2018. Mixed-energy process interactions read from a compound-clinoform delta (paleo–Orinoco Delta, Trinidad): preservation of river and tide signals by mud-induced wave damping. *Journal of Sedimentary Research,* 88**,** 75-90.

Peters, S. E. & Loss, D. P. 2012. Storm and fair-weather wave base: A relevant distinction? *Geology,* 40**,** 511-514.

Pistis, M., Loi, A. & Dabard, M.-P. 2016. Influence of relative sea-level variations on the genesis of palaeoplacers, the examples of Sarrabus (Sardinia, Italy) and the Armorican Massif (western France). *Comptes Rendus Geoscience,* 348**,** 150-157.

Plint, A. 1988. Sharp-based shoreface sequences and.

Posamentier, H. & Allen, G. 1993. Siliciclastic sequence stratigraphic patterns in foreland, ramp-type basins. *Geology,* 21**,** 455-458.

Pratson, L. F., Nittrouer, C. A., Wiberg, P. L., Steckler, M. S., Swenson, J. B., Cacchione, D. A., Karson, J. A., Murray, A. B., Wolinsky, M. A. & Gerber, T. P. 2007. Seascape evolution on clastic continental shelves and slopes. *Continental margin sedimentation: from sediment transport to sequence stratigraphy***,** 339-380.

Proust, J.-N., Pouderoux, H., Ando, H., Hesselbo, S. P., Hodgson, D. M., Lofi, J., Rabineau, M. & Sugarman, P. J. 2018. Facies architecture of Miocene subaqueous clinothems of the New Jersey passive margin: Results from IODP-ICDP Expedition 313. *Geosphere,* 14**,** 1564-1591.

Raff, J. L., Shawler, J. L., Ciarletta, D. J., Hein, E. A., Lorenzo-Trueba, J. & Hein, C. J. 2018. Insights into barrier-island stability derived from transgressive/regressive state changes of Parramore Island, Virginia. *Marine Geology,* 403**,** 1-19.

Razin, P., Ghienne, J. F., Loi, A. & Marante, A. 2020. Architecture et dynamique des systèmes sédimentaires de l'Ordovicien antéglaciaire de l'Anti-Atlas. *Géochronique,* 153**,** 25-32.

Ravier, E., Buoncristiani, J.-F., Menzies, J., Guiraud, M., Clerc, S. & Portier, E. 2015. Does porewater or meltwater control tunnel valley genesis? Case studies from the Hirnantian of Morocco. *Palaeogeography, Palaeoclimatology, Palaeoecology,* 418**,** 359-376.

Rodriguez, A. B., Theuerkauf, E. J., Ridge, J. T., Vandusen, B. M. & Fegley, S. R. 2020. Long-term washover fan accretion on a transgressive barrier island challenges the assumption that paleotempestites represent individual tropical cyclones. *Scientific reports,* 10**,** 19755.

Rust, B. R. & Gibling, M. R. 1990. Three-dimensional antidunes as HCS mimics in a fluvial sandstone; the Pennsylvanian South Bar Formation near Sydney, Nova Scotia. *Journal of Sedimentary Research,* 60**,** 540-548.

Sanders, J. E. & Kumar, N. 1975. Evidence of shoreface retreat and in-place "drowning" during Holocene submergence of barriers, shelf off Fire Island, New York. *Geological Society of America Bulletin,* 86**,** 65-76.

Sedgwick, P. E. & Davis Jr, R. A. 2003. Stratigraphy of washover deposits in Florida: implications for recognition in the stratigraphic record. *Marine geology,* 200**,** 31-48.

Southard, J. B., Lambie, J. M., Federico, D. C., Pile, H. T. & Weidman, C. R. 1990. Experiments on bed configurations in fine sands under bidirectional purely oscillatory flow, and the origin of hummocky cross-stratification. *Journal of Sedimentary Research,* 60**,** 1-17.

Swift, D. J. 1975. Barrier-island genesis: evidence from the central Atlantic shelf, eastern USA. *Sedimentary Geology,* 14**,** 1-43.

Switzer, A. D. & Jones, B. G. 2008. Large-scale washover sedimentation in a freshwater lagoon from the southeast Australian coast: sea-level change, tsunami or exceptionally large storm? *The Holocene,* 18**,** 787-803.

Talling, P. J., Allin, J., Armitage, D. A., Arnott, R. W., Cartigny, M. J., Clare, M. A., Felletti, F., Covault, J. A., Girardclos, S. & Hansen, E. 2015. Key future directions for research on turbidity currents and their deposits. *Journal of Sedimentary Research,* 85**,** 153-169.

Talling, P. J., Masson, D. G., Sumner, E. J. & Malgesini, G. 2012. Subaqueous sediment density flows: Depositional processes and deposit types. *Sedimentology,* 59**,** 1937-2003.

Tamura, T. 2012. Beach ridges and prograded beach deposits as palaeoenvironment records. *Earth-Science Reviews,* 114**,** 279-297.

Taylor, A. & Goldring, R. 1993. Description and analysis of bioturbation and ichnofabric. *Journal of the Geological Society,* 150**,** 141-148.

Taylor, A., Goldring, R. & Gowland, S. 2003. Analysis and application of ichnofabrics. *Earth-Science Reviews,* 60**,** 227-259.

Tinterri, R. 2011. Combined flow sedimentary structures and the genetic link between sigmoidal-and hummocky-cross stratification. *GeoActa,* 10**,** 1-43.

Van Yperen, A. E., Poyatos-Moré, M., Holbrook, J. M. & Midtkandal, I. 2020. Internal mouth-bar variability and preservation of subordinate coastal processes in low-accommodation proximal deltaic settings (Cretaceous Dakota Group, New Mexico, USA). *The Depositional Record,* 6**,** 431-458.

Vaucher, R., Martin, E. L., Hormière, H. & Pittet, B. 2016. A genetic link between Konzentrat-and Konservat-Lagerstätten in the Fezouata Shale (lower Ordovician, Morocco). *Palaeogeography, Palaeoclimatology, Palaeoecology,* 460**,** 24-34.

Vaucher, R., Pittet, B., Hormière, H., Martin, E. L. & Lefebvre, B. 2017. A wave-dominated, tide-modulated model for the Lower Ordovician of

the Anti-Atlas, Morocco. *Sedimentology,* 64**,** 777-807.

Vaucher, R., Pittet, B., Humbert, T. & Ferry, S. 2018. Large-scale bedforms induced by supercritical flows and wave–wave interference in the intertidal zone (Cap Ferret, France). *Geo-Marine Letters,* 38**,** 287-305.

Vidal, M., Loi, A., Dabard, M.-P. & Botquelen, A. 2011. A Palaeozoic open shelf benthic assemblage in a protected marine environment. *Palaeogeography, Palaeoclimatology, Palaeoecology,* 306**,** 27-40.

Videt, B., Paris, F., Rubino, J.-L., Boumendjel, K., Dabard, M.-P., Loi, A., Ghienne, J.-F., Marante, A. & Gorini, A. 2010. Biostratigraphical calibration of third order Ordovician sequences on the northern Gondwana platform. *Palaeogeography, Palaeoclimatology, Palaeoecology,* 296**,** 359-375.

Villas, E., Vizcaïno, D., Álvaro, J. J., Destombes, J. & Vennin, E. 2006. Biostratigraphic control of the latest-Ordovician glaciogenic unconformity in Alnif (Eastern Anti-Atlas, Morocco), based on brachiopods. *Geobios,* 39**,** 727-737.

Webby, B. D., Paris, F., Droser, M. L. & Percival, I. G. 2004. *The great Ordovician biodiversification event*, Columbia University Press.

Wolinsky, M. A. & Murray, A. B. 2009. A unifying framework for shoreline migration: 2. Application to wave-dominated coasts. *Journal of Geophysical Research: Earth Surface,* 114.

Yagishita, K. 1994. Antidunes and traction-carpet deposits in deep-water channel sandstones, Cretaceous, British Columbia, Canada. *Journal of Sedimentary Research,* 64**,** 34-41.

Zecchin, M. 2007. The architectural variability of small-scale cycles in shelf and ramp clastic systems: the controlling factors. *Earth-Science Reviews,* 84**,** 21-55.

Zecchin, M. & Catuneanu, O. 2015. High-resolution sequence stratigraphy of clastic shelves III: Applications to reservoir geology. *Marine and Petroleum Geology,* 62**,** 161-175.

Zecchin, M. & Catuneanu, O. 2020. High-resolution sequence stratigraphy of clastic shelves VII: 3D variability of stacking patterns. *Marine and Petroleum Geology,* 121**,** 104582.

Zecchin, M., Catuneanu, O. & Caffau, M. 2019. Wave-ravinement surfaces:

classification and key characteristics. *Earth-science reviews,* 188**,** 210-239.

CHAPTER THREE

Sedimentology, stratigraphy of the pre-glacial deposits of the Rouïd-Aïssa Formation of Late Ordovician time (Morocco)

3.1. Introduction

This chapter focuses on the Rouïd-Aïssa (Er-Rwaidat) Formation which is part of the Ktawa Group (western Anti-Atlas, Morocco). This formation was defined in the western Central Anti-Atlas as a well-developed and thick sandstone cliff in Destombes (1985). Due to its location between two prominent cuestas part of the Jbel Bani cliff, accessibility poses challenges. Hence, the Rouïd-Aïssa Fm was never thoroughly studied except by Destombes (1985). The Rouïd-Aïssa was correlated to the Upper Tiouririne to the east of the study area, where more studies compiled data on the formation (e.g. El Maazouz and Hamoumi, 2007, Loi et al., 2010, Meddour, 2016). During deposition of the Upper Tiouririne (Rouïd-Aïssa?) Fm, this section of the Anti-Atlas might have been subjected to tectonic influences that were not identified in the study area (El Maazouz and Hamoumi, 2007).

Here, we put focus on facies associations descriptions which were never thoroughly defined before. Three relative sea level curve were reconstructed after interpretation of depositional environments from facies associations along the studied transect on different stratigraphic profiles to demonstrate the variety of facies associations, sandstone-amalgamation and difference in thicknesses of units. Finally, the change in progradation orientation of the systems from the underlying, present, and overlying formations is discussed in terms of possible tectonic influences in the region.

3.2. Geological setting

The Jbel Bani cliff (Anti-Atlas, South Morocco) exposes a prominent succession of Late Ordovician deposits along 100s of kilometres (Fig. 3.1). Siliciclastic shallow marine sedimentation prevailed during this time period on the northern platform of the supercontinent Gondwana (Destombes, 1985, Loi et al., 2010, Marante, 2008, Meddour, 2016). These deposits were part of the northern edge of the Tindouf Basin which was inverted during the Variscan orogeny (Burkhard et al., 2006, Pique and Michard, 1989). During Late Ordovician time, the Anti-Atlas was located at high paleolatitudes, ca. 60°S to 70°S and is marked by the Early Paleozoic, Hirnantian glaciation (Fig. 3.1, Cocks and Torsvik, 2021, Dietrich et al., 2019, Ghienne et al., 2023).

The studied region is located in the western Central Anti-Atlas (Fig. 3.1) where the Rouïd-Aïssa Formation was investigated. The Rouïd-Aïssa Fm is sandstone-

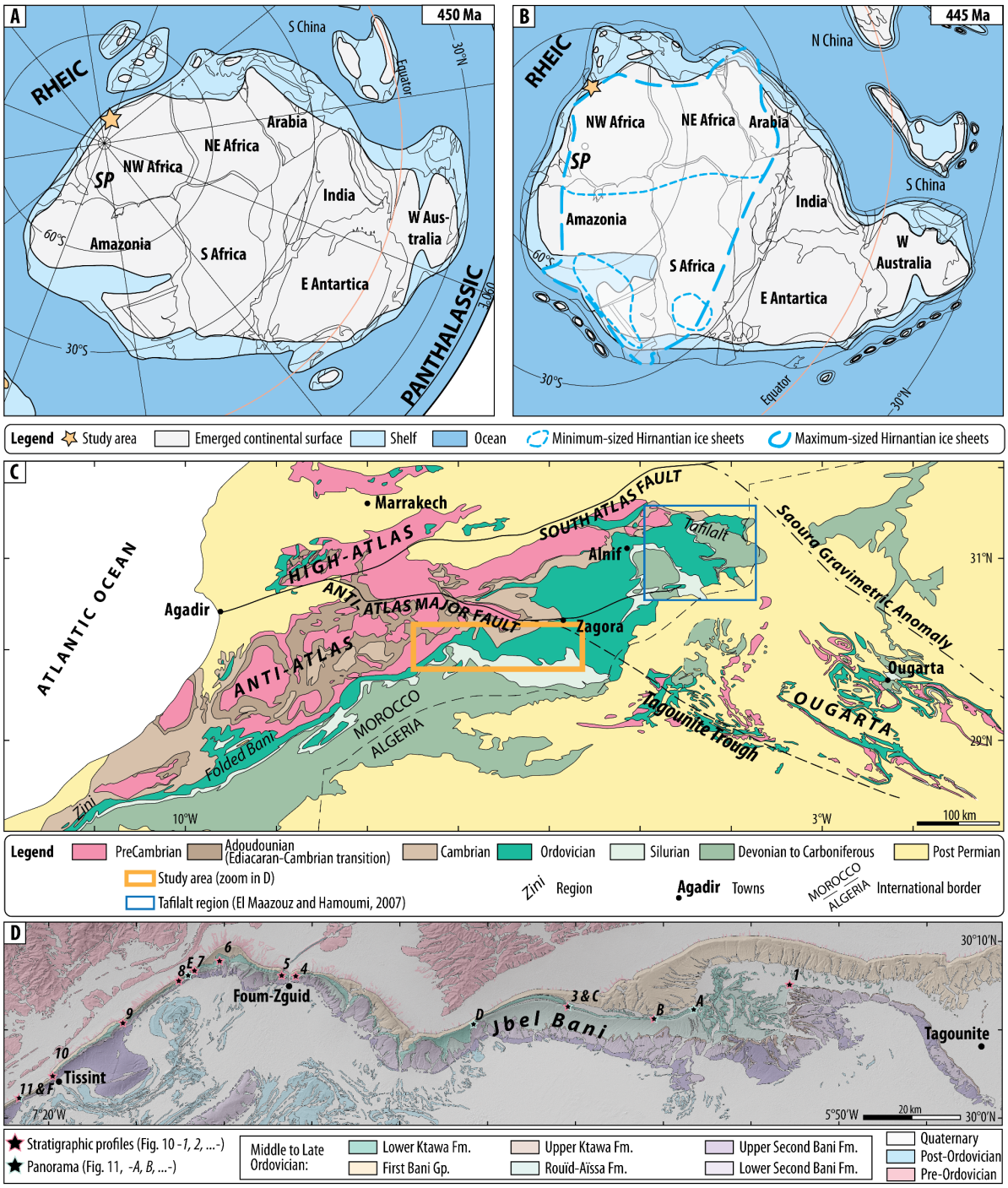

***Figure 3.1**: Context and paleogeographic location of the study area. (A & B) Paleogeographic reconstructions of the Gondwana at 450 Ma (Katian, modified from Cocks and Torsvik, 2021) and 445 Ma (Hirnantian, modified from Torsvik and Cocks, 2013). (C) Simplified geological map of southern Morocco and western Algeria, highlighting significant features (modified from Ghienne et al., 2007, Hollard et al., 1985, Ennih and Liegeois, 2001). (D) Detailed geological map of the Jbel Bani cliff between the localities of Tissint and Tagounite. Location of stratigraphic profiles and panorama are included. Geological map modified after (Choubert et al., 1970, Choubert et al., 1989, Ennadifi, 1971). Background Digital Elevation Model: NASA (2019).*

dominated and enclaved in the Lower and

Upper Ktawa Fms, both mudstone-dominated (Sanbian-Katian, Destombes, 1985). The Rouïd-Aïssa Fm is of Late Katian age (Late Ordovician) where the sediments composing the formation are deposited a few Myr prior to the Late Ordovician glaciation maximum at 445.2 Ma (Hirnantian, Fig. 3.1B). As such, new chitinozoan biozones data point out that the Rouïd-Aïssa Fm bears *Nigerica* (ca. 448.5-447 Ma) to perhaps *Merga* (ca. 447-445 Ma, Ghienne, Paris, Vandenbroucke, and De Backer, unpublished pers. comm.). This would make a maximum depositional age between 448.5 and 445 Ma. The glacigenic incisions partly eroded the Rouïd-Aïssa Fm to the W of the studied transect.

The Ktawa Group, to which the Rouïd-Aïssa Fm belongs to, is also located and exposed between two prominent cuestas making the First and Second Bani Groups (i.e. under- and overlying the Ktawa Group respectively). Hence, direct access to outcrops is challenging due to its location. Only Destombes (1985) gave close interests to the Rouïd-Aïssa Fm and mapped it over the Anti-Atlas. Paleontological studies superficially mention it (Babin and Descombes, 1990, Benssaou et al., 2020, Gutiérrez-Marco et al., 2022). Furthermore, confusion on correlations in the western Anti-Atlas is enhanced by the second name given to the Rouïd-Aïssa Fm by Destombes (1985): Er-Rwaidat. Finally, lithostratigraphic correlations across the Anti-Atlas are unfeasible due to the fact that the Ktawa Group is mudstone-dominated in the region of Tagounite (Fig. 3.1, i.e. Tagounite Trough or depocenter, east of the study area). This region is located in-between the western Central and eastern Central to Oriental Anti-Atlas, making the comprehension of the Ktawa Group and the Rouïd-Aïssa Fm, of interest here, more difficult. Correlations to the eastern (Central/Oriental) Anti-Atlas were made with the Upper Tiouririne Fm which after biostratigraphic (chitinozoans) calibrations and correlations would be different (see Chapter 4 and Destombes, 1985). This correlation is dependent on the locality and further biostratigraphic data need to be acquired.

3.3. Methods

Eleven stratigraphic profiles were logged at a decimetre scale along a ca. 150 km-long transect (Appendix C). The transect, oriented E-W, is located along the Jbel Bani cliff in Southern Morocco (Fig. 3.1D). Facies analysis was conducted through grain-size, sedimentary structures and ichnology in order to interpret facies associations and their depositional environments to some extent. Three of the logs were calibrated in thickness from 3D

photogrammetric reconstructions acquired with an Unmanned Aerial Vehicle and panorama views of outcrops were made for 4 other locations where only the Lower Ktawa Fm was logged. The stacking pattern of facies associations enabled the extrapolation of interpreted depositional environments to relative sea level (RSL) curves. RSL curves were reconstructed for 3 stratigraphic profiles and correlated to one another. The Maximum Regressive Surface (MRS) was placed at the turnaround from the regressive to transgressive units (i.e. retrogradation to progradation), where the Maximum Flooding Surface (MFS) was placed at the opposite trend (i.e. from transgressive to regressive units, progradation to retrogradation, e.g. Catuneanu et al., 2009, Van Wagoner et al., 1988).

The present chapter is an overview of the Rouïd-Aïssa Fm where detailed stratigraphic profiles and description of facies associations can improve the knowledge about this not well-studied formation. An overview on tectonic influence is also discussed to better assess a possible change and shift in the proximal-to-distal trend from the underlying First Bani Group and Lower Ktawa Fm to the Rouïd-Aïssa Fm studied here.

3.4. Facies associations

Mudstones, ferruginous horizons and silts and sandstone ripples were described in Chapter 2 (2.4. Facies associations). Mudstones and silts and rippled sandstones were interpreted as deposits from offshore to upper offshore depositional environments. Ferruginous horizons are condensed levels forming during retrogradation phases and are markers of the peak rate of transgression. Here, 6 facies associations (FA) are described. All of the Rouïd-Aïssa Fm facies associations are summarized in Table 3.1.

3.4.1. Isolated sandstones bearing HCS sandstones and shell concentrations, with silts and sand ripple-marked interbeds

Description: Thick isolated Hummocky Cross-Stratifications (HCS) sandstones mainly compose this facies association (Fig. 3.2). The HCS-bearing fine to medium-grained sandstones are intercalated with a heterogeneous facies association composed of silts, sometimes highly bioturbated, rippled-marked sandstones and hummocky-like ripples (Fig. 3.2A, B & D). The HCS are 10 cm to 1 m thick, demonstrate laminated to slightly quartzose massive or carbonated textures, and have a lensed shape up to a few meters in wavelength (Figs 3.2A and 3.3A & B).

***Table 3.1**: Summary of facies associations in the studied interval for the Rouïd-Aïssa Formation. The mudstones, ferruginous horizons and silts and sandstone ripple-marked facies associations were described in Chapter 2.*

Main lithologies	Sedimentary structures	Interpreted depositional processes	Depositional environments
Mudstones	Finely laminated, fissile shales and silts. Occasionally highly bioturbated	Calm, subaqueous setting, dominated by decantation of suspended load	Offshore
Ferruginous horizons	Dark bordeau, highly competent and ferruginous. Abundant concretions. Phosphate and/or manganese pebbles, ferruginous to phosphatic oolites	Combination of chemical precipitation and low sedimentation rates	Offshore
Isolated sandstones bearing HCS sandstones and shell concentrations, with silts and sand ripple-marked interbeds	Laminated silts and intercalations of rippled sandstones. Starved to climbing uni- to bidirectional ripples, sometimes sigmoidal and aggrading laminae (i.e. hummocky-like ripples). Erosive- to conformable-based. Horizontal bioturbation common	Laminated silts and intercalations of rippled sandstones. Starved to climbing uni- to bidirectional ripples, sometimes sigmoidal and aggrading laminae (i.e. hummocky-like ripples). Erosive- to conformable-based. Horizontal bioturbation common	Upper offshore
Isolated sandstones bearing HCS sandstones and shell concentrations, with silts and sand ripple-marked interbeds	HCS sandstones: fine-grained, 10 to 1 m thick, laminated to slightly quartzose or carbonated textures, lensed shape. Erosive based, often platy spalling laminations gently inclined or massive texture (lamination still visible). Shell lenses common along lamina, few mm to cm thick. Climbing to symmetrical ripples at the HCS top. Hummock to flat bedforms. Uncommon bioturbation. Intercalated with silts (sometimes highly bioturbated), sand ripples, and hummocky-like ripples	Isolated HCS sandstones: oscillatory flow reworking a current transporting sediments offshore such as floods or storms. Long period of oscillations. Waning flows during deposition of ripples. Shell lenses: winnowing of current carrying clasts in hyperconcentration. Silts, sand ripples and hummocky-like ripples: calm environment interrupted by flood to storm triggered currents, subjected to oscillatory component during deposition. High bioturbation might be due to change in bioturbation intensity and/or sedimentation rate	Upper offshore transition
Stacked to amalgamated HCS sandstones bearing shell concentrations	Fine- to medium-grained sandstones, few centimetres to several metres thick HCS. Stacked HCS: well defined hummock, platy spalling along lamina and parting lineations, lensed shaped of a few metres in wavelength. Amalgamated HCS: continuous bedsets, crosscutting relationship. Erosive base (sub-horizontal undulations, decimetric gullies, plurimetric troughs). Both: sub-planar to low-angle lamina, occasional symmetrical to polygonal ripples. Shell and mud clasts lenses along lamina. Sometimes moderately bioturbated	HCS: High frequency of storm-derived currents without calm periods. Bimodal current-decantation phase and alignment of particles in an upper flow regime to make the platy spalling and parting lineations of stacked HCS. Good sorting of sandstone. No to regular reworking. Clasts in concentrations: winnowing of current dragging hyperconcentrated clasts	Shoreface

Table 3.1 *(Continued).*

Main lithologies	Sedimentary structures	Interpreted depositional processes	Depositional environments
Coarse cross-bedded sandstones bearing rip-up and shell clasts in concentrations	Well-sorted coarse- to very-coarse-grained sandstones, dm to m thick beds. Tabular to tangential cross-, trough-cross laminations, herringbones and sub planar laminations. Common erosion within layers and reactivation surfaces. Trough at the base of layers, several m wide and dm deep. Uncommon ripples at the bed surface. Rare bioturbation but includes *Skolithos* and *Diplocraterion* isp. Common mud clasts and shell beds aligned along lamina. Floating roughly angular very-coarse sand clasts along cross-lamina. Pebbles up to 2.5 cm	Proximity of delivery system and emerged very proximal environment from coarseness of matrix, large mud clasts and pebble. Tractive currents with frequent and rapid changes in vigorous flow conditions	Shallow tidal-dominated environment including flood-ebb delta, sand/mouth bars, and tide-influenced channels
Silty- and medium-grained intensely bioturbated sandstones	Unsorted silty very-fine to medium sandstones. High to intense bioturbation (BI 4-5). Several cm to dm thick beds. Primary sedimentary structures hindered by high intensity of bioturbation. Diffuse undulating to lensed shape layers. When medium-grained, more continuous layers compared to very-fine-grained. Sporadic HCS, cross-lamina, horizontal (*Cruziana*) bioturbation	Brackish to marine environments. Inputs of sediments by tractive to oscillatory currents. High rates of biogenic activity or low rates of sedimentation and reworking	Lagoon to estuary/tidal flat in a restricted to protected marine environment
Lag deposits bearing pebble and shell clasts	Pebble and shell clasts in matrix supported fabric. Matrix either carbonated or coarse- to very-coarse-grained sand. Cm to few dm thick layers. Occur at the top of sandstone beds, in shales, or in between HCS-bearing sandstones. Often ferruginous patina. Irregular base common. Concave up and down organisation of shell clasts. Pebbles up to 8 cm in diameter. When pebble lags are in mudstones, pebbles are composed of conglomerates	Reworking and winnowing of older and/or proximal deposits in a setting with low sediment input. Erosion from wave ravinement during transgression	Transgressive lag
Highly deformed sandstones	Sandy-silty ball-and-pillow structures. Few dm to m in length with elongated shape of the structures. FA located directly below a glacial incision	Soft-sediment deformation structures associated with fluid escape/dewatering of mildly compacted sediments. Glacial or sediment loading triggering mechanism of deformation	Undefined

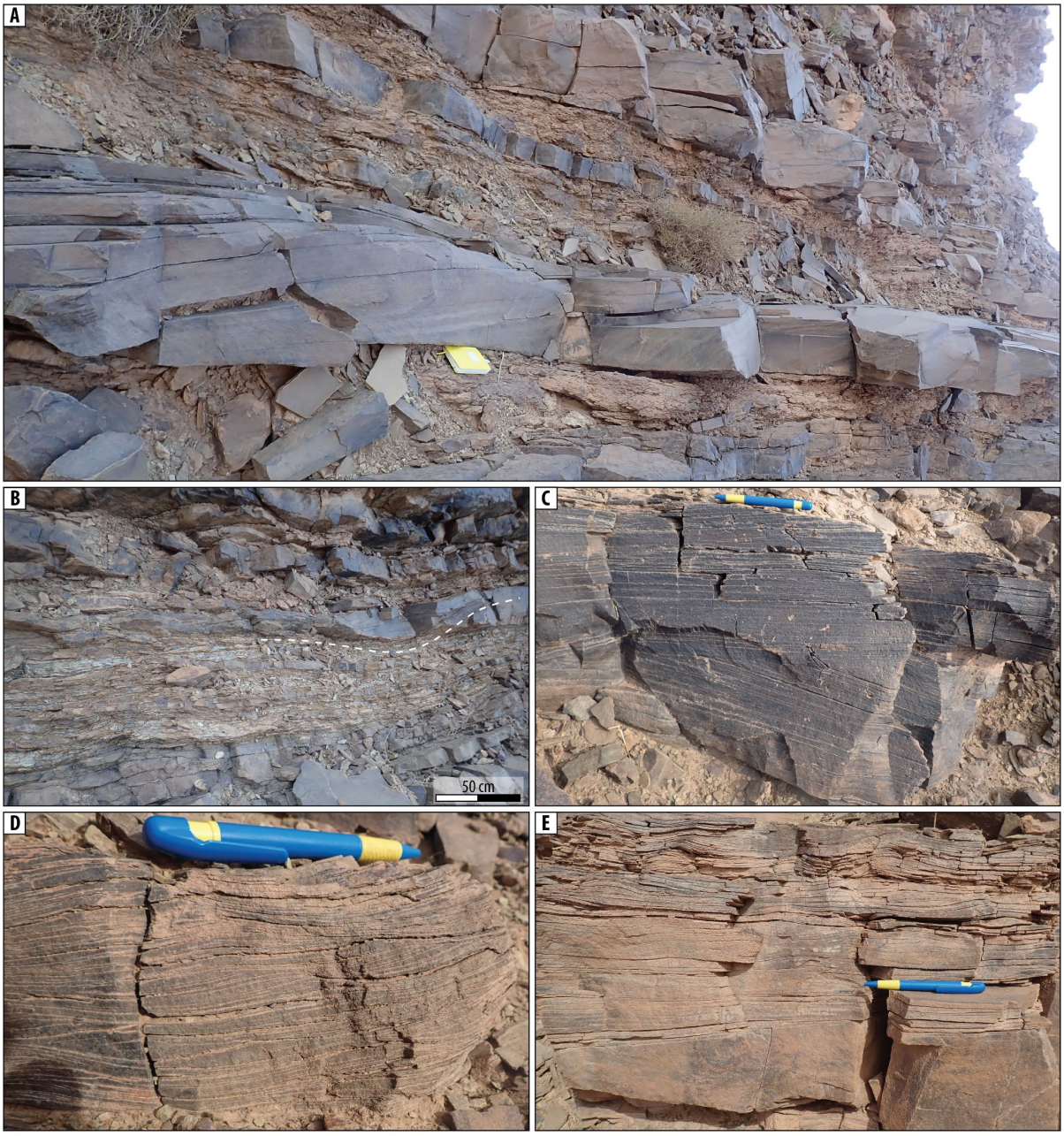

***Figure 3.2**: Isolated sandstones bearing HCS sandstones (and shell concentrations), with silts and rippled-marked sandstones interbeds facies association. (A) Large amplitude isolated HCS sandstone with hummock shape in bioturbated silts to heterolithic facies association. Quartzose texture of the HCS where laminations can be observed dipping toward the left. Notebook for scale: 24 cm. (B) Erosive based HCS/SCS outlined with a flat top outcropping in silts and rippled-sandstones. (C) Isolated HCS. Slaty texture of HCS laminae. Upper subhorizontal HCS sandstone is erosive on low-angle HCS. (D) Stack of climbing-aggrading ripples observed at the top on an isolated HCS. Few erosive bases. (E) Isolated HCS with flat top. Massive base, erosive. Thick (cm) slaty subhorizontal laminae overlying massive texture. Climbing-aggrading to symmetrical ripples at the top. (C-E) Pen for scale: 13.7 cm.*

The base is sometimes erosive of a few centimetres to decimetres deep and filled with Swaley-Cross-Stratified (SCS) sandstone (Fig. 3.2C). Overall, HCS

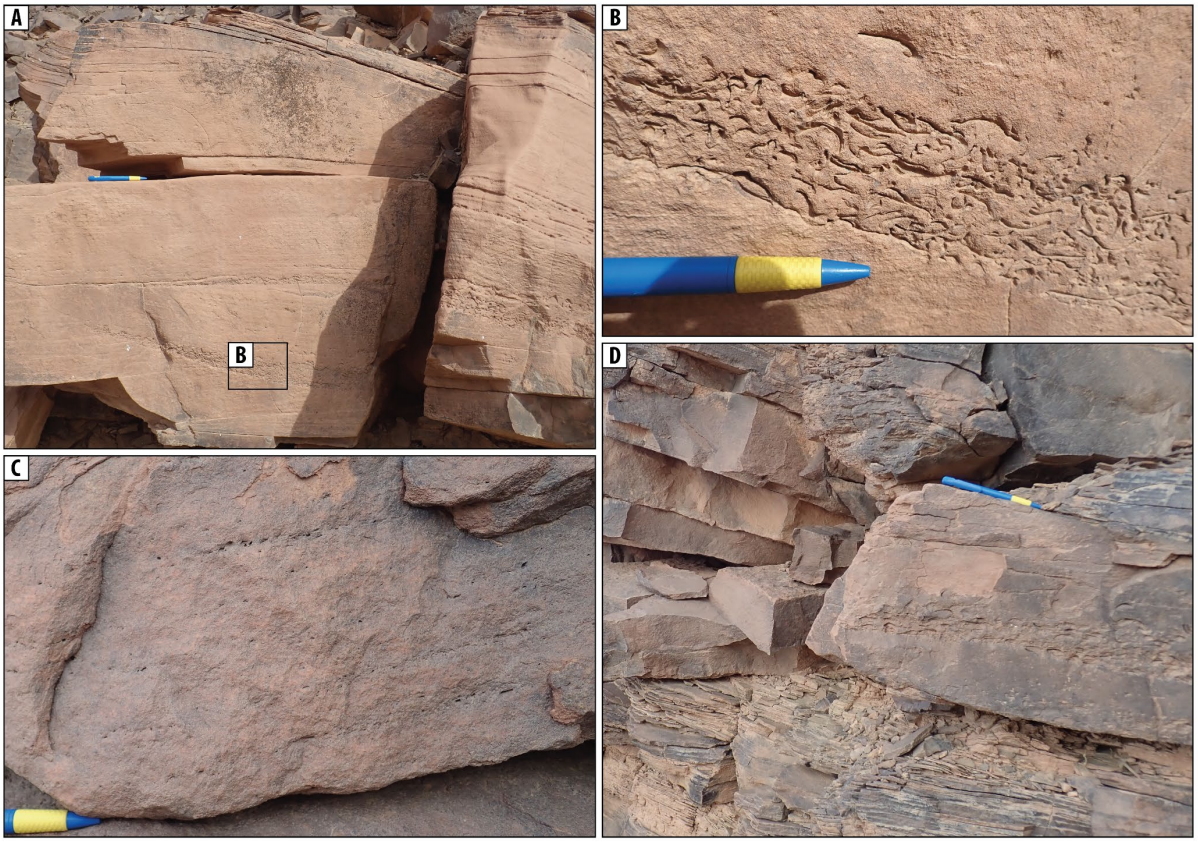

***Figure 3.3**: Shell imprints concentrations. (A-B) Observed in 'isolated sandstones bearing HCS sandstones' facies association. (C-D) Observed in 'stacked to amalgamated HCS sandstones' facies association. (A) Multiple shell concentrations along laminae. Thickening of concentration toward the lower part of the lamina. Zoom of lower shell concentration layer in (B): Concave up and down of shells settlements. (C) Several thin layers of shells to rip-up clasts imprints aligned along low-angle laminations. Observed at the base of a several m stack of amalgamated HCS. Quartzose texture of the medium-grained sandstone. (D) Centimeter-thick shell concentrations in HCS part of stacked HCS sandstones. Shells are mainly concave down. Pen for scale: 13.7 cm.*

sandstones often show a platy spalling along lamination where lamination is still visible (Fig. 3.2C & E). Laminae are gently inclined. Shell lenses are sometimes recognized along a lamina, from a few millimetres to centimetres in thickness (Fig. 3.3A & B). The top is often of composed climbing to symmetrical ripples (Fig. 3.3E). HCS bedforms vary from hummocks to flat. Bioturbation is not common.

Interpretation: Silts are interpreted as deposited in a calm environment. Rippled-sandstones interrupting the silty background would result from low-density sediment gravity flows (Talling et al., 2012). Processes emplacing these hummocky-like ripples could be floods or storms, where the triggered currents would be subjected to an oscillatory component during deposition (Jelby et al., 2020,

Myrow, 2005, Myrow and Southard, 1996, Talling et al., 2015). Meter-scaled wavelength HCS might suggest longer periods of oscillations of larger storm waves. Shell lenses would occur during the winnowing of the current-carrying clasts in hyperconcentration (Jelby et al., 2020, Kreisa and Bambach, 1982). The grading in HCS of low-angle lamination to climbing/symmetrical ripples suggests waning flows (Dott Jr and Bourgeois, 1982, Kreisa and Bambach, 1982, Leckie and Walker, 1982). High bioturbation recognized in this FA could be related to a change in bioturbation intensity and/or sedimentation rate (Gowland, 1996, Keen et al., 2012). The silts and sandstone ripples are then interpreted as deposited in the upper offshore limit. Superimposing the high occurrence of these isolated HCS sandstones suggests that the depositional environment is located above the storm wave base within the upper offshore transition.

3.4.2. Stacked to amalgamated HCS sandstones bearing shell concentrations

Description: In this FA, HCS-bearing sandstone beds consist of well-sorted fine- to medium-grained sandstones of a few centimetres to several metres in thickness (Fig. 3.4). The HCS beds show platy spalling along lamina and parting lineations with a well-defined hummock shape when HCS beds are stacked on top of each other (Fig. 3.4A, B & D). Stacked HCS are organized in lenses of a few metres in wavelength. When HCS beds are amalgamated, their appearance is completely massive where laminae are sometimes still visible (Fig. 3.4C). Amalgamated HCS beds are continuous over the outcrop and are crosscutting each other. Their base is erosive, from sub-horizontal undulations to decimetric gullies and plurimetric troughs (Fig.3. 4A & C). Both stacked and amalgamated HCS show sub-horizontal to low-angle laminations

Figure 3.4*: Stacked to amalgamated HCS sandstones (bearing shell concentrations) facies association. (A) Outcrop scaled picture of stacked to amalgamated sandstones, showing mainly a massive texture of beds. Cross-cutting relationship between sandstone layers. At least 4 thickening-upward parasequences of very high-order can be observed in a lower order thickening upward sequence. (B) Stack of HCS sandstones. Subhorizontal laminations prevail to rarer massive texture observed at the base of layers. No to little erosion between HCS beds. (C) Stacked to amalgamated HCS sandstones. Massive amalgamated sandstones are sharp- to erosive- based. Stacked HCS with subhorizontal lamination underlying massive amalgamated ones. Notebook for scale: 24 cm. (D) Parting lineation observed in subhorizontal slaty laminations of stacked HCS sandstones. Pen for scale: 13.7 cm. (E) Symmetrical rippled-surface with undulating crests.*

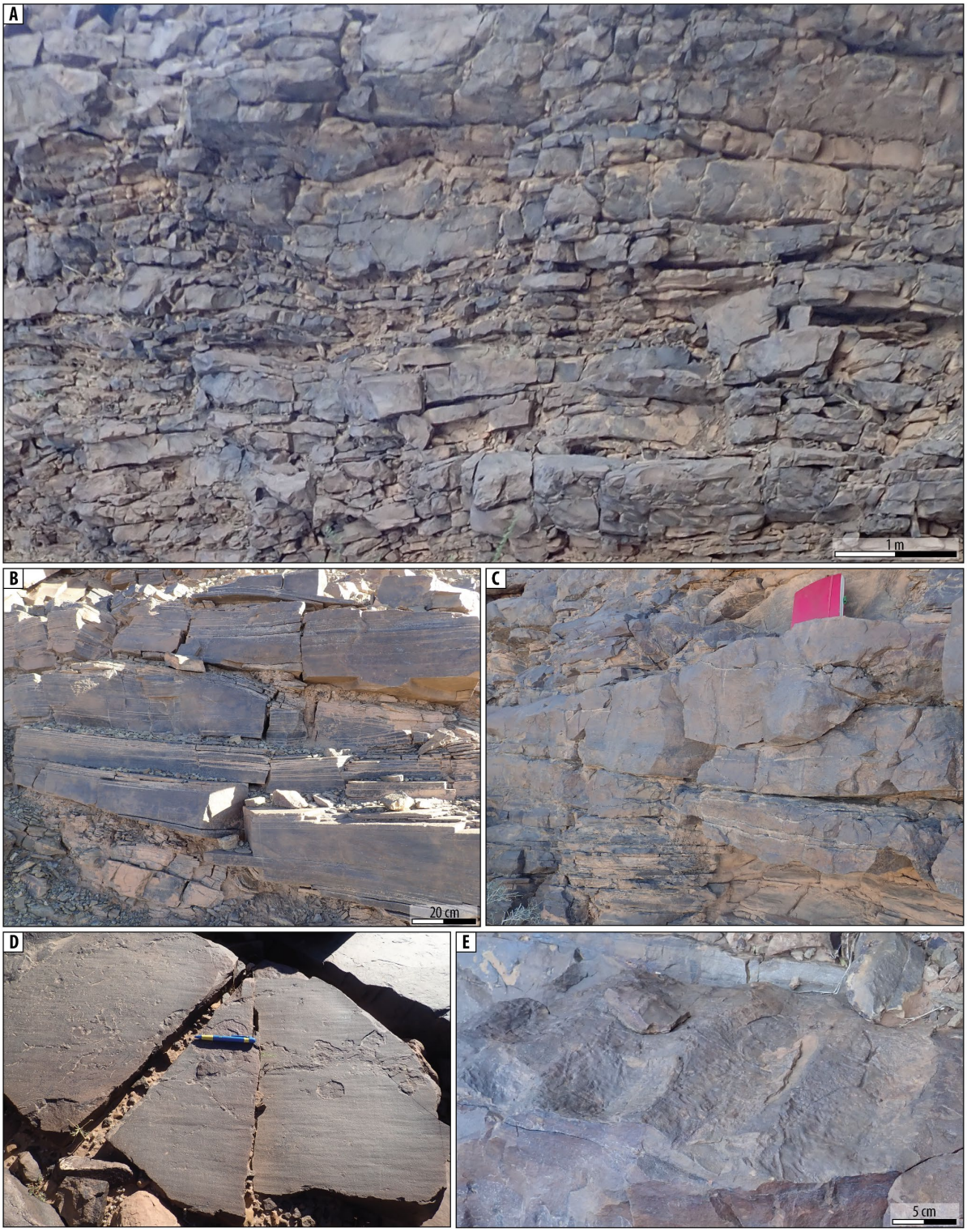

(Fig. 3.4B). Their top is sometimes composed of symmetrical to polygonal ripples (Fig. 3.4E). Shell and mud clast lenses can be observed along laminae (Fig. 3.3C & D). Some stack of layers can be moderately bioturbated. This FA is usually organized in very high order (5^{th} order?) coarsening and thickening upward parasequences, making a lower order

parasequence of coarsening and thickening upward (Fig. 3.4A).

Interpretation: HCS sandstones are interpreted as deposited by storm- or flood-derived processes (Jelby et al., 2020). The absence of silts suggests a high frequency of storm-derived currents without calm periods. The quartzose texture of both the stacked to amalgamated HCS would imply a good sorting of sandstones. Stacked HCS are characterized by none to little erosion, where amalgamated HCS are cross-cutting one and another. Hence, no to regular reworking is implied. Constant wave influence is suggested by the dominance of HCS structures, erosions and absence of fines (Dott Jr and Bourgeois, 1982, Dumas and Arnott, 2006, Li et al., 2015, MacEachern et al., 2005). Shell to mud clasts lenses would be emplaced during winnowing of the current dragging hyperconcentrated clasts (Bayet-Goll et al., 2015, Cattaneo and Steel, 2003, Ichaso and Dalrymple, 2009, Li et al., 2011). This facies association is then understood as being deposited in shoreface environments.

3.4.3. Coarse cross-bedded sandstones bearing rip-up and shell clasts in concentrations

Description: This facies association consists of well-sorted coarse- to very-coarse-grained sandstones of decimetric to metric thick beds (Figs 3.5 & 3.6). The sandstones show tabular to tangential cross-, trough-cross laminations, as well as herringbones to sub-horizontal laminations (Fig. 3.5 B, C & D). Erosion within a bed and reactivation surfaces are common. The base of the layers is erosive, making troughs up to several metres wide and several decimetres deep. Ripples are uncommon at the bed surface. Bioturbation is rare, but when visible, it is characterized mainly by *Skolithos* to more rarely *Diplocraterion* isp. (Fig. 3.5E). Large mud clasts and shell beds are common and are aligned along laminae (Fig. 3.5D and 6D). This FA can be poorly-sorted. Floating roughly angular very-coarse sand clasts can

Figure 3.5*: Coarse cross-bedded sandstones bearing rip-up and shell clasts in concentrations facies association. (A) Centi- to decimeter-thick sandstones beds composed of deep truncations, sub-horizontal, cross- to trough-cross-laminations. Notebook for scale: 24 cm. (B) Cross- to trough-cross laminations and herringbone sedimentary structure in a sandstone composed of centimeter-thick erosive-based layers, with zoom in (C) of the herringbone structure. (D) Imprints of decimeter to centimeter rip-up clast aligned along subhorizontal to trough-cross-laminations in erosive-based sandstones. (E) Cross- to trough-cross laminations with diferent progradation directions in erosive-based sandstones Bio.: bioturbation (B) to (E) Pen for scale: 13.7 cm.*

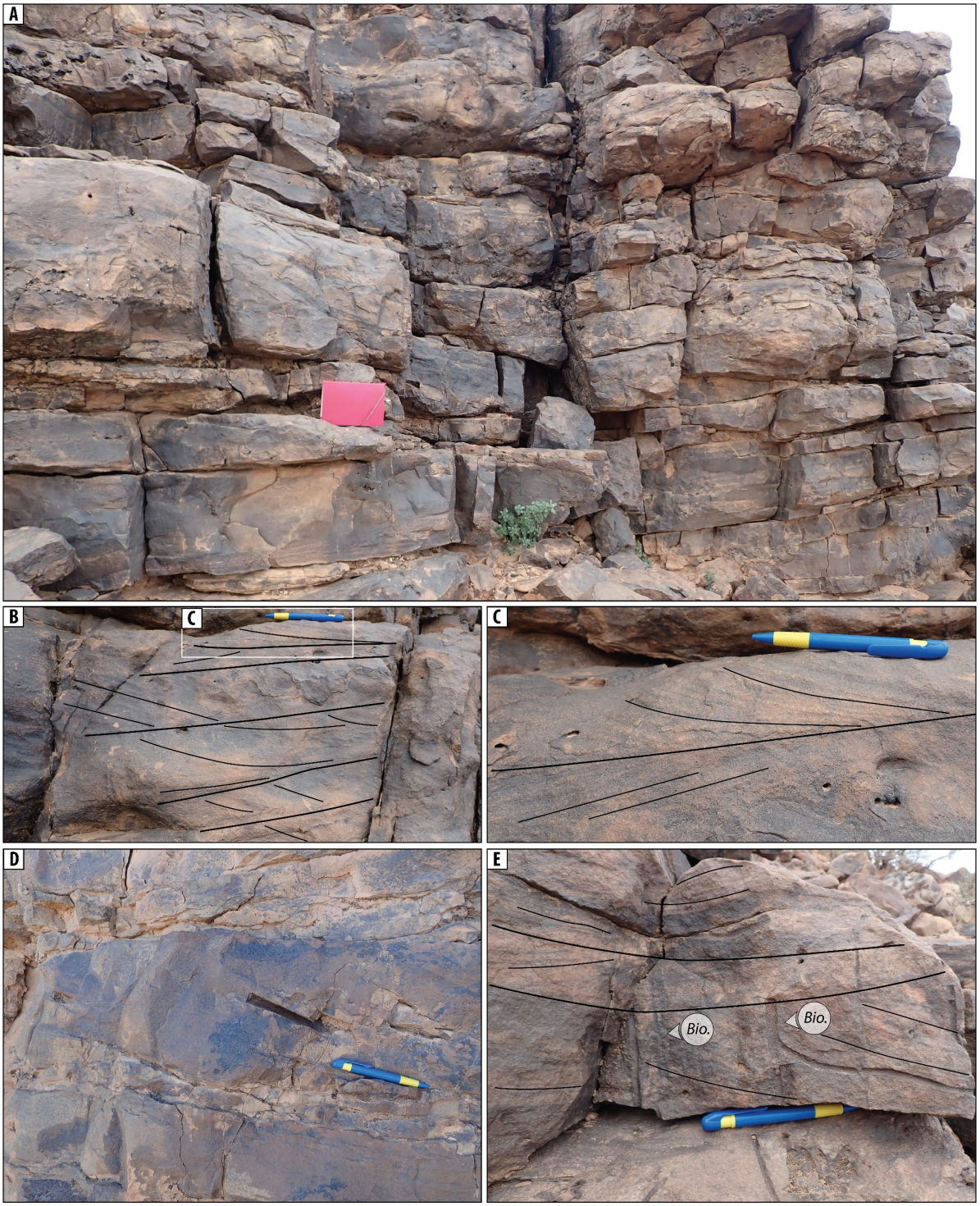

be observed sometimes along cross-laminae (Fig. 3.6B & C). Pebbles of up to 2.5 cm can also be observed in a coarse- to very-coarse-grained matrix (Fig. 3.6C).

Interpretation: The coarseness of this FA coupled with pebble and mud clasts implies the proximity of the delivery system. The plethora of sedimentary structures (e.g. herringbone to cross-stratifications and reactivation surfaces) showing tractive characteristics are indicative of frequent and rapid changes in vigorous flow

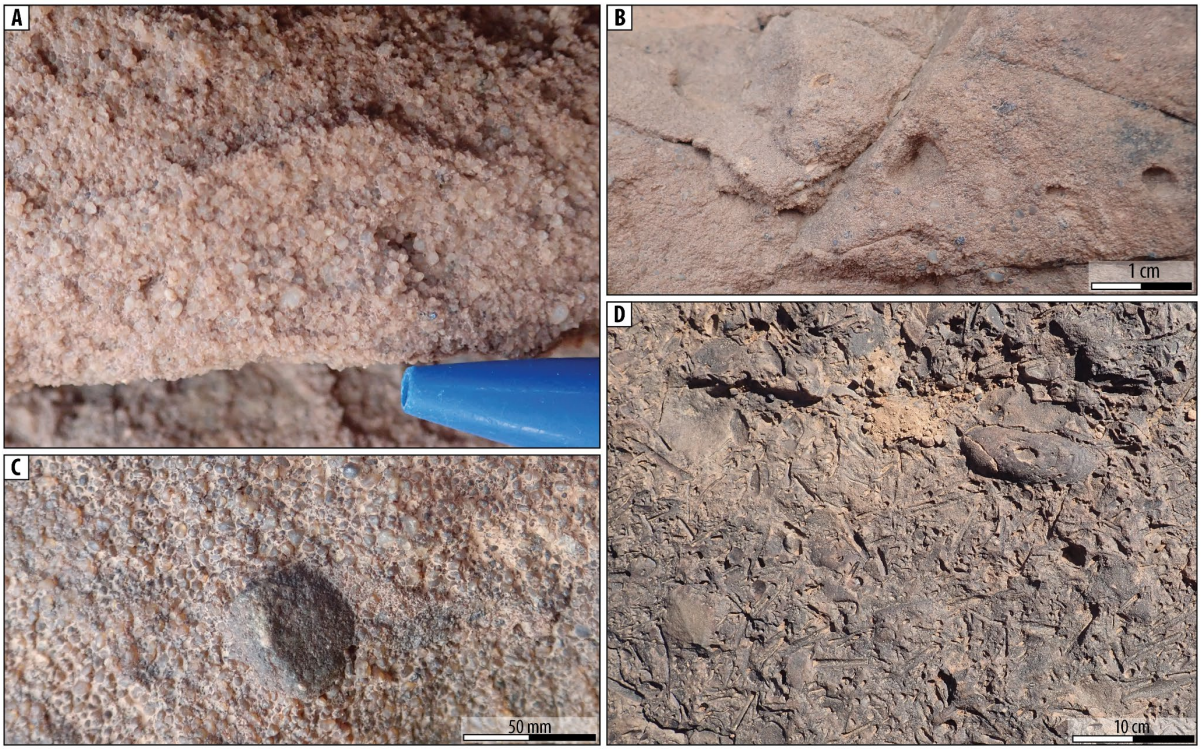

***Figure 3.6**: Detail on grain-size and clasts composing the coarse cross-bedded sandstones bearing rip-up and shell clasts in concentrations facies association. (A) Common grain-size of coarse cross-bedded sandstones facies associations. (B) Subangular granules floating in medium to coarse-grained sandstones. (C) Subangular pebble in rounded, medium- to coarse-grained sandstone. (D) Shell concentration with no clear organization of deposition, with undefined bioturbation marks, observed at the top of a sandstone layer.*

conditions suggesting tidal processes (Davis and Dalrymple, 2012, Longhitano et al., 2021, Peng et al., 2018, Sun et al., 2020). Granules to pebbles and large mud clasts imprints are diagnostic of a (emerged) very proximal environment. This FA is interpreted as depicting a shallow tidal-dominated environment including flood-ebb delta, sand/mouth bars, and tide-influenced channels.

3.4.4. Silty and medium-grained intensely bioturbated sandstones

Description: Intensely bioturbated sandstones are made of unsorted silty very-fine-grained sandstones (Fig. 3.7A) to unsorted silty medium-grained sandstones (Fig. 3.7B). Both subfacies are characterized by high to intense bioturbation (i.e. 60-99% / bioturbation index 4-5 Taylor and Goldring, 1993, Taylor et al., 2003). The thickness of the beds is of a several centimetres to decimetres. Primary sedimentary structures are hindered by the high intensity of bioturbation. The silty sandy beds have a diffuse undulating to lensed shape where

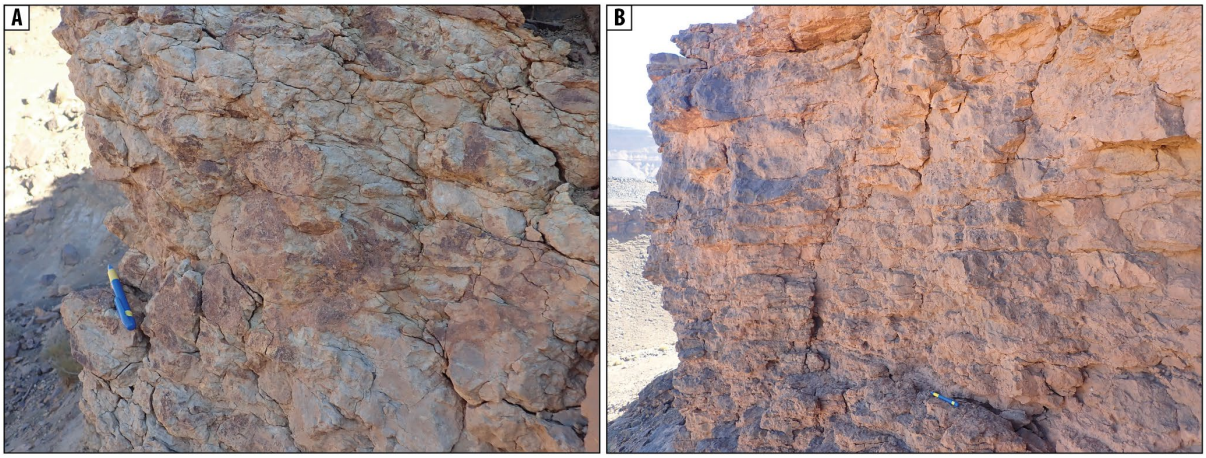

Figure 3.7*: Silty very-fine and medium-grained intensely bioturbated sandstones facies association. (A) Centimeter-thick silty very-fine sandstones intensely bioturbated with diffuse undulating lensed-shape. (B) Centimeter- to decimeter-thick medium-grained sandstones arranged in a thickening-upward sequence. Few erosive bases and undulating bedding of continuous layers. Pen for scale: 13.7 cm.*

the medium sand bed are more continuous over the outcrop (Fig. 7A). The wavelength of the undulations can be due to ripples shape. Sporadic HCS, cross-beds, and horizontal (*Cruziana*) bioturbation can be observed these intensely bioturbated sandstones.

Interpretation: Bioturbation during Ordovician time is an indicator of brackish o marine environments (Buatois and Mángano, 2007). The presence of rare ripples, HCS and cross-bedding, depending on whether the sandstones are silty or medium-grained, suggests input by tractive and oscillatory currents. The high intensity bioturbation hindering almost any primary structures would imply either high rates of biogenic activity or low rates of sedimentation and reworking (Gowland, 1996, Keen et al., 2012). These features would suggest a lagoonal depositional environment to an estuary/tidal flat in a restricted to protected marine environment (Bayet-Goll, 2022, Hein et al., 2013, Loi et al., 2010, Van Yperen et al., 2020, Vidal et al., 2011).

3.4.5. Lag deposits bearing pebble and shell clasts

Description: This FA is composed of pebble and shell clasts in a matrix supported fabric (Fig. 3.8). The matrix is either carbonated (Fig. 3.8A) or of coarse- to very-coarse-grained sand (Fig. 3.8D and E). The layers are of a centimetre to a few decimetres in thickness. These layers usually occur at the top of other FAs sandstone beds (Fig. 3.8A, C, D, F), in mudstones or are in between HCS-bearing sandstones (Fig. 3.8C). The beds often

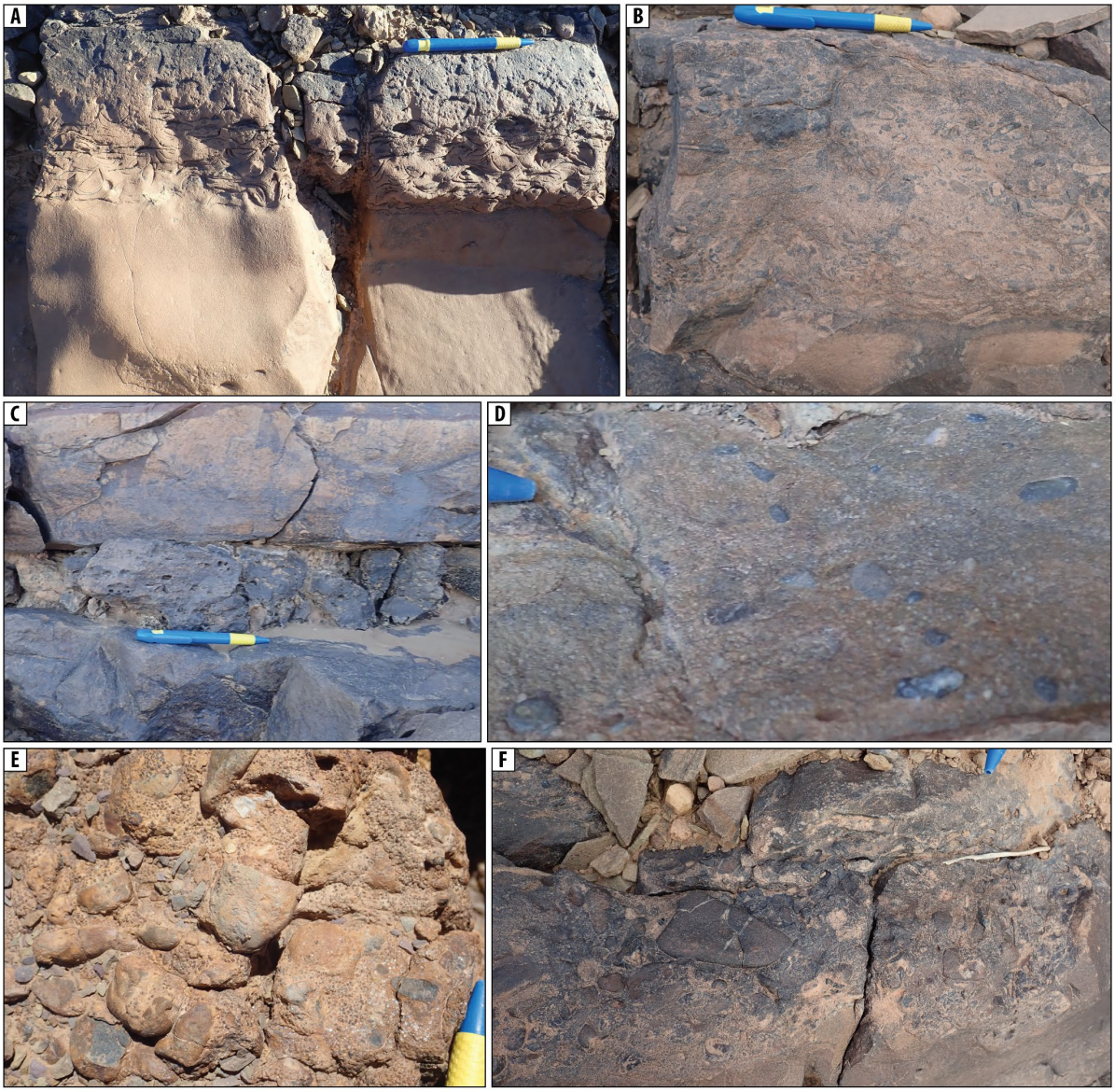

***Figure 3.8**: Lag deposits bearing pebble and shell clasts facies association. (A) to (C) Shell lag deposits. (D) to (F) Pebble lag deposits. (A) Shell lag deposit in a carbonated fine-grained texture. Shells have a concave up and down organization. (B) Shell lag bioturbated deposit in fine-grained sandstones. (C) Decimeter-thick highly ferruginized layer with imprints of shells, observed in a stack of amalgamated HCS sandstones. (D) Millimeter- to centimeter-thick, erosive-based medium- to coarse-grained sandstone. Centimetric pebbles seem to be roughly aligned with two different orientations. (E) Centimeter-thick pebble and ferruginous oolitic lag layer observed in mudstones, composed of centimetric subrounded to broken pebbles. Some pebbles are conglomeratic. (F) Centimeter-thick pebble lag layer, composed of pebbles ranging from 1 to 8.5 cm, observed at the top of a finer-grained sandstone layer. Pen for scale: 13.7 cm.*

show a ferruginous patina. Their base is often irregular. Shell clasts in these lags have both concave up and down organization (Fig. 3.8A). Pebble clasts can be up to 8 cm in diameter and do not seem to be aligned (Fig. 3.8F), although a few

seems to be deposited with the same direction of alignment (Fig. 3.8D). When pebble lags occur in mudstones, the pebbles seem to be composed of conglomerates, e.g. an agglomeration of a broken angular pebble and ferruginous oolithic sandstones which also makes up the matrix of the lag (Fig. 3.8E). The layers are rarely moderately bioturbated.

Interpretation: Basal erosion of the layers and concentration of pebble and shell clasts suggest reworking and winnowing of older and/or proximal deposits in a setting with low sediment supply (Cattaneo and Steel, 2003, Heward, 1981, Ichaso and Dalrymple, 2009, Isla et al., 2018, Li, Bhattacharya and Zhu, 2011). This hypothesis is supported by the fact that some layers bear conglomerate pebbles. Local concentration and alignment of clasts would imply erosion from a wave ravinement during transgression (Zecchin et al., 2019). This FA is interpreted as a transgressive lag (e.g. Ichaso and Dalrymple, 2009, Isla, Schwarz and Veiga, 2018).

3.4.6. Highly deformed sandstones

Description: This FA is appearing on only one of the stratigraphic profiles, though it has particular characteristic features. Highly deformed sandstones are characterized by sandy-silty ball-and-pillow structures (Fig. 3.9). These structures are from a few decimeters to meters in length with an elongated, along former bedding, shape. The meters wide structures are composed of smaller amplitude structures of the same shape. The outer part of the structures becomes more and more slaty, likely due to the content of silts in this facies. This FA is located directly below a glacial incision, where sandstones above the incision also show ball-and-pillow structures to load casts.

Interpretation: The ball-and-pillow to load casts structures are defined at soft-sediment deformation structures (Lowe, 1975, Maltman, 2012). They are usually associated with fluid escape/dewatering due to fluidization/liquefaction of mildly compacted sediments (Lowe, 1975, Owen and Moretti, 2011, Woźniak et al., 2021). Here, we suggest that the triggering mechanisms would be glacial or sediment loading due to the position of the facies association just underlying a glacial incision filled with a thick stack of sandstones (Boulton et al., 2001, Shanmugam, 2016, Woźniak et al., 2021).

3.5. Architecture

The base of the Rouïd-Aïssa Fm is put at the base of the first thick sandstone and medium- to coarse-grained unit observed. A coarsening and thickening-

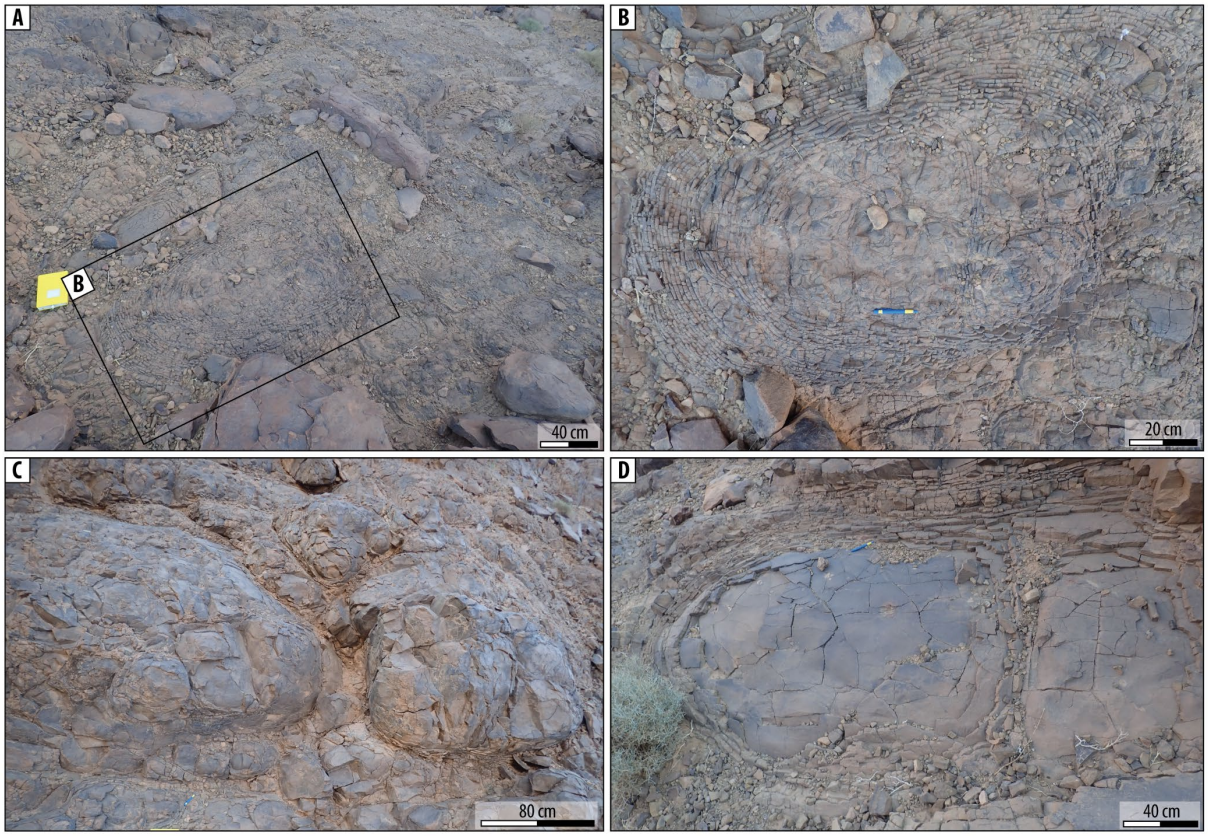

***Figure 3.9**: Highly deformed sandstones facies association. (A) Sandy-silty ball-and-pillow structures with zoom in (B): Multiple ball-and-pillow structures observed in larger structure. Outer part is well-laminated, likely composed of more silts than the center of the structure. (C) Meter-thick, mainly sandy, ball-and-pillow structures composed of several decimetric structures. The right one shows an overturned structure. The layer at the base demonstrates a load cast. (D) Meter-thick silty-sandy sandstone composed of 2 ball-and-pillow structures, well-laminated.*

upward sequence is observed below the base put for the Rouïd-Aïssa Fm. However, the sandstone unit belonging to this R/T cycle is only composed of a thin (i.e. ca. 2 to 3 m) package of stacked HCS to cross-bedded sandstones (Fig. 3.10). This sequence seems correlable along the profile.

The Rouïd-Aïssa Fm is between ca. 100 m to 250 m thick to the West, below the glacial incisions, and is composed of thick packages of sandstones (Fig. 3.10, logs 7 to 11, and Fig. 3.11E-F). From West to East, these prominent sandstones packages become not amalgamated anymore and outcrop as several thinner packages of

***Figure 3.10**: 2D transect with precise stratigraphic profiles and facies associations of the Rouïd-Aïssa Formation. Numbers at the top of each log refer to locations in Fig. 3.1D. Colors next to logs reflect interpreted facies associations. The figure (and following ones) is oriented E-W in order to match the orientation of the Jbel Bani cliff outcrop that faces North. Glacial incision after Dietrich et al. (2019).*

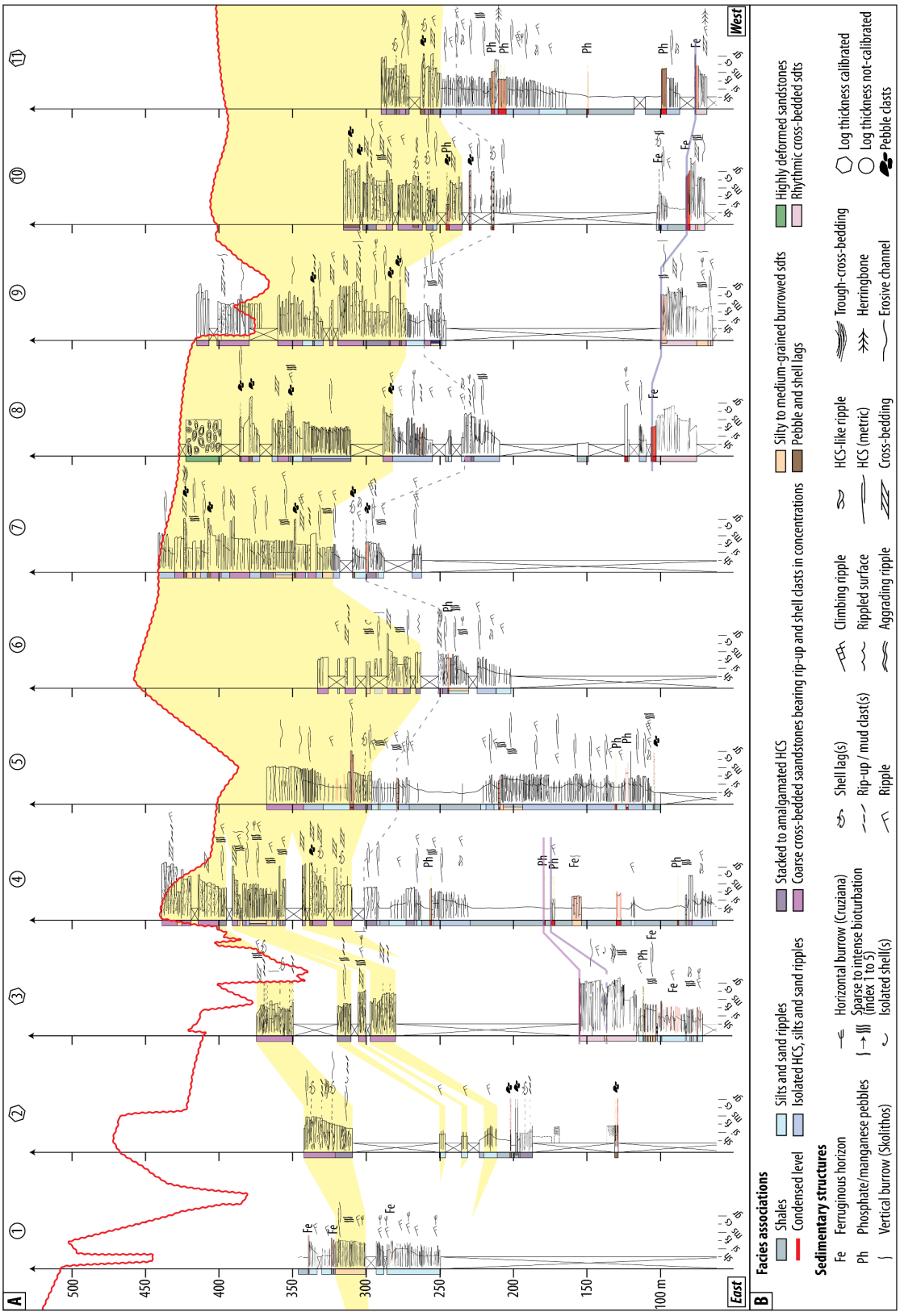

sandstones of ca. 10 to 40 m in thickness (Fig. 3.10, log 3 and Fig. 3.11C & D). Finally, to the extreme east of the transect, one sandstone-dominated package of several ca. 20 m thick outcrop (Fig. 3.10, log 1 & 3 and Fig. 3.11A & B).

Three profiles (log 1, 3, and 9, Fig. 3.12) were chosen to depict the thinning, finning and proximal-to-distal trends of facies associations and sandstones units from West to East, where correlations of sandstone units are based on R/T cycles recognized in each stratigraphic profile (Fig. 3.12).

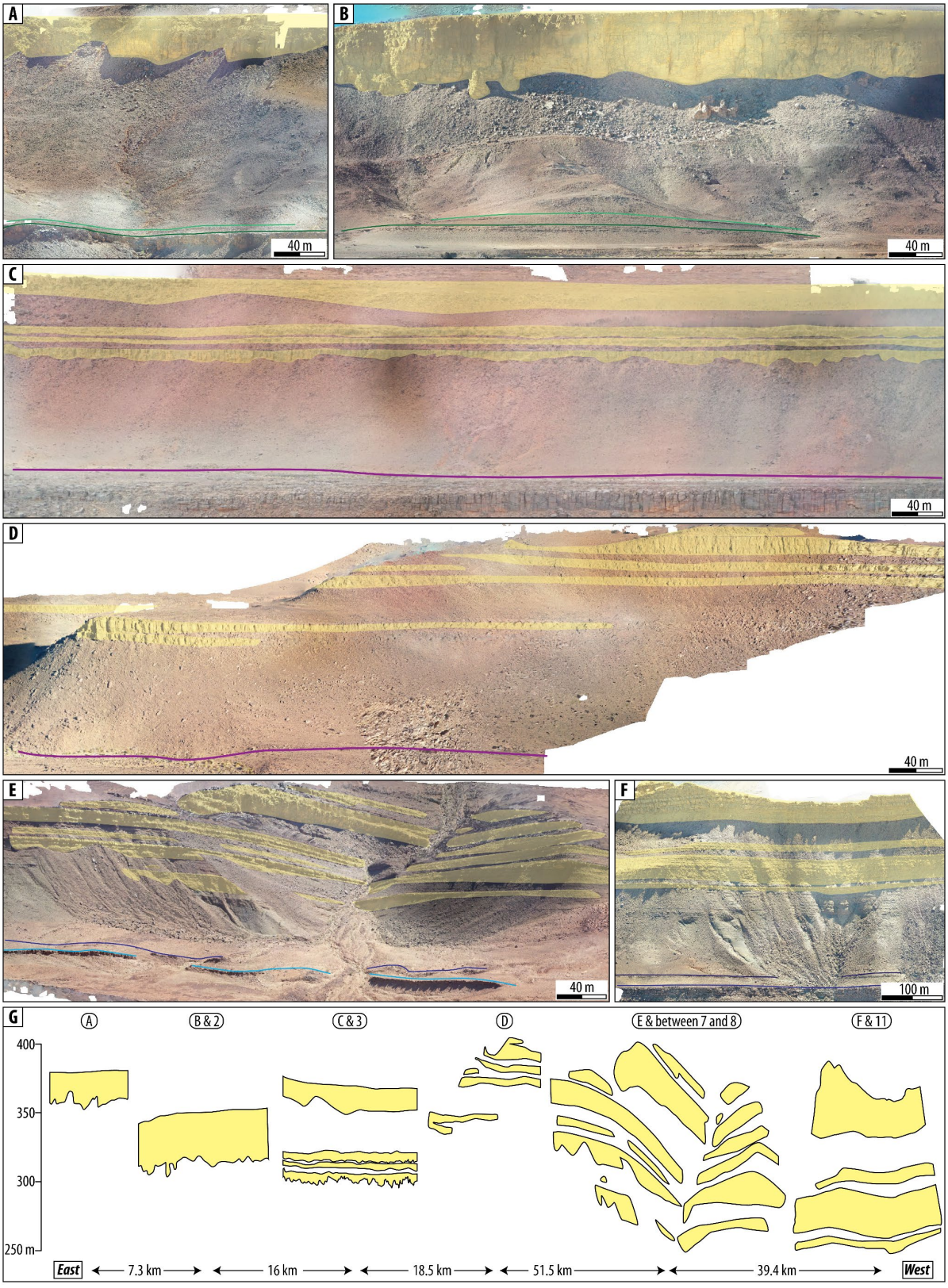

***Figure 3.11**: Panorama of the Rouïd-Aïssa Formation at different localities. (A-F) Panorama views of profiles from East (A) to West (F). Colored lines at the bottom of each subfigure is the top of the underlying member last outcropping of the Lower Ktawa Fm. These change depending on the locality on the transect (Chapter 2). Light green: condensed level overlying the Abbas Mb. Dark Green: Abbas Mb. Purple: Bou-Hajaj Mb. Dark blue: Tissint Mb. Light blue: Foum-Zguid Mb. (G) Thicknesses of the sandstones units of (A) to (F), plotted with a flat datum (at 0 m) with lateral distances between each subfigure. Yellow: sandstone-dominated package. For location, see Fig. 3.1D.*

Profile 9 (most Western): This profile is ca. 170 m long, was separated in 4 major sandstone units and encompasses 5 R/T cycles.

The first R/T cycle is ca. 20 m and silt-dominated. It is composed of a thickening- and coarsening-upward sequence of silts and rippled-marked sandstones, alternating bioturbated sandstones and silts and sand ripples and a sharp-based erosive thick HCS sandstone. A thin layer of coarse-grained cross-laminated sandstone is observed at the base of the alternating FAs and might represent a WRS. The MRS of the first cycle is placed at the base of the 4 m thick HCS which is also marked by a WRS. Above the HCS, a fining and thinning upward sequence composed of silts and sand ripples occur. This cycle seems to be correlable along the transect (logs 4 to 11, Fig. 3.10). The second cycle is ca. 30 m thick, sandstone-dominated and contains the first unit. It is composed of silts and ripples-marked sandstones sharply overlaid by medium-grained cross-laminated sandstones. The limit between the two FAs is interpreted as a ravinement and downward shift of the system from upper offshore to tidal depositional environments. Medium- to coarse-grained sandstones with thin intercalations of pebbles lags overlay the silts and sand ripples FA. The MRS is placed within the coarsest and thickest sandstone packages. Fifteen meters of amalgamated HCS are overlying the tidal deposits, where the MFS is located. The third sequence (ca. 35 m thick) is associated to the Unit 2 and is composed of amalgamated HCS and tidal deposits. The MRS is located in the tidal sediments at ca. 300 m from datum. The fourth cycle contains Unit 3. It is composed of silts and rippled-marked sandstones where the MFS is located between units 3 and 4. Tidal

***Figure 3.12**: Correlations of selected stratigraphic profiles of the Rouïd-Aïssa Formation. Note that this representation has an uneven datum (height scales start at 0 m at the top surface of the First Bani Group). Legend see Fig. 3.10.*

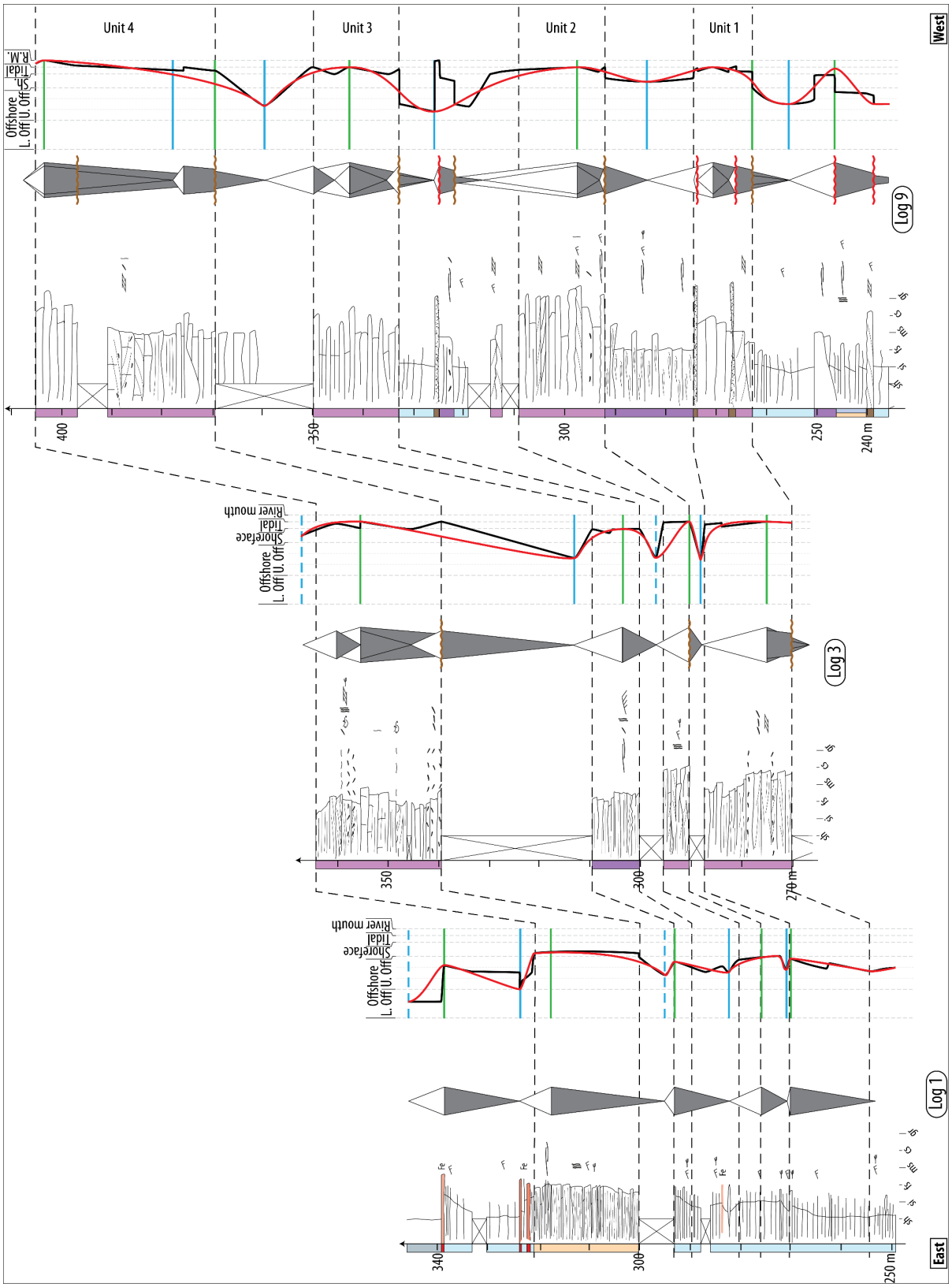

deposits are sharply overlying the silts and sand ripples FA. A tidal ravinement is thought to be at the limit between the two FAs, and the MRS is located in the tidal deposits. The fifth cycle is bearing Unit 4 and is composed of two stacks ca. 20 and 8 m of medium- to coarse-grained cross-bedded sandstones deposits. Tidal

ravinements would be found at the base of each stack, and the MRS would be located in the upper coarser tidal package.

Each of those 4 units would be correlated to the ones observed in log 3, based on lithostratigraphy and stacking of R/T cycles.

Profile 3: Four sand packages compose this stratigraphic profile making 4 R/T cycles.

Units 1 and 2 are composed of tidal-dominated FA of ca. 17 m and 5 m thick making at least ca. 20 m and 7 m thick R/T cycles. These might represent two major relative sea level drop. The third sequence is ca. 20 m (Unit 3) thick and is only composed of amalgamated HCS outcropping over ca. 10 m where the MRS is located. Thirty meters above this unit, a ca. 25 m thick stack of tidal deposits is observed and is embedding Unit 4. This cycle might represent another major basinward shift of the system. The MRS is located in the tidal deposits. MFS are located in between each sandstone packages in debris. The sharp-base of Unit 1, 2 and 4 may represent a tidal ravinement.

Profile 1 (most Eastern): is ca. 90 m thick and mainly composed of silts and sand ripples and intensely bioturbated sandstones. Coarsening- and thickening upward to thinning- and fining-upward sequences in the silts and rippled-marked sandstones part enabled the interpretation of five R/T cycles of ca. 5 to 20 m in thickness. MRS are located at the coarsest and thickest layers. Cycles between 255 and 295 m were tentatively correlated to Units 1 to 3 based on R/T cycles. The sixth cycle is composed of one sand package correlated to Unit 4. This unit is composed of a ca. 20 m thick stack of highly bioturbated sandstones at ca. 320 m above the datum. The MRS is located in these sandstones. Two condensed levels outcrop in the next 2 to 3 meters above the top of the bioturbated sandstones. The fifth cycle is composed of coarsening- and thickening upward silts and rippled-marked sandstones topped by a condensed level. Mudstones outcrop above the condensed level. This cycle was not correlated to the other profiles.

3.6. Regional paleogeography

The Rouïd-Aïssa Fm seems to demonstrate a congruence of the proximal-to-distal trend toward the East from stratigraphic profiles correlation, facies associations, and thinning trends of the sandstones units. This proximal-to-distal trend from the Rouïd-Aïssa Fm is compared with the underlying Lower Ktawa trend (Chapter 2), isopachs maps (Destombes,

1985) and possible reactivation of faults influencing the different trends.

3.6.1. Progradation direction

The studied stratigraphic profiles of the Rouïd-Aïssa Fm demonstrate a clear West to East proximal-to-distal trend of facies associations. These span, from West to East respectively, from several thick sandstones packages dominated by tidal deposits, to a thin muddy-sandstone unit of intensely bioturbated sediments (Figs 3.10 & 3.12). A thinning trend of the sandstone units follows the same pattern from West to East (Fig. 3.11). Hence, it is suggested that the proximal-to-distal trend of the Rouïd-Aïssa Fm is West-East.

However, the underlying Lower Ktawa Fm seems to prograde from South to North (+/- 45°) through megalobe shaped geometries, laterally restricted to up to ca. 100 km (Chapter 2 and 4). Whether the deposits composing the Rouïd-Aïssa Fm also belong to megalobes fully amalgamated to the W of the transect or clinoforms prograding toward the E with also complete amalgamation of deposits to the W is unclear.

Hence, the Rouïd-Aïssa Fm demonstrating a proximal-to-distal trend toward the East and the underlying Lower Ktawa Fm toward the North, a shift in the proximal-to-distal trend during the deposition of the Ktawa Group seems to occur. As such, a shift from a South-North progradation trend with a continuous eastward lateral shift of megalobes for the Lower Ktawa has been hypothesized (Chapter 2 and 5) that is succeeded by a progradation trend from West to East for the Rouïd-Aïssa Fm.

3.6.2. Isopachs

Isopachs maps from Destombes (1985, Fig. 40b)) indicate a clear W-E strike of the isopachs for the First Bani Group deposits, underlying the Lower Ktawa and Rouïd-Aïssa Fms. The Lower Ktawa and Rouïd-Aïssa Fms (no distinction) isopachs demonstrate roughly the same strike in the study area. At the extreme east of the studied transect, the isopachs show a turn in orientation to SSW-NNE until Alnif (i.e. ca 200 km NE of the study area, location on Fig. 3.1C) to a shift to NNW-SSE orientation from Alnif (i.e. following the strike of the Ougarta range further SE). This shift in orientation from a W-E to NE-SW seems to be the premise of the locality of the depocenter for the Ktawa Group at least (i.e. Tagounite Trough). The Upper Ktawa Fm overlying the Rouïd-Aïssa Fm, which has been partly eroded in the study area, exhibits the same NNW-SSE strike of the isopachs, where the thickest deposits are

roughly shifted to the West, compared of the underlying formations. Hence, the shift in isopachs strike from the First Bani to the Ktawa Group from W-E to NNW-SSE would be in agreement with the shift from megalobe prograding toward the North with a shift in feeder source to E from base to top of the Lower Ktawa to clinoforms prograding toward the E for the Rouïd-Aïssa deposits. All of these deposits would tend to fill the Tagounite Trough through time.

3.6.3. Tectonic influence

Although the basin was defined as intracratonic and tectonically stable during Ordovician time (Burkhard et al., 2006), some authors point toward possible tectonic influences in the Anti-Atlas during Late Ordovician time. El Maazouz, and Hamoumi (2007) studied Late Ordovician deposits in the Oriental Anti-Atlas in the Tafilalt region, ca. 280 km toward the NE from the study area (Fig. 3.1C). They favour an extensive tectonic event with a NW-SE strike related to vertical reactivation of Pan-African faults in the Tafilalt region during Sandbian (i.e. during deposition of the Lower Ktawa Fm). These faults have not been recognized in the western Central Anti-Atlas, although, reactivation of Pan-African faults might be hypothesized to why the Tagounite Trough sits along a Pan-African suture, considering that the strike of reactivated Pan-African faults in the Tafilalt region is the same as the strike of the Tagounite Trough (i.e. NW-SE). The reactivation of these faults might have controlled the shift from W-E to NW-SE of the strike of isopachs from the First Bani Group to the Ktawa Group respectively. This tectonic event would have been recognized also in Morocco and Algeria (Beuf, 1971, Fabre, 1976) and by volcanic events in the Armorican Massif and Iberia (Caroff et al., 2009, Navidad et al., 2010).

In the Armorican Massif, volcaniclastic deposits correspond to the Rosan Fm (Caroff et al., 2009), correlated to the Rouïd-Aïssa Fm (Chapter 4). The Rouïd-Aïssa Fm is thought to be deposited during Late Katian. However, the reactivation of faults would happen during the Sandbian (El Maazouz and Hamoumi, 2007). This would postpone the reactivation of Pan-African faults hypothesized by ca. 10 Myr in the studied region. This hypothesis would hence infer that reactivation of these faults would happen in a range of deposition of the Lower Ktawa Fm to the Rouïd-Aïssa Fm. If the reactivation of faults would occur before or during deposition of the Rouïd-Aïssa Fm, it could reinforce the cause of shift of the proximal-to-distal trend of the

western Central Anti-Atlas. In Iberia, volcanic deposits of Late Ordovician time were dated at ca. 455.2 Ma which would be syn- to post-deposition of the Tissint Mb (Navidad et al., 2010). This age would be in agreement with the start of the shift to the East of the megalobes of the Lower Ktawa Fm and the shift of the maximum point of subsidence of the datum toward the East as well (see Chapter 5).

3.6.4. Morphology

The Rouïd-Aïssa Fm appears at odd in the mudstone-dominated succession of the Ktawa Group. This thick sandstone package appears to be related to the Whitewater, global cooling event, and the global relative sea level fall(s) between ca. 449 and 446 Ma (see Chapter 5, Haq and Schutter, 2008, Bergström et al., 2009).

During Ordovician time, another thick sandstone unit named the Zini sandstones of Early Ordovician in age was recognized in a mudstone-dominated background, i.e. the Outer Feijas Group (ca. 1500 m thick, Early to early Middle Ordovician, Destombes, 1985). This unit, 450 m thick in the Zini area, is thinning toward the North-East, to reach ca. 30 m in the Folded Bani region (ca. 180 km away from the Zini region) and disappearing in the Tissint area (for location, see Fig. 3.1C). This apparent thinning was interpreted as an erosion of deposits due to tectonic influences (Destombes, 1985). Hence, the apparent thinning of the Zini sandstones, its location in a mudstone-dominated background and the possible tectonic influence mirror the characteristics of the Rouïd-Aïssa Fm. A detailed study on the Zini sandstones and comparison to the Rouïd-Aïssa Fm would improve the understanding of why the Rouïd-Aïssa Fm appears at odd in the Ktawa Group.

3.7. Summary

Nine facies associations were recognized in the Rouïd-Aïssa Formation. Depositional environments interpreted from facies associations range from offshore, offshore transition to shoreface dominated by storm-wave actions, tidal environment with restricted environments, and deformed sandstones from glacial or sediment loading from the overlying layer. These sediments were deposited prior the Hirnantian glacial maximum with a maximum range of 448.5 to 444.7 Ma (*Nigerica* and *Merga* chitinozoans biozones).

The Rouïd-Aïssa Fm seems to exhibit a West to East proximal-to-distal trend interpreted from facies associations and thinning trends. The underlying Lower Ktawa Fm is composed of members which

would show a proximal-to-distal trend from South to North with a progressive shift of "megalobe shapes", i.e. sandstone dominated packages, from West to East. Reactivation of Pan-African fractures during Late Ordovician time might be responsible for the shift of the proximal-to-distal trend, where reactivated faults and volcanism were recognized in the region. This hypothesis seems to be supported by the shift in orientation of the maximum thickness of the formations composing the Ktawa Group and underlying First Bani Group.

References

Babin, C. & Descombes, J. 1990. Les mollusques bivalves et rostroconches ordoviciens de l'Anti-Atlas marocain: intérêt paléogéographique de leur inventaire. *Géologie Méditerranéenne,* 17**,** 243-261.

Bayet-Goll, A. 2022. Ordovician matground and mixground ecosystems in shoreface–offshore and barrier-island environments from Central Iran, northern Gondwana. *Geological Magazine,* 159**,** 925-953.

Bayet-Goll, A., De Carvalho, C. N., Mahmudy-Gharaei, M. H. & Nadaf, R. 2015. Ichnology and sedimentology of a shallow marine Upper Cretaceous depositional system (Neyzar Formation, Kopet-Dagh, Iran): Palaeoceanographic influence on ichnodiversity. *Cretaceous Research,* 56**,** 628-646.

Benssaou, M., Abioui, M., Ettayfi, N., Lhamyani, B., Boutaleb, S. & Maynard, J. B. 2020. The Ordovician iron ore of the Anti-Atlas, Morocco: Environment and dynamics of depositional process. *Ore Geology Reviews,* 120**,** 103447.

Bergström, S. M., Chen, X., Gutiérrez-Marco, J. C. & Dronov, A. 2009. The new chronostratigraphic classification of the Ordovician System and its relations to major regional series and stages and to δ13C chemostratigraphy. *Lethaia,* 42**,** 97-107.

Beuf, S. 1971. *Grès du Paléozoïque inférieur au Sahara*, Editions technip.

Boulton, G., Dobbie, K. & Zatsepin, S. 2001. Sediment deformation beneath glaciers and its coupling to the subglacial hydraulic system. *Quaternary International,* 86**,** 3-28.

Buatois, L. A. & Mángano, M. G. 2007. Invertebrate ichnology of continental freshwater

environments. *Trace Fossils.* Elsevier.

Burkhard, M., Caritg, S., Helg, U., Robert-Charrue, C. & Soulaimani, A. 2006. Tectonics of the anti-atlas of Morocco. *Comptes Rendus Geoscience,* 338**,** 11-24.

Caroff, M., Vidal, M., Bénard, A. & Darboux, J.-R. 2009. A late-Ordovician phreatomagmatic complex in marine soft-substrate environment: The Crozon volcanic system, Armorican Massif (France). *Journal of Volcanology and Geothermal Research,* 184**,** 351-366.

Cattaneo, A. & Steel, R. J. 2003. Transgressive deposits: a review of their variability. *Earth-Science Reviews,* 62**,** 187-228.

Catuneanu, O., Abreu, V., Bhattacharya, J., Blum, M., Dalrymple, R., Eriksson, P., Fielding, C. R., Fisher, W., Galloway, W. & Gibling, M. 2009. Towards the standardization of sequence stratigraphy. *Earth-Science Reviews,* 92**,** 1-33.

Choubert, G., Destombes, J., Faure-Muret, A., Gauthier, H., Hindermeyer, J., Hollard, H. & Jouravsky, G. 1970. Carte géologique de l'Anti-Atlas central et de la zone synclinale de Ouarzazate: feuilles Ouarzazate-Alougoum et Telouet sud. *Notes et Mém. Serv. Géol. Maroc,* 138.

Choubert, G., Faure-Muret, A. & Destombes, J 1989. Carte géologique du Maroc, Zagora-Coude du Dra-Hamada du Dra (pp). Echelle 1/200 000. *Notes Mém. Serv. Mines Carte géol. Maroc*.

Cocks, L. R. M. & Torsvik, T. H. 2021. Ordovician palaeogeography and climate change. *Gondwana Research,* 100**,** 53-72.

Davis, R. A. & Dalrymple, R. W. 2012. *Principles of tidal sedimentology*, Springer.

Destombes, J. 1985. Lower palaeozoic rocks of Morocco. *Lower Palaeozoic of north-western and west-central Africa***,** 91-336.

Dietrich, P., Ghienne, J.-F., Lajeunesse, P., Normandeau, A., Deschamps, R. & Razin, P. 2019. Deglacial sequences and glacio-isostatic adjustment: Quaternary compared with Ordovician glaciations. *Geological Society, London, Special Publications,* 475**,** 149-179.

Dott Jr, R. & Bourgeois, J. 1982. Hummocky stratification: significance of its variable bedding sequences. *Geological Society of America Bulletin,* 93**,** 663-680.

Dumas, S. & Arnott, R. 2006. Origin of hummocky and swaley cross-stratification—The controlling influence of unidirectional current strength and aggradation rate. *Geology,* 34**,** 1073-1076.

El Maazouz, B. & Hamoumi, N. 2007. Différenciation paléogéographique à l'Ordovicien supérieur dans le Tafilalt (Anti-Atlas oriental, Maroc) sous l'interaction de la glaciation et de la tectonique. *Comptes Rendus. Géoscience,* 339**,** 562-571.

Ennadifi, Y. 1971. Carte géologique des Plaines du Dra au sud de l'Anti-Atlas central. Agadir-Tissint-Oued Zemoul. 1: 200.000. *Notes Mém. Serv. Mines Carte géol. Maroc,* 219.

Ennih, N. & Liégeois, J.-P. 2001. The Moroccan Anti-Atlas: the West African craton passive margin with limited Pan-African activity. Implications for the northern limit of the craton. *Precambrian Research,* 112**,** 289-302.

Fabre, J. 1976. *Introduction à la géologie du Sahara algérien et des régions voisines: La couverture phanérozoïque*, SNED.

Ghienne, J.-F., Abdallah, H., Deschamps, R., Guiraud, M., Gutiérrez-Marco, J. C., Konaté, M., Meinhold, G., Moussa, A. & Rubino, J.-L. 2023. The Ordovician record of North and West Africa: unravelling sea-level variations, Gondwana tectonics, and the glacial impact.

Gowland, S. 1996. Facies characteristics and depositional models of highly bioturbated shallow marine siliciclastic strata: an example from the Fulmar Formation (Late Jurassic), UK Central Graben. *Geological Society, London, Special Publications,* 114**,** 185-214.

Gutiérrez-Marco, J. C., Muir, L. A. & Mitchell, C. E. 2022. Upper Ordovician planktic and benthic graptolites and a possible hydroid from the Tafilalt Biota, southeastern Morocco.

Haq, B. U. & Schutter, S. R. 2008. A chronology of Paleozoic sea-level changes. *Science,* 322**,** 64-68.

Hein, C. J., Fitzgerald, D. M., Cleary, W. J., Albernaz, M. B., De Menezes, J. T. & Klein, A. H. D. F. 2013. Evidence for a transgressive barrier within a regressive strandplain system: Implications for complex coastal response to environmental change. *Sedimentology,* 60**,** 469-502.

Heward, A. P. 1981. A review of wave-dominated clastic shoreline deposits. *Earth-Science Reviews,* 17**,** 223-276.

Ichaso, A. A. & Dalrymple, R. W. 2009. Tide-and wave-generated fluid mud deposits in the Tilje Formation (Jurassic), offshore Norway. *Geology,* 37**,** 539-542.

Isla, M. F., Schwarz, E. & Veiga, G. D. 2018. Bedset characterization within a wave-dominated shallow-marine succession: an evolutionary model related to sediment imbalances. *Sedimentary Geology,* 374**,** 36-52.

Jelby, M. E., Grundvåg, S. A., Helland-Hansen, W., Olaussen, S. & Stemmerik, L. 2020. Tempestite facies variability and storm-depositional processes across a wide ramp: Towards a polygenetic model for hummocky cross-stratification. *Sedimentology,* 67**,** 742-781.

Keen, T. R., Slingerland, R., Bentley, S. J., Furukawa, Y., Teague, W. J. & Dykes, J. D. 2012. Sediment transport on continental shelves: storm bed formation and preservation in heterogeneous sediments. *Sediments, Morphology and Sedimentary Processes on Continental Shelves: Advances in Technologies, Research, and Applications***,** 295-310.

Kreisa, R. & Bambach, R. 1982. The role of storm processes in generating shell beds in Paleozoic shelf environments. *Cyclic and event stratification.* Springer.

Leckie, D. A. & Walker, R. G. 1982. Storm- and tide-dominated shorelines in Cretaceous Moosebar-Lower Gates interval—outcrop equivalents of deep basin gas trap in western Canada. *AAPG bulletin,* 66**,** 138-157.

Li, W., Bhattacharya, J. & Zhu, Y. 2011. Architecture of a forced regressive systems tract in the Turonian Ferron "Notom Delta", southern Utah, USA. *Marine and Petroleum Geology,* 28**,** 1517-1529.

Li, Z., Bhattacharya, J. & Schieber, J. 2015. Evaluating along-strike variation using thin-bedded facies analysis, Upper Cretaceous Ferron Notom Delta, Utah. *Sedimentology,* 62**,** 2060-2089.

Loi, A., Ghienne, J.-F., Dabard, M.-P., Paris, F., Botquelen, A., Christ, N., Elaouad-Debbaj, Z., Gorini, A., Vidal, M. & Videt, B. 2010. The Late Ordovician glacio-eustatic record from a high-latitude storm-dominated shelf succession: The Bou Ingarf section (Anti-Atlas, Southern Morocco).

Palaeogeography, Palaeoclimatology, Palaeoecology, 296**,** 332-358.

Longhitano, S. G., Chiarella, D., Gugliotta, M. & Ventra, D. 2021. Coarse-grained deltas approaching shallow-water canyon heads: A case study from the Lower Pleistocene Messina Strait, Southern Italy. *Sedimentology,* 68**,** 2523-2562.

Lowe, D. R. 1975. Water escape structures in coarse-grained sediments. *Sedimentology,* 22**,** 157-204.

Maceachern, J. A., Bann, K. L., Bhattacharya, J. P. & Howell, C. D. 2005. Ichnology of deltas: organism responses to the dynamic interplay of rivers, waves, storms, and tides.

Maltman, A. 2012. *The geological deformation of sediments*, Springer Science & Business Media.

Marante, A. 2008. *Architecture et dynamique des systèmes sédimentaires silico-clastiques sur la" plate-forme géante" nord-gondwanienne: l'Ordivicien moyen de l'Anti-Atlas marocain.* Bordeaux 3.

Meddour, A. 2016. *Les séries de l'Ordovicien moyen et supérieur de l'Anti-Atlas oriental (Maroc): stratigraphie, sédimentologie et paléogeographie des systèmes de plate-forme silico-clastique.* Bordeaux 3.

Myrow, P. 2005. SEDIMENTARY ENVIRONMENTS| Storms and Storm Deposits.

Myrow, P. M. & Southard, J. B. 1996. Tempestite deposition. *Journal of Sedimentary Research,* 66**,** 875-887.

NASA/METI/AIST/Japan Spacesystems and U.S./Japan ASTER Science Team (2019). *ASTER Global Digital Elevation Model V003* [Data set]. NASA EOSDIS Land Processes Distributed Active Archive Center. https://doi.org/10.5067/ASTER/ASTGTM.003

Navidad, M., Castiñeiras, P., Casas, J. M., Liesa, M., Suárez, J. F., Barnolas, A., Carreras, J. & Gil-Peña, I. 2010. Geochemical characterization and isotopic age of Caradocian magmatism in the northeastern Iberian Peninsula: Insights into the Late Ordovician evolution of the northern Gondwana margin. *Gondwana Research,* 17**,** 325-337.

Owen, G. & Moretti, M. 2011. Identifying triggers for liquefaction-induced soft-sediment deformation in sands. *Sedimentary Geology,* 235**,** 141-147.

Peng, Y., Steel, R. J., Rossi, V. M. & Olariu, C. 2018. Mixed-energy process interactions read from a compound-clinoform delta (paleo–Orinoco Delta, Trinidad): preservation of river and tide signals by mud-induced wave damping. *Journal of Sedimentary Research,* 88**,** 75-90.

Pique, A. & Michard, A. 1989. Moroccan Hercynides; a synopsis; the Paleozoic sedimentary and tectonic evolution at the northern margin of West Africa. *American Journal of science,* 289**,** 286-330.

Shanmugam, G. 2016. The seismite problem. *Journal of Palaeogeography,* 5**,** 318-362.

Sun, Z., Zhang, J., Liu, Y., Shen, W., Li, Y. & Li, L. 2020. Sedimentological signatures and identification of Paleocene sedimentary facies in the Lishui sag, East China Sea Shelf basin. *Canadian Journal of Earth Sciences,* 57**,** 377-395.

Talling, P. J., Allin, J., Armitage, D. A., Arnott, R. W., Cartigny, M. J., Clare, M. A., Felletti, F., Covault, J. A., Girardclos, S. & Hansen, E. 2015. Key future directions for research on turbidity currents and their deposits. *Journal of Sedimentary Research,* 85**,** 153-169.

Talling, P. J., Masson, D. G., Sumner, E. J. & Malgesini, G. 2012. Subaqueous sediment density flows: Depositional processes and deposit types. *Sedimentology,* 59**,** 1937-2003.

Torsvik, T. H. & Cocks, L. R. M. 2013. Gondwana from top to base in space and time. *Gondwana Research,* 24**,** 999-1030.

Van Wagoner, J. C., Posamentier, H. W., Mitchum, R. M., Vail, P. R., Sarg, J. F., Loutit, T. & Hardenbol, J. 1988. An overview of the fundamentals of sequence stratigraphy and key definitions.

Van Yperen, A. E., Poyatos-Moré, M., Holbrook, J. M. & Midtkandal, I. 2020. Internal mouth-bar variability and preservation of subordinate coastal processes in low-accommodation proximal deltaic settings (Cretaceous Dakota Group, New Mexico, USA). *The Depositional Record,* 6**,** 431-458.

Vidal, M., Loi, A., Dabard, M.-P. & Botquelen, A. 2011. A Palaeozoic open shelf benthic assemblage in a protected marine environment. *Palaeogeography,*

Palaeoclimatology, Palaeoecology, 306**,** 27-40.

Woźniak, P. P., Belzyt, S., Pisarska-Jamroży, M., Woronko, B., Lamsters, K., Nartišs, M. & Bitinas, A. 2021. Liquefaction and re-liquefaction of sediments induced by uneven loading and glacigenic earthquakes: implications of results from the Latvian Baltic Sea coast. *Sedimentary Geology,* 421**,** 105944.

Zecchin, M., Catuneanu, O. & Caffau, M. 2019. Wave-ravinement surfaces: classification and key characteristics. *Earth-science reviews,* 188**,** 210-239.

Depositional facies and stratigraphic architecture recording relative sea level variations (Ktawa Group, Morocco): the onset of the Early Paleozoic glaciation

Abstract

This study investigates the relative sea level (RSL) signal recorded during the Late Ordovician along the northern Gondwana shallow marine platform, within a glaciated context. The sediment succession from the Ktawa Group in the Anti-Atlas (southern Morocco) records a storm-dominated siliciclastic succession deposited on the northern rim of the Tindouf basin and spanning ca. 13 Myr of deposition. The purpose of this study is to investigate whether the Ktawa Group recorded local or global eustatic RSL variations and ultimately, whether these variations are induced by major glacial advances. Correlation of sandstone units along the ca. 150 km long studied transect was conducted in order to reconstruct a composite RSL curve for the Ktawa Group in the western Central Anti-Atlas. The RSL curve was deduced from depositional environments interpreted from the stacking pattern of facies associations. Seven third-order regressive/transgressive cycles were recognized in the sedimentary record calibrated in age from chitinozoans biozones. A new correlation scheme for the Ktawa Group along the Anti-Atlas is proposed here. The extracted RSL curve was then compared to global RSL variations, geochemical proxies and RSL curve from other sites in the region (i.e. Ougarta, Hoggar, Sardinia, and Armorican Massif). Reasonable congruence and correlations enabled the recognition of major glacially induced events in the studied area such as the Guttenberg Isotopic Carbon Excursion, Kope, Waynesville, and Whitewater events, within an error bar of ca. 1 Ma. Thus the deposition of the Ktawa Group was likely driven by allocyclic, glacially related, eustasy.

4.1. Introduction

The depositional environments interpreted from ancient sediment successions are critical for the reconstruction of a relative sea level curve. This sea level curve is then useful for regional to global correlations with other basins, and gives information on the paleoclimate for example. In particular, within an ice-house context, the sedimentary record from shallow marine siliciclastic sediments deposited on passive margins can help to unravel glacial events such as growth and retreats of ice sheets. Indeed, glacial events cause eustatic sea-level changes of large amplitude, several tens to a hundred of meters, through the retention and release of large volumes of water (Sømme et al., 2009).

The Early Paleozoic glaciation, spanning from at least the early Late Ordovician to potentially as late as the Middle Silurian, was a period of climatic and biotic upheaval (Pohl et al., 2014, Saltzman, and Young, 2005). The apex of the Early Paleozoic glaciation, i.e. the largest extent of the ice cover, is thought to have occurred during the Hirnantian, ca. 445.2 Ma ago, with ice masses attaining latitudes as low as 45°S (Fig. 4.1, Ghienne et al., 2007). However, the assignment of the age at which continental-scale ice sheets nucleated, is still debated. It has been argued that the glaciation started >10 Ma before the Hirnantian maximum phase, around 455 Ma ago (Finnegan et al., 2011, Trotter et al., 2008), while others suggest that ice sheets could have been present on Gondwana as early as the Middle Ordovician, i.e. ca. 467 Ma ago (Dabard et al., 2015, Loi et al., 2010, Pohl et al., 2016). Such an uncertainty may arise from the fact that ice sheets nucleated on the stable Gondwana supercontinent, with limited subsidence, so that associated glacigenic sediments are poorly preserved or most generally completely missing (Ghienne et al., 2007). The lack of a consensus concerning the onset of the Early Paleozoic

Figure 4.1*: Context and location of the study area. (A-B) Paleogeographic reconstructions of Gondwana at 450 Ma (Katian, modified from Cocks and Torsvik, 2021) and 445 Ma (Hirnantian, modified from Torsvik and Cocks, 2013). Location of key outcrops: 1. Hoggar, 2. Ougarta, 3. Armorican Massif, 4. Sardinia. (C) Geological map of southern Morocco and western Algeria highlighting major features, modified from Ghienne et al., 2007, Hollard et al., 1985. (D) Detailed geological map of the Jbel Bani cliff between the localities of Tissint and Tagounite, including locations of selected stratigraphic profiles from 1 to 7. Geological map modified after Choubert et al. (1970), Choubert et al. (1989), Ennadifi (1971). Background Digital Elevation Model: NASA (2019).*

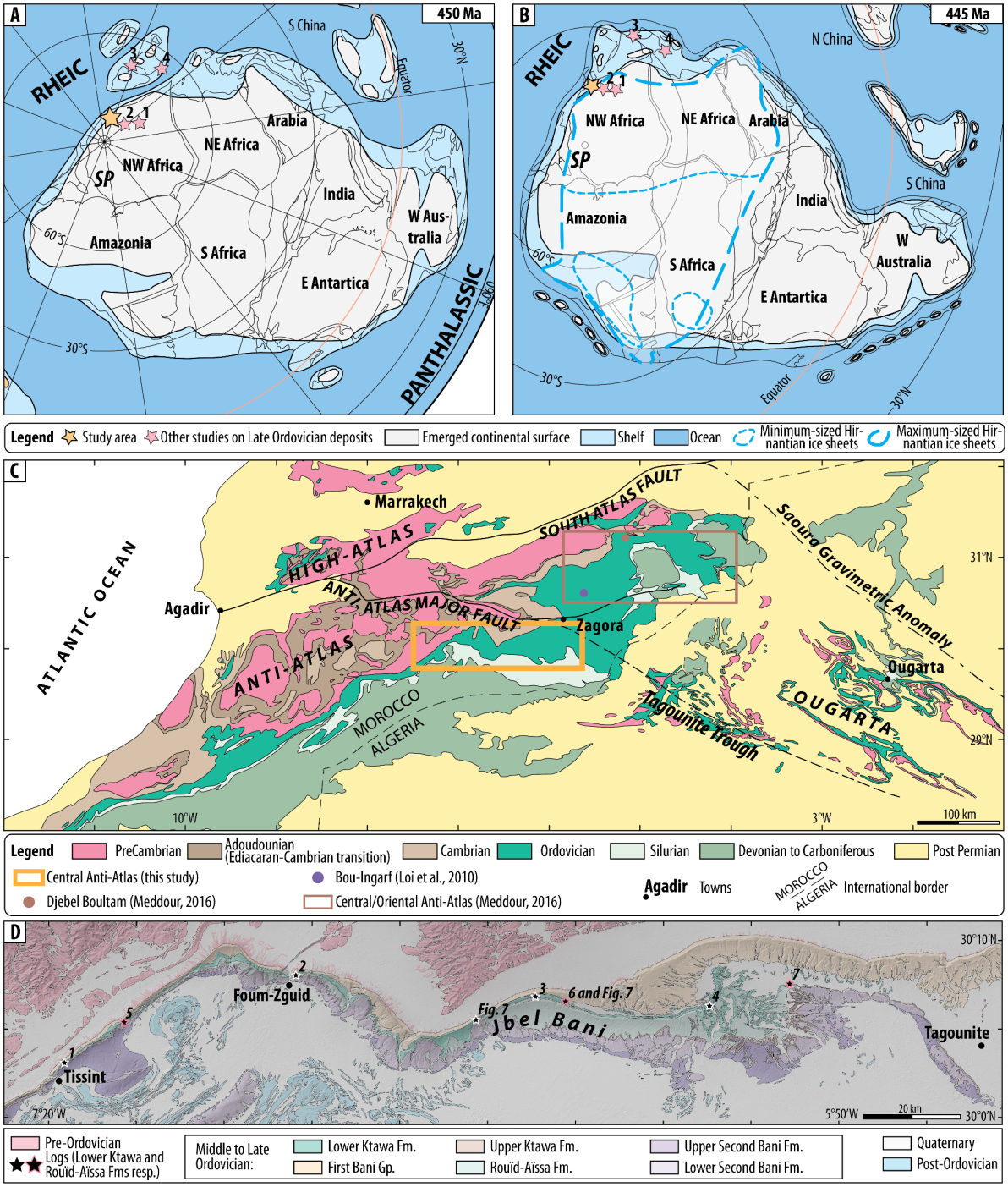

glaciation, in turns, hinders the exploration of climate-glaciation-biotic processes feedbacks during the turnaround from greenhouse to icehouse states.

Onset dates of glaciations are potentially recorded within the stratigraphic record of continental platforms far from any direct glacial influence, in the form of a sedimentary signal indicating large amplitude eustatic sea-level variations (Alley et al., 2005, Clark, and Mix, 2002, Loi et al., 2010, Shennan et al., 2006). The use of far-field stratigraphic architecture as a proxy to infer the inception of glaciations, however, relies on our ability to extract

paleo-sea level variations from the observation of sedimentary facies and their interpretation in terms of depositional environments and paleobathymetry. The aim of this contribution is to investigate and correlate the stacking patterns and sedimentary architecture of an early Late Ordovician succession located on the North Gondwana platform away from direct glacial action (Fig. 4.1A). Stratigraphic profiles were surveyed along a 150 km-long continuous exposure of the Jbel Bani (Anti-Atlas, Morocco) between the towns of Tissint and Zagora (Fig. 4.1C and D). The sedimentary signals recording eustatic sea-level variations were correlated at the local scale, with nearby outcrops in southern Morocco as well as with key outcrops at the regional-scale and global scale.

4.2. Geological setting

The Anti-Atlas mountain range in southern Morocco exhibits up to 10 km of Palaeozoic sedimentary successions on the northern edge of the Tindouf intracratonic basin (Michard et al., 2008). The basin was inverted during the Variscan orogeny in the Late Carboniferous to Permian (Burkhard et al., 2006, Hoepffner et al., 2005, Pique, and Michard, 1989). During deposition of siliciclastic shallow marine sediments, the basin domain was part of the northern passive margin and platform of Gondwana (Fig. 4.1A, Burkhard et al., 2006, Destombes, 1985, Michard et al., 2008). During Middle to Late Ordovician times, the northern rim of the Tindouf basin was located close to the South Pole, between 60° and 70° (Fig. 4.1A and B, Cocks, and Torsvik, 2021). The end of the Ordovician is marked by the Hirnantian glacial maximum (i.e. 442.2 Ma), which itself is well recorded by glacigenic deposits, glacial incisions to incised valleys in the Tindouf basin and surrounding areas (Fig. 4.2, Dietrich et al., 2019, Ghienne et al., 2014, Ghienne et al., 2007, Le Heron, 2007).

The Jbel Bani is a prominent cliff composed of Middle to Late Ordovician deposits that is continuous over 100s of km (Fig. 4.1D). The cliff is made up of several competent sandstone packages, which are organized as cuestas standing out from recessive badlands made of shally-silty lithologies. Three lithostratigraphic units were defined as groups by Destombes (1985) and are composed of from the base to the top: (i) the First Bani Group of late Middle to early Late Ordovician (Darriwilian to Early Sandbian, Marante, 2008); (ii) the Ktawa Group (unit of interest), mid-Sandbian to Katian in age; and (iii) the Second Bani Group mainly

made of glacigenic deposits, Hirnantian in age.

The Ktawa Group has been further subdivided in 3 formations by Destombes (1985): (a) the Lower Ktawa Formation (ca. 250 m thick, mid-Sandbian to mid-Katian), (b) the Rouïd-Aïssa/Er-Rwaidat Formation (ca. 200 m thick, ca. Late Katian), and (c) the Upper Ktawa Formation (Late Katian, Fig. 3.2). The Lower Ktawa Fm is composed of a shally-silty background with several sandstone cuestas standing out and referred to as members (Fig. 4.2, Destombes, 1985, Chapter 2). The sandstone bodies (i.e. members) have a lateral extent of up to hundred kilometers, laterally fainting, and they outcrop over different parts of the study area. Above and in contrast, the Rouïd-Aïssa Fm is dominated by amalgamating sandstone units. The latest package preceding the glacial incision is called the Lower Second Bani Fm whereas the Hirnantian glacial incisions and the related infill are recorded by the Upper Second Bani Fm. In the studied region, the glacial incisions have nearly completely eroded the Lower Second Bani, Upper Ktawa Fms and part of the Rouïd-Aïssa Fm and a hiatus occurs at the base of the Upper Second Bani Fm.

Several glacial events have been recognized before, during and after the deposition of the Ktawa Group. The First Bani Group (underlying the Ktawa) and the Upper Second Bani Fm. (overlying the Ktawa) have been interpreted as related to major events of sea level fall and presence of ice sheets (Dabard et al., 2015, Loi et al., 2010, Rasmussen et al., 2016, Turner et al., 2011). These advances may be related to $\delta^{13}C$ isotopic carbon excursions (ICE), namely the DICE (Darriwilian) during deposition of the First Bani Group, the GICE (Guttenberg, early Katian in age) during deposition of the Ktawa, and the HICE (Hirnantian) during deposition of the Upper Second Bani Fm (e.g. Ainsaar et al., 2010, Bergström et al., 2009, Bergström et al., 2010a, Bergström et al., 2010b, Turner et al., 2012).

Here, focus is put on the Relative Sea Level (RSL) curve interpreted from the deposits of the Lower Ktawa and Rouïd-Aïssa Fms. We investigated whether the recorded signal in the sedimentary archive is influenced by glacio-eustatic RSL variations and related to known excursions in geochemical proxies. To do so, the reconstructed RSL curve for the Ktawa Group was correlated to the global relative sea level curve, geochemical proxies and relative sea level curves reconstructed for nearby locations from existing studies

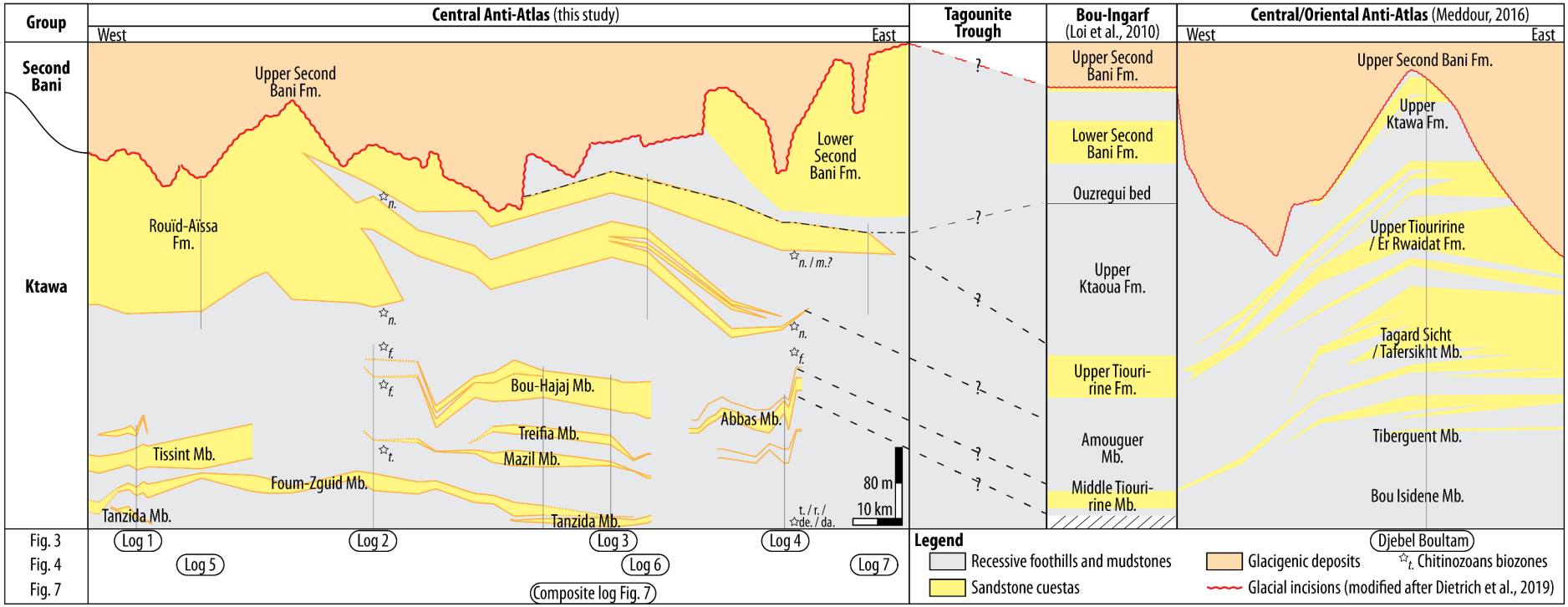

Figure 4.2: *Sandstone bodies as identified in the Central to Oriental Anti-Atlas. Left: transect of the present study in the Central Anti-Atlas with selected logs, locations of main formations and members, constraint by chitinozoans biozone samples (Ghienne, Paris, Vandenbroucke, and Debacker, unpublished pers. comm.). Right: log and transect modified from Loi et al. (2010) and Meddour (2016) respectively in the Central to Oriental Anti-Atlas. Note the Tagounite Trough dominated by mudstones separating the western to eastern Central Anti-Atlas where lithostratigraphic correlations were not possible. The base of the transects (i.e. datum) is the top of the First Bani Group sandstones. Glacigenic deposits modified from Dietrich et al. (2019). da.: Dalbyensis, de.: Deunffi, f.: Fistulosa, m.: Merga, n. Nigerica, r.: Robusta, t.: Tanvillensis.*

(Ainsaar et al., 2010, Cocco et al., 2023, Dabard et al., 2009, Elrick, 2022, Ghienne et al., 2007, Haq, and Schutter, 2008, Loi et al., 2023, Loi et al., 2010, Männik et al., 2021, Meddour, 2016, Videt et al., 2010).

4.3. Methods

Field data

RSL curves were extracted from stratigraphic profiles based on the interpretation of depositional environments, which themselves were inferred based on sedimentary facies associations and stacking patterns. Hereafter, 4 stratigraphic profiles of the Lower Ktawa Fm and 3 profiles of the Rouïd-Aïssa Fm are presented in order to identify the different regression and transgression (R/T) cycles based on their embedded members. These sections belong to a dataset of 42 stratigraphic profiles logged in the field along the Jbel Bani between the towns of Tissint and Zagora at a decimetric precision (Chapters 2 and 3). After logging, the field-based thicknesses of 4 out of the 8 profiles were corrected via photogrammetric reconstruction from drone-based images. Individual units were correlated laterally between logs through visual correlation of packages from satellite and drone-based images.

Interpretation scheme

After recognition of facies associations based on the lithology, sedimentary structures, stacking patterns (i.e. genetic units) and taphonomy (Harlet et al., in sub., Chapter 2), depositional environments were interpreted and RSL curves reconstructed. For extrapolation of the RSL curves, a sedimentary scheme including 8 marine environments was used (Table 4.1). These include the range from offshore through storm-dominated to shoreface environments, as well as tidal/estuarine river mouth environments. This interpretative scheme is based on common stratigraphic models and justified by the combined effects of deposition and preservation potential. RSL curves were then extracted from the sedimentary facies and interpreted stratigraphic bounding surfaces, including Maximum Regressive Surface (MRS) and Maximum Flooding Surface (MFS). The MRS is defined as the turnaround from progradation (i.e. regression) to retrogradation (i.e. transgression) of the shoreline (e.g. Catuneanu et al., 2009, Van Wagoner et al., 1988). It is positioned in practice within the upper sandstone packages of coarsening-upward parasequences (i.e. shallowing upward). The MFS is defined as the change of depositional trend from retrogradation to progradation (Catuneanu et al., 2009) and is

***Table 4.1**: Summary of facies associations in the studied interval for the Ktawa Group.*

Main lithologies	Sedimentary structures	Interpreted depositional processes	Depositional environments
Mudstones	Finely laminated, fissile shales and silts. Occasionally highly bioturbated	Calm, subaqueous setting, dominated by decantation of suspended load	Offshore
Ferruginous horizons	Dark burgundy, highly competent and ferruginous. Abundant concretions. Phosphate and/or manganese pebbles, ferruginous to phosphatic oolites	Combination of chemical precipitation and low sedimentation rates	Offshore
Silts and sandstone ripple-marked	Laminated silts and intercalations of rippled sandstones. Starved to climbing uni- to bidirectional ripples, sometimes sigmoidal and aggrading laminae (i.e. hummocky-like ripples). Erosive- to conformable-based. Horizontal bioturbation common	Silts: calm environment. Ripples: tractive currents such as low-density sediment gravity flows, recurrent trigger processes such as flood or storms. Bidirectional and hummocky-like ripples: oscillatory flows, wave influenced	Upper offshore
Silts and isolated sandstones bearing Hummocky Cross-Stratification (HCS)	Isolated sandstone beds containing well-defined HCS intercalated with laminated silts and sand ripples. Typical grading of HCS-bearing sandstones: 1) flat and sharp base, without clear evidence of sole marks; 2) massive basal zone; 3) low-angle laminasets including truncations, lamina spall into platy pieces and parting lineations; 4) ripples, sometimes climbing to aggrading. HCS bedforms: hummocks to sharp brinkpoint, from straight to linguoid crestlines with irregular meter-scale pseudo-wavelengths	Silts and sand ripples: calm environment disrupted by distal, low-density sediment gravity flows. HCS: combined oscillatory flows (i.e. oscillation by waves superimposed on an unidirectional density current); spectrum of storm- or flood-derived events including turbidity currents and hyperpycnal flows	Upper offshore transition
Stacked HCS sandstones	HCS-bearing sandstones with similar typical grading with pronounced pinch and swell, well-developed platy spalling with parting lineations. Well-sorted sandstones from fine- to medium-grained. Common climbing ripples at the beds top. Stacking of HCS beds with a conformable or local and limited truncations resembling swaley-cross stratification. Contains lenses of matrix-supported coquina clasts	HCS beds emplaced by frequent storm-derived processes. Coquina lenses: atypical drag of bioclasts in local hyper concentration due to reworking mechanical sorting related to specific flow dynamics	Limit offshore/shoreface (below fair-weather wave base)
Quartzose amalgamated HCS sandstones	Well-sorted fine- to medium-grained HCS sandstones, fully amalgamated. Erosive bases from sub-horizontal undulations, gullies to troughs. Sub-horizontal, low-angle, HCS, sigmoidal, tangential and trough cross-laminations. Rare shell bioclasts, rip-up clasts, coarse sand and granules aligned within the lamination	Regular reworking. Constant wave-influence and wave-induced currents	Shoreface

Table 4.1 *(Continued).*

Main lithologies	Sedimentary structures	Interpreted depositional processes	Depositional environments
Coarse-grained cross-bedded sandstones	Alternations of well-sorted medium- to very coarse-sandstones. Mud chips, shell lags and coarse sand to granules layers occasional aligned along lamina. Erosive bases lenses of up to 5-10 m in width and 2 m deep, filled with cross-bedded sandstones	Tidal processes (neap-spring cycles and flood-ebb tides). Mud chips: ripped-up fragments from desiccated mud indicative of nearby emersion. Frosted texture: abrasion/corrosion in an aeolian environment. Flood-ebb currents where sand dunes and bars are moving and mud layers deposited during slack waters. Erosive lenses: tidal/intertidal channels. Bioturbation facies: zones protected from currents, possibly marshes.	Tidal/intertidal channels, tidal flat/flood-ebb delta (i.e. tidal dominated system) with a fluvial influence such as a river mouth system and/or inner estuary
Dune-bedded	Dune bedsets with planar, tabular, tangential, sigmoidal cross-beds. Rhythmic organization with contraction-dilatation cycles and reactivation surfaces. Quartzose texture common. Rare rippled-surfaces at the beds top. Mud interbeds common. Rare vertical and horizontal ichnofacies		
Cross-bedded bioturbated	Cross-, trough- and subplanar laminations. Occasional herringbone cross-stratification. Rare ripples. Abundant bioturbation: *Diplocraterion* isp., *Skolithos*, "oblique" ichnofacies		
Fully-bioturbated	Intense bioturbation (91-99%, BI: 5) hindering primary sedimentary structures. Rare ripples making undulating layers		
Well-sorted	Reddish-purple, homogenous, poorly-sorted, medium- to coarse-grained sandstones. Granules, round to angular, sometimes with frosted surface texture, rare small pebbles and shells beds. Trough- to cross-laminated beds. No bioturbation		
Bearing rip-up and shell clasts in concentrations (Rouïd-Aïssa Fm exclusively)	Tabular to tangential cross-lamina, trough-cross-, herringbone, and sub-planar laminations. Common erosive bases and reactivation surfaces. Uncommon ripples at the layers surfaces. Rare bioturbation includes *Skolithos* and *Diplocraterion* isp. Common mud clasts and shell concentrations aligned along laminae. Floating roughly angular granules to pebbles incorporated		
Intensely bioturbated muddy-sandstones	Mixture of unsorted muddy very fine- to medium-grained sandstones. High to intense bioturbation (60-99% i.e. index 4-5). Hindrance of primary sedimentary structures from intense bioturbation. Few vertical to horizontal burrows observed. Diffuse undulations of the bedding. Sporadic low-angle cross-stratification (possible HCS), climbing ripples and muddy intervals	Sediment input by tractive and oscillatory currents. Biogenic reworking supplanting primary deposition rate. Intermittent storm-derived processes	Back-barrier/lagoon or lower shoreface

generally loosely placed within the shales above condensed levels.

Regional and global correlations

The reconstructed RSL curve for the Lower Ktawa and Rouïd-Aïssa Fms was compared and tentatively correlated to the global RSL curve of Haq and Schutter (2008), to published $\delta^{18}O$ and $\delta^{13}C$ proxies (Ainsaar et al., 2010, Elrick, 2022, Männik et al., 2021) and to global, American and Baltoscandia events of the Late Ordovician. The inferred composite RSL curve of the Ktawa Group was correlated by biostratigraphic age and 3rd order sea level cycles to related curves of other study sites on the Northern Gondwana platform (Cocco et al., 2023, Dabard et al., 2009, Ghienne et al., 2007, Loi et al., 2023, Videt et al., 2010), and to existing studies in the Anti-Atlas (Loi et al., 2010, Meddour, 2016). The goal is to decipher whether the signals recognized in the Ktawa is observed all along North Gondwana.

4.4. Stratigraphic signals in the study area

The Lower Ktawa Fm is dominated by mudstones with intercalation of flat sandstone bodies, a few 10s m in thickness and with lateral extent of ca. 50–100 km. In contrast, the Rouïd-Aïssa Fm is dominated by succession of sandstones to the West and mudstones to the East (Fig. 4.2). Calibration in age of both formations was performed by Ghienne, Paris, VandenBroucke and De Backer (unpublished pers. comm.) through chitinozoans biozones (Fig. 4.3).

7 members were defined in the Lower Ktawa Fm (Fig. 4.2, Chapter 2). Each member is marked in the field as a prominent sandstone cuesta and understood as embedded within at least one MRS of 3rd order R/T cycle. Given the lateral variations within the Lower Ktawa Fm, stratigraphic profiles at different locations express or oversee different members, which can introduce a bias in the reconstruction of the different RSL curves (Fig. 4.3).

Figure 4.3*: Correlations of the Lower Ktawa Formation members. Selected stratigraphic profiles including: field log, interpreted RSL fluctuations with key stratigraphic surfaces, and correlations. For Figs 3 and 4: solid lines between profiles denote that physical lithostratigraphic correlations were verified by satellite and drone images, whereas dotted lines are hypothesized correlations. The vertical arrowed line between logs 1 and 2 marks the uncertainty in correlation of the Tissint Member (log 1) to log 2 due to the lateral disappearance of the sandstone body.*

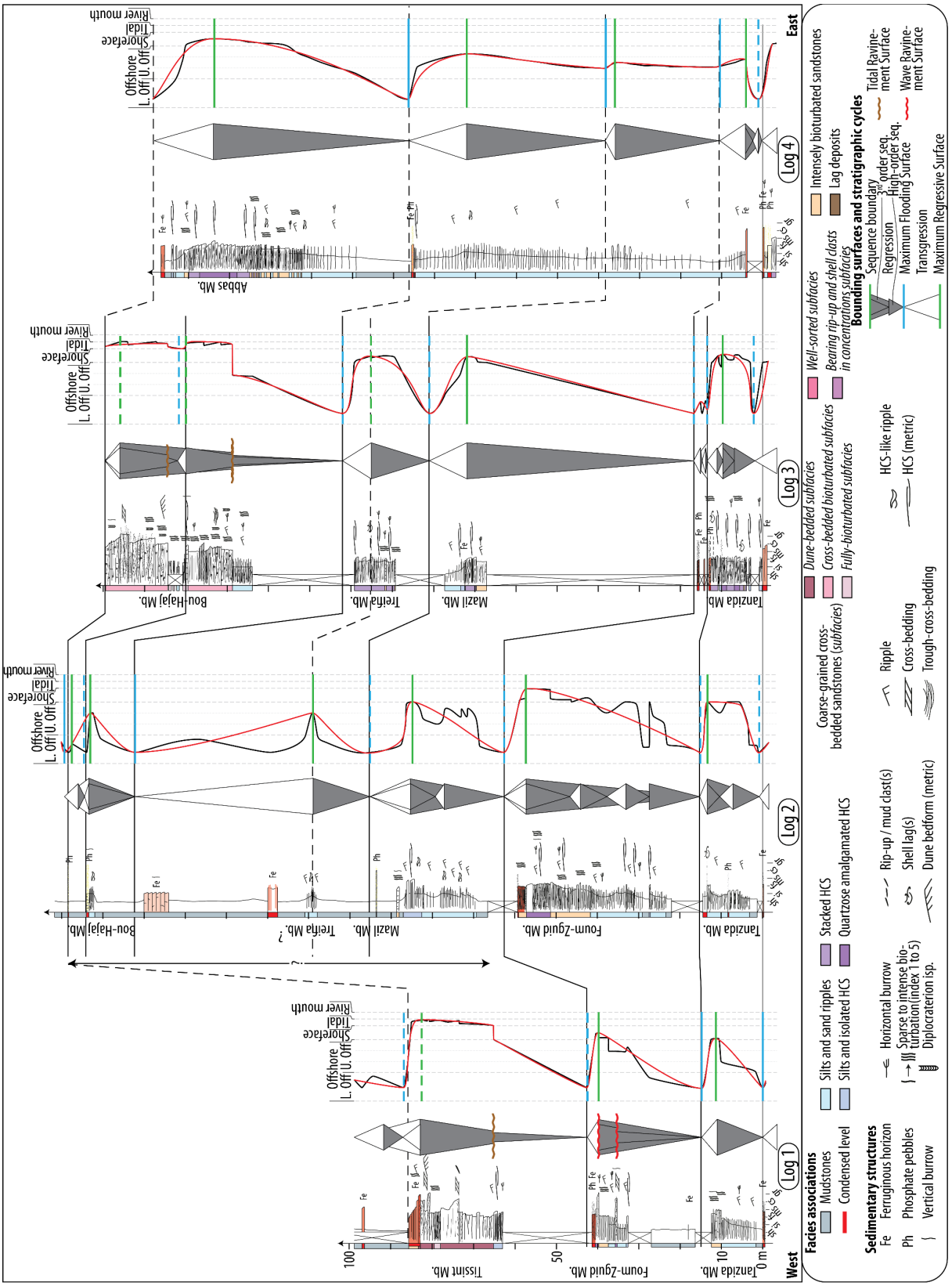

About 60-150 m of recessive foothills separate the last sandstone members of the Lower Ktawa Fm from the first sandstone exposures of the Rouïd-Aïssa Fm, and presumably consist of a fine-grained offshore signature. The Rouïd-Aïssa Fm is made up by thick sandstone packages to the W that thin and pinch out to

the E within a mudstone-dominated background. The Rouïd-Aïssa Fm is dominated by sandstones and thus recognition of individual members is challenging due to an intricate amalgamation. Nevertheless, 4 R/T cycles were recognized, which thin out from the West to the East and thus toward the shale-dominated part of the transect (Fig. 4.4).

4.4.1. Age constrains

Samples for chitinozoan biozone age calibration were collected from 2 stratigraphic logs (Fig. 3.2, logs 2 and 6) of the transect (Ghienne, Paris, VandenBroucke, and De Backer, unpublished pers. comm.). Here, the age correspondence scheme of Webby et al. (2004) is used to follow the method used in the nearby Bou Ingarf section of Loi et al. (2010), although a slight deviation from the most recent scale of the International Commission on Stratigraphy might occur (ca. 1 Myr). Chitinozoan biozones (Fig. 4.2) include *Deunffi*/*Dalbyensis* (ca. 459/457 Ma) that are identified immediately above the First Bani Group to the east of the studied transect, whereas the base of the Rouïd-Aïssa Fm bears the *Nigerica* biozone (ca. 448.5 Ma).

A time span of ca. 10-11 Myr may thus be envisioned for the deposition of the Lower Ktawa Formation. Notably, the base of the Ktawa Group (i.e. the top of the First Bani Group) in the Bou Ingarf section ca. 100 km eastward of the studied region is attributed to the *Ponceti* biozone (ca. 460 Ma), which might indicate that deposition was diachronous (Videt et al., 2010). Since 6 to 7 members, contingent on correlations (see 4.5.1), are recognized within the Lower Ktawa interval, a rough average estimate of 1.6 +/- 0.4 Myr per sequence can be postulated. The members are thus understood as representing 3rd order sequences. Moreover, the age assignment of the Rouïd-Aïssa Fm to the *Nigerica* biozone is well constrained (ca. 448.5 to 447 Ma) and perhaps up to *Merga* (ca. 447 to 444.7 Ma). Hence the Rouïd-Aïssa sediments would be deposited during ca. 1.5 to 3.5 Myr.

4.4.2. The Lower Ktawa Formation

Profile 1: This stratigraphic log is ca. 85 m thick and contains 3 of the defined Lower Ktawa Members (Fig. 4.3).

The lowermost sequence is ca. 13 m thick and entails the Tanzida Mb. It is composed of a coarsening- and thickening-

Figure 4.4*: Detailed stratigraphic profiles of the Rouïd-Aïssa Formation. Note that this representation has an uneven datum (height scales start at 0 m at the top surface of the First Bani Group). For legend, see Fig. 3.3.*

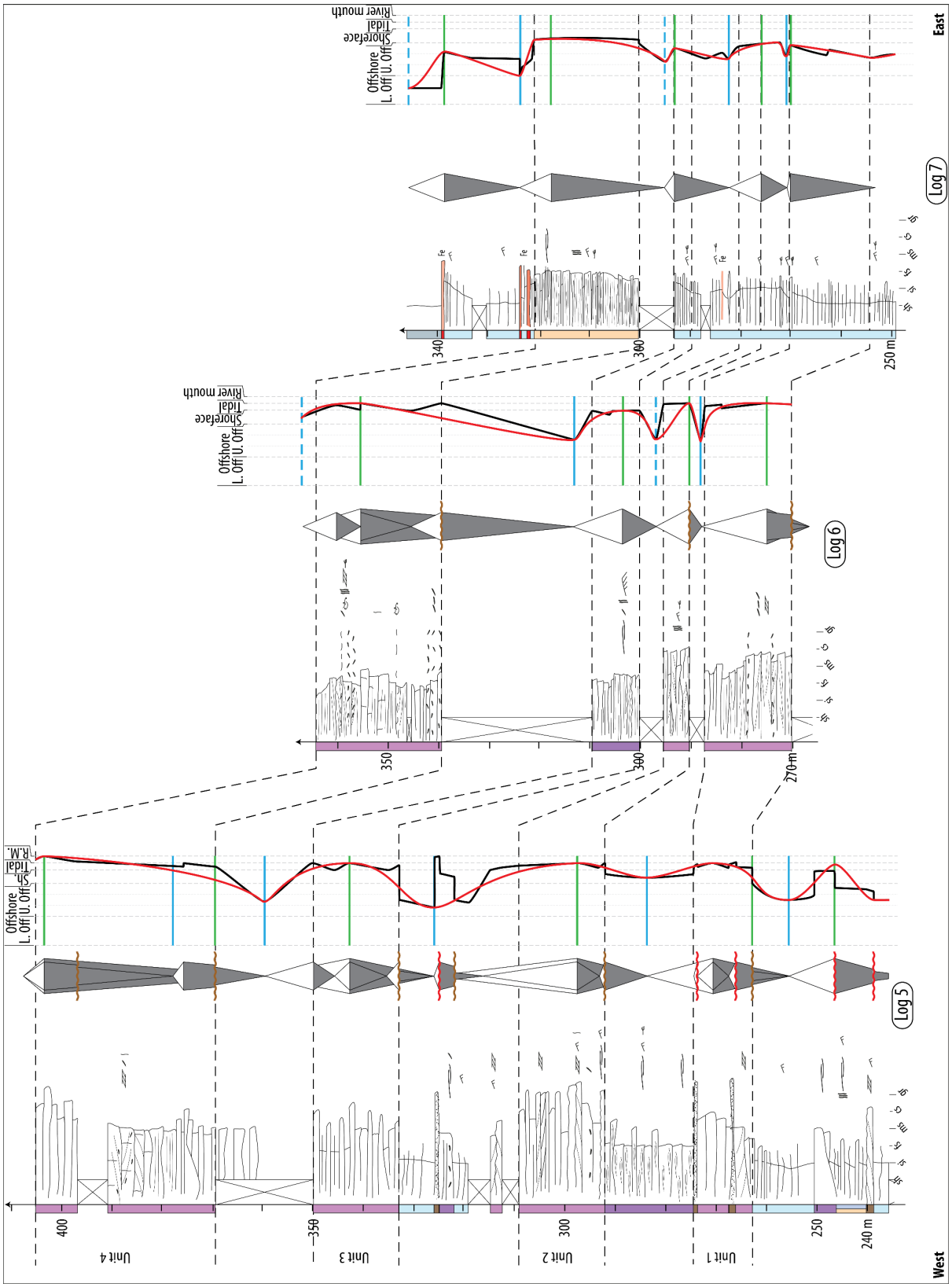

upward sequence of shales, silts and sand ripples, and intensely bioturbated sandstones. The associated MRS is placed somewhere between the base and top of the bioturbated sandstones. No condensed level

was observed that would highlight a transgressive extremum.

The second sequence is ca. 28 m thick and includes the Foum-Zguid Mb. It is coarsening- and thickening-upward and composed of silts and sand ripples and bioturbated sandstones with a sharp base. Thin intercalations of granule layers were recognized within the bioturbated sandstones, which potentially represent lags related to wave ravinement surfaces (WRS) from high-order sea-level fluctuations. The MRS is located within the bioturbated sandstones. The sequence is topped by condensed levels bearing phosphatic pebbles and marking the maximum rate of transgression.

The third cycle is ca. 55 m thick and exposes 25 m of prominent sandstones that include the Tissint Member. The Tissint Mb itself overlies with a sharp base on top of a ca. 5 m-thick suite of silts and isolated HCS. The ca. 20 m-thick Tissint sandstones are medium to coarse-grained, cross-bedded to bioturbated and interpreted as a complex of tidal deposits. The sharp base and abrupt transition in sedimentary facies likely indicate a downward shift (i.e. sudden sea-level drop). The overall ca. 20 m of tidal deposits seems to coarsen upward and hence, might be deposited in regression. The last few meters of exposures are fining upward and are highly ferruginized, the latter interpreted as condensed levels formed during transgression. Above this member, the succession forms a recessive foothill and is characterized by the absence of a prominent sandstone cuesta up to the first appearance of the sandstones of the Rouïd-Aïssa Fm.

Profile 2: This stratigraphic profile covers ca. 170 m of sediment thickness. It exposes most of the Lower Ktawa Fm members with different expressions. They are either well-defined (Tanzida, Foum-Zguid, Mazil) or only slightly-defined (Treifia, Bou-Hajaj), and only the Tissint Mb appears to be absent. Five to six sequences can be recognized (Fig. 4.3).

The first R/T cycle is ca. 15 m thick and includes the Tanzida Mb. It thickens upward in two high-order parasequences from shales to silt and sand ripples to a few sandstone beds. The top of the coarsening upward sequence contains a shell lag, possibly linked to a WRS, followed by a condensed ferruginous layer taken as the mark of the maximum transgression rate. The thickest and coarsest sandstone beds are thought to represent the MRS.

The second sequence is ca. 45 m and embeds the Foum-Zguid Mb. The first order stacking pattern is a coarsening- and thickening-upward sequence composed of

shales, silts and sand ripples, intensely bioturbated sandstones and amalgamated HCS sandstones. It is modulated by 4 higher order fluctuations developed over ca. 10 m thickness each. The top of the amalgamated HCS is massive over a few meters in thickness. This layer is thought to represent the MRS. A thick ferruginous horizon (>1 m) overprinted on bioturbated sandstones and a pebble lag is overlying the amalgamated HCS and represents the early transgression of this cycle.

The third cycle (ca. 30 m thick) is associated to the Mazil Mb. It is composed of a coarsening-and thickening-upward series of shales, silts, sand ripples and isolated HCS, which reverses upward into a fining and thinning trend back to shales. Two higher order fluctuations modulate the main signal. The MRS is placed within the HCS sandstones. A condensed level bearing phosphatic pebbles is outcropping within the shales ca. 5 m above the top of the coarsening-thinning sequence.

The fourth cycle is ca. 55 m thick and largely dominated by shales. Only a thin (ca. 3 m) coarsening/thickening-upward parasequence of silts, sand ripples and HCS-like ripples is observed that subsequently fines and thins-upward back into shales. This bare signal may correspond to the MRS of the Treifia Mb, based on the sole observation that it occurs above the Mazil Mb and below the Bou-Hajaj Mb.

Finally, the fifth cycle embeds the Bou-Hajaj Mb, which is only expressed as a few thin and fine-grained sandstones bearing HCS-like ripples in this log. Two ferruginous condensed levels separated by ca. 5 m of shales with phosphate pebbles attest for transgressive signals and may represent two high order pulses within the Bou-Hajaj Mb.

Profile 3: Five of the Lower Ktawa Members are exposed within this stratigraphic log covering ca. 160 m thickness of deposits (Fig. 4.3).

The first cycle is ca. 15 m thick and associated with the Tanzida Mb. Its lower part exposes a thin HCS sandstone bed occurring within silt, whereas the middle and upper part are composed of an alternation of stacked to amalgamated HCS, including several shell and granule lags. The MRS is located within the amalgamated HCS. The sandstone dominated package is overlain by a condensed ferruginous layer.

The second sequence is composed of two strong ferruginous condensed levels separated by ca. 1 m of recessive finer-grained material. These two layers are

tentatively correlated from satellite images to the sequence of the Foum-Zguid Mb and might represent two high-order pulses within this 3rd order cycle.

The third cycle is ca. 65 m thick and attributed to the Mazil Mb. The lower part is largely covered by debris on a recessive foothill and interpreted as fine-grained whereas it comprises ca. 10 m of sandstones in the upper part. The sandstone dominated Mazil Mb is composed, from bottom to top, of intensely bioturbated sandstones, stacked HCS, fining again into silts and isolated HCS, and sand ripples. The MRS can be placed within the stacked HCS. No condensed level was observed between this cycle and the overlying cycle.

The third cycle is ca. 20 m thick and contains the Treifia Mb. The latter outcrops as a ca. 10 m thick package of stacked HCS, where a few thin intensely bioturbated horizons are recognized. The MRS is located somewhere within the stacked HCS unit. No condensed horizons were observed above this sequence.

Finally, the fourth cycle is around 60 m thick and contains the Bou-Hajaj Mb. The latter is locally composed in this section of two thick stacks of coarse-grained and cross-bedded tidal deposits (10 to 15 m in thickness) outcropping on top of silts and sand ripples or highly bioturbated sandstones. This compound tidal package may represent an abrupt RSL drop from upper offshore to shallow tidal depositional environments.

Profile 4: Four main R/T cycles were recognized in this 150 m long profile, that contains on average the most distal signature of the transect (Fig. 4.3). Direct correlations of members via satellite or aerial photographs between this profile and the others is obstructed by a ca. 10 km long debris cover between profiles 3 and 4.

The first cycle is ca. 10 m thick and peaks with a condensed ferruginous horizon overlaid by silts and sand ripples. This cycle might be attributed to the Tanzida and/or Foum-Zguid Mbs.

The second cycle is approximately 25 m thick. It contains mainly offshore deposits made up of shales, silt and sand ripples, and it coarsens- and thickens upward and is followed by a thinning- and fining-upward sequence. It is unclear whether this sequence could belong to the Foum-Zguid Mb or possibly to the Mazil Mb.

The third cycle is ca. 45-50 m thick and is mainly composed of silts and sand ripples peaking with a ca. 10 m thick horizon containing HCS-like ripples. The MRS is defined at the coarsest part. It may

correspond to either the Mazil or Treifia Mb. It fines upwards over a stack of ca. 10 m silts and sand ripples ending in a ferruginous condensed horizon. This signal represents the onset of transgression and maximum rate of transgression.

The fourth cycle is ca. 60 m thick and comprises the Abbas Mb, the latter being possibly coeval to the Bou-Hajaj Mb. It starts from a 10 m thick excursion in shales, coarsening-upward into silts and sand ripples, and into sandstones. These sandstones themselves evolve from alternations of highly bioturbated beds with HCS-like ripples at their base, to beds containing plurimetric long HCS, progressively grading into stacked HCS. The coarsening trend ends up in quartzose amalgamated HCS, made of coarsening- and thickening- upward individual beds. The thicker and coarser amalgamated HCS are subsequently overlaid by a thinning- and fining-upward sequence composed of the opposite stacking pattern, yet condensed over 10 m. A ferruginous condensed level is observed within the shales a few meters above this fining upward sequence. This stacking pattern corresponds to a regressive trend up to the height of amalgamated HCS and then to transgressive pattern from the amalgamated HCS upward. The MRS is tentatively placed at the turnaround where the amalgamated HCS are the coarsest and thickest. The ferruginous horizon marks the maximum rate of transgression.

4.4.3. The Rouïd-Aïssa Formation

Three stratigraphic profiles were selected to depict the evolution of the Rouïd-Aïssa Fm (Fig. 4.4). Profile 5 is 170 m thick and contains multiple coarse-grained sandstone packages over its entire thickness. Profile 6 is 95 m thick, with 4 well defined sandstone units, whereas profile 7 contains mainly offshore series and fine-grained sandstone over ca. 90 m thickness. Whereas the westernmost profile exhibit up to 140 m of sandstones, the most eastern profile exposes only 1 fine-grained sandstone unit ca. 20 m in thickness.

Sandstone units identified in the Rouïd-Aïssa profiles 5 and 6, although separated by 80 km, show similar facies associations related to high energy proximal environments (Fig. 4.4). However, the total thickness of sandstone deposit as well as the thickness of beds decreases eastward between profiles 5 and 6. Furthermore, channelized beds and deep truncations are more abundant in the westward profile 5 than in profile 6, the latter exhibiting a simple stacking of beds. Approximately 40 km eastward, profile 7 exhibits mainly lower shoreface to offshore deposits over most of the outcrop. Most of

the lower part of the profile contains mudstone to siltstone with thin fine-grained sandstone intercalations containing ripples. Three coarsening- and then fining-upward sequences can be recognized. Above, one single interval, ca. 20 m in thickness, of fine-grained bioturbated sandstone suggest slightly more proximal depositional environment.

4.5. Correlations

4.5.1. Correlation of members within the study area

Despite the almost continuous exposure over 150 km, any correlation of members within the Ktawa Group when these are not physically connected, even over short distances, remains a challenge. This is due to 1) the very flat depositional system, which is common to the entire North Gondwana platform during Ordovician time, 2) the absence of a clear reference datum, and 3) the lack of a strong proximal-distal polarization indicator.

Here, for simplification, the reference level (i.e. flat datum) is taken as the topmost sandstone beds of the underlying First Bani Group, which generally mark a prominent cliff followed by an abrupt recession in the landscape. Although this lithographic limit likely corresponds to a span of sea levels, and might even be diachronous over the study area, it is the only reference marker for all stratigraphic logs. Note: a detailed investigation of the effect of sedimentary loading on the seabed morphology for each individual member is developed in Chapter 5.

Several uncertainties arise in the understanding of each members' lateral continuity. The Tanzida Mb outcrops variably over different parts of the study area, and may consist of a composite unit of high-order RSL fluctuations during the retreat related to the First Bani Group. The Foum-Zguid Mb. is the only unit relatively constrained as a standalone body over the study area. It is unclear whether the Tissint Mb, expressed only in the western part of the study area (Fig. 4.3, Profile 1), could belong to the same RSL cycle as either the Mazil, Treifia, lower or upper Bou-Hajaj sequences, or to an individual cycle not expressed in other areas. It is further questionable whether the Abbas Mb might be a lateral continuity of the lower or upper Bou-Hajaj sequences, or a standalone member and RSL cycle.

Tissint Member

The Tissint Mb (log 1, Fig. 4.3) is composed of sharp based, proximal (tidal dominated) deposits which suggest a major and possibly abrupt RSL fall (Fig. 4.4).

Given the height of the Tissint Mb 85 m above the reference of the First Bani sandstones, a lateral connection to several of the other members' sequence is possible. The Tissint Mb may connect to either the Mazil or Treifia Mbs or both (log 2, Fig. 4.3), which occur at a height of ca. 94 and 108 above the First Bani sandstones, respectively. In this case, the Tissint Mb would record the proximal part of the Mazil/Treifia Mbs, for the same RSL cycle(s). Alternatively, the Tissint Mb could correspond to the same RSL drop as the upper Bou-Hajaj sequence (log 3, Fig. 4.3). Indeed, both record proximal tidal deposits. Furthermore, both tidal sandstones are located at compatible heights above the reference level to be correlated: even though the upper Bou-Hajaj sequence is located at a height of ca. 160 m from the reference level (i.e. 75 m higher than the Tissint Mb relative to the datum), this represents an apparent dip of 0.05º only, considering ca. 90 km of lateral separation between both exposures. Such a height difference may be related to differences in isostatic adjustment due to preexisting sediment load, or an uneven datum line. As such, both sandstone units from the Tissint and upper Bou-Hajaj sequences could correspond to separate embayments deposited during a single RSL fall. Additionally, the Tissint Mb records 2 stacks of tidal deposits separated by a few meters of highly bioturbated sandstones, as also recorded in the upper Bou-Hajaj sequence, an observation that may represent another insight of their correlation. Finally, the Tissint Mb could belong to a separate RSL cycle that would not be exposed in the eastern parts of the transect. In this case, the eastern expression of the Tissint Mb. would either be absent because not deposited or largely eroded during a ravinement. If this turns out to be true, the only marker of the cycle might correspond to a condensed level marking the subsequent transgression, and its recognition and correlation within the mudstone dominated badland talus is a challenge in the field.

As the Tissint Mb records a major RSL drop, its possible correlation to another member has implication for the entire RSL curve of the study area, and ultimately, to any attempt to connect the Lower Ktawa RSL changes to a global eustatic signal. The implications are thus further discussed in light of the global and regional scale signals below. Briefly, if the Tissint and Bou-Hajaj Mbs are coeval, only one major RSL drop would be recorded during deposition of the Lower Ktawa Fm. If the Bou-Hajaj and Tissint Mbs are deposited during different cycles, then 2 major RSL fall would be interpreted (i.e.

one from Tissint, and one from the Bou-Hajaj Mb) during deposition of the Lower Ktawa Fm.

Abbas Member

The Abbas Member outcrops at a relatively similar height from the datum (ca. 140 m) as the Bou-Hajaj Mb (ca. 160 m), and could thus record the same RSL cycle (Fig. 4.3). However, the members cannot be physically correlated as a ca. 10 km part of the cliff exposure is obstructed by rockfalls. More importantly, the sandstones of the Abbas Mb record a thinning together with a deepening of the associated depositional environment toward the West, i.e. toward the Bou-Hajaj Mb. This westward-deepening trend is not compatible with a direct connection to the Bou-Hajaj sandstones recording the most proximal deposits within the entire Lower Ktawa. Thus, the Abbas Mb might belong to a different depositional system. It is thus envisioned that the Abbas and Bou-Hajaj Mbs pertain to the same 3rd order RSL drop yet, they may express two different high-order fluctuations within the 3rd order drop. They are furthermore not necessarily physically connected, in that they can represent expressions from two different lobes from two different source feeders. It remains that the major RSL drop recorded in the upper Bou-Hajaj sequence is not present in the Abbas Mb. Rather, the Abbas Mb contains 3 minor sequences of stacked HCS sandstone beds, which might be distal signals of the several RSL cycles recorded as the lower to upper Bou-Hajaj sequences.

Rouïd-Aïssa Formation

Visual correlations of sandstone units from satellite images are delicate within the Rouïd-Aïssa Fm. Furthermore, glacial incisions from the Hirnantian advance variably erode within the Rouïd-Aïssa Fm (Fig. 4.2). Thus, no direct physical correlation was possible between the different sandstone units. Between the sandstone dominated profiles 5 and 6, the thick sandstone units 1-3 are tentatively correlated to each other by packages (Fig. 4.4). The connection to profile 7 is solely based on R/T cycles interpreted from the logs. It is hypothesized that the three sandstone units 1 to 3 of profiles 5 and 6 correspond to the three lower R/T cycles of profile 7. From the field indications, the Rouïd-Aïssa Fm hence seems to contain 4 main units and a West to East orientation of the proximal to distal polarization over the ca. 120 km long exposure separating the 3 profiles.

RSL fluctuations

From the interpretation of the different members within the Lower Ktawa

and Rouïd-Aïssa Formation Fms, a composite RSL curve can be extracted (Fig. 4.5). Within the Lower Ktawa Fm, the lowermost and oldest Tanzida Mb is taken here as the signature of a 3rd order RSL cycle, although relatively thin, laterally discontinuous, and close to the uppermost sandstones of the First Bani Group. The Foum-Zguid Mb is confidently interpreted as a 3rd order R/T cycle associated to a cycle of RSL fluctuations. Here, the Tissint Mb is taken as a standalone unit, representing a major RSL drop based on the comparison to the global (see 4.5.2) and regional RSL curves (see 4.5.3). The Mazil and Treifia Mbs are interpreted as 2 R/T cycles, yet given the facies associations in-between both members suggesting low amplitude RSL variations, they may correspond to a single 3rd order RSL cycle modulated by a higher frequency variation (see 4.5.2). The Abbas Mb represents a cycle that is likely related to the lower Bou-Hajaj sequence. The upper Bou-Hajaj Mb represents a major RSL fluctuation occurring after the 4 previous events. A long-lasting flooding/RSL high is recorded by fines-dominated, recessive foothills over the entire transect between the end of the Lower Ktawa Members and the first occurrence of Rouïd-Aïssa sandstones (Fig. 4.5). The Rouïd-Aïssa Fm mainly records thick shoreface to tidal deposits and might record a major RSL fall (Fig. 4.4). The observation of 4 distinct units within this formation would point towards 4 successive high frequency cycles and suggest a long lasting RSL lowstand during deposition of the Rouïd-Aïssa Fm (Fig. 4.5).

4.5.2. Correlations at the global scale

The Ktawa signal of the western Central Anti-Atlas (this study) was compared with the calibrated global relative sea level fluctuation curve from Haq and Schutter (2008) as well as $\delta^{18}O$ data on conodont-apatite data (Elrick, 2022), $\delta^{13}C$ data from carbonates (Ainsaar et al., 2010), and to the timing of global, North American and Baltoscandian glacial events documented in the literature (Fig. 4.5). As a reference, increased ice volumes are understood as associated with higher $\delta^{18}O$. Indeed, a decrease in water temperature (cooling event) would be associated with an increase in $\delta^{18}O$ precipitation whereas increased freshwater influx (from meltwater) leads to lower $\delta^{18}O$ values (Bergström, Young, and Schmitz, 2010b, Männik et al., 2021). Concerning $\delta^{13}C$, it is known to be an indicator of environmental changes, where positive excursions would be linked to higher organic carbon production and burial, and so linked to

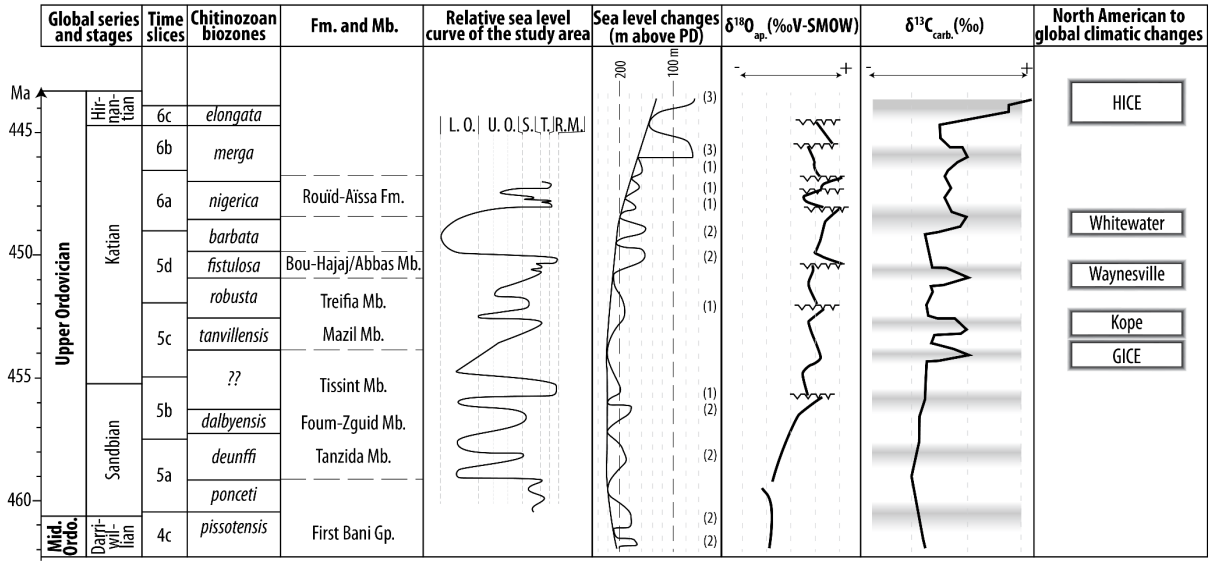

Figure 4.5*: Time constraint on the Ktawa Group and members with interpreted composite relative sea level curve for the studied region, and comparison to global scale data, including global relative sea level curve δ¹⁸O and δ¹³C curve as well as known climatic events. Time slices and chitinozoans biozones from Webby et al., (2004). For chitinozoans sampling locations and log in Fig. 4.2. Relative sea level curve interpreted from sedimentary facies: L.O.: lower offshore, U.O.: upper offshore, S.: shoreface, T.: tidal, R.M.: river mouth. Global sea level curve from Haq and Schutter, (2008) in m above present day (PD). Symbols (1), (2), (3) indicate the relative magnitude of each excursion: < 25 m, 25 to 75 m, > 75 m resp. δ¹⁸O curve modified after Elrick (2022). Jagged lines: sequence boundaries recognized by Männik et al. (2021). δ¹³C curve modified after Ainsaar et al. (2010) and Männik et al. (2021). Grey horizontal belts denote probable cooling to glacial events identified during the Late Ordovician period modified after Männik et al. (2021). North American to global climatic changes: GICE and HICE: Guttenberg and Hirnantian Isotopic Carbon Excursion resp. Time slices and chitinozoans biozones from Webby et al. (2004).*

intense nutrient upwelling in glacial times (Ainsaar et al., 2010, Brenchley et al., 1994).

From the sampled regions, the oldest chitinozoans found within the Lower Ktawa Fm in the area are *Deunffi*/*Dalbyensis*, and thus suggest deposition started at least at 459-457 Ma. Younger than this age, from the global relative sea level curve, 3 global RSL fall events are observed with peaks at ca. 458.5, 456 and 455.5 Ma and excursions with amplitude of 40, 45 and 25 m respectively (Fig. 4.5). These might be correlated to the Tanzida, Foum-Zguid and Tissint Mbs respectively, which are constrained within this timespan and bracketed as older or within the *Tanvillensis* biozone (i.e. ca. 453.5 Ma), and younger than the start of *Deunffi* (i.e. 459 Ma). A minor excursion in $\delta^{13}C$ at 458 Ma may record the sea level

excursion related to the Tanzida Mb. This excursion is not recorded in the $\delta^{18}O$ data. Sporadic information from Argentina ($\delta^{18}O$ peak, Albanesi et al., 2020) and Estonia (paleokarst surface, Calner et al., 2010) also suggest a glacial event that may coincide with the Tanzida Mb. The second global RSL fall event at 456 Ma, tentatively related to the Foum-Zguid Mb, is not related to excursions in the $\delta^{18}O$ and $\delta^{13}C$ curves.

The third global fall event at 455.5 Ma is associated to the Tissint Member, although this member is not well constrained in age. The sea level drop and slight positive excursions of both the $\delta^{18}O$ and $\delta^{13}C$ proxies at ca. 455.5 Ma were recognized as a cooling event in Laurentia (Buggisch et al., 2010). It further correlates with major hiatuses in other sections of North Gondwana, e.g. in the Hoggar and Armorican Massif (see 4.5.3., Fig. 4.6). Interestingly, the GICE, at 454 Ma, one of the 2 major Late Ordovician isotopic excursions often interpreted as a glacially related RSL fall event, is not associated with a major sea level drop in the global sea level curve (Fig. 4.6, Ainsaar et al., 2010, Bergström et al., 2009, Bergström et al., 2010a, Holland, and Patzkowsky, 1998, Saltzman, and Young, 2005). It is thus also conceivable that the Tissint Mb, recording the most proximal facies associations within the study zone, could be associated with the 454 Ma GICE rather than the 455.5 Ma excursion.

The 3 RSL fall at 458.5, 456 and 455.5 Ma are followed in the global relative sea level curve by a global RSL fall of lesser magnitude (30 m) yet spread over a longer timespan at ca. 453.5-451 Ma (Fig. 3.5). This timespan overlaps with the events of the Mazil and Treifia Mbs, as *Tanvillensis* (ca. 454-452.5 Ma) is found at the base of Mazil and *Fistulosa* (ca. 451-450 Ma) above Treifia. In that sense, both members should be deposited within this single 3rd order RSL regression. This is supported by the sediment record in-between the two sandstone members, which displays no important deepening between both events and thus a relatively low-amplitude RSL variation. Interestingly, the timespan of deposition of the Mazil and Treifia Mbs could also be related to the excursions of the GICE or Kope events, also known as Ravkere in Baltoscandia (ca. 454 Ma and 453 Ma. respectively), which also appear close but slightly shifted in time with the $\delta^{18}O$ excursions (Bergström et al., 2009, Elrick, 2022, Saltzman, and Young, 2005).

A major sea level drop (ca. 55 m) at 450.5 Ma (spanning over 451-449,5 Ma) in the global relative sea level curve

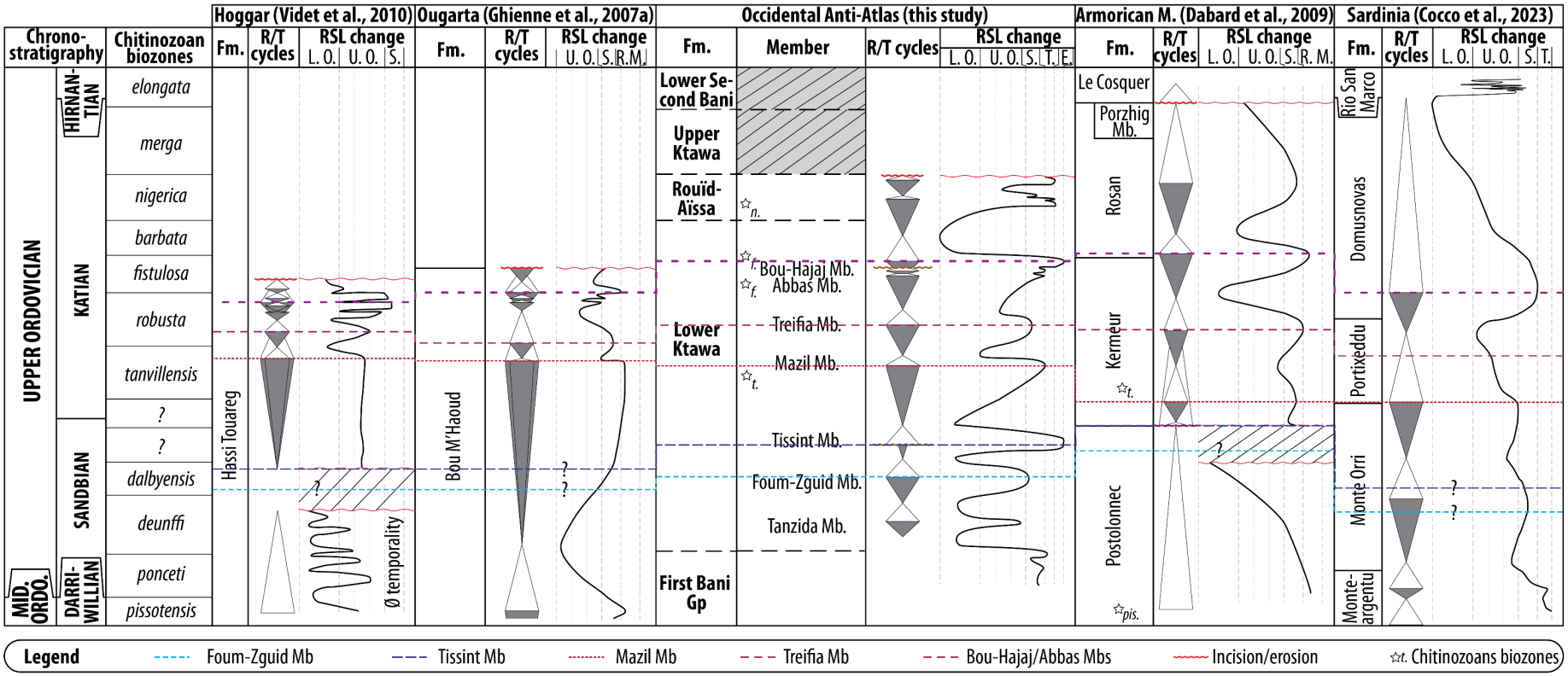

***Figure 4.6**: Comparison of sedimentary successions across the northern Gondwana platform. Compilation and comparison of sections from the Hoggar, Ougarta (Ghienne et al., 2007, Videt et al., 2010), the western Central Anti-Atlas (this study), Armorican Massif (Dabard et al., 2009) and Sardinia (Cocco et al., 2023, Loi et al., 2023). Locations of the profiles see Fig. 4.1A and B. Colored lines are tentative correlations of the Ktawa members to other localities. Stars: documented chitinozoan biozones. pis.: Pissotensis, t.: Tanvillensis, f.: Fistulosa, n.: Nigerica.*

corresponds to an onset during *Fistulosa* and termination within *Barbata* biozones (Fig. 4.5). This excursion could thus be correlated to the Bou-Hajaj Mb, which is constricted to the *Fistulosa* biozone (ca. 451-450 Ma). Laterally to the East, the Abbas Mb, which might be correlated to Bou-Hajaj, is capped by *Nigerica* (ca. 448.5-447 Ma). An association of the Bou-Hajaj Mb to this major sea level drop is further supported by the sedimentary record within the upper Bou-Hajaj sequence, which exhibits the most proximal facies associations within the Lower Ktawa Fm (i.e. tidal deposits). The R/T cycle recorded in the Bou-Hajaj Mb is also recognized in isotopes data. Positive excursions in both $\delta^{18}O$ and $\delta^{13}C$ are observed at the same time as the deposition of the Bou-Hajaj Mb. (Ainsaar et al., 2010, Elrick, 2022). The $\delta^{13}C$ excursion has been recognized as the Waynesville event in Baltica (Calner, Lehnert, and Nõlvak, 2010) and is Middle Katian in age.

The transition between the Bou-Hajaj Mb and the Rouïd-Aïssa Fm, where mainly shales are outcropping in the field, occurs during the biozones of *Fistulosa* (ca. 451-450 Ma) and *Nigerica* (ca. 448.5-447 Ma, Fig. 3.5).

Finally, at the global scale, 4 regressions at ca. 449, 448, 447, and 446.5 Ma record drops of 50, 30, 30, 20 m superimposed on a long-term trend of sea level drop of ca. 50 m (Fig. 4.5). The 4 sandstone units identified within the Rouïd-Aïssa Fm, deposited during *Nigerica* (ca. 448.5-447 Ma), could correspond to some or all of these global relative sea level drops. The first regressive event could be linked to the Whitewater glacial event recognized in both the $\delta^{18}O$ and $\delta^{13}C$ data of Bergström et al. (2009). Several other positive excursions in $\delta^{18}O$ and $\delta^{13}C$ were observed above the Whitewater event, but they were never correlated to a glacial event.

Altogether, the sandstone members recorded in this study in the western Central Ktawa Gp and their associated 3rd order R/T sequences can be understood as related to global glacio-eustatic events. The position of the Ktawa Gp on the stable intracratonic basin part of the Gondwana supercontinent likely limited the occurrence of other local superimposed signals, e.g. tectonics. Additionally, the shallow marine environments recorded in the study area likely helped the record and preservation of glacio-eustatic signals: proximal enough for a clear record, but distal enough for preservation.

4.5.3. Correlations across the northern Gondwana platform

The signal interpreted from the Ktawa Group logged in the western Central Anti Atlas region (this study) was then compared with other sedimentary successions of a similar age on or close to the northern Gondwana marine platform: the Hoggar Massif (Ghienne et al., 2007, Videt et al., 2010), the Ougarta range (Ghienne et al., 2007, Videt et al., 2010), the Armorican Massif (Dabard et al., 2009, Dabard et al., 2015), and Sardinia (Cocco et al., 2023, Loi et al., 2023) (Fig. 4.6). Based on the 3rd order RSL cycles constrained in age by chitinozoan biozones, most of the RSL signal of the Ktawa can be recognized across other outcrops, as developed hereafter.

Hoggar profile

The Hoggar profile (Algeria, Fig. 4.6) is composed of a single formation: the Hassi Touareg Fm, which outcrops below the Late Ordovician glacial incisions (Ghienne et al., 2007, Videt et al., 2010). A lack of time constraint for the 5 first cycles within the Hoggar profile impedes a precise correlation of the R/T cycles recorded by the Tanzida and Foum-Zguid Mbs. A hiatus present around the *Dalbyensis* biozone could be coeval to the sharp-based Tissint Mb composed of proximal tidal deposits. A long-lasting RSL steady-state (*Dalbyensis* to *Tanvillensis*) is recorded in the Hoggar profile at an age compatible with the Mazil Mb, and is followed by a second fall (onset of *Robusta*), which could correspond to the cycle recorded by the Treifia Mb. A major RSL fall with several high-order fluctuations is observed within the end of *Robusta* to the onset of *Fistulosa* biozones of the Hoggar section. This composite signal might be correlated to the Bou-Hajaj Mb, which is subdivided in 2 high-order cycles (Lower / Upper Bou-Hajaj). The lower Bou-Hajaj sequence, which is thought to be coeval to the Abbas Mb and the upper Bou-Hajaj sequence, would be the Ktawa expressions of the high-order cycles in the Hoggar section.

Ougarta profile

The Ougarta section (Fig. 4.6), currently located ca. 400 km eastward from the studied region, is also composed of a single formation: Bou M'Haoud (Ghienne et al., 2007). This profile shows a similar trend as the RSL curve inferred from the Hoggar section. The signals from the Tanzida, Foum-Zguid and Tissint Mbs are not recognized in the Ougarta section. Three regressive events occur between *Dalbyensis* and *Fistulosa*, which occur during deposition of the Mazil, Treifia, and Bou-Hajaj cycles. The last RSL fall is also

composed of several high frequency cycles, which could, as in the Hoggar section, correspond to the superimposed cycles within the Abbas/Bou-Hajaj.

Armorican profile

The Armorican section from Brittany (France, Fig. 4.6) belongs to the microcontinent Armorica that was part of northern Gondwana and located close to the studied region according to paleogeographic reconstructions (Fig. 3.1A and B). This section was calibrated by chitinozoan biozones (Fig. 4.6, Dabard et al., 2009, Dabard et al., 2015). The lower part of the section (Postolonnec Fm) starts in the *Pissotensis* biozone and the overlying Kermeur Fm. shows *Tanvillensis* chitinozoans. These two formations are separated by a major hiatus, where the first layer of the Kermeur Fm is a transgressive pebble lag where *Deunffi*/*Dalbyensis* species were found. In the absence of 3rd order R/T cycles in the exposed Postolonnec Fm, it is hypothesized that the record of cycles coeval to the Ktawa's Tanzida and Foum-Zguid cycles has been eroded away, or not deposited. The limit between the Postolonnec Fm and the overlying Kermeur Fm is a hiatus interpreted as an abrupt sea level fall. This hiatus and overlying deposits could, similarly to the Ougarta and Hoggar sections, be correlated to the sharp-based Tissint Mb composed of proximal tidal deposits. Notably, Dabard et al. (2015) hypothesized that this hiatus marks the Sandbian/Katian boundary, and that it would be "the onset of a severe glaciation", "potentially overestimated owing to the erosion of some regressive sequences in the uppermost part of the Postolonnec Fm". Two RSL lowstands occur above the hiatus during deposition of the Kermeur Fm (*Tanvillensis* and *Robusta* resp.) and are interpreted as related to the Ktawa's Mazil and Treifia Mbs, respectively. Supporting this interpretation, *Tanvillensis* chitinozoans were found in deposits making the 1st cycle of the Kermeur Fm and below the base of the Mazil Mb. Interestingly, no consequent deepening is interpreted between the two lowstands of the Kermeur Fm, coherent with the sedimentary signal between the Mazil and Treifia Mbs that similarly suggest no important deepening between both members. The next RSL lowstand marks the limit between the Kermeur and Rosan Fms and is a major fall that fits with the major RSL low of the Ktawa's Bou-Hajaj Mb. Finally, a long lasting RSL low peaking during *Nigerica* likely coincides with the Rouïd-Aïssa Fm in the western Central Anti-Atlas. Thus the Rouïd-Aïssa Fm would correspond to the same RSL cycle that of the Rosan Fm,

although the RSL excursion of the Rosan Fm seems of a lesser magnitude.

Sardinia profile

The Sardinia profile (Fig. 4.6, Cocco et al., 2023) was biostratigraphically correlated to the profile in the Armorican Massif by Loi et al. (2023). Three main RSL cycles are recorded. The (second) R/T cycle at the limit between the Monte Orni and Portixeddu Fms would belong to the *Tanvillensis* biozone. Hence, a correlation to the R/T cycle associated to the Mazil Mb, also in *Tanvillensis* is emphasized. From this correlation, we suggest that the R/T cycle in the Monte Orni Fm (older than Portixeddu) would be correlated to the Foum-Zguid and/or Tissint R/T cycle(s). Even though no clear RSL cycle is recorded in the Portixeddu Fm, the rate of RSL rise seems to decelerate, a signal that could be correlated to the deposition of the Treifia sandstones. A major RSL fall is recorded during the deposition of the Domusnovas Fm that would be coeval to the major RSL change of the Bou-Hajaj Mb. The high order RSL changes associated to the Bou-Hajaj Mb and visible in the Hoggar and Ougarta sections are not recorded in the Sardinia profile, as in the Armorican Massif.

4.5.4. Correlations within the Ktawa Group

Correlations of the Ktawa Group within Morocco has been a 40 years-long challenge due to the specific setting in the region. The sandstone and mudstone successions of the Jbel Bani Range are exposed over at least 720 km from the region of the Jbel Zini (folded Bani) in the W to the zone of Tafilalt in the E (Fig. 4.1C). However, in the region of Tagounite, they are separated by a ca. 40 km broad area dominated entirely by mudstones, starting at the eastern end of the study region (Fig. 4.1C). Thus, no physical correlations are possible in the field and nomenclatures differ to the E and W of the so-called “Tagounite trough”. Interestingly, this Tagounite trough furthermore coincides with the continuation of the Ougarta range that exhibit successions of a similar age, as well as with the Anti-Atlas Major Fault, and a major regional gravimetric anomaly (Fig. 4.1C, Ennih and Liégeois, 2001).

Original schemes by Destombes (1985) suggested that the Bou-Hajaj Mb in the western Central Anti-Atlas corresponds to the Middle Tiouririne Mb in the eastern Central to Oriental Anti-Atlas, and that the western Rouïd-Aïssa Fm (also “Er-Rwaidat”) corresponds to the eastern Upper Tiouririne Fm. However, the chitinozoan

biozones presented here depict a new correlation scheme with another outcrop to the East of the Tagounite trough calibrated by chitinozoans: the Bou Ingarf section surveyed by Loi et al. (2010), located approx. 100 km NE of the study area (Figs 4.1C and 4.7).

Bou Ingarf section

The Bou Ingarf section starts within the first beds above the First Bani sandstones, yet the profile starts within the *Tanvillensis* biozone (Fig. 4.7). *Tanvillensis* chitinozoans were found at the base of the Mazil Mb. In the absence of further constraints in the western Anti-Atlas, it cannot be excluded that all the Tanzida, Foum-Zguid, Tissint and Mazil Mbs are also emplaced within the *Tanvillensis* biozone and as such, the Middle Tiouririne could represent an amalgamation of some or all of these members. However, given the suggested correlations to the global relative sea level curve and their time constraints, the Middle Tiouririne Mb should be time equivalent to the Mazil only. The Middle Tiouririne Mb was correlated to the GICE event by Loi et al. (2010) associated to a high amplitude R/T cycle and possibly a glacial event. The Treifia Mb might be correlated to the low amplitude RSL fall occurring during deposition of the Amouguer Mb. The Bou-Hajaj Mb in the study area is well constrained in age within the *Fistulosa* biozone, as is the (lower part of) Upper Tiouririne Fm in the Bou Ingarf section. Both of these members record the largest amplitude fall in RSL in the region. Indeed, the Upper Tiouririne Fm is sharp based and records up to upper shoreface sediments, whereas the Bou-Hajaj Mb is composed of its lower and upper sequences, with the upper Bou-Hajaj sequence forming a channel complex filled with tidal deposits. We suggest that the limit between the sequences would correlate to the sharp base of the Upper Tiouririne Fm. Furthermore, the Bou-Hajaj Mb would correlate with a RSL drop of ca. 55 m according to the global relative sea level curve of Haq and Schutter (2008), which is in good agreement with the drop of ca. 50 m

Figure 4.7*: Correlations of sections from the Ktawa Group in the Anti-Atlas. Left: composite relative sea level curve and detailed stratigraphic profile of the study area (western Central Anti-Atlas). Center: relative sea level curve and simplified stratigraphic profile of Bou Ingarf (Central Anti-Atlas) modified after Loi et al. (2010). Right: relative sea level curve and simplified stratigraphic profile of Djebel Boultam (Central/Oriental Anti-Atlas) modified after Meddour (2016). Dotted brown lines are tentative correlations based on chitinozoans biozones and 3rd order cycles. Locations of profiles see Fig. 4.1C and D. Legend see Fig. 4.3.*

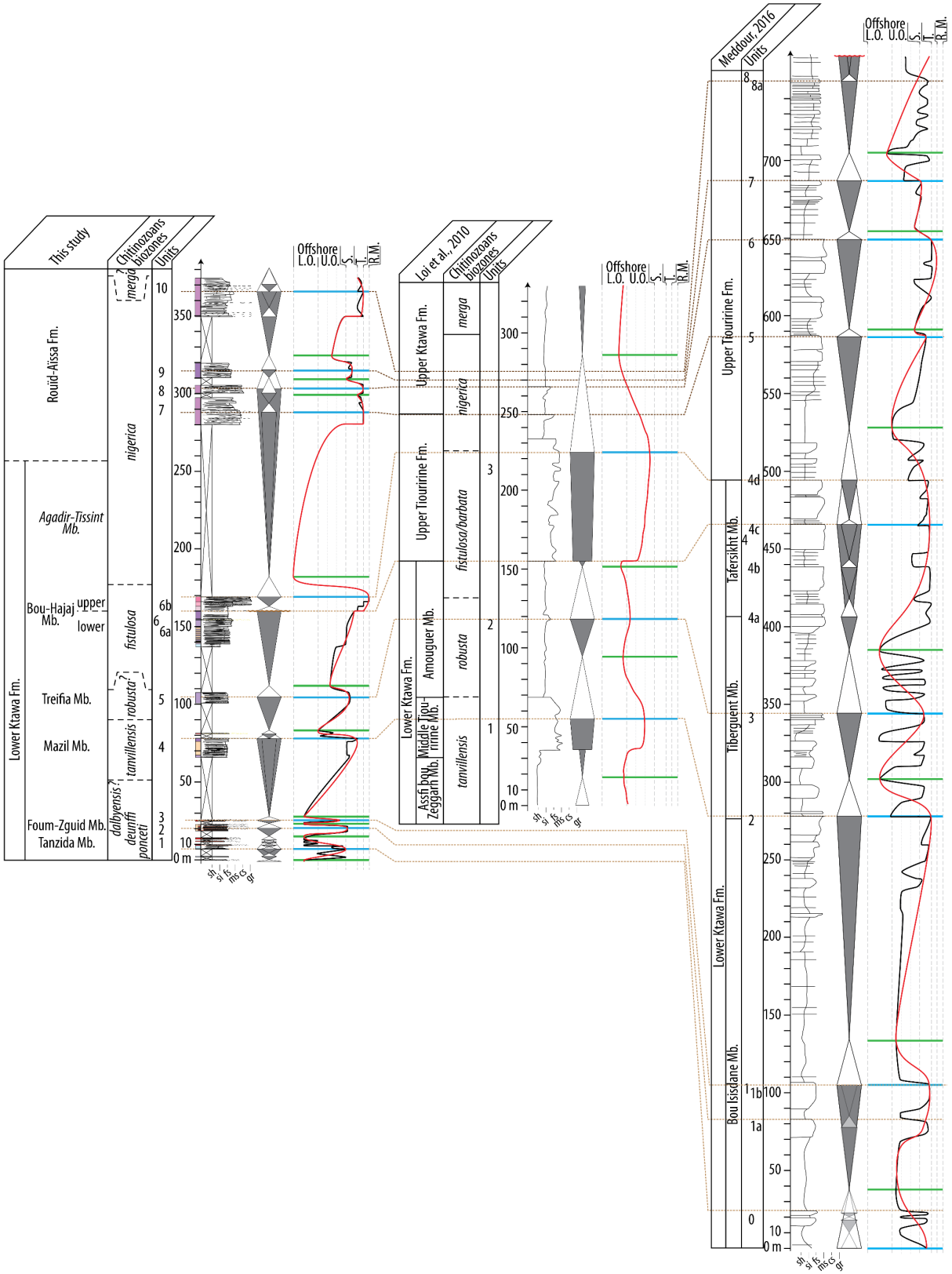

modelled by Loi et al. (2010) for the Upper Tiouririne Fm and their interpretation that it records a glacial event. Intriguingly, the Rouïd-Aïssa Fm that records the most important RSL fall in the studied region (made of 4 high frequency low amplitude R/T cycles) within the *Nigerica* to *Merga* biozones is not well expressed in the Bou

Ingarf section. If any, one can suggest that two minor events observed in the Bou Ingarf section at ca. 250 and 265 m could be correlated to the sandstone packages of the Rouïd-Aïssa Fm. Moreover, only one 3rd order MFS is recorded in the Bou Ingarf section during the *Nigerica* biozone at ca. 285 m (and before *Merga*). Hence, the transgression occurring after deposition of the Upper Tiouririne regressive part may be correlated to the Rouïd-Aïssa Fm belonging as well to the *Nigerica* biozone (and maybe up to *Merga*). Hence, there exists a major discrepancy within the *Nigerica* and *Merga* biozones between the study region and the section of Bou Ingarf of Loi et al. (2010).

Alnif region

Meddour (2016) studied the Ktawa Fm in the Central to Oriental Anti-Atlas, in the region of Alnif ca. 200 km NE from the studied region (Fig. 4.1C). The Lower Ktawa and Upper Tiouririne Fms (up to the glacial incisions) were subdivided in 8 R/T cycles in the Djebel Boultam section (Fig. 4.7). Correlations between the Djebel Boultam and Bou Ingarf profiles were conducted in Meddour (2016) based on the formations and members proposed by Destombes (2006a) (Table 4.2). Here, we propose a new correlation scheme based on 3rd order cycles and the findings within the western Central Anti Atlas (Fig. 4.7 and Table 4.2). Here, the subdivision of the Djebel Boultam is based on sandstone packages and R/T cycles, and differ slightly from the T/R subdivisions and hierarchy of orders suggested initially in Meddour (2016). The Unit 0 (ca. 25 m) in the Djebel Boultam section is not recognized as a 3rd order cycle. However, two thin parasequences of fine-grained bioturbated sandstones are outcropping, which could be correlated to the Tanzida Mb in the studied region. Unit 1 is composed of two higher order R/T cycles (1a and 1b) making a 3rd order one, which could be correlated to the Foum-Zguid and Tissint Mbs. The Mazil and Treifia Mbs would be correlated to the Unit 2 and 3 in the Alnif region. These two cycles seem to record the same RSL pattern in both areas. Indeed, Unit 2 and the Mazil Mb deposits record shallower depositional environments than the Unit 3 and Treifia Mb. Unit 4 is correlated to the Bou-Hajaj Mb, both recording the shallowest depositional environments of the Lower Ktawa Fm. Unit 4 is, however, composed of 4 sub units, whereas only 2 sequences are defined for the Bou-Hajaj Mb. This may be due to the fact that the Djebel Boultam profile representing the Ktawa in the Alnif region would record deeper depositional environments than the composite profile of Ktawa in the studied region. Furthermore, the tidal deposits and underlying

***Table 4.2**: Correlations from the western Central Anti-Atlas (this study) to the Bou Ingarf section (Central Anti-Atlas, Loi et al., 2010) and Djebel Boultam profile (eastern Central to Oriental Anti-Atlas, Meddour, 2016) by the means of biostratigraphic chitinozoans biozones and 3rd order R/T cycles respectively. Correlations were performed by Meddour (2016) to the Bou Ingarf profile (Loi et al., 2010) to which we hypothesized a new set of correlation.*

<table>
<tr><th colspan="2">Occidental Anti-Atlas (this study)</th><th colspan="2">Bou Ingarf (Loi et al., 2010)</th><th colspan="3">Central/Oriental Anti-Atlas, Djebel Boultam section (Meddour, 2016)</th></tr>
<tr><td colspan="2"></td><td colspan="2">Biostratigraphic correlations</td><td colspan="2">Interpreted correlations from 3rd order R/T cycles</td><td>Meddour's correlation to Loi et al., 2010 (based on Fm. and Mb. from Destombes, 2006a)</td></tr>
<tr><td>Fm and Mb</td><td>Units</td><td>Fm and Mb</td><td>Units</td><td>Fm and Mb</td><td>Units</td><td>Fm and Mb</td><td>Units</td></tr>
<tr><td rowspan="4">Rouïd-Aïssa Fm</td><td>10</td><td rowspan="4">Upper Ktawa Fm?</td><td rowspan="4"></td><td rowspan="4">Upper Tiouririne Fm</td><td>8a</td><td rowspan="4"></td><td rowspan="4"></td></tr>
<tr><td>9</td><td>7</td></tr>
<tr><td>8</td><td>6</td></tr>
<tr><td>7</td><td>5</td></tr>
<tr><td>Bou-Hajaj Mb</td><td>6b / 6a</td><td>Upper Tiouririne Fm</td><td>3</td><td>Tafersikht Mb</td><td>4</td><td>4d / 4a to c</td><td>Upper Tiouririne Fm</td><td>5 / 6 / 7 / 8a</td></tr>
<tr><td>Treifia Mb</td><td>5</td><td>Amouguer Mb</td><td>2</td><td>Tiberguent Mb</td><td>3</td><td></td><td>Tiberguent Mb</td><td>4c / 4d</td></tr>
<tr><td>Mazil Mb</td><td>4</td><td>Middle Tiouririne Fm</td><td>1</td><td>Bou Isisdane & Tiberguent Mbs</td><td>2</td><td></td><td>Bou Isisdane & Tiberguent Mbs</td><td>2 / 3 / 4a / 4b</td></tr>
<tr><td>Tissint Mb</td><td>3</td><td rowspan="3"></td><td rowspan="3"></td><td rowspan="3">Bou Isisdane Mb</td><td rowspan="2">1</td><td>1a</td><td rowspan="3"></td><td rowspan="3"></td></tr>
<tr><td>Foum-Zguid Mb</td><td>2</td><td>1b</td></tr>
<tr><td>Tanzida Mb</td><td>1</td><td>0</td><td></td></tr>
</table>

ravinement in the studied region could have eroded some parts of the Bou-Hajaj Mb. Finally, Units 5 to 8 in the Djebel Boultam section are correlated to the 4 sandstone packages of the Rouïd-Aïssa Fm in the studied area. Note that Meddour (2016) suggest a correlation of Units 5 to 8 with the Upper Tiouririne Fm of Loi et al. (2010), whereas here, Units 5-8 are considered equivalent to the Rouïd-Aïssa Fm, which is absent in the Loi et al (2010) profile. In summary, we propose the following correlations: the Foum-Zguid Mb is coeval to the Bou Isisdane Mb, Mazil and Treifia to Tiberguent, and Bou-Hajaj to Tafersikht in the western Central to eastern Central/Oriental Anti-Atlas respectively (Table 4.2). The Rouïd-Aïssa Fm is correlated to the Meddour's attributed Upper Tiouririne Fm which would be younger than the Upper Tiouririne Fm attributed by Loi et al. (2010) in the region of Bou Ingarf (Table 4.2). These correlations, however, would benefit from biostratigraphic constrains in the eastern area for confirmation.

4.6. Conclusion

The Ktawa Group in the western Central Anti-Atlas is composed of 7 members in the Lower Ktawa Fm and at least 4 sandstone packages in the overlying

Rouïd-Aïssa Fm. Based on the existing chitinozoan time constrains, each member of the Lower Ktawa Fm would correspond to an average of 1.6 Myr of deposition, and thus each member is assumed to record the MRS of one individual third-order relative sea level cycle, whereas the Rouïd-Aïssa deposits would be deposited during a long-lasting lowstand of ca. 1.5 to 3.5 Myr. Correlations along the studied transect was attempted to enable the reconstruction of a single relative sea level curve for the Central Anti-Atlas, westward from the Tagounite Trough. Hence, the RSL curve of the Ktawa Group is composed of 7 third-order regressive/transgressive cycles occurring prior to the Hirnantian glaciation. These cycles were correlated to the global relative sea level curve, which fits within an error window of less than 1 Ma and suggests that the deposition of the Ktawa Group was likely driven by allocyclic eustasy. Further correlations were conducted with geochemical proxies (i.e. $\delta^{18}O$ and $\delta^{13}C$), and to major glacially induced events such as the GICE, Kope, Waynesville, and Whitewater were recognized in the deposits of the Ktawa Group. Relative sea level changes inferred from deposits of nearby regions (e.g. Ougarta, Hoggar, Sardinia, and Armorican Massif) were correlated to those of the Ktawa Group, with relatively good agreement. Finally, correlations were attempted between the eastern Central to Oriental Anti-Atlas located eastward from the study region, which are separated by a mudstone-dominated trough in the region of Tagounite, the latter interrupting any lithostratigraphic correlation. In particular, in the Bou Ingarf region it is suggested that the Upper Tiouririne Fm is correlated to the Bou-Hajaj Mb, whereas the Rouïd-Aïssa Fm is expressed only discontinuously within the entire Anti-Atlas. The sea-level variations related to the entire Ktawa Group and Rouïd-Aïssa Fm are of an amplitude of several tens of meters, a magnitude that implies large volumes of water stored (and released) as ice-masses on the continent. The lateral variations in the expression of the different members within the Ktawa Group imply that the coastal morphology and/or autogenic processes greatly influenced the allogenic relative sea level variations due to growth and retreat of Late Ordovician ice masses.

References

Ainsaar, L., Kaljo, D., Martma, T., Meidla, T., Männik, P., Nõlvak, J. & Tinn, O. 2010. Middle and Upper Ordovician carbon isotope chemostratigraphy in Baltoscandia: a correlation standard and clues to environmental history. *Palaeogeography,*

Palaeoclimatology, Palaeoecology, 294**,** 189-201.

Albanesi, G. L., Barnes, C. R., Trotter, J. A., Williams, I. S. & Bergström, S. M. 2020. Comparative Lower-Middle Ordovician conodont oxygen isotope palaeothermometry of the Argentine Precordillera and Laurentian margins. *Palaeogeography, Palaeoclimatology, Palaeoecology,* 549**,** 109115.

Alley, R. B., Clark, P. U., Huybrechts, P. & Joughin, I. 2005. Ice-sheet and sea-level changes. *science,* 310**,** 456-460.

Bergström, S. M., Chen, X., Gutiérrez-Marco, J. C. & Dronov, A. 2009. The new chronostratigraphic classification of the Ordovician System and its relations to major regional series and stages and to δ13C chemostratigraphy. *Lethaia,* 42**,** 97-107.

Bergström, S. M., Schmitz, B., Saltzman, M. R. & Huff, W. D. 2010a. The Upper Ordovician Guttenberg δ13C excursion (GICE) in North America and Baltoscandia: Occurrence, chronostratigraphic significance, and paleoenvironmental relationships. *Geological Society of America Special Papers,* 466**,** 37-67.

Bergström, S. M., Young, S. & Schmitz, B. 2010b. Katian (Upper Ordovician) δ13C chemostratigraphy and sequence stratigraphy in the United States and Baltoscandia: a regional comparison. *Palaeogeography, Palaeoclimatology, Palaeoecology,* 296**,** 217-234.

Brenchley, P., Marshall, J., Carden, G., Robertson, D., Long, D., Meidla, T., Hints, L. & Anderson, T. 1994. Bathymetric and isotopic evidence for a short-lived Late Ordovician glaciation in a greenhouse period. *Geology,* 22**,** 295-298.

Buggisch, W., Joachimski, M. M., Lehnert, O., Bergström, S. M., Repetski, J. E. & Webers, G. F. 2010. Did intense volcanism trigger the first Late Ordovician icehouse? *Geology,* 38**,** 327-330.

Burkhard, M., Caritg, S., Helg, U., Robert-Charrue, C. & Soulaimani, A. 2006. Tectonics of the anti-atlas of Morocco. *Comptes Rendus Geoscience,* 338**,** 11-24.

Calner, M., Lehnert, O. & Nõlvak, J. 2010. Palaeokarst evidence for widespread regression and subaerial exposure in the middle Katian (Upper Ordovician) of Baltoscandia: significance for global climate. *Palaeogeography, Palaeoclimatology, Palaeoecology,* 296**,** 235-247.

Catuneanu, O., Abreu, V., Bhattacharya, J., Blum, M., Dalrymple, R., Eriksson, P., Fielding, C. R., Fisher, W., Galloway, W. & Gibling, M. 2009. Towards the standardization of sequence stratigraphy. *Earth-Science Reviews,* 92**,** 1-33.

Choubert, G., Destombes, J., Faure-Muret, A., Gauthier, H., Hindermeyer, J., Hollard, H. & Jouravsky, G. 1970. Carte géologique de l'Anti-Atlas central et de la zone synclinale de Ouarzazate: feuilles Ouarzazate-Alougoum et Telouet sud. *Notes et Mém. Serv. Géol. Maroc,* 138.

Choubert, G., Faure-Muret, A. & Destombes, J 1989. Carte géologique du Maroc, Zagora-Coude du Dra-Hamada du Dra (pp). Echelle 1/200 000. *Notes Mém. Serv. Mines Carte géol. Maroc*.

Clark, P. U. & Mix, A. C. 2002. Ice sheets and sea level of the Last Glacial Maximum. *Quaternary Science Reviews,* 21**,** 1-7.

Cocco, F., Loi, A., Funedda, A., Casini, L., Ghienne, J.-F., Pillola, G. L., Vidal, M., Meloni, M. A. & Oggiano, G. 2023. Ordovician tectonics of the South European Variscan Realm: new insights from Sardinia. *International Journal of Earth Sciences,* 112**,** 321-344.

Cocks, L. R. M. & Torsvik, T. H. 2021. Ordovician palaeogeography and climate change. *Gondwana Research,* 100**,** 53-72.

Dabard, M.-P., Guillocheau, F., Loi, A., Paris, F. & Ballèvre, M. 2009. Evolution de la plate-forme paléozoïque centre-armoricaine de l'Ordovicien au Dévonien. *12ème Congrès Français de Sédimentologie,* 65**,** 5-102.

Dabard, M.-P., Loi, A., Paris, F., Ghienne, J.-F., Pistis, M. & Vidal, M. 2015. Sea-level curve for the Middle to early Late Ordovician in the Armorican Massif (western France): Icehouse third-order glacio-eustatic cycles. *Palaeogeography,*

Palaeoclimatology, Palaeoecology, 436**,** 96-111.

Destombes, J. 1985. Lower palaeozoic rocks of Morocco. *Lower Palaeozoic of north-western and west-central Africa***,** 91-336.

Destombes, J. 2006a. Carte géologique u 1/200 00 de l'Anti-Atlas marocain, Plaéozoïque inférieur, Sommaire général sur les mémoires explicatifs. 149p.

Dietrich, P., Ghienne, J.-F., Lajeunesse, P., Normandeau, A., Deschamps, R. & Razin, P. 2019. Deglacial sequences and glacio-isostatic adjustment: Quaternary compared with Ordovician glaciations. *Geological Society, London, Special Publications,* 475**,** 149-179.

Elrick, M. 2022. Orbital-scale climate changes detected in Lower and Middle Ordovician cyclic limestones using oxygen isotopes of conodont apatite. *Palaeogeography, Palaeoclimatology, Palaeoecology,* 603**,** 111209.

Ennadifi, Y. 1971. Carte géologique des Plaines du Dra au sud de l'Anti-Atlas central. Agadir-Tissint-Oued Zemoul. 1: 200.000. *Notes Mém. Serv. Mines Carte géol. Maroc,* 219.

Ennih, N. Liégeois, J., 2001. The Moroccan Anti-Atlas: The West African craton passive margin with limited Pan-African activity. Implications for the northern limit of the craton. *Precambrian Research*, 112 (3-4): 289-302.

Finnegan, S., Bergmann, K., Eiler, J. M., Jones, D. S., Fike, D. A., Eisenman, I., Hughes, N. C., Tripati, A. K. & Fischer, W. W. 2011. The magnitude and duration of Late Ordovician–Early Silurian glaciation. *Science,* 331**,** 903-906.

Ghienne, J.-F., Desrochers, A., Vandenbroucke, T. R., Achab, A., Asselin, E., Dabard, M.-P., Farley, C., Loi, A., Paris, F. & Wickson, S. 2014. A Cenozoic-style scenario for the end-Ordovician glaciation. *Nature Communications,* 5**,** 4485.

Ghienne, J. F., Le Heron, D. P., Moreau, J., Denis, M. & Deynoux, M. 2007. The Late Ordovician glacial sedimentary system of the North Gondwana platform. *Glacial sedimentary processes and products***,** 295-319.

Haq, B. U. & Schutter, S. R. 2008. A chronology of Paleozoic sea-level changes. *Science,* 322**,** 64-68.

Hoepffner, C., Soulaimani, A. & Piqué, A. 2005. The moroccan hercynides. *Journal of African Earth Sciences,* 43**,** 144-165.

Holland, S. & Patzkowsky, M. 1998. Sequence stratigraphy and relative sea-level history of the Middle and Upper Ordovician of the Nashville Dome, Tennessee. *Journal of Sedimentary Research,* 68**,** 684-699.

Hollard, H., Choubert, G., Bronner, G., Marchand, J. & Sougy, J. 1985. Carte géologique du Maroc, scale 1: 1,000,000. *Serv. Carte géol. Maroc,* 260.

Le Heron, D. P. 2007. Late Ordovician glacial record of the Anti-Atlas, Morocco. *Sedimentary Geology,* 201**,** 93-110.

Loi, A., Cocco, F., Oggiano, G., Funedda, A., Vidal, M., Ferretti, A., Leone, F., Barca, S., Naitza, S. & Ghienne, J.-F. 2023. The Ordovician of Sardinia (Italy): from the 'Sardic Phase'to the end-Ordovician glaciation, palaeogeography and geodynamic context.

Loi, A., Ghienne, J.-F., Dabard, M.-P., Paris, F., Botquelen, A., Christ, N., Elaouad-Debbaj, Z., Gorini, A., Vidal, M. & Videt, B. 2010. The Late Ordovician glacio-eustatic record from a high-latitude storm-dominated shelf succession: The Bou Ingarf section (Anti-Atlas, Southern Morocco). *Palaeogeography, Palaeoclimatology, Palaeoecology,* 296**,** 332-358.

Männik, P., Lehnert, O., Nolvak, J. & Joachimski, M. M. 2021. Climate changes in the pre-Hirnantian Late Ordovician based on δ18Ophos studies from Estonia. *Palaeogeography, Palaeoclimatology, Palaeoecology,* 569**,** 110347.

Marante, A. 2008. *Architecture et dynamique des systèmes sédimentaires silico-clastiques sur la" plate-forme géante" nord-gondwanienne: l'Ordivicien moyen de l'Anti-Atlas marocain.* Bordeaux 3.

Meddour, A. 2016. *Les séries de l'Ordovicien moyen et supérieur de*

l'Anti-Atlas oriental (Maroc): stratigraphie, sédimentologie et paléogeographie des systèmes de plate-forme silico-clastique. Bordeaux 3.

Michard, A., Hœpffner, C., Soulaimani, A. & Baidder, L. 2008. The variscan belt. *Continental Evolution: The Geology of Morocco: Structure, Stratigraphy, and Tectonics of the Africa-Atlantic-Mediterranean Triple Junction.* Springer.

NASA/METI/AIST/Japan Spacesystems and U.S./Japan ASTER Science Team (2019). *ASTER Global Digital Elevation Model V003* [Data set]. NASA EOSDIS Land Processes Distributed Active Archive Center. https://doi.org/10.5067/ASTER/ASTGTM.003

Pique, A. & Michard, A. 1989. Moroccan Hercynides; a synopsis; the Paleozoic sedimentary and tectonic evolution at the northern margin of West Africa. *American Journal of science,* 289**,** 286-330.

Pohl, A., Donnadieu, Y., Le Hir, G., Buoncristiani, J.-F. & Vennin, E. 2014. Effect of the Ordovician paleogeography on the (in) stability of the climate. *Climate of the Past,* 10**,** 2053-2066.

Pohl, A., Donnadieu, Y., Le Hir, G., Ladant, J. B., Dumas, C., Alvarez-Solas, J. & Vandenbroucke, T. R. 2016. Glacial onset predated Late Ordovician climate cooling. *Paleoceanography,* 31**,** 800-821.

Rasmussen, C. M., Ullmann, C. V., Jakobsen, K. G., Lindskog, A., Hansen, J., Hansen, T., Eriksson, M. E., Dronov, A., Frei, R. & Korte, C. 2016. Onset of main Phanerozoic marine radiation sparked by emerging Mid Ordovician icehouse. *Scientific Reports,* 6**,** 18884.

Saltzman, M. R. & Young, S. A. 2005. Long-lived glaciation in the Late Ordovician? Isotopic and sequence-stratigraphic evidence from western Laurentia. *Geology,* 33**,** 109-112.

Shennan, I., Bradley, S., Milne, G., Brooks, A., Bassett, S. & Hamilton, S. 2006. Relative sea-level changes, glacial isostatic modelling and ice-sheet reconstructions from the British Isles since the Last Glacial Maximum. *Journal of Quaternary Science: Published for the Quaternary Research Association,* 21**,** 585-599.

Sømme, T. O., Helland-Hansen, W. & Granjeon, D. 2009. Impact of eustatic amplitude variations on shelf morphology, sediment dispersal, and sequence stratigraphic interpretation: Icehouse versus greenhouse systems. *Geology,* 37**,** 587-590.

Torsvik, T. H. & Cocks, L. R. M. 2013. Gondwana from top to base in space and time. *Gondwana Research,* 24**,** 999-1030.

Trotter, J. A., Williams, I. S., Barnes, C. R., Lécuyer, C. & Nicoll, R. S. 2008. Did cooling oceans trigger Ordovician biodiversification? Evidence from conodont thermometry. *Science,* 321**,** 550-554.

Turner, B. R., Armstrong, H. A. & Holt, P. 2011. Visions of ice sheets in the early Ordovician greenhouse world: Evidence from the Peninsula Formation, Cape Peninsula, South Africa. *Sedimentary Geology,* 236**,** 226-238.

Turner, B. R., Armstrong, H. A., Wilson, C. R. & Makhlouf, I. M. 2012. High frequency eustatic sea-level changes during the Middle to early Late Ordovician of southern Jordan: Indirect evidence for a Darriwilian Ice Age in Gondwana. *Sedimentary Geology,* 251**,** 34-48.

Van Wagoner, J. C., Posamentier, H. W., Mitchum, R. M., Vail, P. R., Sarg, J. F., Loutit, T. & Hardenbol, J. 1988. An overview of the fundamentals of sequence stratigraphy and key definitions.

Videt, B., Paris, F., Rubino, J.-L., Boumendjel, K., Dabard, M.-P., Loi, A., Ghienne, J.-F., Marante, A. & Gorini, A. 2010. Biostratigraphical calibration of third order Ordovician sequences on the northern Gondwana platform. *Palaeogeography, Palaeoclimatology, Palaeoecology,* 296**,** 359-375.

Webby, B. D., Cooper, R. A., Bergström, S. M. & Paris, F. 2004. Stratigraphic framework and time slices. *The great Ordovician biodiversification event.* Columbia University Press.

CHAPTER FIVE

Isostatic adjustment due to sediment loading of the Lower Ktawa Formation in the Anti-Atlas (Morocco)

Abstract

Sediment isostatic adjustment may be a fundamental autocyclic driver for the emplacement of large-scale shallow marine systems over long timescales (>10 Myr). Feedback processes between the progradation of a sediment lobe during a relative sea level lowstand and flexural response of the basement due to loading result in a seabed morphology that may dictate the location of the subsequent lobe. In particular deflection, i.e. the bending occurring at a distance laterally from the loading point, may create depressions and increased accommodation space.

Here, we take advantage of a large scale field outcrop, spreading over ca. 150 km lateral distance and recording ca. 10 Myr of shallow-marine offshore to river mouth deposition. The Lower Ktawa Fm in southern Morocco consists of seven lens-shaped sandstone bodies in an otherwise mudstone-dominated succession. These sandstone bodies spreading over 50 to 100 km laterally, referred to as members, are understood as prograding megalobes emplaced during lowstand periods. The shift in location betweensuccessive lobes suggests that feedback processes occur between the progradation of successive sediment megalobes. In that sense, the flexural response to the sediment loading by a megalobe is thought to create depressions on the seabed morphology laterally to a deposited lobe, which dictate the emplacement of the subsequent lobe.

This hypothesis was tested using a subsidence model based on 3D flexure of an infinite elastic layer, constant in thickness, using the Matlab code Flex3D. Seven sandstone members and sequences of the Lower Ktawa Fm were extrapolated in 3D based on the geological information and used as inputs for the model. The response in terms of seabed morphology was modelled for each subsequent member and confronted to the deposition of the subsequent lobe, in a step by step process of deposition and isostatic adjustment. The dimensions, timescale, and seabed response are all in agreement with an interpretation of the Lower Ktawa Fm as a large scale deposition zone with a South to North progradation of lobes in a flat shallow marine system. Interestingly, the depositional environments interpreted from the sediments in the field (i.e. sedimentary facies associations) are in good agreement with the seabed paleo-bathymetry from the subsidence models.

5.1. Introduction

The emplacement of sediment successions over extended periods is an intricate interplay between relative sea-level variations, sediment dynamics, and subsidence (Higgins, 2016, Milliman et al., 1989, Polanco et al., 2024, Steckler et al., 2022, Syvitski et al., 2022). On a shallow-marine passive margin, the areas where large-scale drainage networks deliver and deposit sediment (i.e. delta in a broad sense), represent active zones with complex relationships between sediment deposition, erosion, compaction and isostatic adjustment. The understanding of how and where successive sediment bodies are deposited thus remains a challenge.

Continental-scale drainage networks are stable geomorphologic features over 10s Myr (e.g. the Nile, Lena…). Such drainages deliver sediments in a basin over a radius that can extend over 100s km (Coleman et al., 1998, Maloney et al., 2018, Overeem et al., 2022). Modern deltas such as the Lena, Nile or Ganges-Brahmaputra have a subaerial extent of 100s of km and some ancient deltaic systems may have reached up to 1.6 million km² (Klausen et al., 2019, Lin and Bhattacharya, 2021). However, the subaqueous part of a deltaic system may develop over a much larger area (Patruno and Helland-Hansen, 2018, Proust et al., 2018). Once sediment is delivered on a delta, a variety of processes contribute to its spreading, such as wave reworking, tidal currents, turbidity currents, and longshore currents (Hampson, 2010, Hampson and Premwichein, 2017, Mitchell et al., 2012). The monitoring of modern coastlines in the Holocene (i.e. in the context of a deglacial sea level rise) has contributed to understand the processes of sediment emplacement and redistribution over short timescale (<10 kyr). However, a long term perspective (>10 Myr) on the processes of lobe construction and shift is lacking, and can best be accessed through combining data from ancient successions with numerical models.

To fill this gap, numerical modelling of subsidence was applied to an extensive field dataset of sediment log profiles collected from the Lower Ktawa Fm (Early Late Ordovician, i.e. ca. 460 to 449 Ma) in southern Morocco. The dataset was acquired over a continuous exposure of ca. 150 km in length and covers a thickness of up to ca. 180 m of sediment that represents ca. 10 Myr time with chronostratigraphic tiepoints. The Ktawa deposits feature shallow marine environments characterized by very flat geometries with laterally limited sand-sheet packages protruding from offshore

mudstone successions (Chapter 2). The continuous exposures provide a unique opportunity to observe the lateral evolution of these sand-sheets over 10s to 100s km. These exposures offer a valuable insight into pseudo-3D perspectives and extended time scales, enabling a deeper understanding of their depositional processes. In particular, it will be highlighted how sediment isostatic adjustment constitute an autocyclic driver of the localization of sediment bodies. Indeed, feedback effects between sediment loading, the response in sediment isostatic adjustment, and resulting lateral deflection are thought to drive the creation and location of accommodation space and emplacement of subsequent sedimentary successions over long timescales.

5.2. Geological setting

5.2.1 The Lower Ktawa Formation

The Anti-Atlas mountain range (southern Morocco) during Ordovician time was part of the northern passive margin of the supercontinent Gondwana and northern rim of the Tindouf Basin (Cocks and Torsvik, 2021, Michard et al., 2008). The Anti-Atlas exposes up to 10 km of sedimentary successions since the PreCambrian, with PreCambrian to Ordovician deposits cumulating a thickness of ca. 5,5 km (Fig. 5.1A, Destombes, 1985). The studied Lower Ktawa Fm (mid-Sandbian to mid-Katian, Chapter 2, Álvaro et al., 2022, Loi et al., 2010) is part of the Ktawa Group, overlying ca. 500 m of sandstone-dominated sediments of the First Bani Group (Middle to Late Ordovician, Marante, 2008). In the studied region, the Lower Ktawa Fm consists of ca. 200 m of mudstone and sandstone alternations (Fig. 5.1B). Seven prominent lensed-shaped sandstone-dominated units of ca. 10 to 40 m in thickness and 10s to more than 100 km in length, were defined as "members" (Chapter 2). Thickening upward successions, from mudstones to sandstones, represent deposition during periods of relative sea level fall and seaward progradation of sediment masses. The lowstand interval is recorded by the sandstone members, whereas only minor deposits were left during the retrogradation of the coastline during sea level rise. Each cycle of mudstone to sandstone to mudstone thus records a cycle of fluctuation of the relative sea level (RSL). Each cycle was calibrated in time to a duration of ca. 1 to 2 Myr, and thus represent 3rd order RSL cycles (Chapter 4).

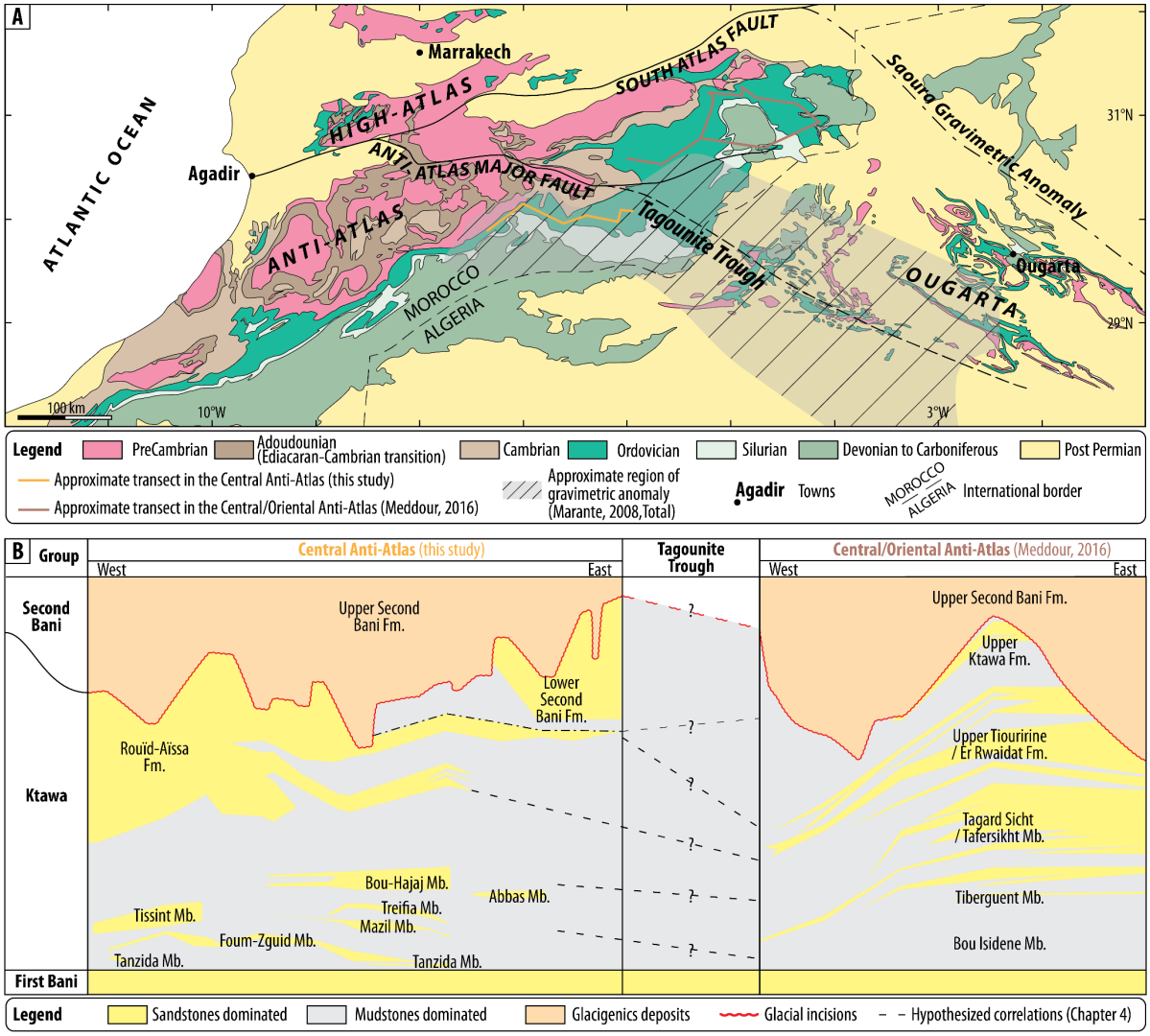

***Figure 5.1**: Context and location of the Lower Ktawa Formation in the Anti-Atlas, South Morocco. (A) Simplified geological map of South Morocco and West Algeria highlighting major features (modified from Ghienne et al., 2007, Hollard et al., 1985, Ennih et Liegeois, 2001, Marante, 2008 and Total). (B) Correlations of sandstone- and mudstone-dominated regions across the Anti-Atlas. The Tagounite trough dominated by mudstones is separating the western Central to the eastern Central/Oriental Anti-Atlas, not enabling lithostratigraphic correlations between the two regions. Central/Oriental Anti-Atlas modified after Meddour, 2016. All members highlighted belong to the Lower Ktawa Fm.*

5.2.2 The Tagounite trough

The Lower Ktawa Fm is exposed along the Jbel Bani cliff, which spreads roughly West to East over more than 500 km in length. Within the western Central part of the Anti-Atlas (Tissint-Zagora region), the Lower Ktawa evolves from sandstone rich to mudstone-dominated from West to East (Fig. 5.1B, Chapter 2). In the Oriental Anti-Atlas (ca. 250 km North-Eastward) however, the trend is a depletion in sandstone from East to West (Meddour, 2016). In between, in the region of Tagounite, a mudstone-dominated area is dominated by offshore

mudstone deposits (Fig. 5.1). This so-called "Tagounite trough" may be perceived as a depocenter for the Lower Ktawa Fm (Destombes, 1985). Furthermore, the Tagounite trough makes a discontinuity in the physical lithostratigraphic correlations of sandstone members on each side of this region, and thus original nomenclatures by Destombes (1985) made the distinction in members composing the Lower Ktawa Fm between the western Central and eastern Central to Oriental Anti-Atlas.

Interestingly, the Tagounite trough is located at the confluence or continuity of major tectonic features (Fig. 5.1A). It sits in the northwestern continuity of the Ougarta Range, of Cambrian-Ordovician age. Moreover, it is established at the South-East end of the Anti-Atlas Major Fault, a major fault that was active at least during the Variscan orogeny (Hoepffner et al., 2005, Pique and Michard, 1989). Additionally, the Tagounite trough is located at a high gravimetric anomaly zone (Marante, 2008, Total) and a few 100 of kms South of the gravimetric anomaly of Saoura (Ennih and Liégeois, 2001). Finally, the limit of the West African Craton (WAC) run to the North alongside the Anti-Atlas and plunges southeastward roughly along the Tagounite trough and Ougarta Range. Thus, more than a simple depocenter, the Tagounite trough may correlate with a major tectonic limit for the entire North-West African region.

5.2.3. Orientation of the system

Within the western Central Anti-Atlas, successive sandstone members stack on each other with a seemingly eastward progradation direction that ends in the offshore mudstones of the Tagounite trough (Fig. 5.1B). Mirroring this trend, in the eastern Central/Oriental Anti-Atlas, proximal shoreface deposits are evolving toward more distal sediment signatures to the West (Meddour, 2016). This might suggest that the proximal to distal polarization points from East to West toward the Tagounite trough. Such a scenario could mean that the Tagounite trough represents a depocenter, with the Central and Oriental Anti-Atlas being two conjugated shorelines facing each other (Fig. 5.2A).

Another view can be put forward: the sandstone-dominated parts of the Lower Ktawa Fm in the Central and Oriental Anti-Atlas may correspond to two separated zones of sediment delivery, however both prograding to the North (Fig. 5.2B). In that sense, the perceived Tagounite trough would not represent a sink and depocenter of sediments, but rather a zone with limited sediment delivery. In order to settle on the geological meaning of the Tagounite

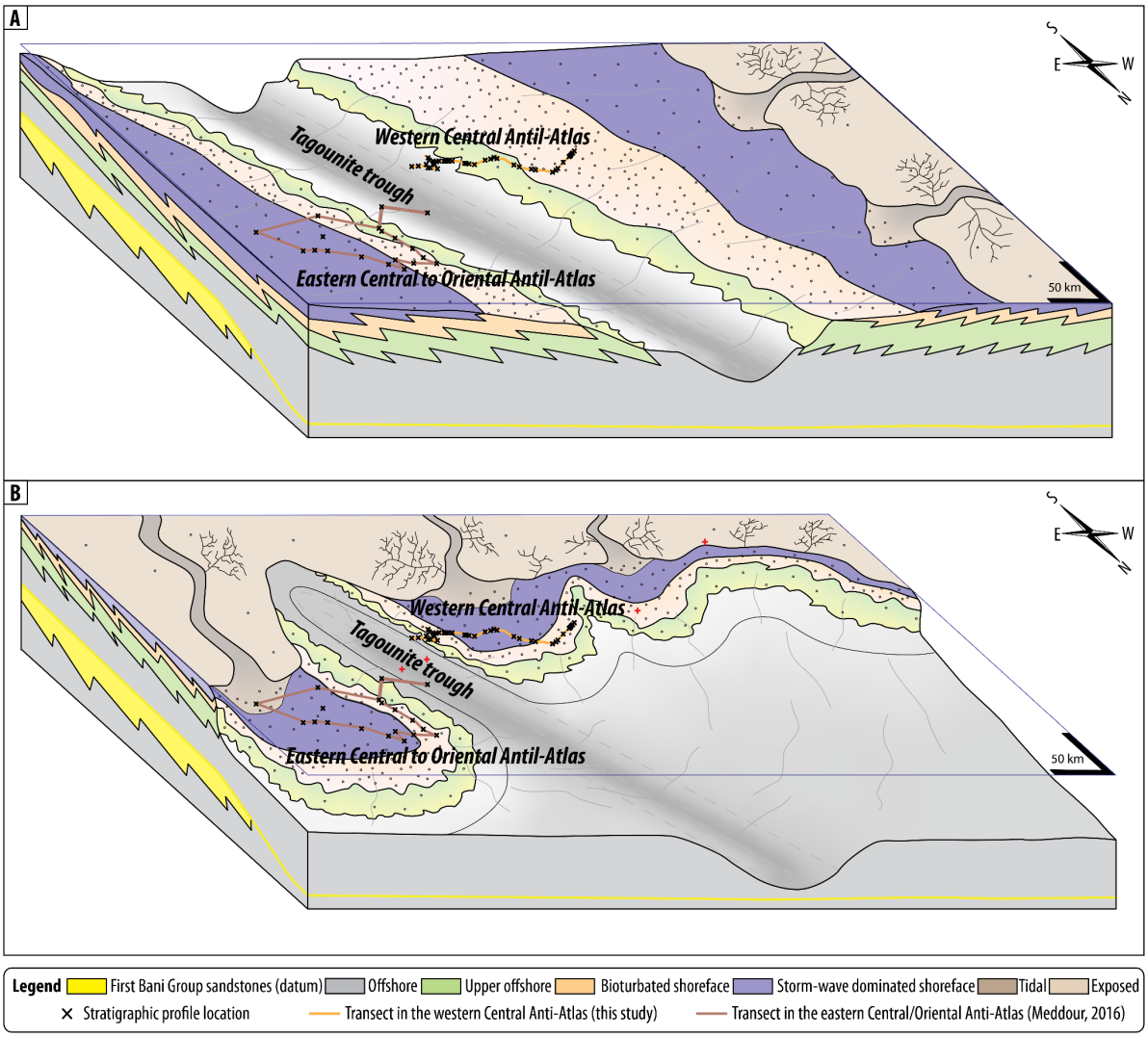

***Figure 5.2**: 3D reconstructions of the hypothesized proximal-to-distal trend recorded in the Anti-Atlas. (A) Conjugated shorelines facing each other, prograding toward the Tagounite trough. (B) Megalobe geometries prograding toward the North where limited sediment is delivered to the Tagounite trough.*

trough, insights must however be found within the Central and Oriental Anti-Atlas abutting the trough, as the latter offers no clear exposures of markers.

5.2.4. Paleo-markers for the orientation of progradation

The proximal-to-distal polarization in the western Central Anti-Atlas has been estimated to be roughly South to North for the Lower Ktawa Formation (Chapter 2), an orientation similar to what has been

***Figure 5.3**: Semi-3D transect of the study area with simplified depositional environments, detailed in Chapter 2. The figure is oriented E-W in order to match the orientation of the Jbel Bani cliff outcrop that faces North. The base line follows the 2D path of the Jbel Bani cliff with logs pointing up vertically, which represents the basement for flexural models.*

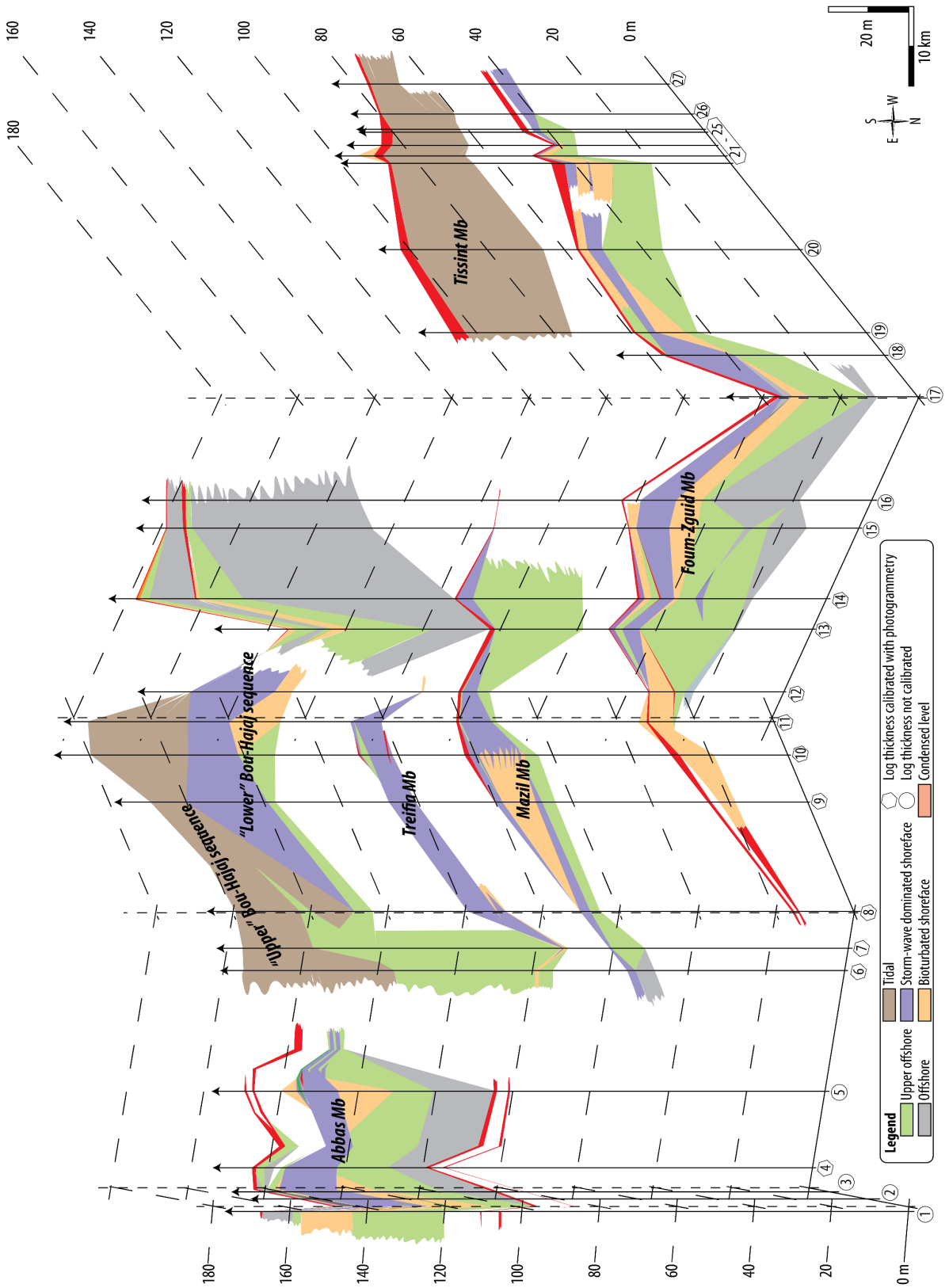

interpreted for the underlying First Bani Group (Marante, 2008). Several arguments are put forward for a S-N orientation. There is an apparent W-E symmetry observed in the thicknesses and distribution of sediment facies associations recorded in the investigated region (Figs 5.3 and 5.4, see Chapter 2). Additionally, the apparent

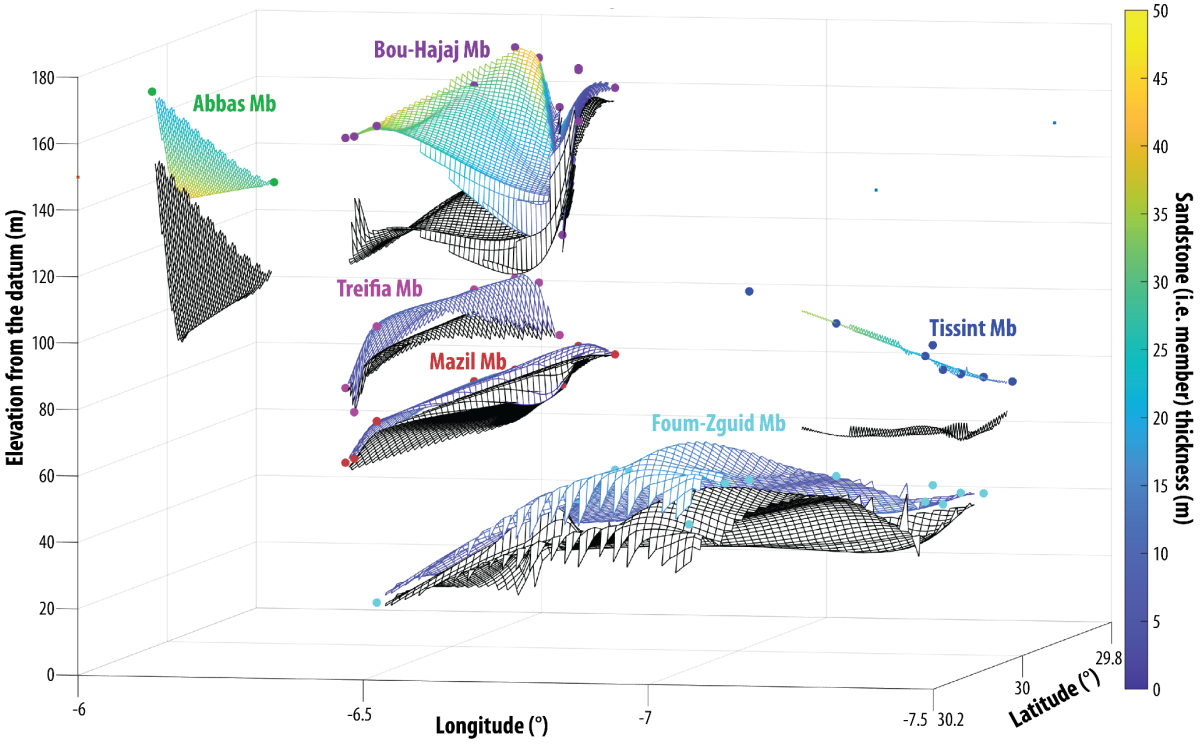

***Figure 5.4**: 3D model of members thicknesses. The black surfaces represent the base of the sandstone-dominated part of each member. The colored surfaces reflect the thicknesses in sandstones of each member. Coloured dots represent the top of each member for each stratigraphic profile. Cubic interpolation was used to model the surface.*

orientation of cross-bedding was measured from 2D outcrops along the transect for each sequence (Fig. 5.5). The orientation of cross-bedding, thought to be a proxy for the orientation of paleocurrents depict a scattered SW to NE pattern. Finally, the apparent flatness of sandstone members on the W-E transect -slopes are estimated at 1 m / km- would result in extremely low slope for a W to E progradation (Figs 5.3 and 5.4). On the S-N oriented exposures however, trends are rather toward a northward deepening (e.g. Foum-Zguid Member, Fig. 5.3). Such geometries thus suggest that the transect cuts perpendicular to the progradation direction, which would have an approximate S-N orientation (Fig. 5.2B).

Thus, one can envision that the successive members within the Lower Ktawa Fm were deposited as megalobe prograding toward the North (+/- 45°, Fig. 5.2B). In such a setting, the shoreline would have a ca. W-E to WNW-ESE strike, and both sandstone-dominated zones in the Central and Oriental Anti-Atlas would correspond to large scale depocenters fed by two drainage systems. Here, the hypothesis investigated isthat the Lower Ktawa Fm within the Central Anti-Atlas was deposited as large-scale megalobe structures prograding toward the North.

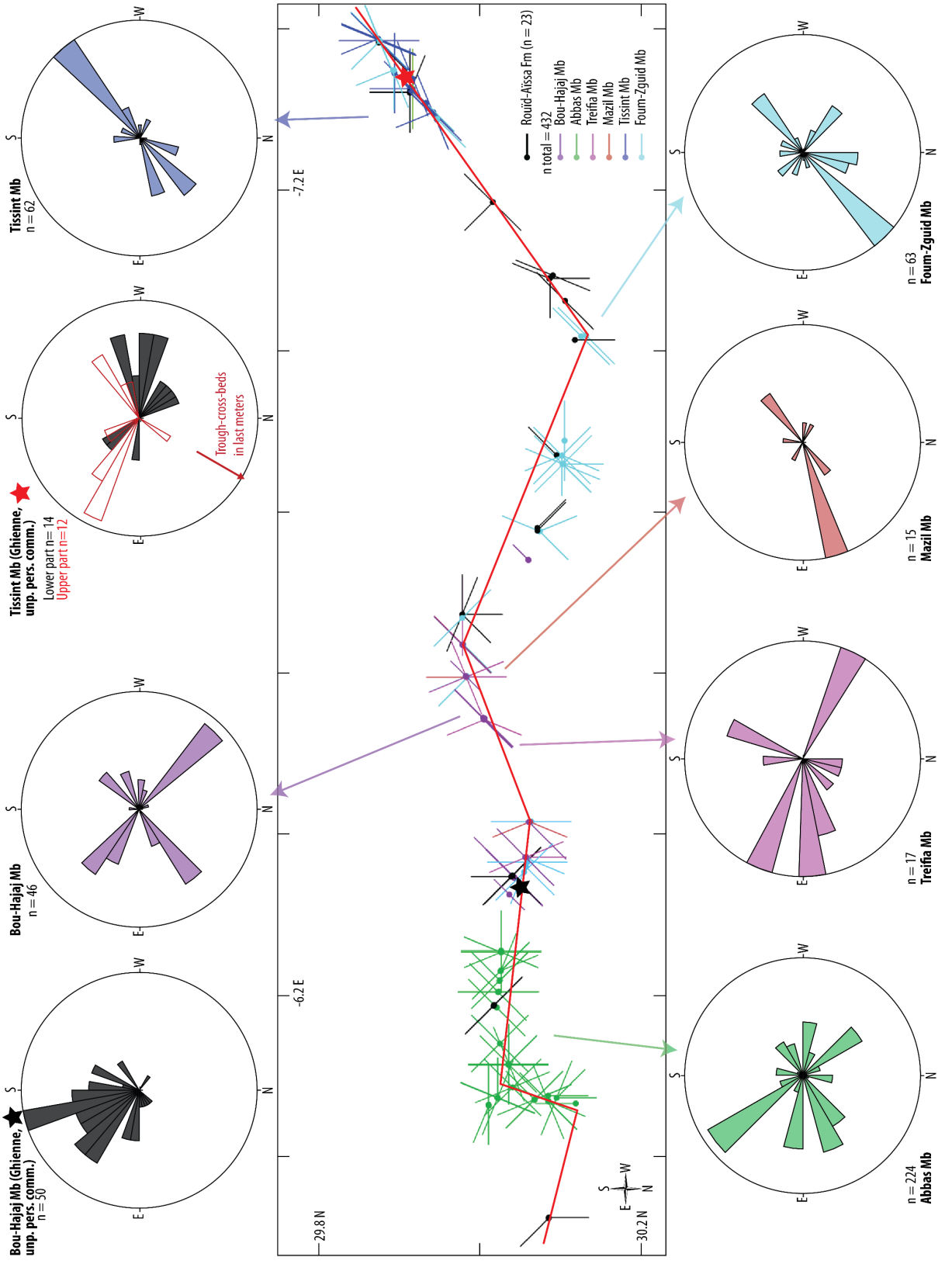

***Figure 5.5**: Paleocurrents measured along 2D outcrops for each sequence. Black paleocurrents modified from Ghienne (unpublished pers. comm.).*

Megalobe shapes were extrapolated from the semi-3D outcrop information, in order to feed a model of subsidence. It is then tested whether sedimentary isostatic

adjustment is capable of explaining the field observation, and discussed how such autocyclic processes may be important drivers in the location of sedimentary bodies on shallow-marine passive margins.

5.3. Methods

5.3.1. Geological dataset

The dataset consists of 27 stratigraphic profiles extracted from a larger database of 42 sections logged in the field along a roughly West-East semi-3D transect ca. 150 km long (Fig. 5.3 and Chapter 2). Seventeen of these profiles were calibrated in thickness by 3D photogrammetry reconstructions. Lateral lithostratigraphic correlation of members between the logs was conducted along the transect through satellite and drone images.

A unit or member is taken as starting at the top of the underlying sandstone beds and up to the top of its according sandstone unit. This choice does thus approximately deposit a unit up to its maximum progradation state, i.e. at the onset of flooding or transgression, before starting the subsequent unit. In practice, a few meters of sediments with a fining upward trend are found above the sandstone tops, and represent deposition during the retrogradation phase, yet this represents a minimal part of an entire sequence. Each member is thus embedded in a sequence of transgression-regression, i.e. a cycle of retrogradation to progradation. Each member is deposited one after the other from the lowermost unit to the uppermost in this order: 1. Foum-Zguid, 2. Tissint, 3. Mazil, 4. Treifia, 5. “lower” Bou-Hajaj and Abbas are contemporaneous, and finally 6. “upper” Bou-Hajaj (Fig. 5.6). The 5 first deposition phases were interpreted as related to 3rd order sequences of a duration of an average of 1.7 Myr, whereas the last “upper” Bou-Hajaj unit is a sudden drop in sea level that may occur out of cycle (Chapter 4).

5.3.2. Extrapolation of lobe shapes in 3D

Megalobes shapes in 3D were extracted from the dataset that is dominantly oriented along the W-E semi-3D transect (Fig. 5.3). A grid of 600x600 km was created centered around the field transect. Moreover, 250 km are added around this grid to avoid boundary effect. The main constraint during extrapolation to megalobe shapes was the thickness of each member on each stratigraphic profile. Isopach contours were drawn by hand in order to fit the thickness recorded at each stratigraphic profile and follow a northward progradation direction (Fig. 5.6). This

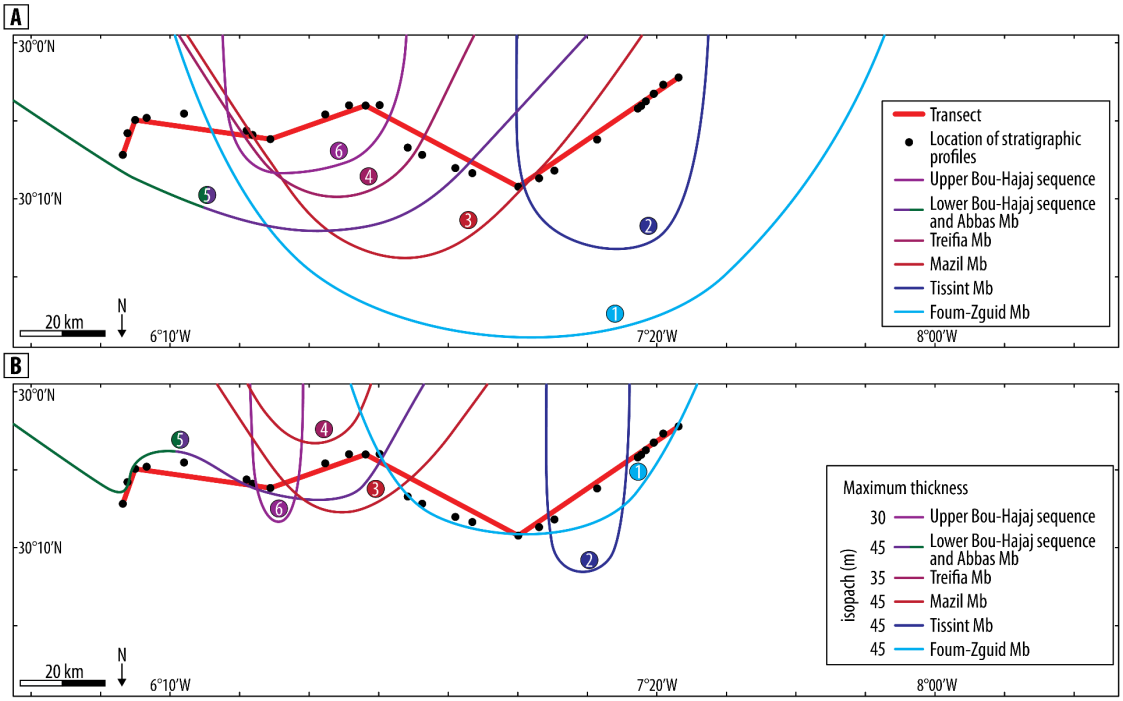

***Figure 5.6**: Megalobe shapes and channel-complexes extrapolated from thicknesses of each member. (A) Maximum extension of megalobes (i.e. isopach of 0 m). (B) Maximum thickness of megalobes.*

South-to-North progradation direction is solely interpreted from the aforementioned geological data and not constrained by data. Each megalobe was started from the southern end of the grid at its maximum thickness

The South-North length of each megalobe was set at ca. 250 km, with the northward prograding nose crossing the transect and a southward artificial end located 200 km from the grid boundary (Fig. 5.6). The maximum thickness of each member was computed as the maximum thickness recorded along the stratigraphic profile. Southward from the transect, the thickness was set stable at the maximum recorded thickness. Finally, the "gridfit" code from D'Errico (2006) was used to create a mesh grid of thicknesses at a step of 5 km on both lateral axes.

When an asymmetry in thickness of deposits was observed in the dataset, it was taken into account in the 3D extrapolation, resulting in asymmetric megalobe shapes (e.g. for the Mazil Mb and Abbas/lower Bou-Hajaj sequences). Two members have been interpreted as tidal to riverine channel complexes with an erosive base, and they have been modelled as straight South-North "channel-complex" shapes (Fig. 5.6).

5.3.3. Subsidence model

The Matlab code Flex3D developed by Cardozo (2009) was used to quantify the

isostatic flexure caused by sediment loading. This code was designed to model the deflection of a thin elastic infinite plate. Of particular interest here, Flex3D takes into account the bending occurring laterally to a load, i.e. it is not a 1D Airy load model. In 3D, the bending of the plate depends on the elastic properties of the lithosphere where the general equation is expressed as (Krauthammer and Ventsel, 2001):

$$D\nabla^2\nabla w + 2\frac{\partial D}{\partial x}\frac{\partial}{\partial x}(\nabla^2 w) + 2\frac{\partial D}{\partial y}\frac{\partial}{\partial y}(\nabla^2 w) + \nabla^2 D(\nabla^2 w) - (1-\nu)\left(\frac{\partial^2 D}{\partial x^2}\frac{\partial^2 w}{\partial y^2} - 2\frac{\partial^2 D}{\partial x \partial y}\frac{\partial^2 w}{\partial x \partial y} + \frac{\partial^2 D}{\partial y^2}\frac{\partial^2 w}{\partial x^2}\right) + \Delta\rho g w = p \quad \text{Eq. 5.1}$$

where w is the deflection of the plate (vertical displacement), $\Delta\rho$ is the density difference between the load and the underlying layer, g is the gravity acceleration, and p is the load. D is the flexural gravity re-defined by Turcotte, and Schubert (2002) as:

$$D = \frac{{T_e}^3 E}{12 * (1-\nu^2)} \quad \text{Eq. 5.2}$$

where E is the Young's Modulus, ν is the Poisson's ratio, and T_e the elastic thickness. In Flex3D, a finite differences method is used to solve Equation 1 numerically.

5.3.4. Input Parameters

Flex3D is used to model the isostasic adjustment due to a local sedimentary load on a flat and horizontal underlying unit, hereafter "the basement". The input parameters for the model consist of a characterisation regarding the load: the thicknesses of the members and their density, as well as values for the underlying basement: the elastic thickness, Poisson's ratio, Young's modulus. A density for the filling of depressions (up to 0 m a.s.l.) completes the parameters, and was taken at 1000 for water. Relative sea level variations are not modelled here.

Parameters have been chosen to reflect the conditions during deposition of the Lower Ktawa Fm (Table 5.1). In that sense, the density of the load was taken as 2400 kg/m3, i.e. a value for sandstone. We justify this value by the fact that the deposition of one sequence represents 1 to 2 Myr and thus the sand is at least well compacted with the remaining pores likely filled with water. Here, the load is notably defined by a single density. A single density likely oversees the variety of facies associations, from mudstones to coarse-

***Table 5.1**: Input parameters*

Parameters	Value
Elastic thickness T_e (km)	7000
Young's Modulus E (GPa)	34.9
Poisson's ratio ν	0.2
Gravity g (m.s^{-2})	9.8
Density of underlying layer (kg.m^{-3})	2700 (quartzified sandstone)
Density of the load (kg.m^{-3})	2400 (sandstone)
Density of the material filling the depression (kg.m^{-3})	1000 (water)

grained sandstones and their respective thicknesses within a sequence. However, density differences between mudstones and sandstones are considered here negligible in regard to the density differences between no-load, water, or sediment. Additionally, each sequence is deposited in the model at once, so that no time-dependent density, depending on the emplacement state is needed.

The basement was considered as in a more compacted or lithified state than the deposited lobes and its density correspond to the heavy range of sandstones (2700 kg/m3), in order to reflect the underlying package made of the thick (ca. 500 m), sandstone-dominated First Bani Group. The elastic thickness of the basement was chosen in the range of sandstone as presented in Reynolds et al. (1991). The elastic thickness is the key parameter for deflection. It defines the flexural rigidity, i.e. how the effect of a load will be spread and bend laterally the underlying basement. Moreover, the Poisson's ratio and Young's Modulus have been set up to medium values for sandstone. This choice was justified by multiple preliminary tests conducted with Young's modulus ranging from 30 to 70 GPa and Poisson's ratio between 0.15 and 0.3, which changed the maximum downward displacement by a few meters to less than 10 m. The chosen parameters were taken to result in a seabed after isostatic adjustment below 0 m a.s.l. for the 1st megalobe (i.e. Foum-Zguid).

5.4. Results

The initial configuration considers the top of the sandstones of the First Bani Group as a flat horizontal layer at sea level, hereafter "the basement". This choice is justified by the field observations of the according sediments that correspond to proximal, shallow marine, shoreface to tidal deposits. Each member is then loaded one after the other, on top of each other, starting from the flat layer of the First Bani sandstones.

Five deposition phases are modelled, corresponding to the different members identified in the field (Chapter 4), from base to top: Foum-Zguid, Tissint, Mazil, Treifia, "lower" Bou-Hajaj with Abbas, and "upper" Bou-Hajaj. Of interest here is the evolution of the downward displacement of the basement and the paleo-bathymetry (i.e. sea bed) resulting after deposition and isostatic adjustment of each megalobe. Furthermore, comparison with the emplacement of the overlying megalobe is investigated to understand whether there is a causal connection between the accommodation space created by the underlying megalobe and the location of the overlying megalobe. Hereafter, each megalobe (and channel-complex) is investigated in order of deposition.

Foum-Zguid Member

The Foum-Zguid Mb and underlying silt-dominated sediments are the first sedimentary load to be deposited on top of the First Bani Group. Its lateral extension is from log 6 to hypothetically several kilometres further West from the end of the investigated transect (Figs 5.6 and 5.7). The sequence embedding the Foum-Zguid Mb has a maximum thickness to 59 m (logs 15-16 and 19-20) of deposits above the datum and it thins and faints out toward both the West (27 m at log 27) and East (12 m at log 8, Fig. 5.3). Interestingly, the member also thins to the North (44.5 m at log 17). Finally, measured paleocurrents show a main SW to NE direction (Fig. 5). The extrapolated lobe is symmetrical with the axial S-N symmetry being localized at log 17 (Fig. 5.7A).

The maximum subsidence (sensus vertical sinking) reaches ca. -80 m and is located below the maximum load at ca. 115 km (Fig. 5.7C). Small forebulges of the First Bani top can be observed at ca. 15 and 200 km. The sea bed after deposition and isostatic adjustment of the Foum-Zguid Mb exhibits an undulating shape, with a high at the centre of the lobe, where it is the thickest and two depressions due to lateral deflection to the East (-17 m at 70 km) and West (-23 m at 150 km) of the high (Fig.5. 7C and D). Interestingly, the following deposited Tissint Mb is roughly lodged within the west-side depression caused by the deflection of the Foum-Zguid Mb (Figs 5.7B and 5.8).

Tissint Member

The Tissint sandstones are the second sedimentary load to be deposited. It is centered around the depression created by the deflection of the underlying Foum-Zguid Mb at ca. 150 km (Fig. 8).

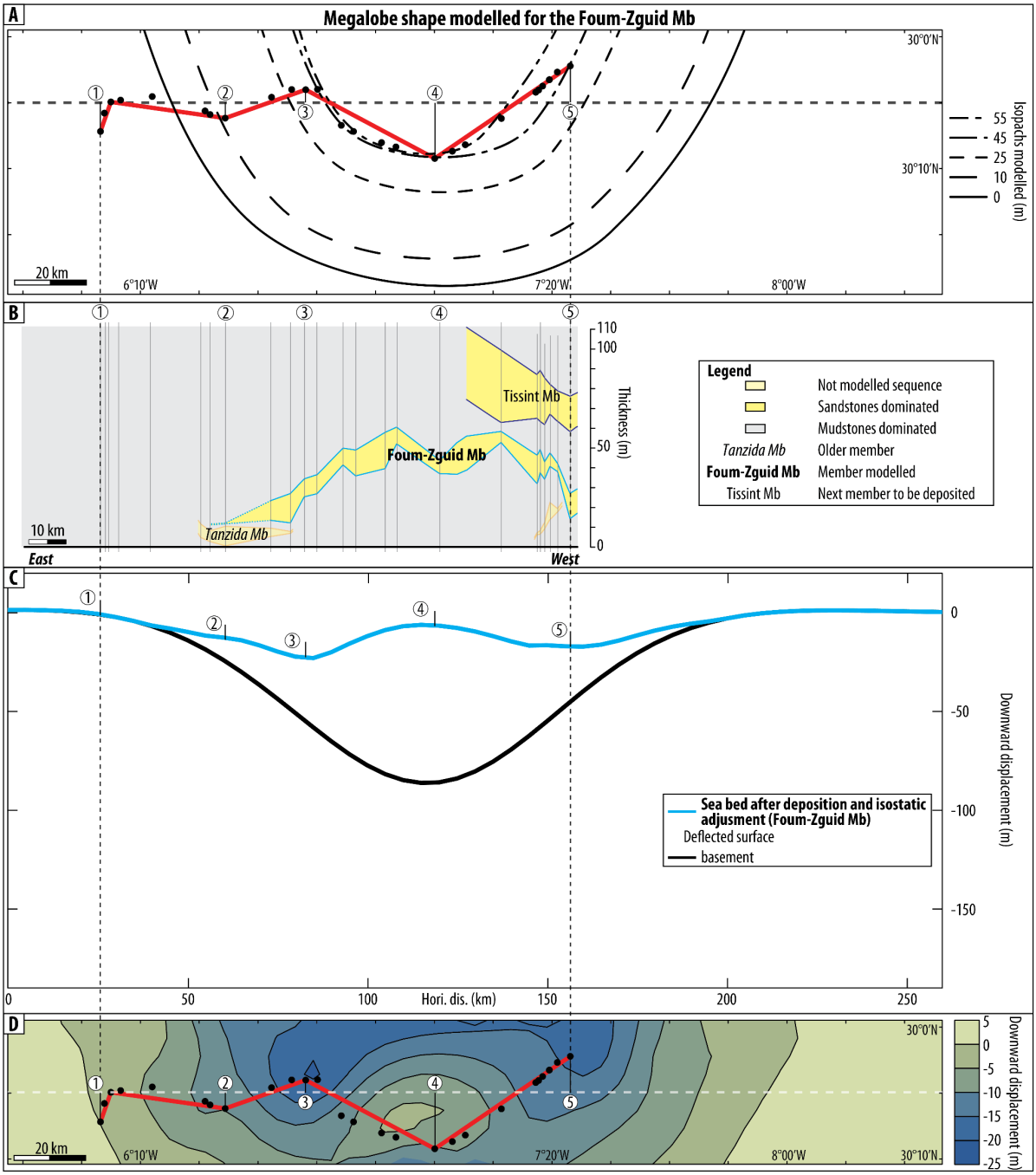

***Figure 5.7**: Extrapolation and isostatic adjustment after deposition of the Foum-Zguid Mb. (A) Detailed isopachs of the megalobe extrapolated, used as input for the model. (B) 2D transect of the sandstone-dominated part of the modelled member, and overlying member. (C) Cross-section of the deflection of the basement and sea bed after deposition and isostatic adjustment of the modelled sequence. Dashed line in (A) and (D). (D) Planar view of the 3D seabed model of the sequence after isostatic adjustment.*

This member is constricted to the West of the study area, located between logs 19 and hypothetically a few kilometers further West from the end of the transect (Figs 5.6 and 5.8). The member has a maximum thickness of 57 m above the top of the Foum-Zguid Mb (log 19) that abruptly thins to 0 m (log 18) just 3 km

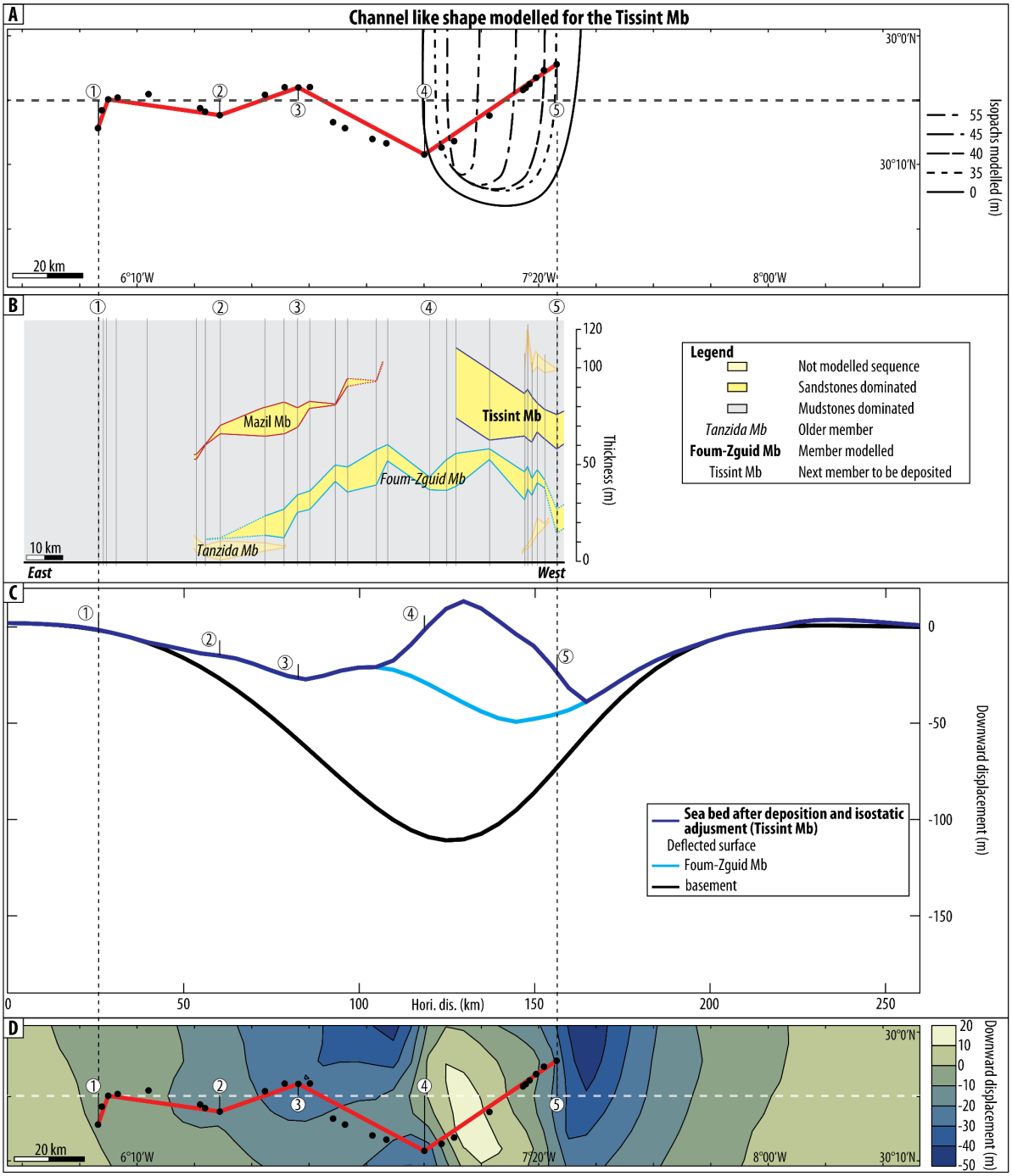

***Figure 5.8**: Extrapolation and isostatic adjustment after deposition of the Tissint Mb. For caption, see Fig 5.7.*

toward the NE (Fig. 5.3). The Tissint Mb thins toward the SW to ca. 35 m (log 19 to 26). Hence, this member is highly asymmetric. Paleocurrents from trough-cross-beds and tidal deposits show a SW-NE orientation, although it be biased by the orientation of this part of the studied transect (Fig. 5.5). Paleocurrents measured by Ghienne (unpublished pers. comm.) of the Tissint Mb (close to the Tissint locality) show a similar trend for trough-cross-beds in the last meters of the member.

Orientations of underlying sedimentary structures demonstrate a direction toward the West. The 3D shape was extrapolated to resemble an asymmetric tidal channel complex (Fig. 5.8A).

The downward displacement due to the deposition of the Tissint Mb is adding ca. 30 m to the subsidence already created by the deposition of the Foum-Zguid Mb (Fig. 5.8C). The total maximum downward displacement is ca. -110 m after deposition of both the Foum-Zguid and Tissint megalobes at ca. 125 km, and is shifted by ca. 10 km toward the W in comparison to the previous member (Fig. 5.8B).

Interestingly, the maximum height of the Tissint surface, located at ca. 130 km, reaches ca. + 13 m a.s.l., coherent with the sedimentary field data that depict shallow-water, tidal deposits for this member (Figs 5.3 and 5.8C and D). After adjustment, two troughs located East and West from the Tissint Mb are present. The accommodation space created by the deposition of the Foum-Zguid sequence at ca. 70 km remains, and seem to coincide with the location of the third member to be deposited, the Mazil Mb (Figs 5.8B and 5.9).

Mazil Member

The Mazil Member was constrained between logs 6 and 15 (Figs 5.6 and 5.9). The sandstone part of this member is located in the eastern sea bed depression resulting from the emplacement of the Foum-Zguid and Tissint Mbs (between 50 and 120 km on the modelled transect, Figs 5.7C and 5.8C). The sequence is the thickest between logs 6 to 11 (ca. 56 to 46 m resp., Figs 5.3 and 5.9A). To the West, the member is deposited on the flank of the Foum-Zguid Mb, and thins down to 35 m on log 15. To the East, the Mazil Mb is poorly constrained. This is due to a lack of exposure between logs 6 and 5, and to the absence of a marker of this member farther eastward in the succession dominated by mudstones below the Abbas Mb. It is thus likely that this member has an important lateral continuation as a mudstone-dominated sequence on the eastern part of the transect but no data constrain is available. In the absence of data, the megalobe shape extrapolated from available thicknesses shows an artifact with an asymmetry, i.e. a steep thinning to the East and gentle slope to the West. Paleocurrents show a main direction toward the ENE (Fig. 5.5).

The maximum of the downward displacement of the basement has been shifted by 15 km toward the East and reaches ca. - 140 m, i.e. 20 m deeper than

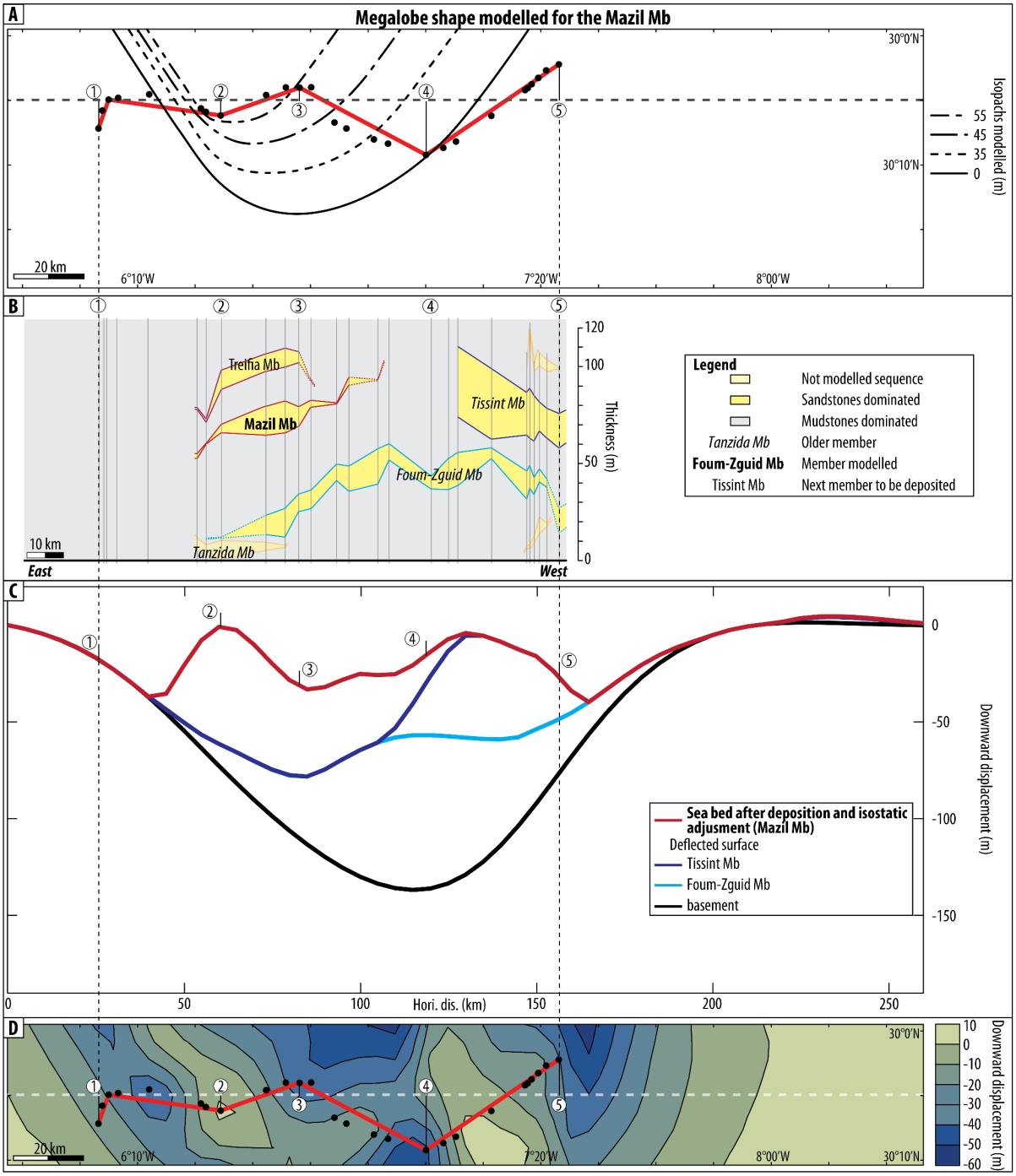

***Figure 5.9**: Extrapolation and isostatic adjustment after deposition of the Mazil Mb. For caption, see Fig 5.7.*

after deposition of the Tissint Mb (Fig. 5.9C).

The sea bed after isostatic adjustment of the Mazil sequence shows a paleo-high at ca. 60 km (Fig. 5.9C and D). This feature is likely an artifact due to the prompt thinning to the East that was artificially extrapolated in the lobe shape due to the lack of data, yet it likely oversees mudstone deposits that may reach almost 40 m in thickness. The forthcoming Treifia

Mb to be deposited is emplaced above the paleo-high created during sedimentation and adjustment of the Mazil sequence (Figs 5.9B and 10).

Treifia Member

The Treifia Member is exposed between logs 6 and 12 (Figs 5.6 and 5.10). It has a constant thickness thickness of ca. 28 m over ca. 20 km (logs 8 to 11) and thins rapidly toward the E and W to 12 m at its extremities (i.e. logs 6, 7 and 12, Figs 5.3 and 5.10A). The exposed sandstone part of the Treifia Mb is deposited above the paleo-high created by deposition of previous members at ca. 60 km (Fig. 5.10). Paleocurrents are oriented ESE-WNW, which could denote the eastern and western side of the megalobe shape (Fig. 5.5). A slight asymmetry of the megalobe shape has been extrapolated following the available thickness data (Fig. 5.10A), which could also be an artifact from available data as for the Mazil Mb. The east side is slightly steeper than the west side, as the Mazil megalobe. The Treifia sedimentary load is deposited above the sea bed high created by deposition of the Mazil Mb and previous members.

The deflection of the basement becomes wider toward the east where the maximum is still located at ca. 115 km for ca. - 140 m deep with an asymmetric shape, i.e. steeper on its west side (Fig. 5.10C).

The sea bed modelled of Treifia is located at a maximum of ca. + 3 m above sea level at ca. 60 km (Fig. 5.10C and D). The accommodation space created by the Foum-Zguid Mb at ca. 70 km, which was partly filled by the deposition of the Mazil Mb and subsided, has been continuously filled until the deposition of the Treifia sequence. The “lower” Bou-Hajaj sequence and Abbas Mb are the fifth sequence to be extrapolated as one megalobe with two advances, which are deposited on top of the paleo-high at ca. 60 km (“lower” Bou-Hajaj part) and on the eastern flank of the datum depression at ca. 20 km (Abbas part, Figs 5.10B and 5.11).

“Lower” Bou-Hajaj sequence and Abbas Member

The “lower” Bou-Hajaj sequence outcrops between logs 9 and 15 for a total thickness of ca. 53 to 46 m respectively (Figs 5.3 and 5.11). Remnants of the sequence are observed on log 7. The “upper” Bou-Hajaj sequence would have replaced part of the lower sequence (i.e. after erosion of the lower sequence and deposition of the upper sequence) on logs 6 and 8 (Fig. 5.3). Hence, for the model, the “lower” Bou-Hajaj sequence is extrapolated between logs 6 to 15 where the

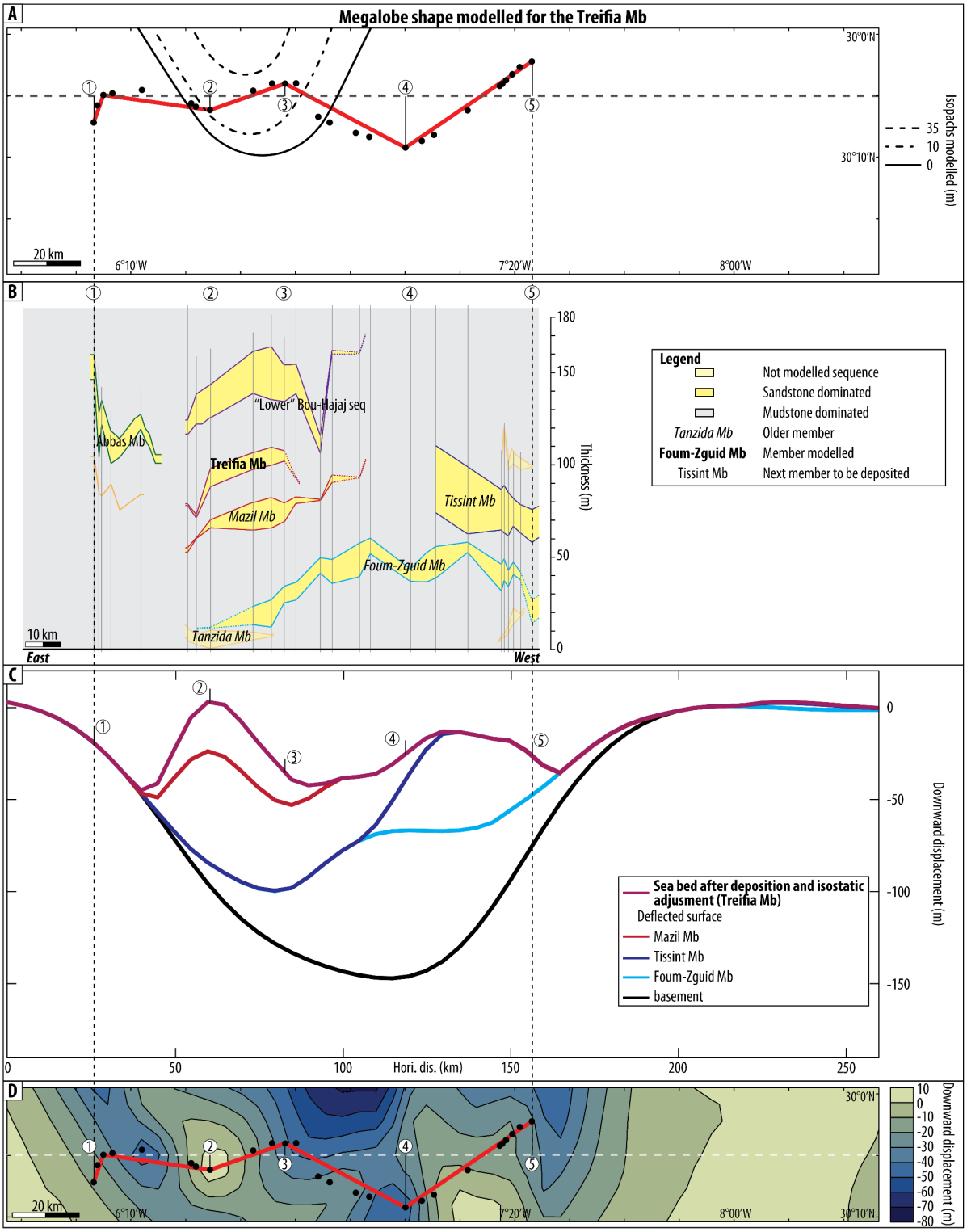

***Figure 5.10**: Extrapolation and isostatic adjustment after deposition of the Treifia Mb. For caption, see Fig 5.7.*

mean value of the sequence between logs 9 and 13 (i.e. 45 m) was put for logs 6 to 8. Logs 14 and 15 have been computed with a thickness of 40 and 20 m respectively since mainly shales outcrop below a few meters of condensed levels. Paleocurrents show a main NW-SE orientation, directed toward the NW, with a minor NE-SW orientation

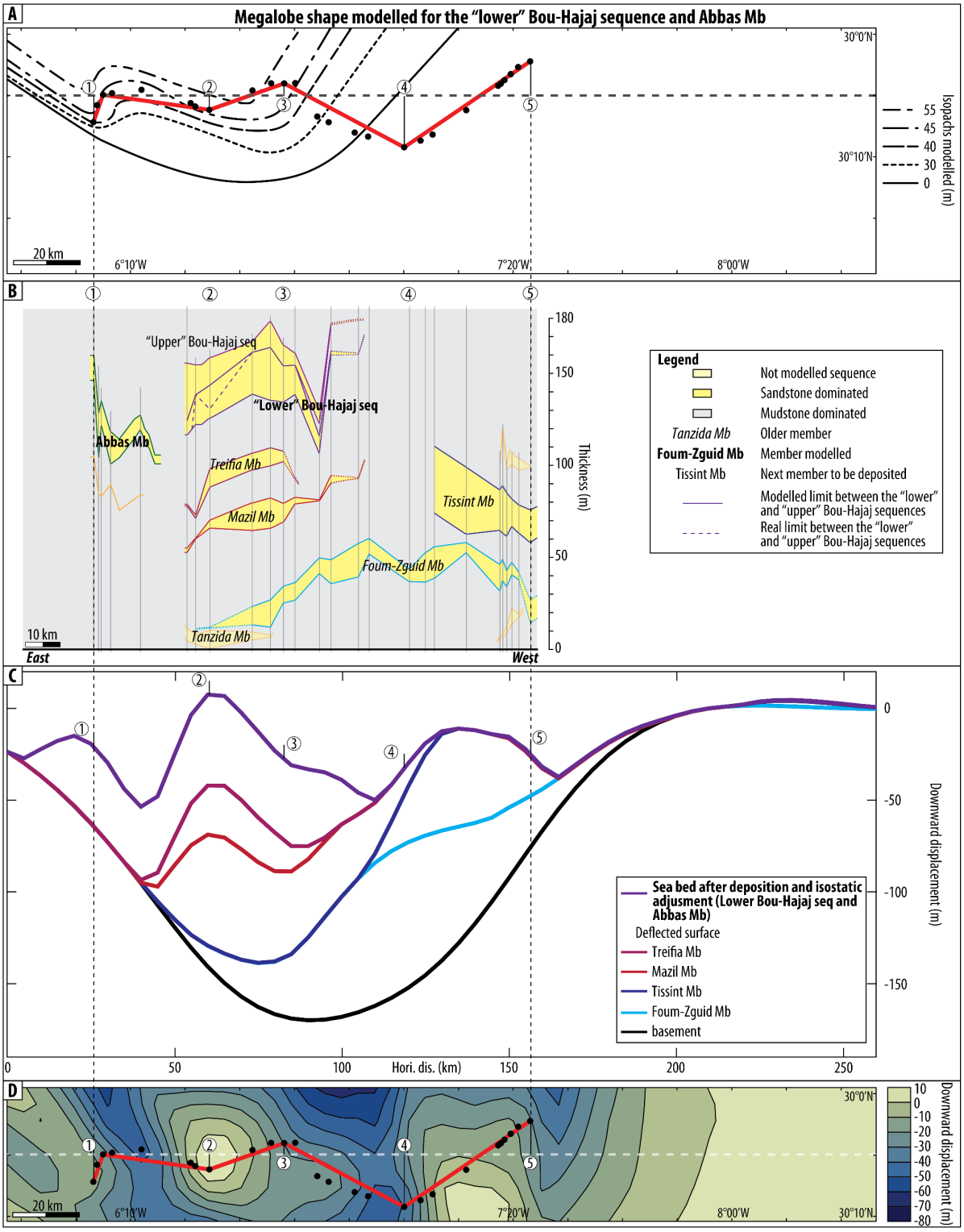

***Figure 5.11**: Extrapolation and isostatic adjustment after deposition of the "lower" Bou-Hajaj sequence and Abbas Mb. For caption, see Fig 5.7.*

and NE direction (Fig. 5.5). These main directions could represent the progradation of the megalobe toward the North +/- 45°. The Abbas Mb is located further E of the Bou-Hajaj Mb where the lithostratigraphic correlation between the two members was not possible due to 10 km of debris covering the outcrops. It is hypothesized

that Abbas and "lower" Bou-Hajaj are roughly contemporaneous in deposition due to similar stacking pattern, altitude from the datum, and global scale correlations of relative sea level (see Chapter 4). The Abbas Mb is located between logs 1 and 5 (Figs 5.3 and 5.11). The surface taken as the previous sequence is a ferruginous condensed level outcropping ca. 40 m below the top of the Abbas Mb. The total thickness of the Abbas sequence is between ca. 40 and 45 m. Paleocurrents record a main direction toward the SE and a minor toward the NE (Fig. 5.5). Finally, since "lower" Bou-Hajaj and Abbas are deposited at the same time, one megalobe shape was extrapolated from the dataset with two advances of lower amplitude and an asymmetry in the isopachs with steeper East than West side (Figs 5.6 and 5.11A).

The advance of the megalobe extrapolated for the "lower" Bou-Hajaj sequence will be deposited on top of the Mazil/Treifia high at ca. 60 km and will fill the accommodation space made from deposition of Mazil and Treifia between ca. 70 and 105 km (Fig. 5.11C). The Abbas megalobe will be deposited on the extreme east part of the transect east flank of the basement.

The maximum of downward displacement of the top of the basement is shifted toward the east after deposition of this megalobe, reaching ca. - 165 m at ca. 90 km (Fig. 5.11C). The depression created by all the members so far seem to create a roughly symmetric trough shape of the basement.

The maximum height of the sea bed of "lower" Bou-Hajaj is ca. + 6 m (Fig. 5.11C and D). This is likely due to the exaggeration in the extrapolation at log 8 (i.e. the real thickness of the sequence is unknown since eroded) and the paleo-sea bed highs already existing for Mazil and Treifia megalobes. The downward displacement obtained after deposition of the Abbas megalobe is largely underestimated since only ca. 40 m of sand were modelled, where at least 70 to 80 m of silt-dominated package is located between the top of the basement and the condensed level taken as the base of the Abbas sequence (i.e. artifacts in Mazil and Treifia extrapolation, see above). Since "lower" Bou-Hajaj and Abbas would be coeval, the extrapolated retreat of the megalobe shape between ca. 30 and 45 km (i.e. between logs 5 and 6, Figs 5.3, 5.6 and 5.11A) is infilling part the depression located. The last sequence to be deposited is "upper" Bou-Hajaj modelled as a channel like complex shape striking South-North, deposited above the paleo-high at ca. 60 km (Fig. 5.12).

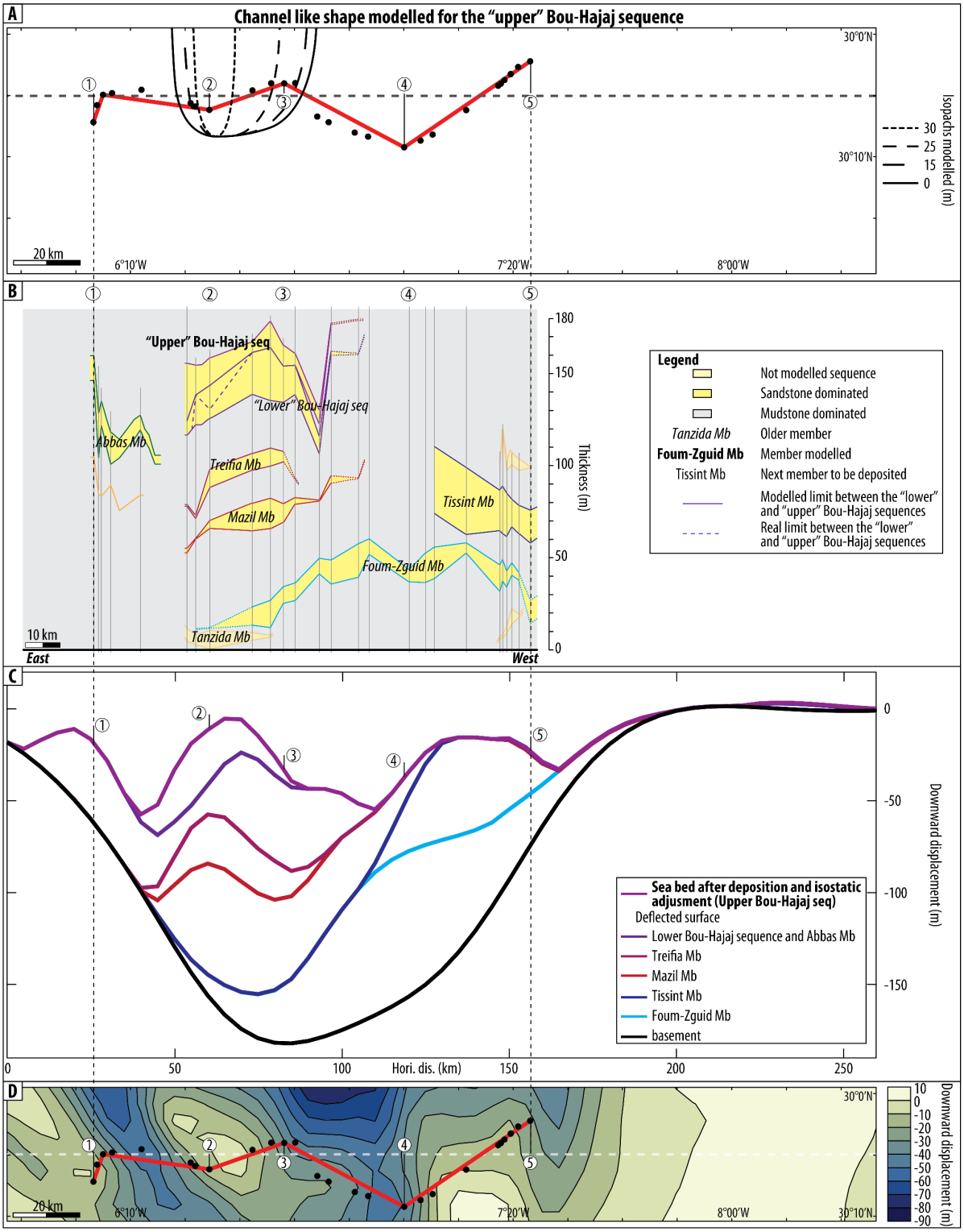

***Figure 5.12**: Extrapolation and isostatic adjustment after deposition of the "upper" Bou-Hajaj sequence. For caption, see Fig 5.7.*

"Upper" Bou-Hajaj sequence

The "upper" Bou-Hajaj sequence is outcropping between logs 6 and 11 overlying or replacing the "lower" Bou-Hajaj sequence (Fig. 5.3). In order to avoid exaggeration of loading, the "lower" Bou-Hajaj sequence (and Abbas Mb) has been

computed twice: one where the "lower" sequence outcrops everywhere between logs 6 and 13 with a mean value between logs 6 and 8 (Fig. 5.11); and another one without the extrapolation of sandstone eroded, as it was observed in the field. The real field data without extrapolation were used for the "upper" Bou-Hajaj sequence, in order show the deflection of all members after erosion of the "lower" part of the sequence and deposition of the "upper" one. The thickest part is located at log 6 (ca. 39 m), rapidly thins toward the West at log 11 for a total thickness of ca. 15 m in ca. 32 km (Figs 5.3 and 5.12A). The "upper" sequence is assumed to disappear in less than 10 km farther East, since no outcrops were available. 10 paleocurrents were measured and show a main SE-NW orientation, with a SE direction. Paleocurrents measured by Ghienne (unpublished pers. comm.) in the "upper" Bou-Hajaj sequence close to the Hassi Taska locality show a major SE direction (Fig. 5.5). These would demonstrate the tidal environment of the deposits of this sequence. The "upper" Bou-Hajaj sequence is extrapolated as a tidal channel with an asymmetric shape (Figs 5.6 and 5.12A).

The maximum downward displacement of the top of the datum to shift once more toward the East to ca. 80 km for a maximum displacement of ca. -170 m and asymmetrical shape of the basement with a steeper East side (Fig. 5.12C).

Finally, the sea bed of the "upper" Bou-Hajaj sequence after deposition and isostatic adjustment is the highest at ca. 75 km at ca. 0 m (Fig. 5.12C and D). This is coherent and reflecting the tidal shallow marine depositional environment interpreted from the field of this part of the sequence. The "upper" Bou-Hajaj deposits will partly infill the depression at ca. 50 km (Fig. 5.12C). The infill of this depression is largely underestimated since no outcrops were available for ca. 10 km.

5.5. Discussion

Within flood dominated deltas, lobe switching is a common coastal process (Coleman, Roberts and Stone, 1998, Maloney et al., 2018). This process usually happens for short-scale lobes of less than ca. 10 km diameter and timescales of ca. 10 ka. A stream carrying sediment in a basin will deposit sediments in a prograding lobe form, which fills up the available accommodation space. River piracy or avulsion will cause the distributary channel to shift and generate a new lobe. The stream pathway will diverge to a nearby location where accommodation is available and another lobe will be emplaced in an

autocyclic process. In the case of the Lower Ktawa Fm, megalobes are dominated by offshore to shoreface deposits, have a larger scale (50-100s km), and they are related to allocyclic cycles of a much longer timescale in comparison to modern lobe switching processes. Here, it is infered that flexural isostasy due to sedimentary loading is causing subsidence of megalobes and autocyclicity of megalobe emplacement.

5.5.1. Autocyclic location process through lateral deflection

Within the Lower Ktawa Fm, and apart for the Tissint Mb, subsequent units are stacked on top of each other with a shift to the East. Whereas this could indicate an Eastward progradation and proximal-distal polarization of the system, the present model depicts another story.

In the present model, the emplacement of a lobe (i.e. loading) combined with the effects of lateral deflection (i.e. lateral bending away from the main load) dictate the morphology of the seabed morphology, creating a depression on each side of the deposited lobe. The accommodation space created will then be filled by the following sequence. Indeed, the position of each member is in good agreement with the location of increased accommodation space due to the previous deposits for almost every member. This is well expressed with the deposition of Tissint in the western part of the transect which is lodged in the deposition created by the Foum-Zguid megalobe (Fig. 5.8). Similarly, the deposition of the Mazil sandstones coincides with the depression created by Foum-Zguid and Tissint (Fig. 5.9). Furthermore, the western part of “lower” Bou-Hajaj is filling the depression created by Treifia and older megalobes, while Abbas is filling the eastern part of the depression created by all preceding megalobes.

It is thus likely that the effect of deflection after deposition dictates the position of forthcoming units. Possibly, river piracy may be involved in terrestrial parts of the system: created depressions would divert the path of rivers, which then plunge and deposit deltaic material in the continuity of the depressions. Hence, the megalobes would prograde toward the North with a shift/avulsion in the feeder source from West to East after the deposition of Tissint. As such, the location of the depositional lobes of the Lower Ktawa Fm may be seen as an autocyclic process. Such a process might have remained unrecognized in other 2D studies.

5.5.2. Eastward shift in the stacking architecture

Apart for the early "channel-complex" of the Tissint Mb, all subsequent lobes stack on top of each other with an eastward shift (Fig. 5.6). This configuration possibly means that the river feeder system was located southeastward from the deltaic depositional zone. Indeed, if depressions divert the path of rivers, and the stack is systematically on the eastward depression, then the drainage system likely occurs on the eastern part of depressions. Such a situation may give the impression of an apparent eastward system progradation, yet this apparent progradation would be oriented perpendicularly to the actual lobe progradation direction.

5.5.3. Artifacts in loads are transferred to artifacts in deflection

Within the frame of units depositing in zones of depressions and available accommodation space, one zone of the profile appears at odd (between 60 and 70 km, Figs 5.9 to 5.12): an artificial paleo-high in seabed results from the Mazil Mb and is transmitted in the forthcoming members. This artifact is explained as the Mazil Mb was only extrapolated for its sandstone part, yet its lateral continuation likely cumulates a thickness of ca. 40 m of mudstone, and was ignored in the extrapolation of the 3D lobe shapes. The resulting artificial paleo-high in modelled seabed lies directly below the depocenter for the subsequent members and is thus continuously nourished for the later steps. This leads to anomalous results for all members above the Mazil megalobe and will be taken into account in forthcoming work. It is however interesting to note that it is essential to feed Flex3D with real data in order to provide a sensible response.

5.5.4. Bathymetry vs type of sediment

The paleo-bathymetry obtained after deposition and adjustment of each member shows interesting correspondence with the type of sediment deposited at each location (Fig. 5.3, detailed in Chapter 2). In particular, the Tissint model shows a maximum height of ca. + 13 m a.s.l. , and corresponds with tidal deposits in the field, i.e. the most proximal type of sediment encountered within the Lower Ktawa Fm (Figs 5.3 and 5.8C).

Similarly, the paleo-seabed after deposition and adjustment of the "lower" Bou-Hajaj and Abbas Mbs expresses well the proximal-to-distal trend in facies associations of both members (Figs 5.3 and 5.11C). The "lower" Bou-Hajaj sequence contains shoreface deposits in the zones that are modelled at the shallowest paleo-

bathymetry (logs 9-11), before and after isostatic adjustment. Toward the West, where 20 m of deepening in paleo-bathymetry is modelled, the sediment facies associations encountered in the field record more distal offshore environments (logs 13 to 16, Fig. 5.3). Furthermore, the location of the paleo-high of this "lower" Bou-Hajaj sequence is located at ca. 70 km on the transect. It thus coincides with the zone that is interpreted from field observation as being eroded by the upper Bou-Hajaj sequence (Figs 5.3, 5.11 and 5.12).

A similar trend is observed for the megalobe of Abbas. The modelled seabed is deepening toward the West of the paleo-high (Fig. 5.11). This is in good agreement with the field observations of sedimentary facies, which display a proximal-to-distal trend toward the West (Fig. 3). Hence, the paleo-bathymetry after isostatic adjustment is in general good agreement with the sedimentary environments recorded in the preserved succession.

5.5.5. Symmetry of lobe shapes

For most members, the dataset of stratigraphic profiles showed an asymmetry in the thickness of deposits as well as in the distribution of facies associations along the transect. Such an asymmetry is interpreted as a result of longshore currents (longshore drift) due to the wave action impacting a coast (here a delta lobe) at an angle to the progradation direction (e.g. Willis et al., 2022). The Foum-Zguid Mb is the only megalobe that pictures an axial symmetry, both in thickness and distribution of facies associations (Fig. 5.3). Intensely bioturbated sandstones are observed in the extreme North and South part of this member which are also the lowest thickness from the datum (logs 11 to 14, 17, 21 to 25) and amalgamated HCS are observed at the centre of the member and thickest part of the sequence (logs 15 and 16, 18 to 20). In the opposite, all other members show an asymmetric profile. The Mazil megalobe shows the strongest asymmetry (Fig. 5.9). Whereas the entire sequence (i.e. including mudstones to sandstones) is the thickest to the East, the proportion of sandstones is lower toward the East (Fig. 5.9B). Given this configuration, one would expect waves impacting from the NE. However, at odd with the asymmetry in thickness, the Mazil Mb exhibits most storm-wave-dominated facies (i.e. stacked to amalgamated HCS) to the West whereas highly bioturbated sandstones dominate to the East (Fig. 5.3). This apparent asymmetry in recorded sedimentary environments, at odds with the thicknesses may be explained by the fact that the lobe shape was inherited from the regression phase whereas stacked to

amalgamated HCS are emplaced during a transgression phase.

5.5.6. Scale, flexural isostasy and timing of adjustment of subaqueous megalobe system

5.5.6.a. Scale of megalobes

Subaerial to subaqueous lobes are usually observed in fluvial dominated delta such as in the Mississippi delta. Quaternary examples have dimensions of ca. 10s m in thickness, span over ca. 10 km and are built and abandoned within a timescale of 10 kyr (Coleman, Roberts and Stone, 1998). Geometries of ca. 100 km long, deposited in ca. 40 kyr for a maximum thickness of ca. 20 m were defined as “superlobe” in the Yellow River system (He et al., 2019). Here, we use the term megalobe to suggest much larger lobe shapes of ca. 100 km in width, up to 60 m in thickness and built over a timescale of a million year. Similar geometries have already been documented in Lin, and Bhattacharya (2021). They recognized a structures similar to the Ktawa’s megalobes, spanning laterally over ca. 200 km and prograding over a length of ca. 400 km in the storm-flood-dominated Gallup Delta. There, each cycle lasting ca. 1.2 Myr represent a succession of ca. 80 m in thickness. Hence, the scale of the megalobes interpreted for the Lower Ktawa Fm is comparable with other storm-(flood-)dominated subaqueous deltas.

5.5.6.b. Effective elastic thickness

In this study, an effective elastic thickness of 7 km was used, which is almost 4 times smaller than the 50 km which are usually used in other studies (e.g. Driscoll and Karner, 1994, Polanco et al., 2024, Tesauro et al., 2012, Watts et al., 2009). This difference reflects that other studies model the effective elastic thickness for a continental crust or passive margins (e.g. Driscoll and Karner, 1994, Tesauro, Kaban and Cloetingh, 2012, Willis, Sun and Ainsworth, 2022). Here however, we consider that adjustment is mainly acclimated by the underlying succession of sediments, since the platform of North Gondwana reaches ca. 5 km in thickness in the area.

5.5.6.c. Timing for isostatic adjustment

Equilibrium of isostatic adjustment is considered as the timescale for which the adjustment to a load is complete. Within the context of the members within the Lower Ktawa Fm, equilibrium is likely largely attained between the emplacement of successive lobes. Indeed, isostatic adjustment due to sediment loading is

generally argued to happen on a timescale of 10^4 to 10^5 years (Allison et al., 2016, Frederick et al., 2019, Polanco et al., 2024, Shirzaei et al., 2021). This is 10 to 100 times faster than the average timescale of 1.7 Myr for the cycles estimated for each Lower Ktawa Member. Hence, isostasy is likely fully adjusted during the transgression of a cycle, and thus the subsequent member will prograde on the equilibrium surface as modelled here. Additionally, an average duration of 1.7 Myr per sequence will deposit ca. 35 to 60 m of sediments. Such a sediment deposition rate is much lower than e.g. the 400 m/Myr modelled in Polanco et al. (2024), and reinforces the idea that equilibrium was likely reached.

5.5.7. The effect of lateral deflection in other modelling tools

Notably, Flex3D does not account for compaction of sediment and do not include a backstripping tool. Whereas multiple codes allow to combine backstripping to model tectonic and total subsidence, these are most generally based on 1D Airy compensation for vertical movement. They thus do not take into account lateral deflection and the lateral bending due to neighboring loads.

In order to compare the results from different methods, a similar simulation was undertaken using the flexural isostasy method from Flex3D (Cardozo, 2009) and a subsidence model including backstripping using BasinVis (Lee et al., 2020). Tests have been conducted on the Foum-Zguid Mb (Fig. 5.13). In BasinVis 2.0 input parameters are the thickness of the load, decompaction parameters (e.g. initial porosity, density, etc), paleo-sea level (set to 0 here) and the paleo-water depth. Depositional environments were simplified in 4 zones: offshore, offshore transition, lower shoreface and shoreface. Each depositional environment was attributed a paleo-water depth of 150, 100, 50, and 10 m respectively. Only log thicknesses were used as inputs. The BasinVis model shows much more localized patterns (Fig. 5.13B). In vertical views, it appears clear that 1D Airy compensation accounts for the entire subsidence, and thus the downward displacement is in the range of the actual thicknesses of the loads. However, in Flex3D, modelled sediment loads have an effect that is spread on the surrounding locations (Fig. 5.13C). Log thicknesses and a grid filling the megalobe with different thicknesses were used as inputs for extrapolation, where only log thicknesses were used in BasinVis. As such, the result

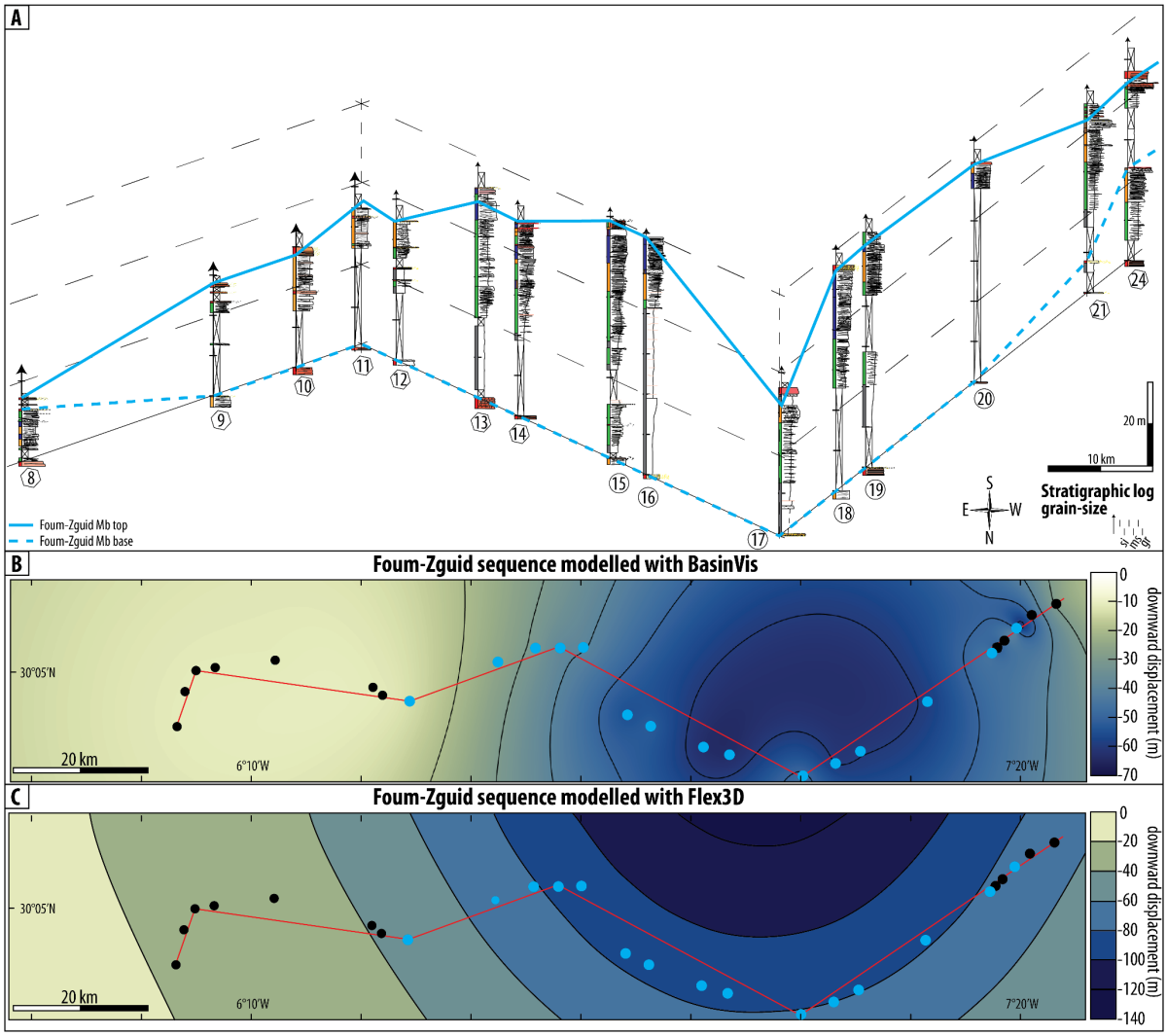

***Figure 5.13**: Comparison between the output from BasinVis using a backstripping method, and Flex3D using flexural isostasy, for the Foum-Zguid sequence. (A) Detailed stratigraphic profiles of the Foum-Zguid sequence logged in the field. Legend of color bars on Fig. 3. (B) Downward displacement modelled with BasinVis. (C) Downward displacement modelled with Flex3D. Blue points: location of logs showed of the Foum-Zguid sequence in (A). Black points: other logs not showed in (A).*

gives more downward displacement, and more spread with inclusion of lateral deflection.

Thus, backstripping is very powerful for modelling the tectonic and/or total subsidence in 1D or sea-level changes after removing compaction effects and paleo-water depth (amongst other parameters) of one stratigraphic profile (e.g. log or core) but has its limits in 3D. As such, several stratigraphic profiles of this study would need to be computed with the backstripping method to reconstruct an age and paleo-water depth RSL curve with the possible subsidence obtained here.

5.6. Conclusion

Here, a large field-based dataset of sediment profiles was confronted to a 3D model of isostatic adjustment. The Lower Ktawa Fm, a shallow marine succession of offshore to shoreface deposits contains sandstone bodies that spread laterally over 50 to 100 km. These are understood as the record of shallow-water sediments that mark the spreading of sediments as megalobe structures that prograde from the South to the North (+/- 45°). Four megalobes and two channel-complexes were extrapolated in 3D from 6 sandstone-dominated members and sequences within the Lower Ktawa Fm. The extrapolated megalobes were used as a load input for isostatic adjustment. The seabed bathymetry after sediment loading and isostatic adjustment of a megalobe demonstrates depressions in the paleo-surface due to lateral deflection. The zones of depressions modelled from Flex3D for each successive lobe correspond to the depocenters for the subsequent member recorded in the field. Additionally, the modelled variations in bathymetry are in good agreement with the variations of sedimentary environments interpreted from field deposits. Thus, the model reflects well the field data, and points toward a feedback effect for the localization of successive megalobes. Lateral deflection, i.e. the bending of the seabed laterally to a loading point, is understood as a major autocyclic process for the emplacement of the shallow-marine deposits of the Lower Ktawa Fm. In that sense, the effective elastic thickness is found to be the main parameter influencing the model outputs here. Notably, the effective thickness used here in the model are soft and reflecting the underlying succession of sandstones, in contrast with many existing models based on a more rigid basement for a continental crust.

Interestingly, in zones where input geometries were simplified, the modelled seabed in turn creates anomalies and a misfit with the field data. Forthcoming work will thus focus on a careful extrapolation of megalobe structures, in order to feed the model with better constrained inputs and reconcile field observations with model outputs in some anomalous zones.

In terms of geology, the results highlight the possibility that the Lower Ktawa Fm was a sediment system prograding from South to North. This interpretation is challenging regarding the regional configuration of deposits in the field. In particular, the origin and significance of a mudstone-dominated depocenter eastward from the study area, called here the “Tagounite trough”, remains

enigmatic. This depression however corresponds to a major feature, which coincides with major gravity anomalies, tectonic faults, and lies in the continuation of the Ougarta Range, a sedimentary succession of similar age as the Lower Ktawa Fm.

Finally, a provenance study might be of interest to decipher if the western and eastern Central to Oriental Anti-Atlas would have the same drainage system. If the western Central Anti-Atlas shows a source to the West and the Oriental to the East, then two conjugated shorelines facing each other would be the best model fit. If both the Central and Oriental Anti-Atlas show a ca. southern source, or at least similar source, then the megalobes prograding from South to North would be the best hypothesis.

References

Allison, M., Yuill, B., Törnqvist, T., Amelung, F., Dixon, T., Erkens, G., Stuurman, R., Jones, C., Milne, G. & Steckler, M. 2016. Global risks and research priorities for coastal subsidence. *Eos (Washington, DC),* 97.

Álvaro, J. J., Benharref, M., Destombes, J., Gutiérrez-Marco, J. C., Hunter, A. W., Lefebvre, B., Van Roy, P. & Zamora, S. 2022. Ordovician stratigraphy and benthic community replacements in the eastern Anti-Atlas, Morocco.

Cardozo, N., 2009. Flex3D Matlab code. 3D flexural modeling. Continuous plate of variable elastic thickness (finite difference solution). https://www.ux.uis.no/~nestor/work/matlabScripts.html

Cocks, L. R. M. & Torsvik, T. H. 2021. Ordovician palaeogeography and climate change. *Gondwana Research,* 100**,** 53-72.

Coleman, J. M., Roberts, H. H. & Stone, G. W. 1998. Mississippi River delta: an overview. *Journal of Coastal Research***,** 699-716.

D'errico, J. R. 2006. Understanding gridfit. *Information available at: http://www. mathworks. com/matlabcentral/fileexchange/loadFile. do,* 55**,** 70-83.

Destombes, J. 1985. Lower palaeozoic rocks of Morocco. *Lower Palaeozoic of north-western and west-central Africa***,** 91-336.

Driscoll, N. W. & Karner, G. D. 1994. Flexural deformation due to Amazon Fan loading: A feedback

mechanism affecting sediment delivery to margins. *Geology,* 22**,** 1015-1018.

Ennih, N. & Liégeois, J.-P. 2001. The Moroccan Anti-Atlas: the West African craton passive margin with limited Pan-African activity. Implications for the northern limit of the craton. *Precambrian Research,* 112**,** 289-302.

Frederick, B. C., Blum, M., Fillon, R. & Roberts, H. 2019. Resolving the contributing factors to Mississippi Delta subsidence: Past and present. *Basin Research,* 31**,** 171-190.

Hampson, G. J. 2010. Sediment dispersal and quantitative stratigraphic architecture across an ancient shelf. *Sedimentology,* 57**,** 96-141.

Hampson, G. J. & Premwichein, K. 2017. Sedimentologic character of ancient muddy subaqueous-deltaic clinoforms: Down Cliff Clay Member, Bridport Sand Formation, Wessex Basin, UK. *Journal of Sedimentary Research,* 87**,** 951-966.

He, L., Xue, C., Ye, S., Amorosi, A., Yuan, H., Yang, S. & Laws, E. A. 2019. New evidence on the spatial-temporal distribution of superlobes in the Yellow River Delta Complex. *Quaternary Science Reviews,* 214**,** 117-138.

Higgins, S. A. 2016. Advances in delta-subsidence research using satellite methods. *Hydrogeology Journal,* 24**,** 587.

Hoepffner, C., Soulaimani, A. & Piqué, A. 2005. The moroccan hercynides. *Journal of African Earth Sciences,* 43**,** 144-165.

Klausen, T. G., Nyberg, B. & Helland-Hansen, W. 2019. The largest delta plain in Earth's history. *Geology,* 47**,** 470-474.

Krauthammer, T. & Ventsel, E. 2001. Thin plates and shells: theory, analysis and applications. *Mercel Dekker Inc., New York*.

Lee, E. Y., Novotny, J. & Wagreich, M. 2020. Compaction trend estimation and applications to sedimentary basin reconstruction (BasinVis 2.0). *Applied Computing and Geosciences,* 5**,** 100015.

Lin, W. & Bhattacharya, J. P. 2021. Storm-flood-dominated delta: a new type of delta in stormy oceans. *Sedimentology,* 68**,** 1109-1136.

Loi, A., Ghienne, J.-F., Dabard, M.-P., Paris, F., Botquelen, A., Christ, N., Elaouad-Debbaj, Z., Gorini, A., Vidal, M. & Videt, B. 2010. The Late Ordovician glacio-eustatic record from a high-latitude storm-dominated shelf succession: The Bou Ingarf section (Anti-Atlas, Southern Morocco). *Palaeogeography, Palaeoclimatology, Palaeoecology,* 296**,** 332-358.

Maloney, J. M., Bentley, S. J., Xu, K., Obelcz, J., Georgiou, I. Y. & Miner, M. D. 2018. Mississippi River subaqueous delta is entering a stage of retrogradation. *Marine Geology,* 400**,** 12-23.

Marante, A. 2008. *Architecture et dynamique des systèmes sédimentaires silico-clastiques sur la" plate-forme géante" nord-gondwanienne: l'Ordivicien moyen de l'Anti-Atlas marocain.* Bordeaux 3.

Meddour, A. 2016. *Les séries de l'Ordovicien moyen et supérieur de l'Anti-Atlas oriental (Maroc): stratigraphie, sédimentologie et paléogeographie des systèmes de plate-forme silico-clastique.* Bordeaux 3.

Michard, A., Hœpffner, C., Soulaimani, A. & Baidder, L. 2008. The variscan belt. *Continental Evolution: The Geology of Morocco: Structure, Stratigraphy, and Tectonics of the Africa-Atlantic-Mediterranean Triple Junction.* Springer.

Milliman, J. D., Broadus, J. M. & Gable, F. 1989. Environmental and economic implications of rising sea level and subsiding deltas: the Nile and Bengal examples. *Ambio***,** 340-345.

Mitchell, N. C., Masselink, G., Huthnance, J. M., Fernandez-Salas, L. M. & Lobo, F. J. 2012. Depths of modern coastal sand clinoforms. *Journal of Sedimentary Research,* 82**,** 469-481.

Overeem, I., Nienhuis, J. H. & Piliouras, A. 2022. Ice-dominated Arctic deltas. *Nature Reviews Earth & Environment,* 3**,** 225-240.

Patruno, S. & Helland-Hansen, W. 2018. Clinoforms and clinoform systems: Review and dynamic classification scheme for shorelines, subaqueous deltas, shelf edges and continental margins. *Earth-Science Reviews,* 185**,** 202-233.

Pique, A. & Michard, A. 1989. Moroccan Hercynides; a synopsis; the Paleozoic sedimentary and tectonic evolution at the northern margin of West Africa. *American Journal of science,* 289**,** 286-330.

Polanco, S., Blum, M., Salles, T., Frederick, B. C., Farrington, R., Ding, X., Mather, B., Mallard, C. & Moresi, L. 2024. Flexural isostatic response of continental-scale deltas to climatically driven sea level changes. *Earth Surface Dynamics,* 12**,** 301-320.

Proust, J.-N., Pouderoux, H., Ando, H., Hesselbo, S. P., Hodgson, D. M., Lofi, J., Rabineau, M. & Sugarman, P. J. 2018. Facies architecture of Miocene subaqueous clinothems of the New Jersey passive margin: Results from IODP-ICDP Expedition 313. *Geosphere,* 14**,** 1564-1591.

Reynolds, D. J., Steckler, M. S. & Coakley, B. J. 1991. The role of the sediment load in sequence stratigraphy: The influence of flexural isostasy and compaction. *Journal of Geophysical Research: Solid Earth,* 96**,** 6931-6949.

Shirzaei, M., Freymueller, J., Törnqvist, T. E., Galloway, D. L., Dura, T. & Minderhoud, P. S. 2021. Measuring, modelling and projecting coastal land subsidence. *Nature Reviews Earth & Environment,* 2**,** 40-58.

Steckler, M. S., Oryan, B., Wilson, C. A., Grall, C., Nooner, S. L., Mondal, D. R., Akhter, S. H., Dewolf, S. & Goodbred, S. L. 2022. Synthesis of the distribution of subsidence of the lower Ganges-Brahmaputra Delta, Bangladesh. *Earth-Science Reviews,* 224**,** 103887.

Syvitski, J., Anthony, E., Saito, Y., Zăinescu, F., Day, J., Bhattacharya, J. P. & Giosan, L. 2022. Large deltas, small deltas: Toward a more rigorous understanding of coastal marine deltas. *Global and Planetary Change,* 218**,** 103958.

Tesauro, M., Kaban, M. K. & Cloetingh, S. A. 2012. Global strength and elastic thickness of the lithosphere. *Global and Planetary Change,* 90**,** 51-57.

Turcotte, D. L. & Schubert, G. 2002. *Geodynamics*, Cambridge university press.

Watts, A., Rodger, M., Peirce, C., Greenroyd, C. & Hobbs, R. 2009. Seismic structure, gravity anomalies, and flexure of the Amazon continental margin, NE Brazil. *Journal of Geophysical Research: Solid Earth,* 114.

Willis, B. J., Sun, T. & Ainsworth, R. B. 2022. Sharp-based shoreface successions reconsidered in three-dimensions: A forward stratigraphic modelling perspective. *The Depositional Record,* 8**,** 685-717.

CHAPTER SIX

Conclusions and outlook

The main goal of this thesis was to gain new insights into the sedimentology and stratigraphy of the Ktawa Group in the Central Anti-Atlas. Facies associations were described in detail, from which depositional environments were interpreted. These enabled, with incorporation of stacking patterns, the reconstruction of two depositional models for the Lower Ktawa Formation deposits. The depositional models differ because two possible depositional environments were interpreted from the intensely bioturbated and amalgamated HCS facies associations. A ramp-like setting was emphasized, where bioturbated sandstones are emplaced in a lower shoreface during regressions, and amalgamated HCS sandstones are deposited as shoals/sand ridges during the ensuing transgressions, above a wave-ravinement surface. The second depositional model put forward is bimodal, with a storm-wave dominated ramp emplaced during a forced regression, overlaid by a barrier-lagoon system during the transgression, above a subaerial unconformity. The barrier-lagoon system is composed of amalgamated HCS sandstones making the barrier, protecting the lagoon/back-barrier from wave-action and reworking where the intensely bioturbated sandstones are deposited. Furthermore, from facies associations symmetry over the studied region and thinning trends of sandstone packages, a South-to-North prograding trend was hypothesized. Deposition of sediments would be shaped as megalobe geometries.

These megalobe shapes were implemented in a flexural model (i.e. Flex3D) in order to model the paleoseabed of each megalobe after isostatic adjustment. Each isostatic adjustment created accommodation space and depressions on the side of the megalobes. Overall, each subsequent megalobe is deposited in the accommodation space created by the deposition and isostatic adjustment of previous members. Each megalobe seems to shift toward the east of the study area, while still prograding toward the North. Hence, we hypothesized that inland, the river may have been captured by the depressions created by the isostatic adjustment, which would be sourced from the South-East.

A composited RSL curve was reconstructed for the Lower Ktawa and Rouïd-Aïssa deposits in the study area. The Lower Ktawa Formation is composed of six 3rd order regressive to transgressive (R/T) cycles (ca. 1.7 Myr per cycle), where two of them represent major fall from offshore to tidal environments at ca. 455.5 and 450 Ma. The Rouïd-Aïssa Formation, ranging from ca. 1.5 to 3.5 Myr, make one major sea level fall, composed of four higher order R/T cycles. This curve was correlated to the global RSL curve and geochemical proxies, i.e. $\delta^{18}O$ and $\delta^{13}C$. These correlations highlighted that almost each regressive event is correlated to a cooling, glacially-induced event. As such, the Guttenberg Isotopic Carbon Excursion, Kope,

Waynesville, and Whitewater events were recognized, within an error bar of ca. 1 Ma. A reasonable congruence of correlations to regional studies in the Ougarta, Hoggar, Armorican Massif and Sardinia was put forward. Hence, this study suggests that the Ktawa Group deposition was driven by glacially-related allocyclic eustasy. The Ktawa Group in the Anti-Atlas hence marks part of the onset of the Late Ordovician glaciation, where the maximum is reached during Hirnantian. Finally, a new correlation scheme across the Anti-Atlas (i.e. correlation between this study in the western Central Anti-Atlas and the eastern Central to Oriental Anti-Atlas) was discussed in the light of new biostratigraphic calibration of the present study, and also based on R/T cycles recognized.

Biostratigraphic calibration is critical for correlations and reconstruction of precise relative sea level curves. As such, sampling of chitinozoans are needed to better constrain the depositional age of each member and sequences. These can be incorporated into a backstripping method in order to produce a more precise sea level curve for the Ktawa Group. The backstripping method will remove compaction and takes into account paleowaterdepth of depositional environments, sea level changes through time, and subsidence of the basin.

Furthermore, the inputs for the flexural model can be improved to incorporate deposits which were not taken into account. The flexural model can also be implemented for the Ktawa Group in the Oriental Anti-Atlas to enhance the understanding of the group deposition and the basin during Late Ordovician time.

Provenance studies on the Ktawa Group can also improve the megalobe geometries prograding toward the North hypothesis. As such, if the source is located to the South or South-East, this model would be the best fit. However, if the source is located to the West of the studied region, then the best fit hypothesis would be a progradation trend toward the East.

Appendix A

Supplementary materials for Chapter 2

Detailed stratigraphic profiles of the Lower Ktawa Formation in the western Central Anti-Atlas

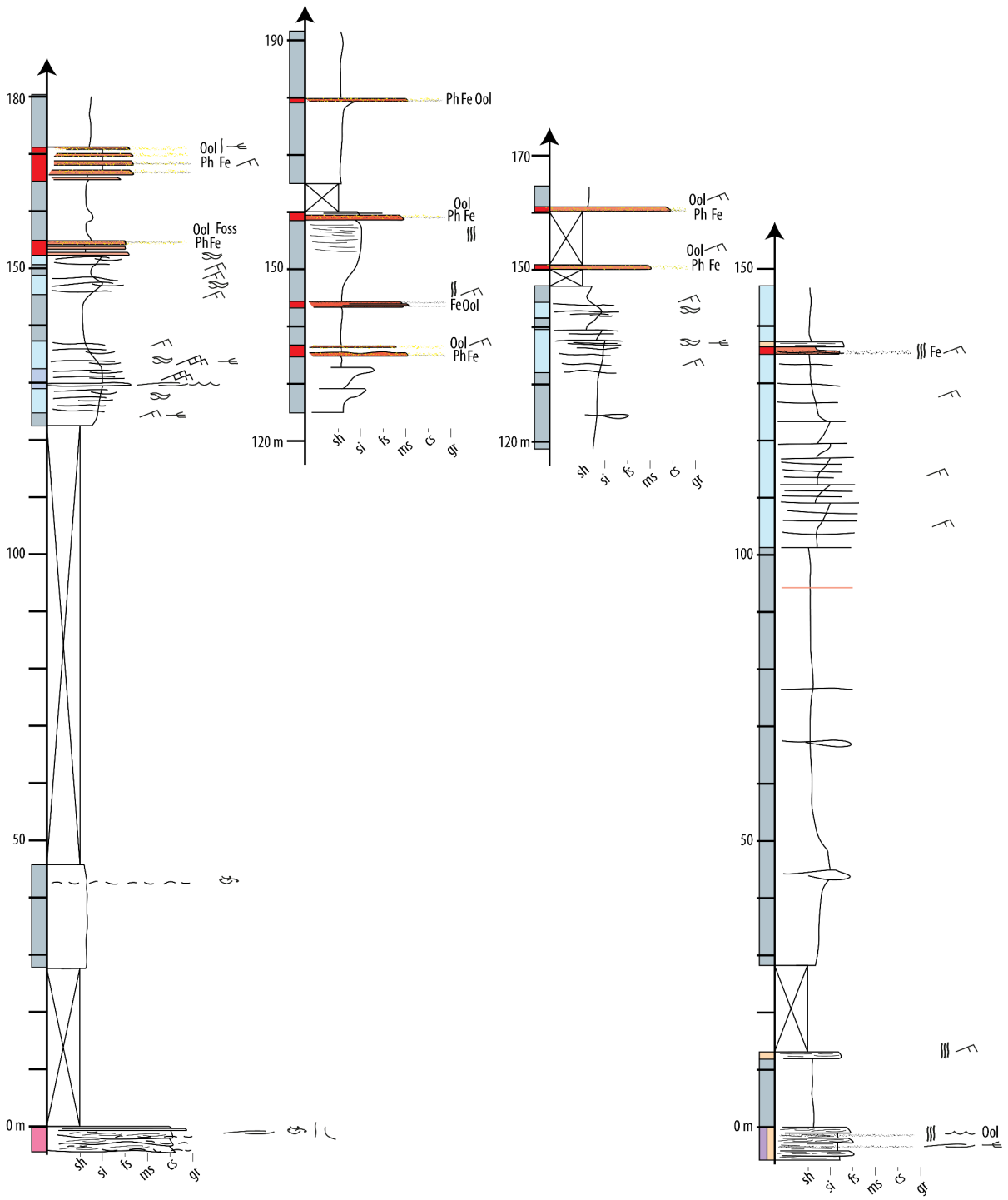

***Supplementary figure A.1**: Detailed stratigraphic profiles of logs 1 and 3 to 5 (left to right respectively). For location, see Fig. 2.3. For legend, see Fig. 2.14.*

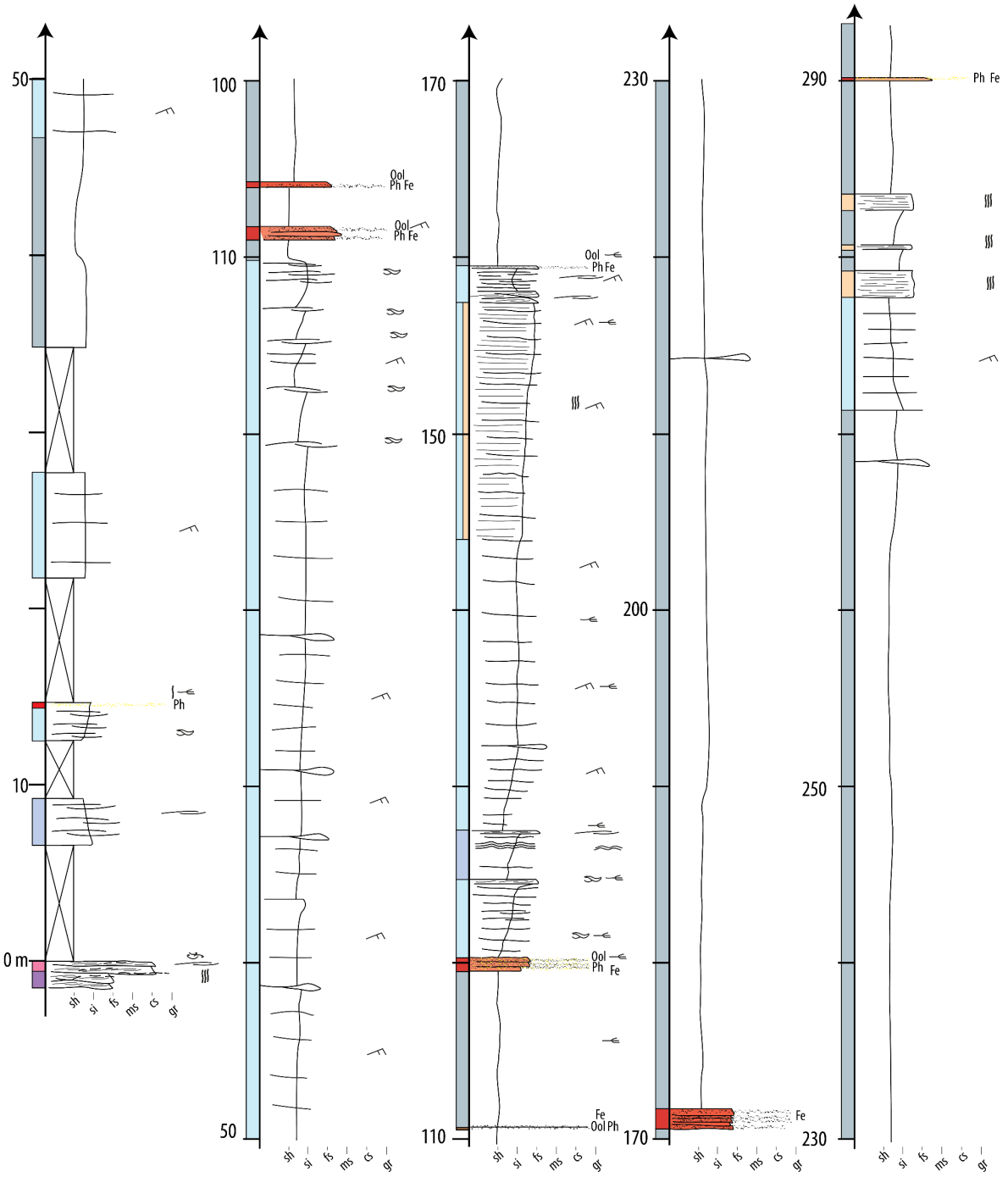

***Supplementary figure A.2**: Detailed stratigraphic profile of log 6. For location, see Fig. 2.3. For legend, see Fig. 2.14.*

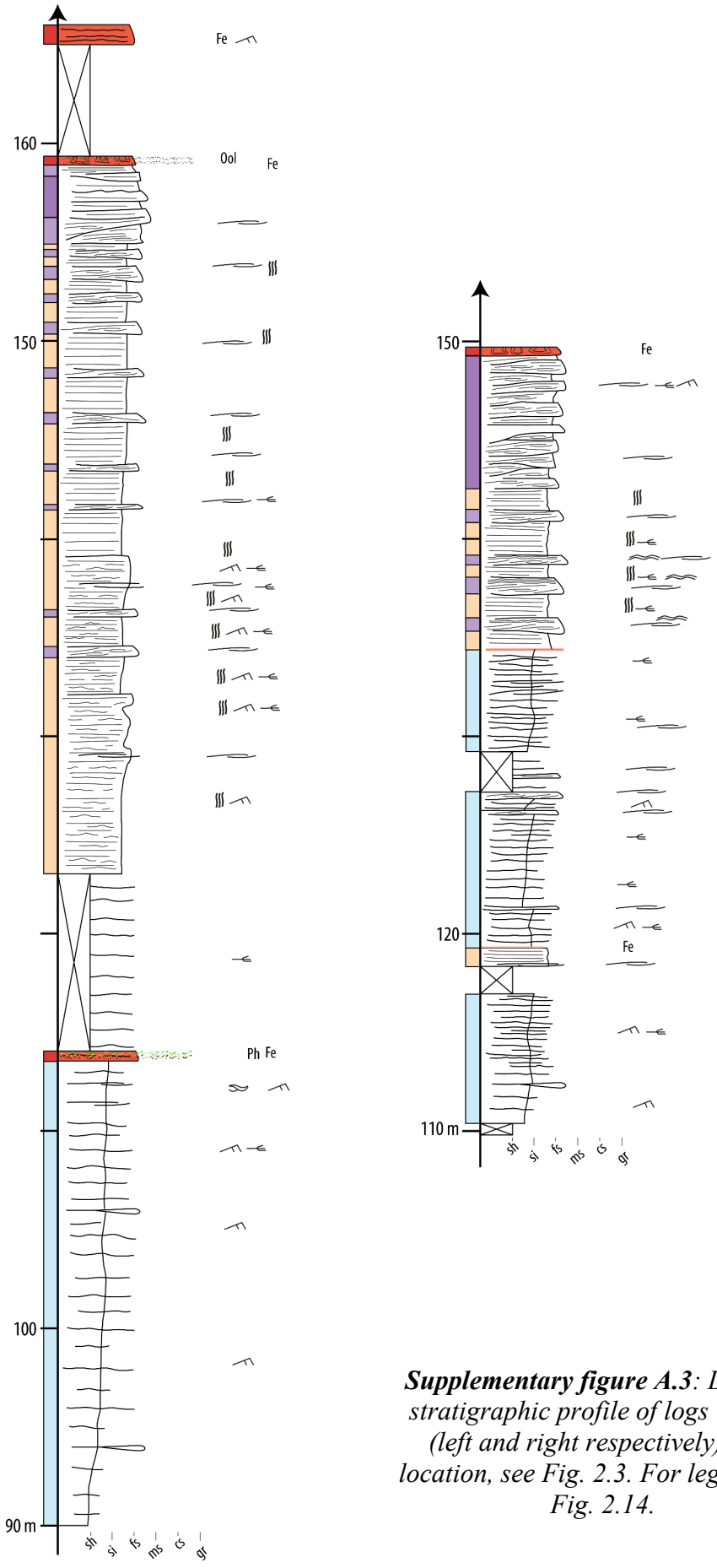

***Supplementary figure A.3**: Detailed stratigraphic profile of logs 7 and 8 (left and right respectively). For location, see Fig. 2.3. For legend, see Fig. 2.14.*

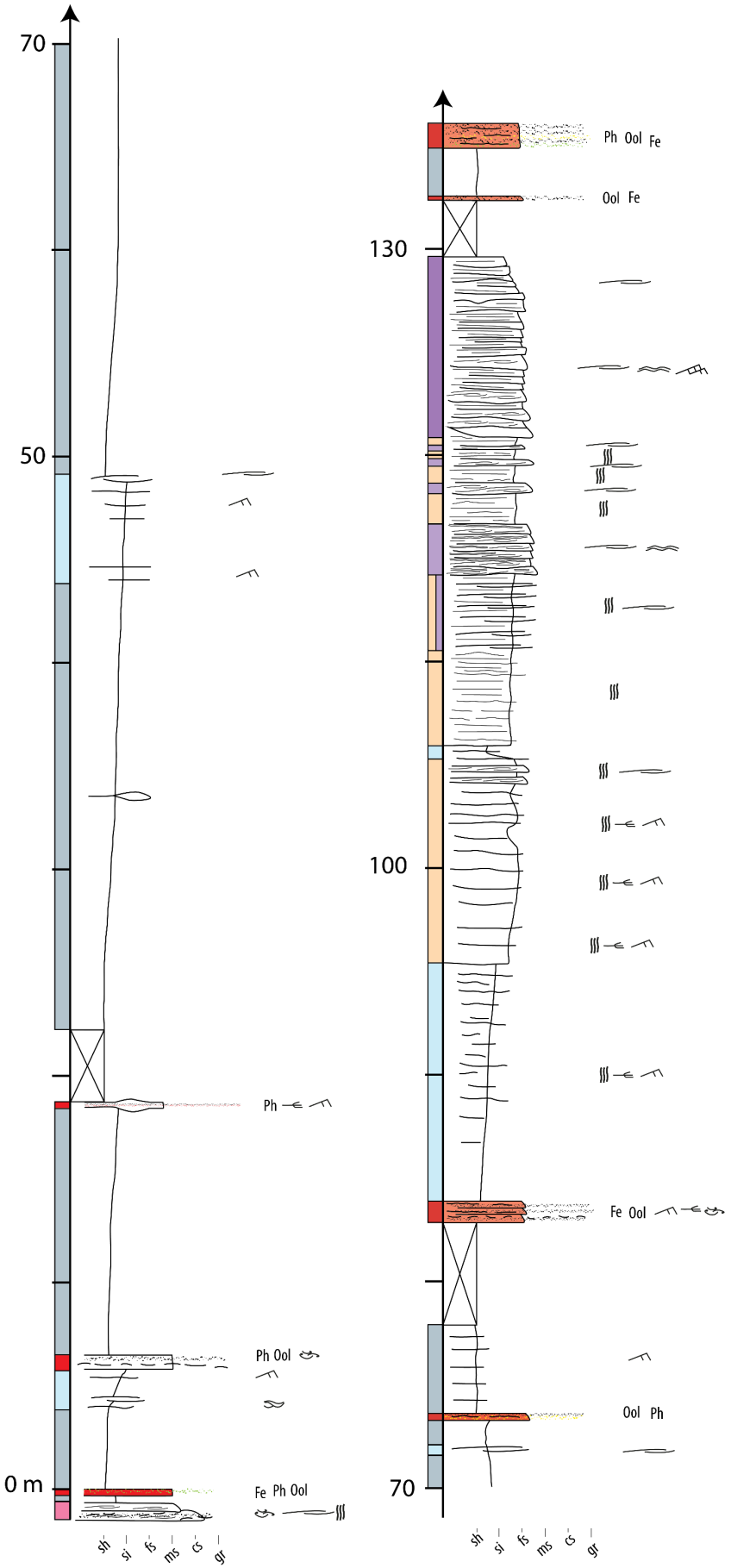

***Supplementary figure A.4**: Detailed stratigraphic profils of log 9. For location, see Fig. 2.3. For legend, see Fig. 2.14.*

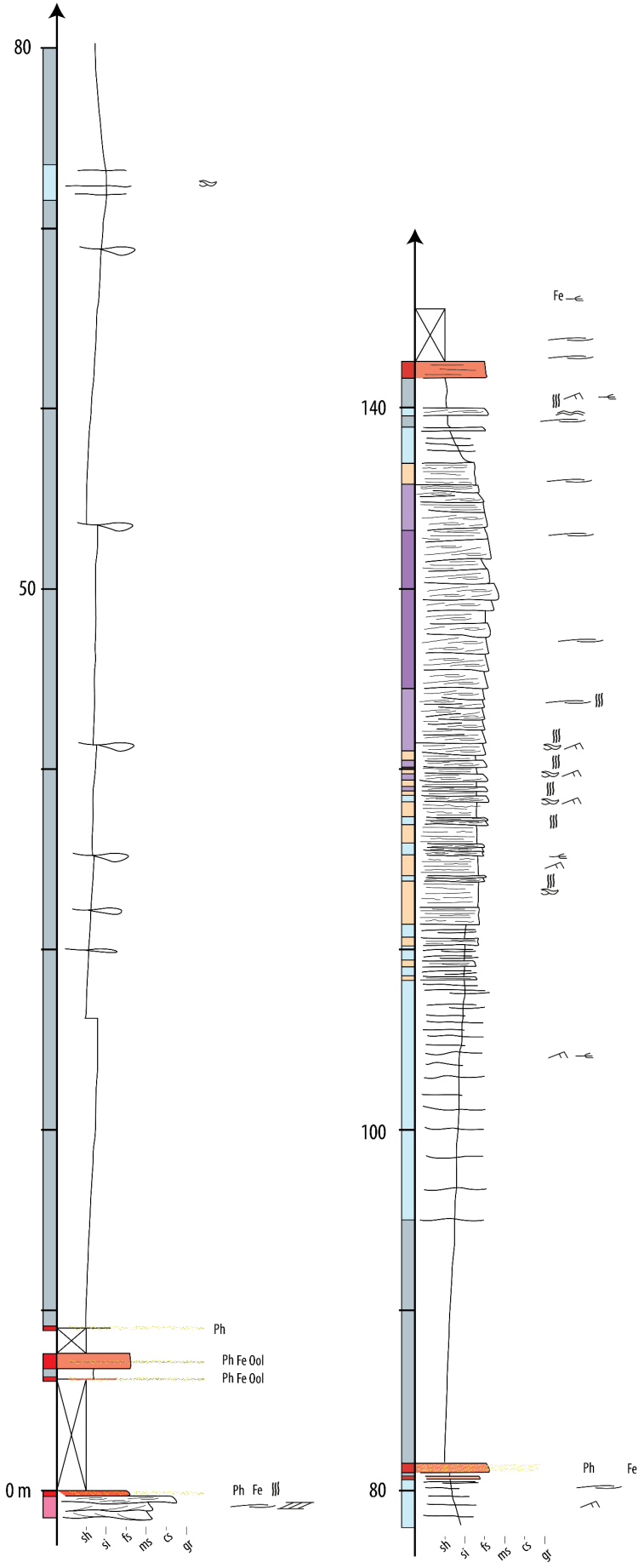

***Supplementary figure A.5**: Detailed stratigraphic profile of log 10. For location, see Fig. 2.3. For legend, see Fig. 2.14.*

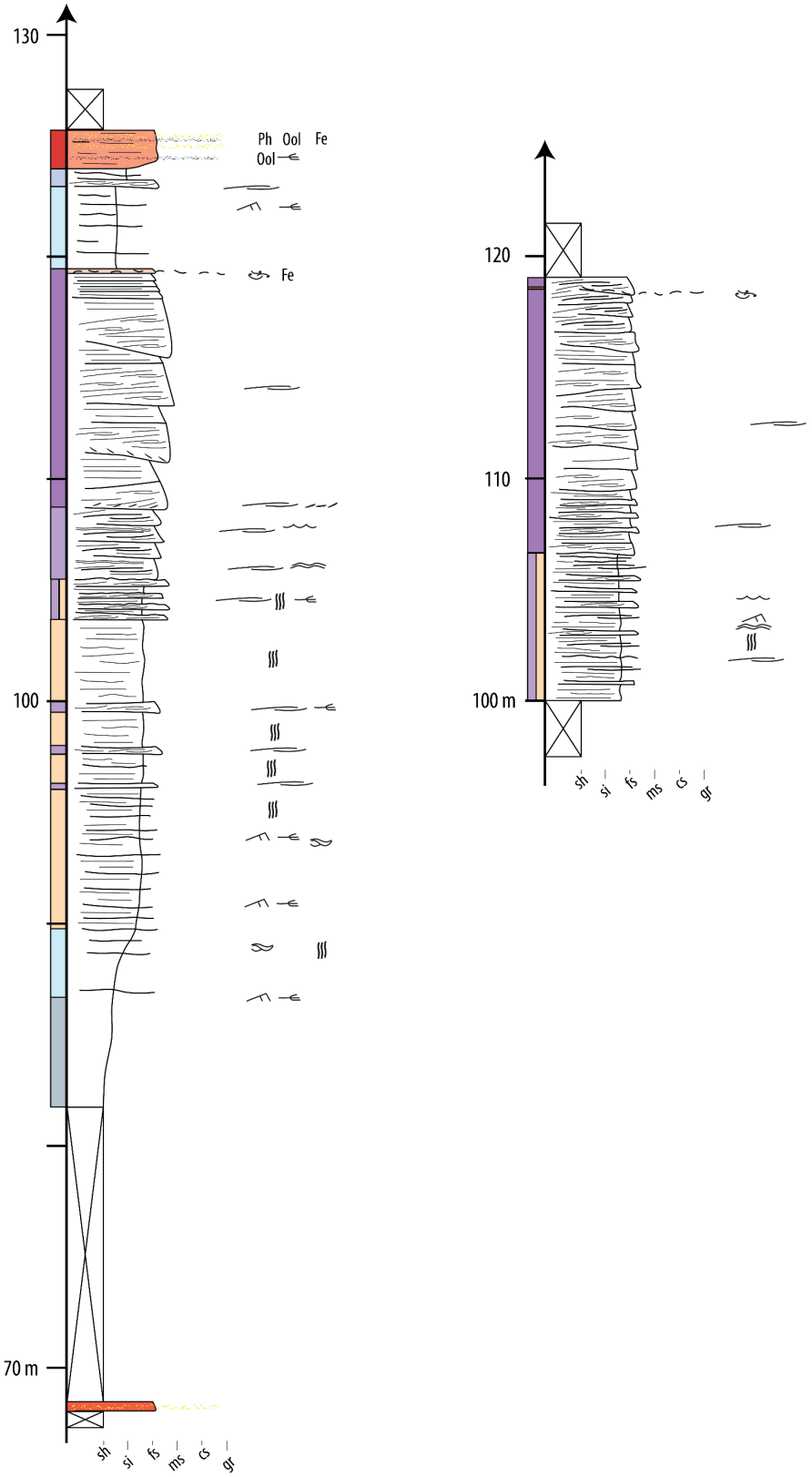

***Supplementary figure A.6**: Detailed stratigraphic profiles of logs 11 and 12 (left and right respectively). For location, see Fig. 2.3. For legend, see Fig. 2.14.*

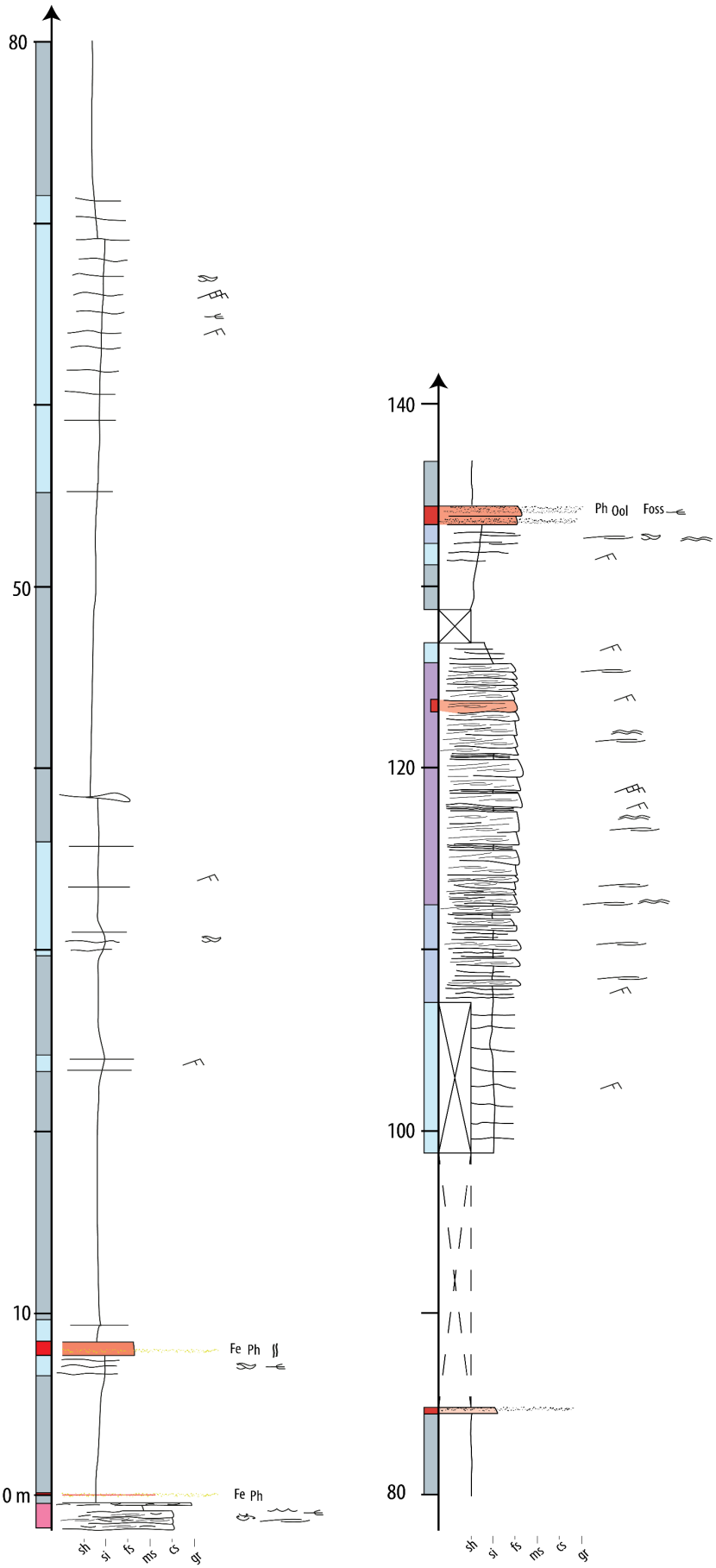

Supplementary figure A.7*: Detailed stratigraphic profile of log 13. For location, see Fig. 2.3. For legend, see Fig. 2.14.*

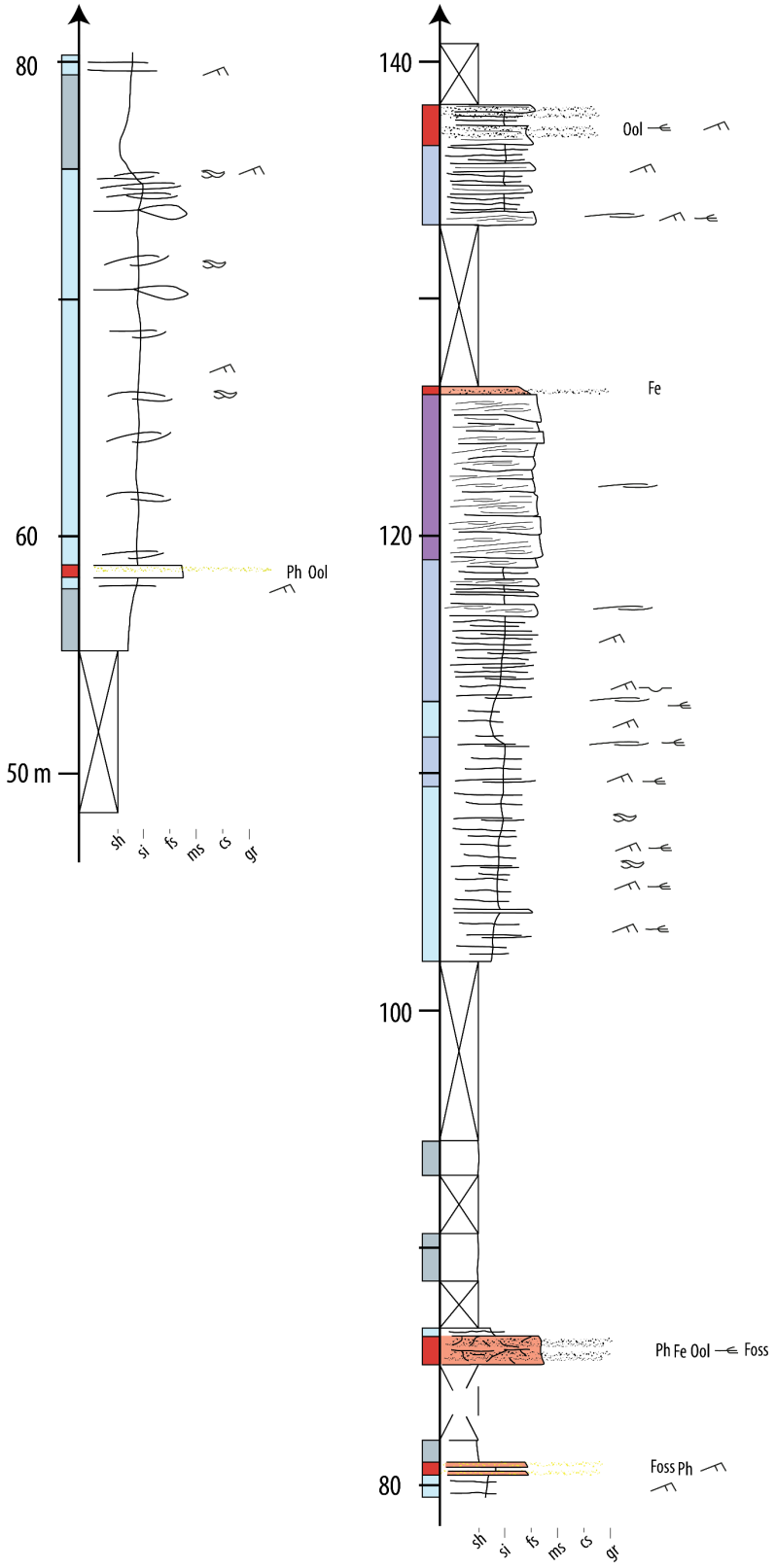

***Supplementary figure A.8**: Detailed stratigraphic profile of log 14. For location, see Fig. 2.3. For legend, see Fig. 2.14.*

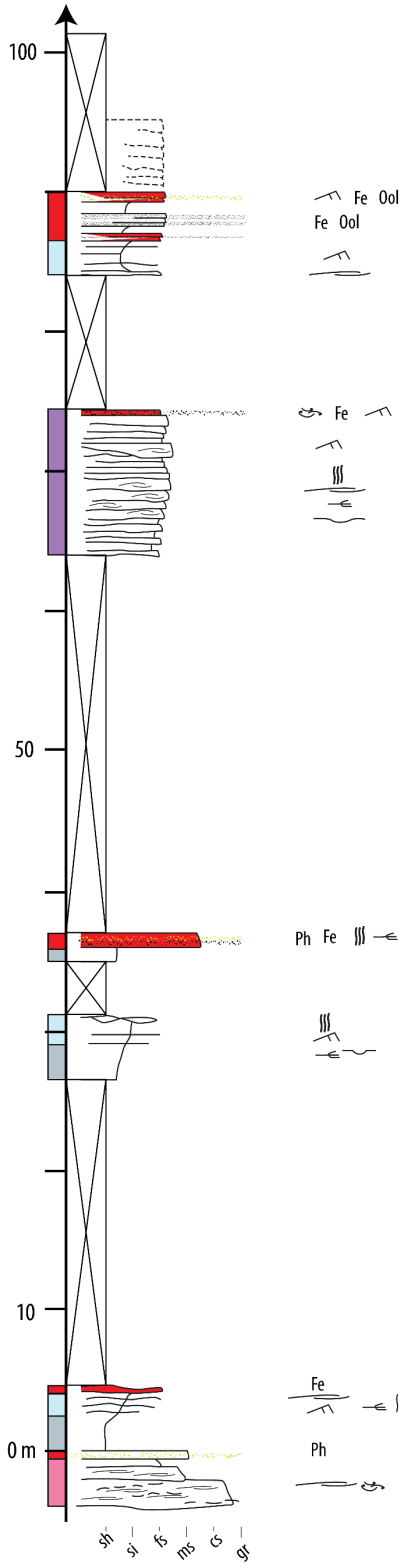

Supplementary figure A.9: *Detailed stratigraphic profile of log 15. For location, see Fig. 2.3. For legend, see Fig. 2.14.*

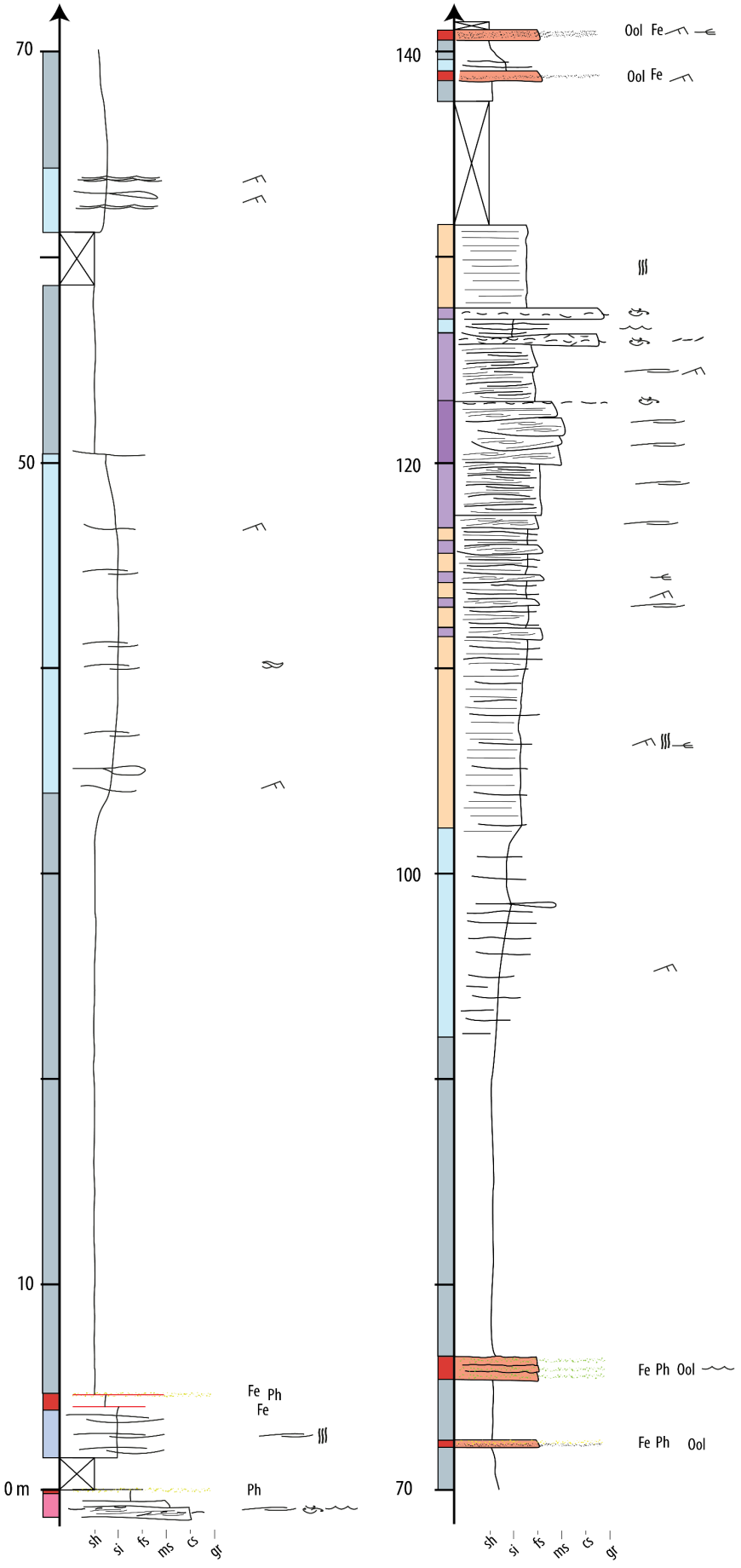

***Supplementary figure A.10**: Detailed stratigraphic profile of log 16. For location, see Fig. 2.3. For legend, see Fig. 2.14.*

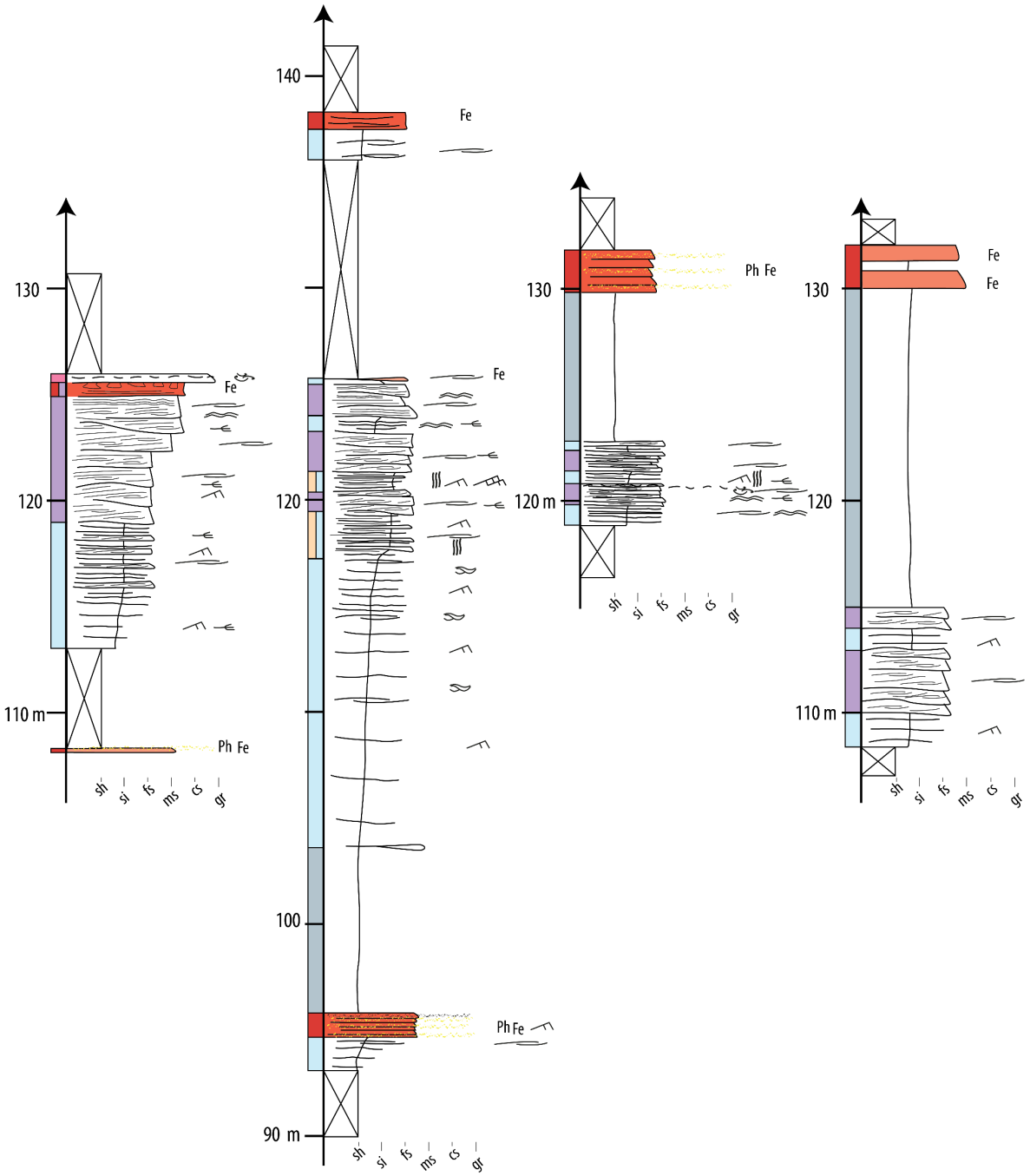

***Supplementary figure A.11**: Detailed stratigraphic profiles of logs 17 to 20 (left to right respectively). For location, see Fig. 2.3. For legend, see Fig. 2.14.*

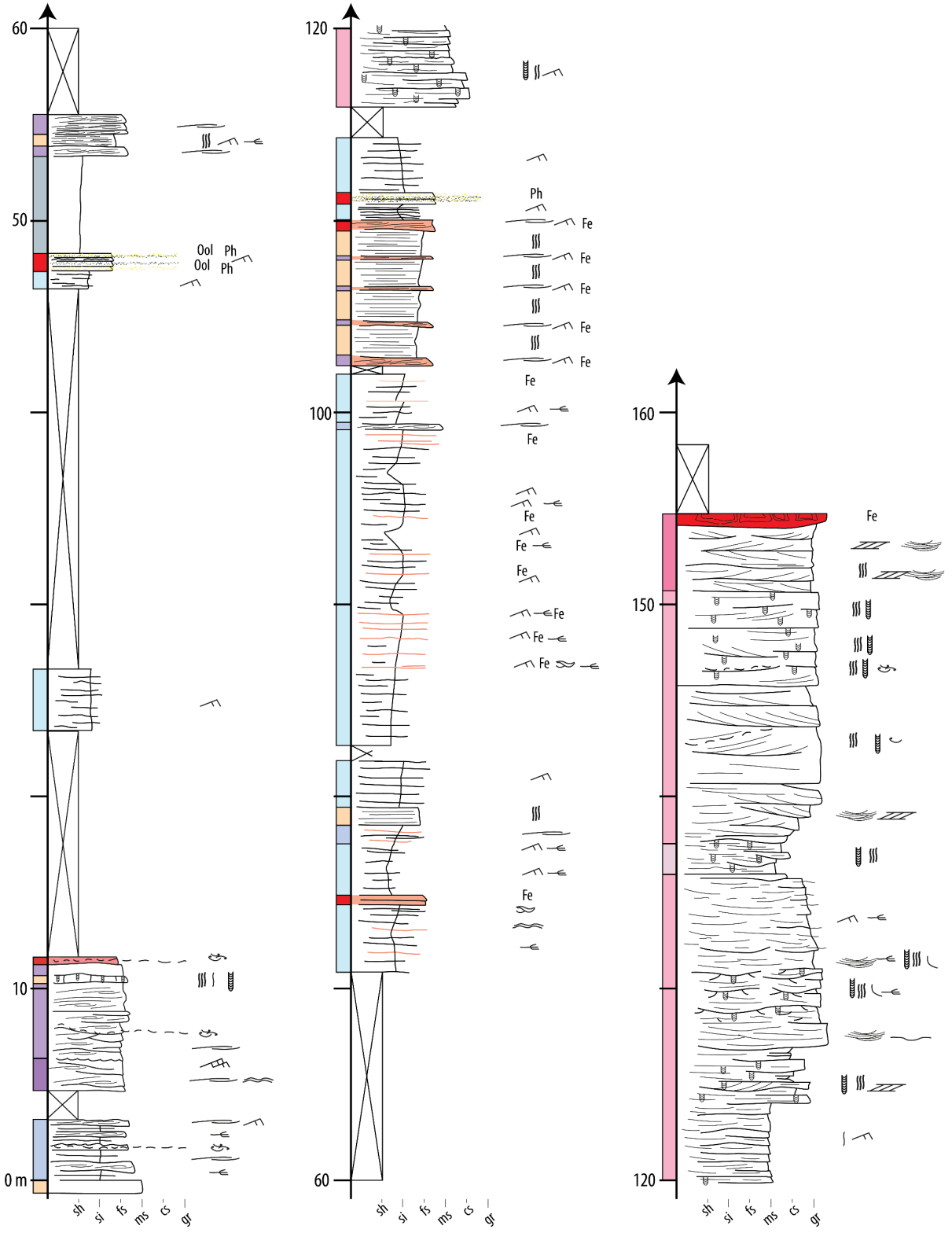

***Supplementary figure A.12**: Detailed stratigraphic profile of log 21. For location, see Fig. 2.3. For legend, see Fig. 2.14.*

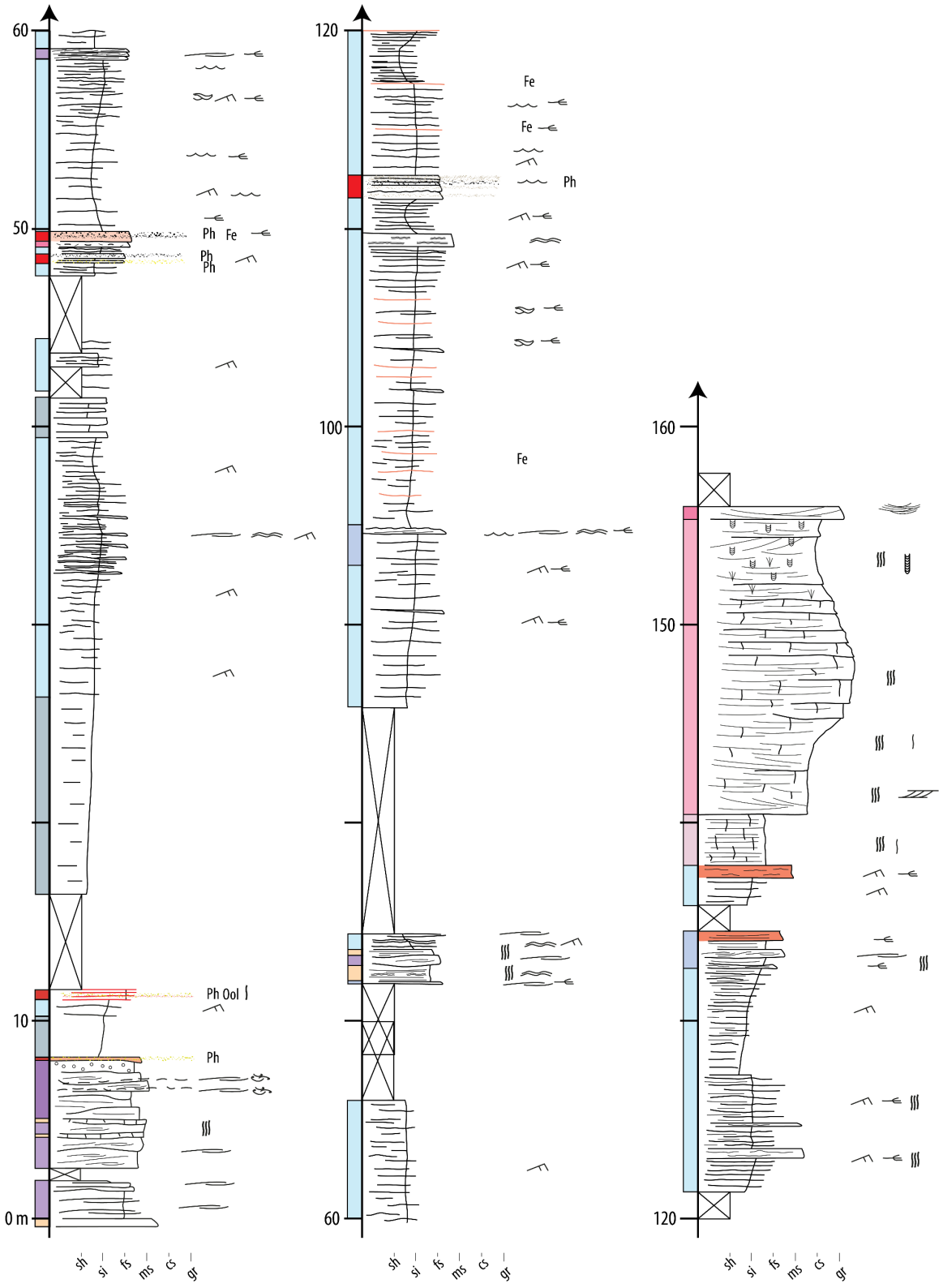

***Supplementary figure A.13**: Detailed stratigraphic profile of log 22. For location, see Fig. 2.3. For legend, see Fig. 2.14.*

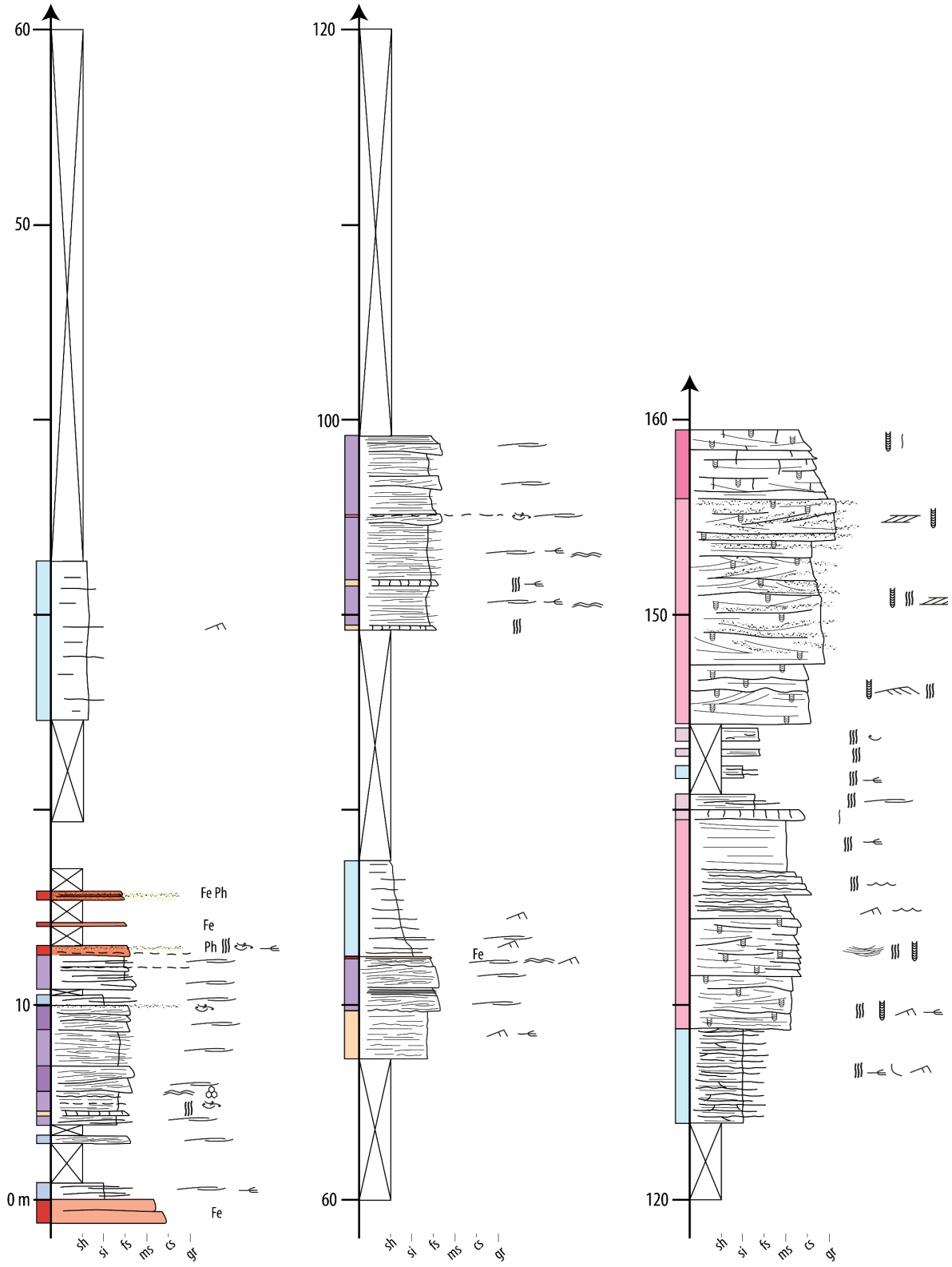

***Supplementary figure A.14**: Detailed stratigraphic profile of log 23. For location, see Fig. 2.3. For legend, see Fig. 2.14.*

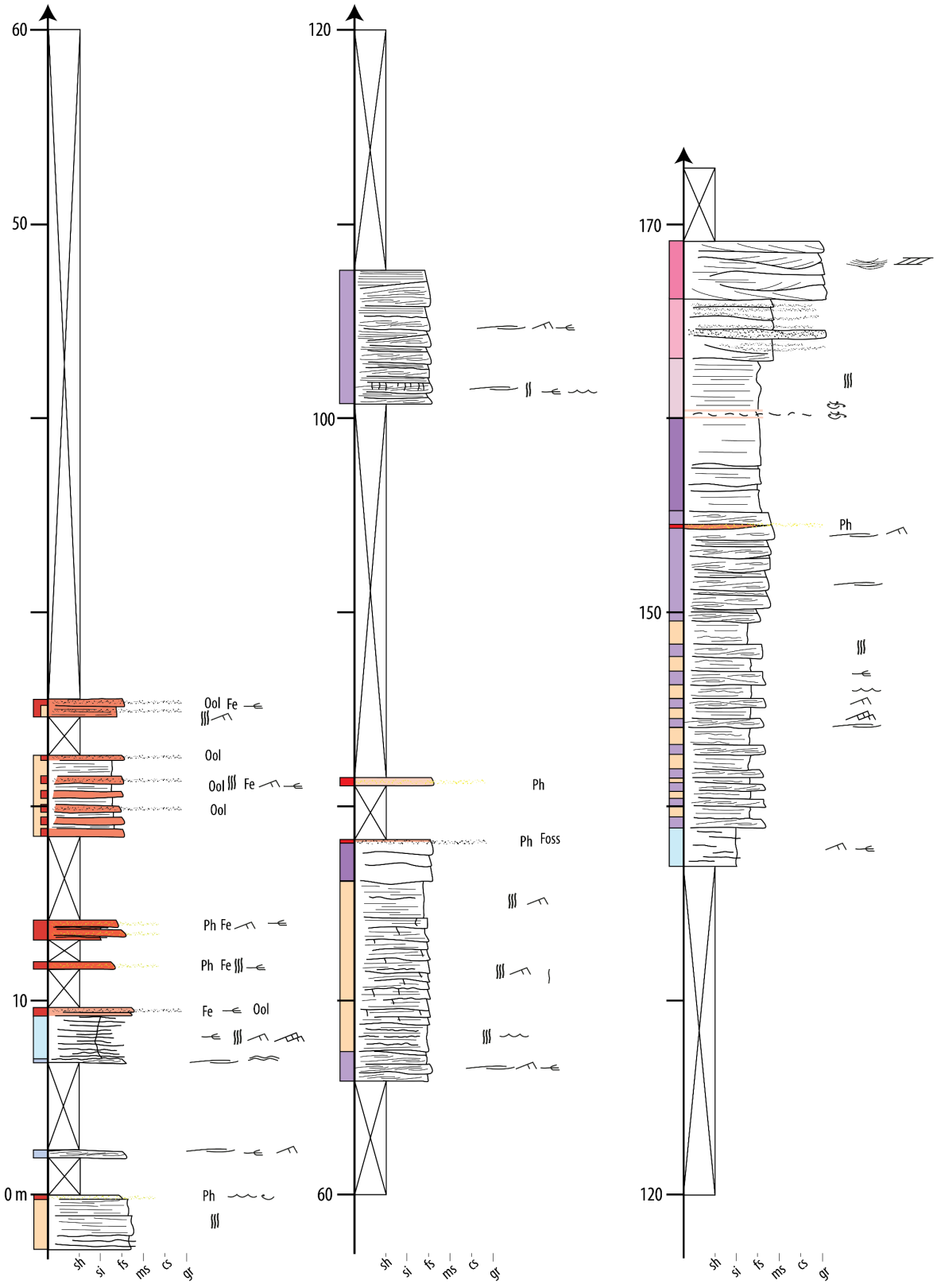

***Supplementary figure A.15**: Detailed stratigraphic profile of log 24. For location, see Fig. 2.3. For legend, see Fig. 2.14.*

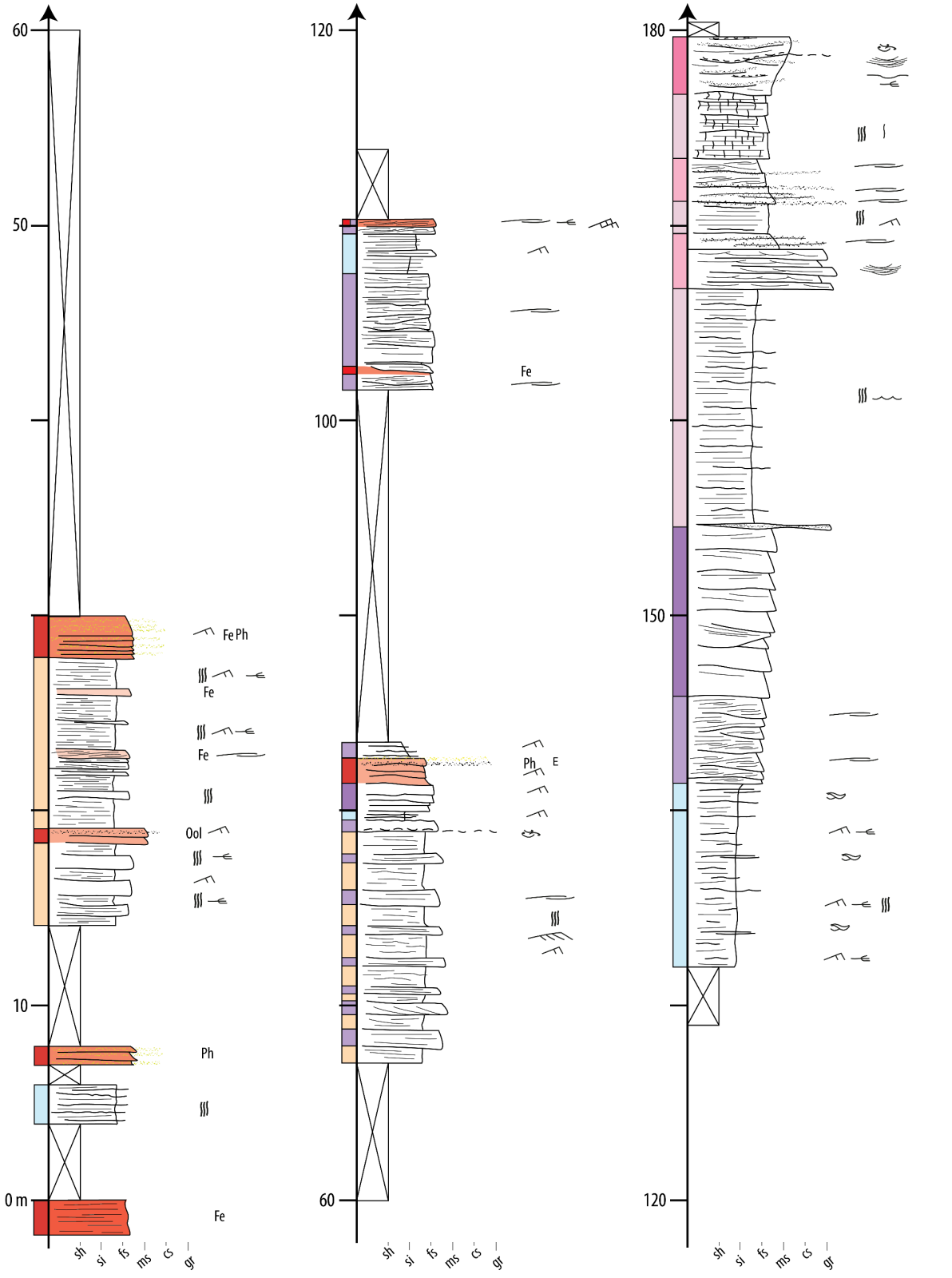

***Supplementary figure A.16**: Detailed stratigraphic profile of log 25. For location, see Fig. 2.3. For legend, see Fig. 2.14.*

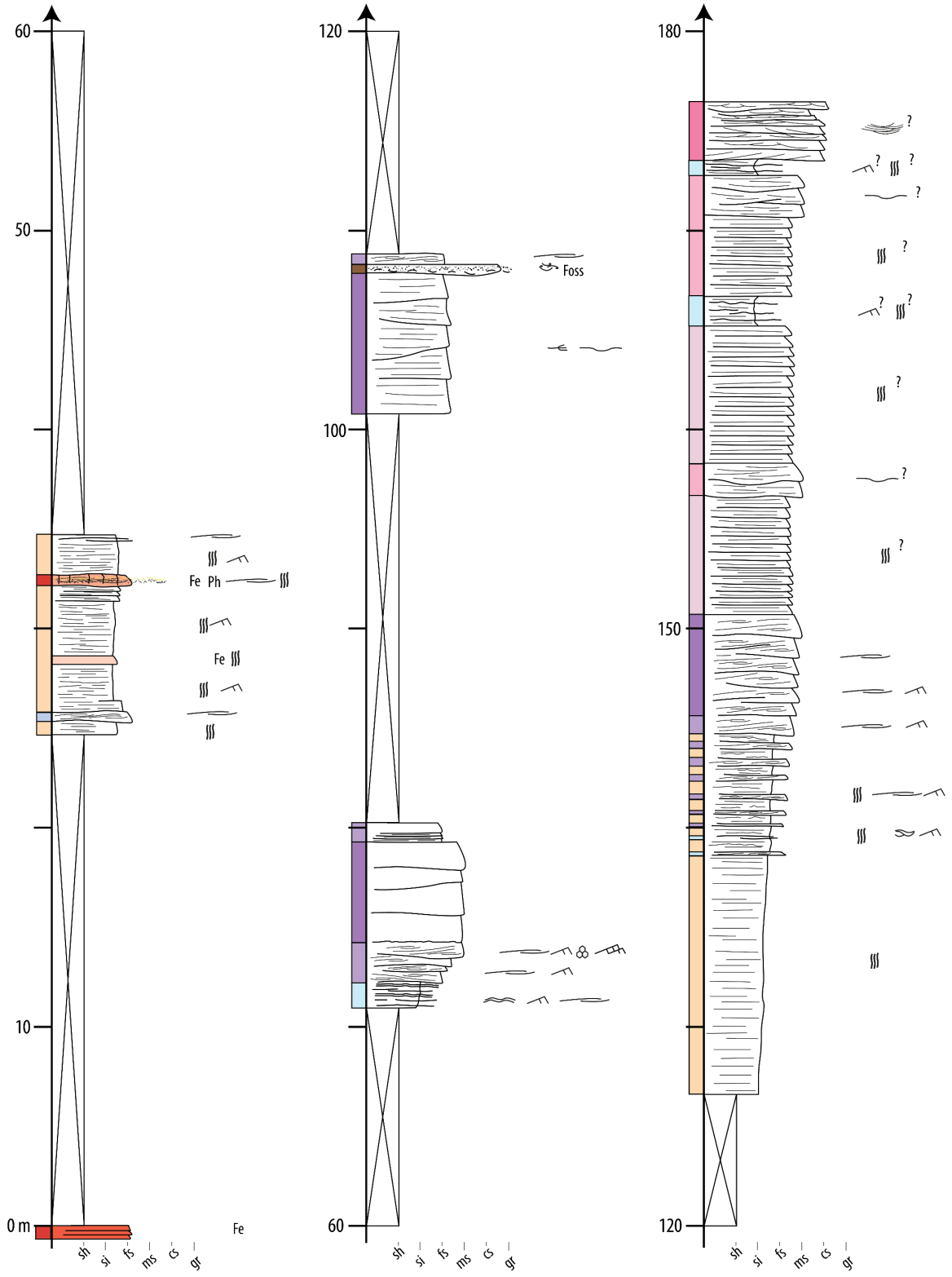

***Supplementary figure A.17**: Detailed stratigraphic profile of log 26. For location, see Fig. 2.3. For legend, see Fig. 2.14.*

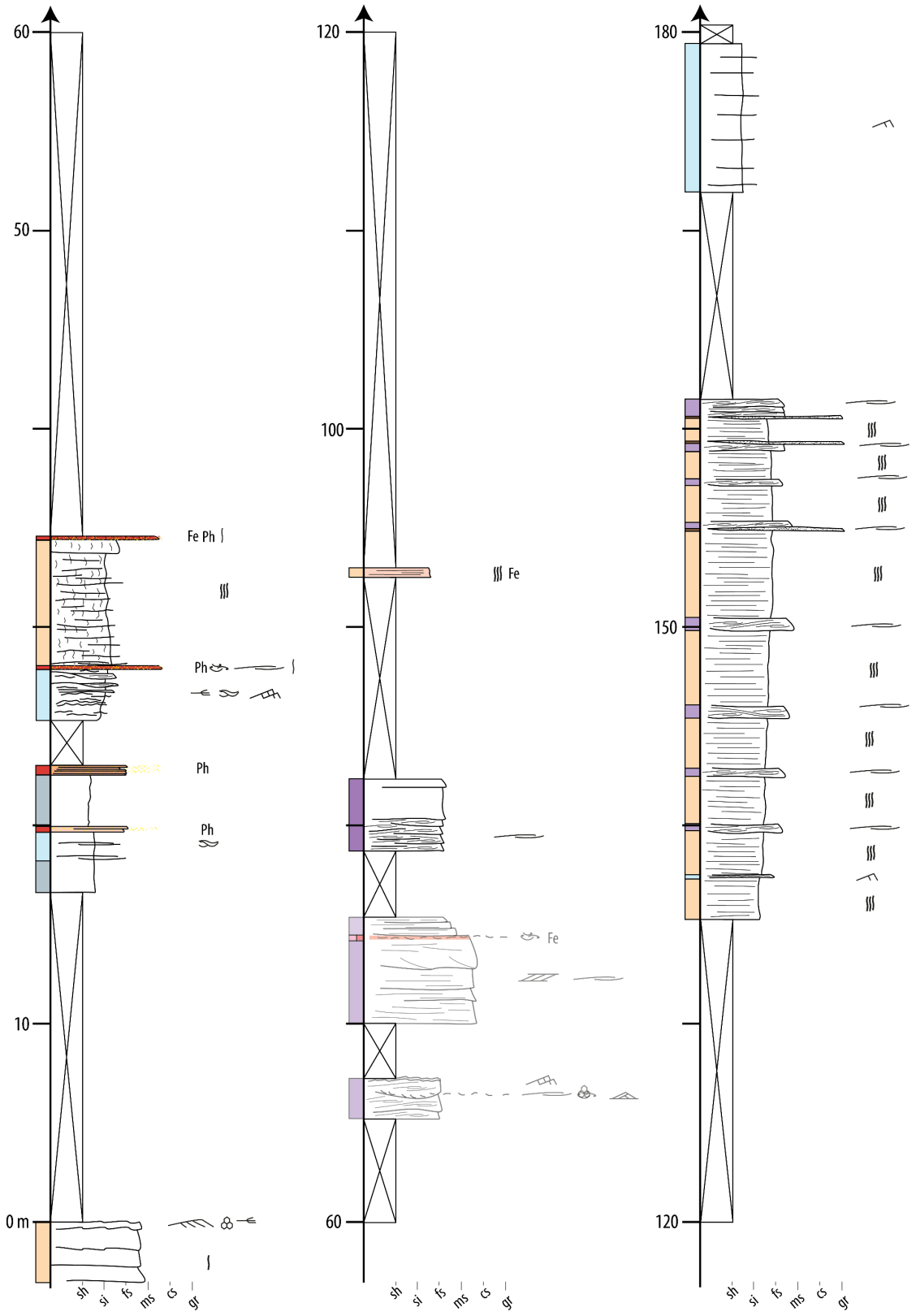

***Supplementary figure A.18**: Detailed stratigraphic profile of log 27. For location, see Fig. 2.3. For legend, see Fig. 2.14.*

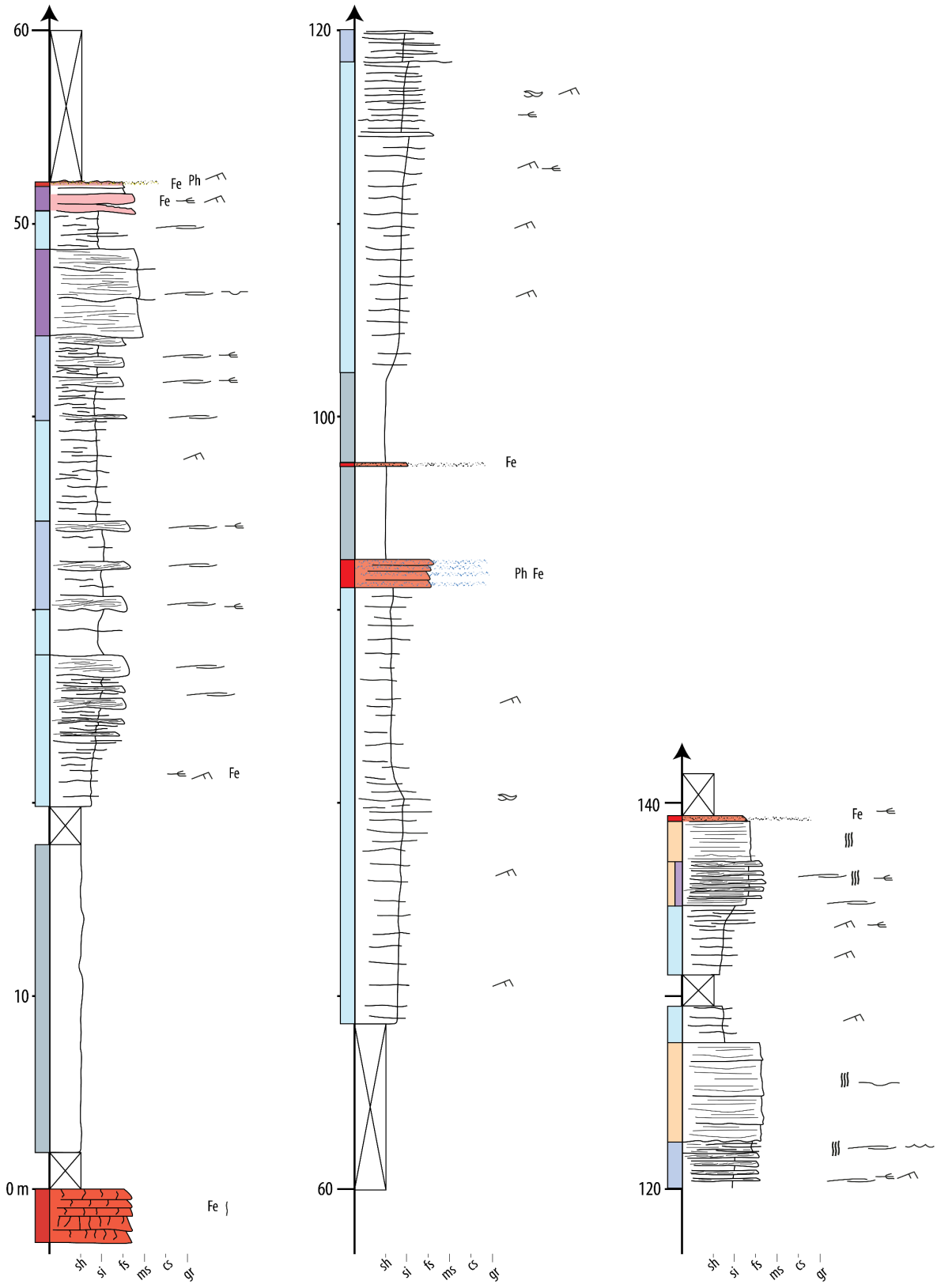

***Supplementary figure A.19**: Detailed stratigraphic profile of log 28. For location, see Fig. 2.3. For legend, see Fig. 2.14.*

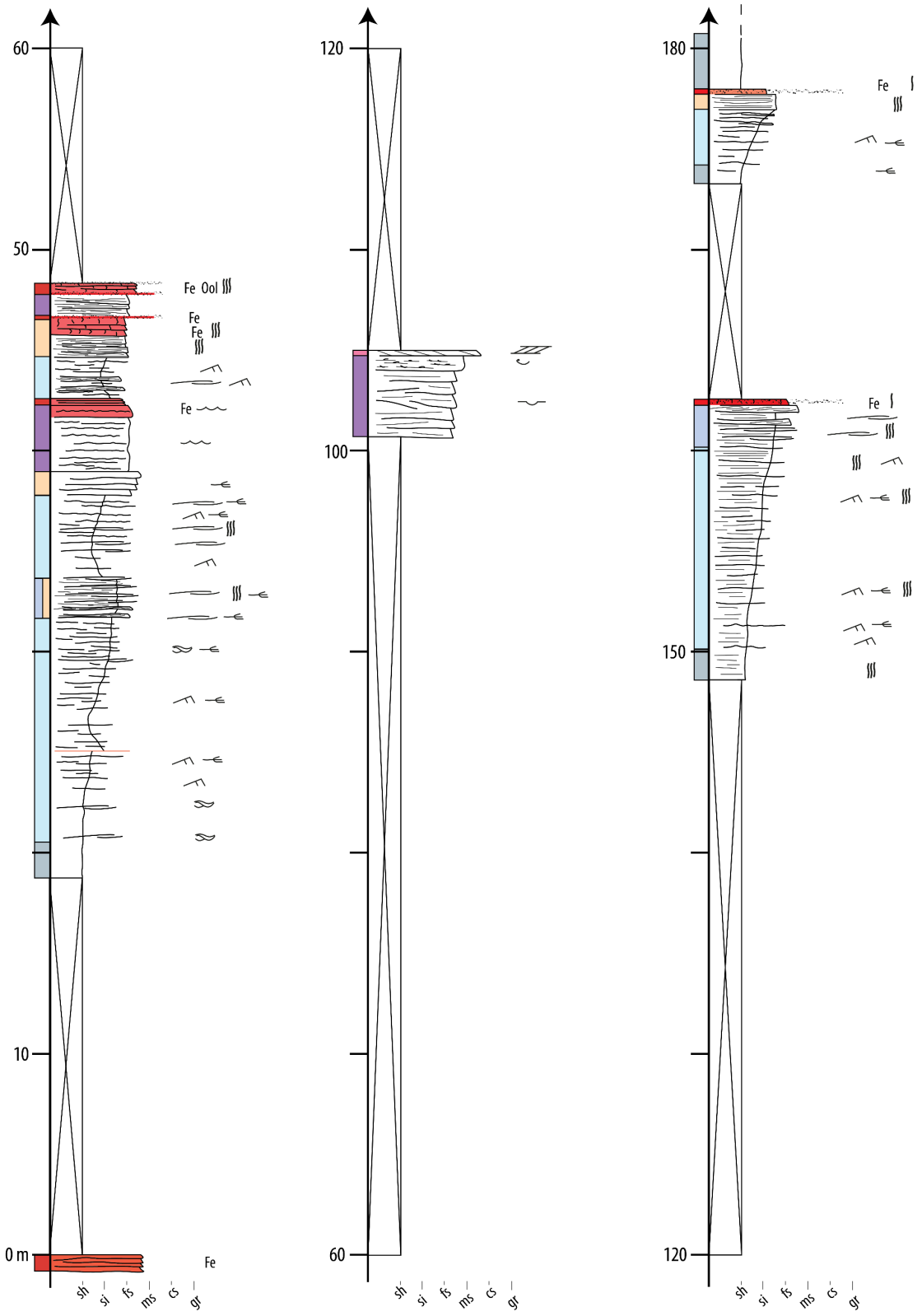

Supplementary figure A.20: *Detailed stratigraphic profile of log 29. For location, see Fig. 2.3. For legend, see Fig. 2.14.*

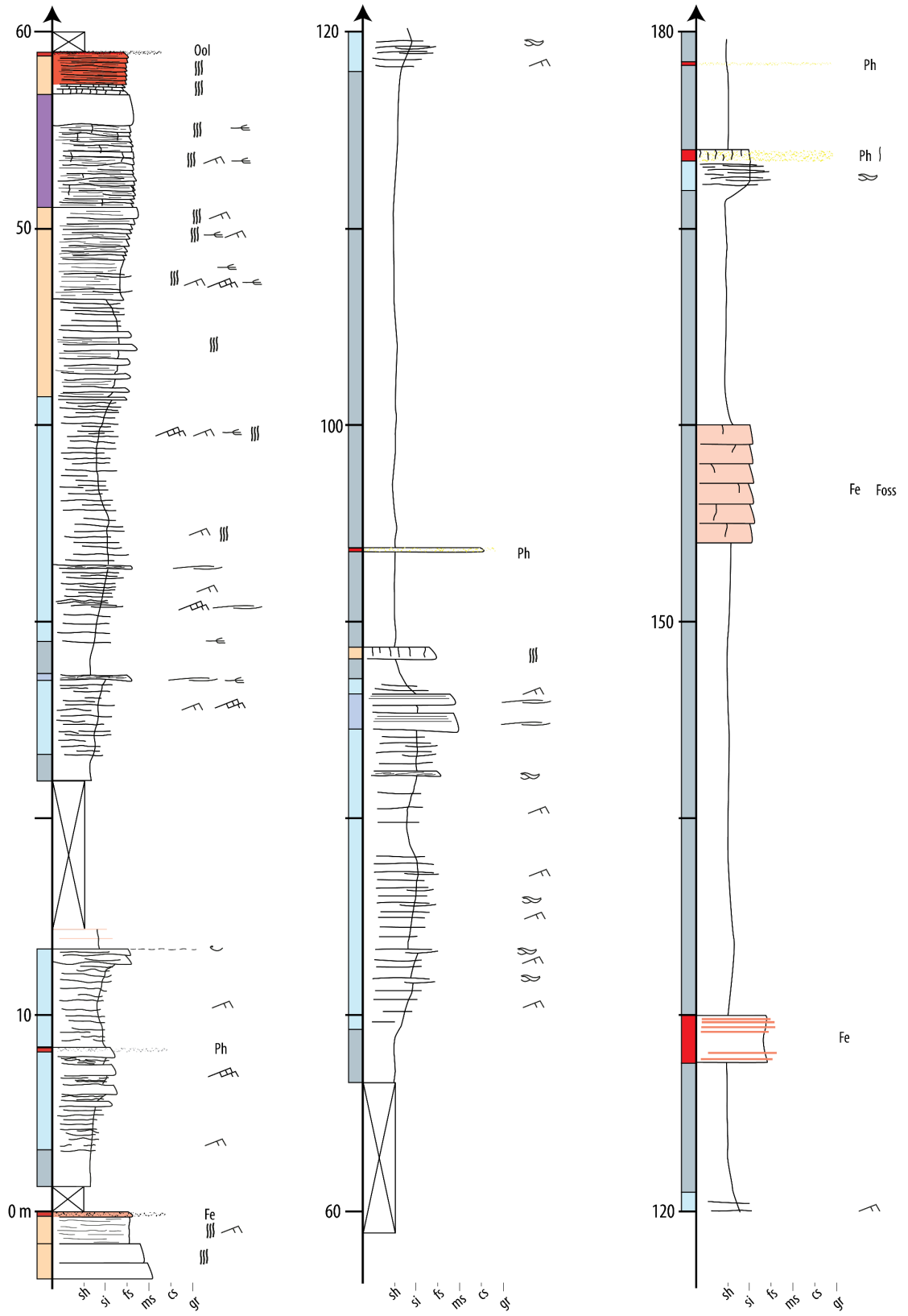

***Supplementary figure A.21**: Detailed stratigraphic profile of log 30. For location, see Fig. 2.3. For legend, see Fig. 2.14.*

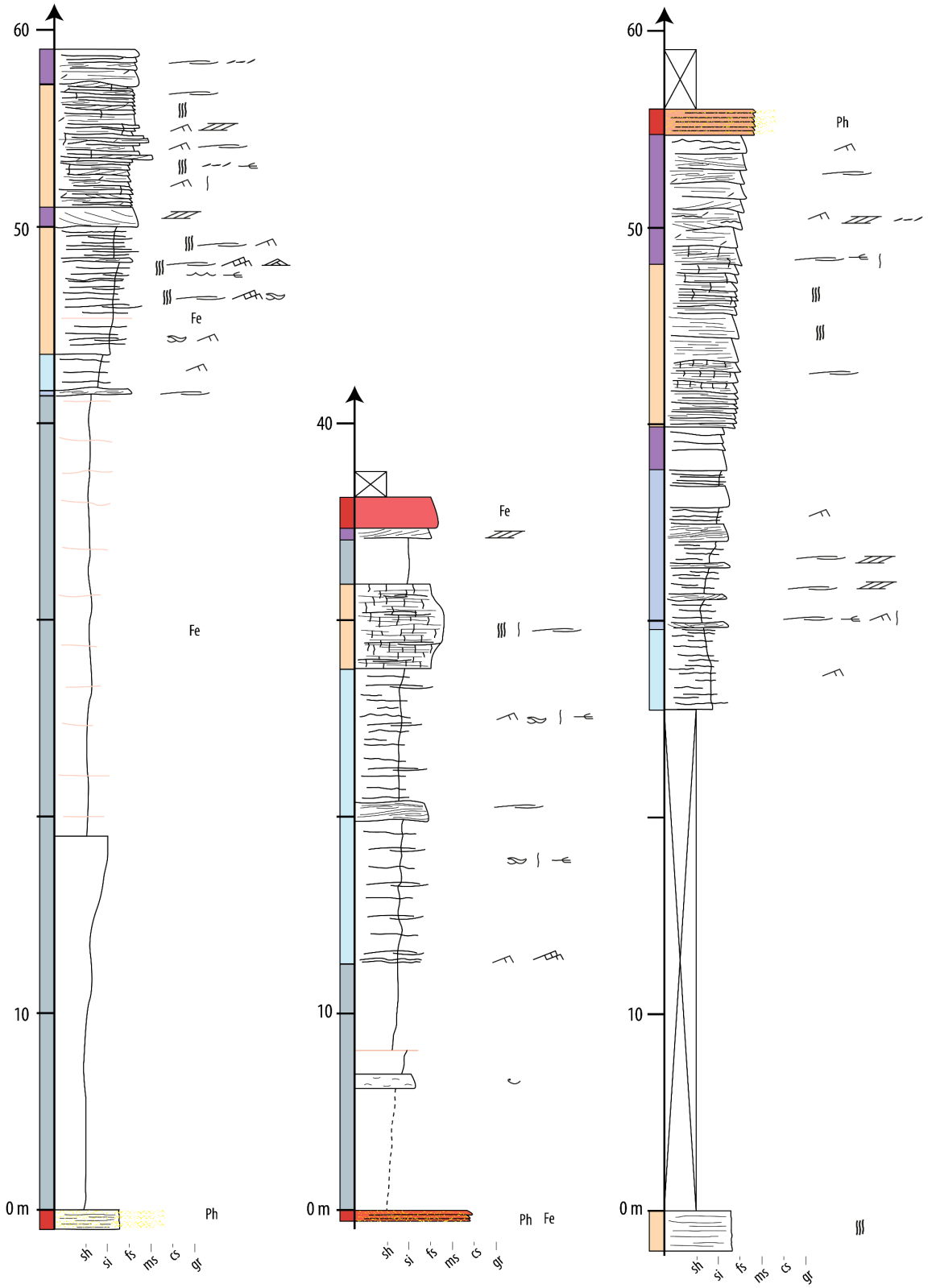

***Supplementary figure A.22**: Detailed stratigraphic profiles of logs 31 to 33 (left to right respectively). For location, see Fig. 2.3. For legend, see Fig. 2.14.*

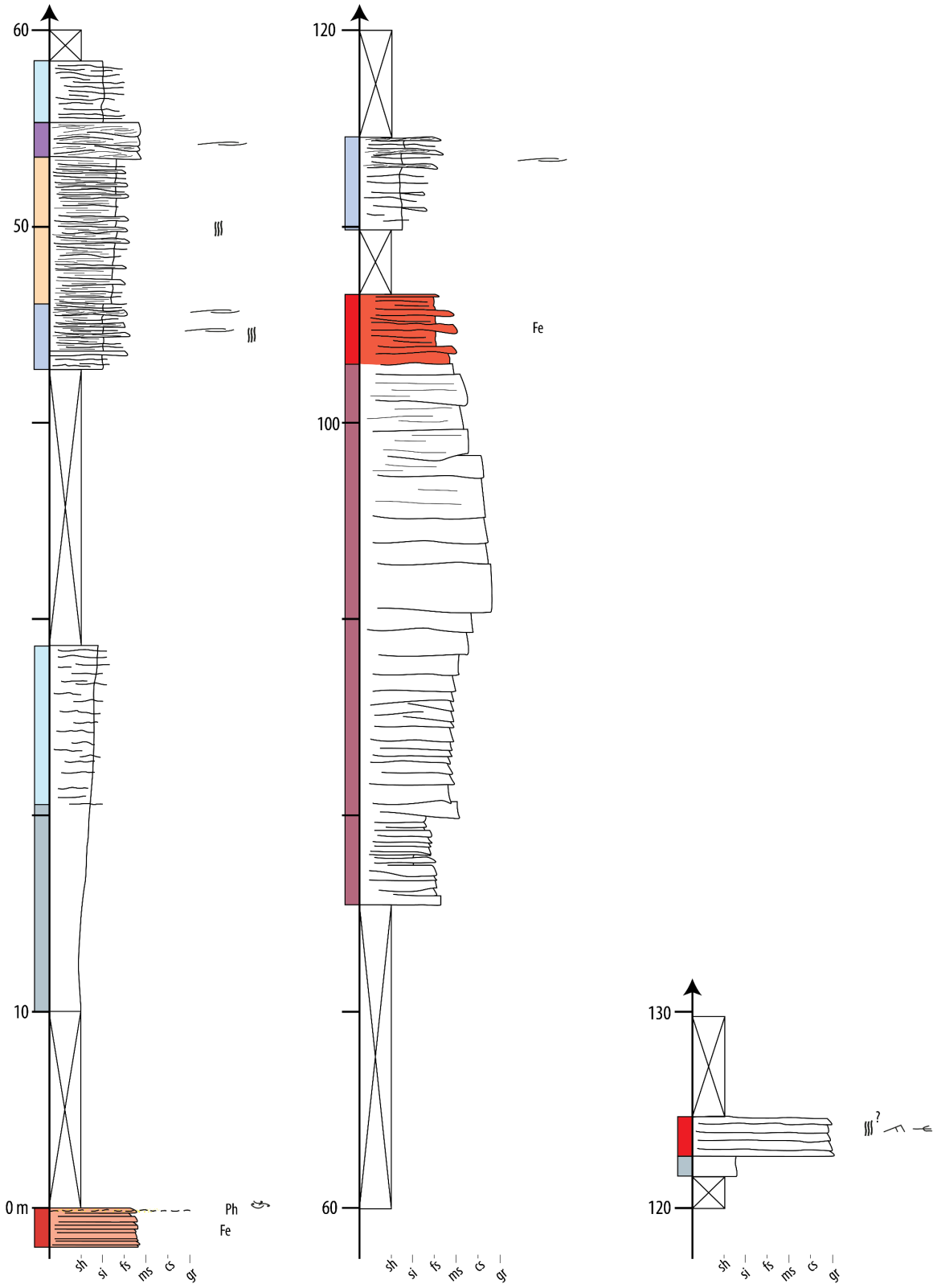

***Supplementary figure A.23**: Detailed stratigraphic profile of log 34. For location, see Fig. 2.3. For legend, see Fig. 2.14.*

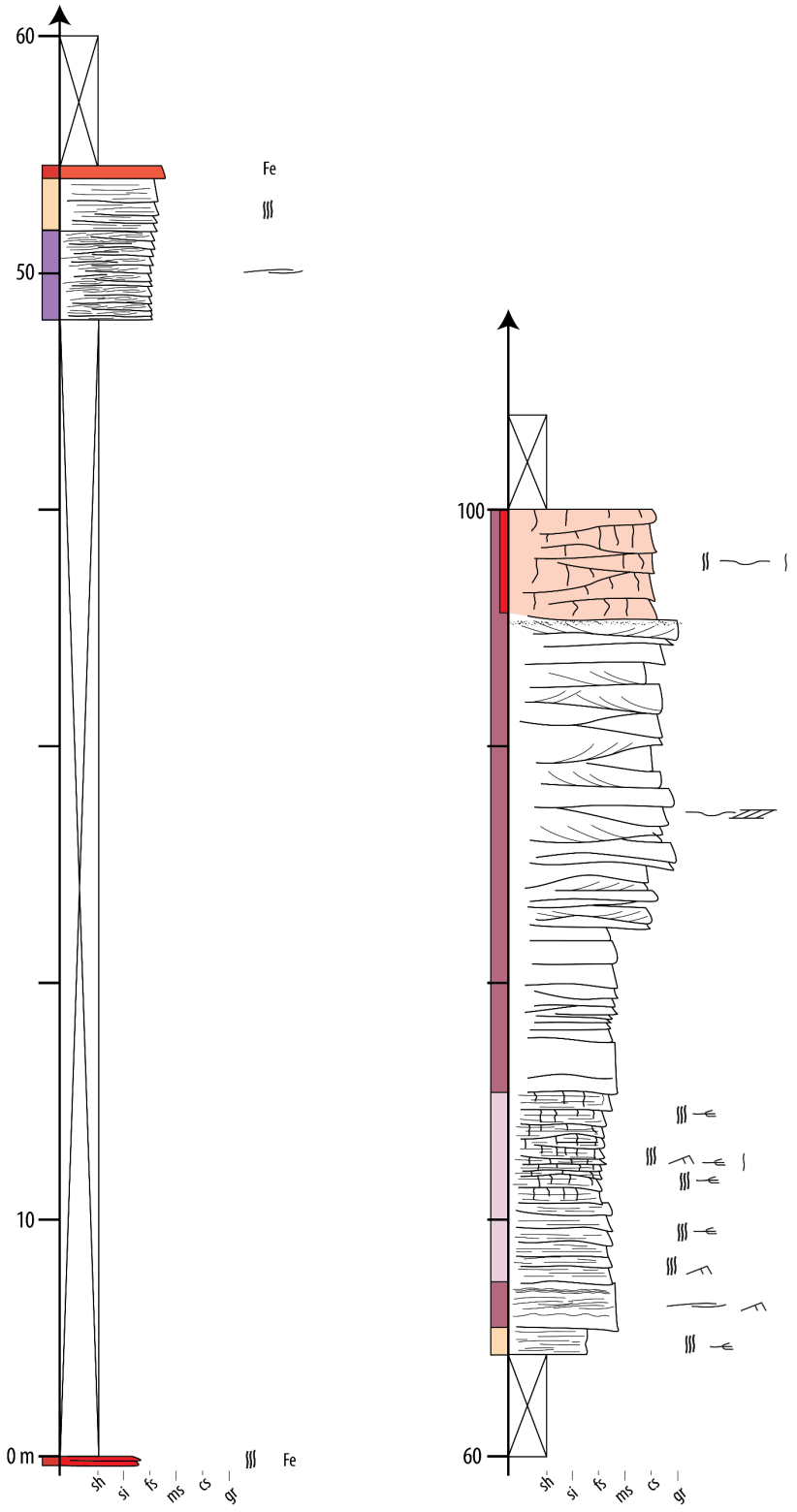

***Supplementary figure A.24**: Detailed stratigraphic profile of log 35. For location, see Fig. 2.3. For legend, see Fig. 2.14.*

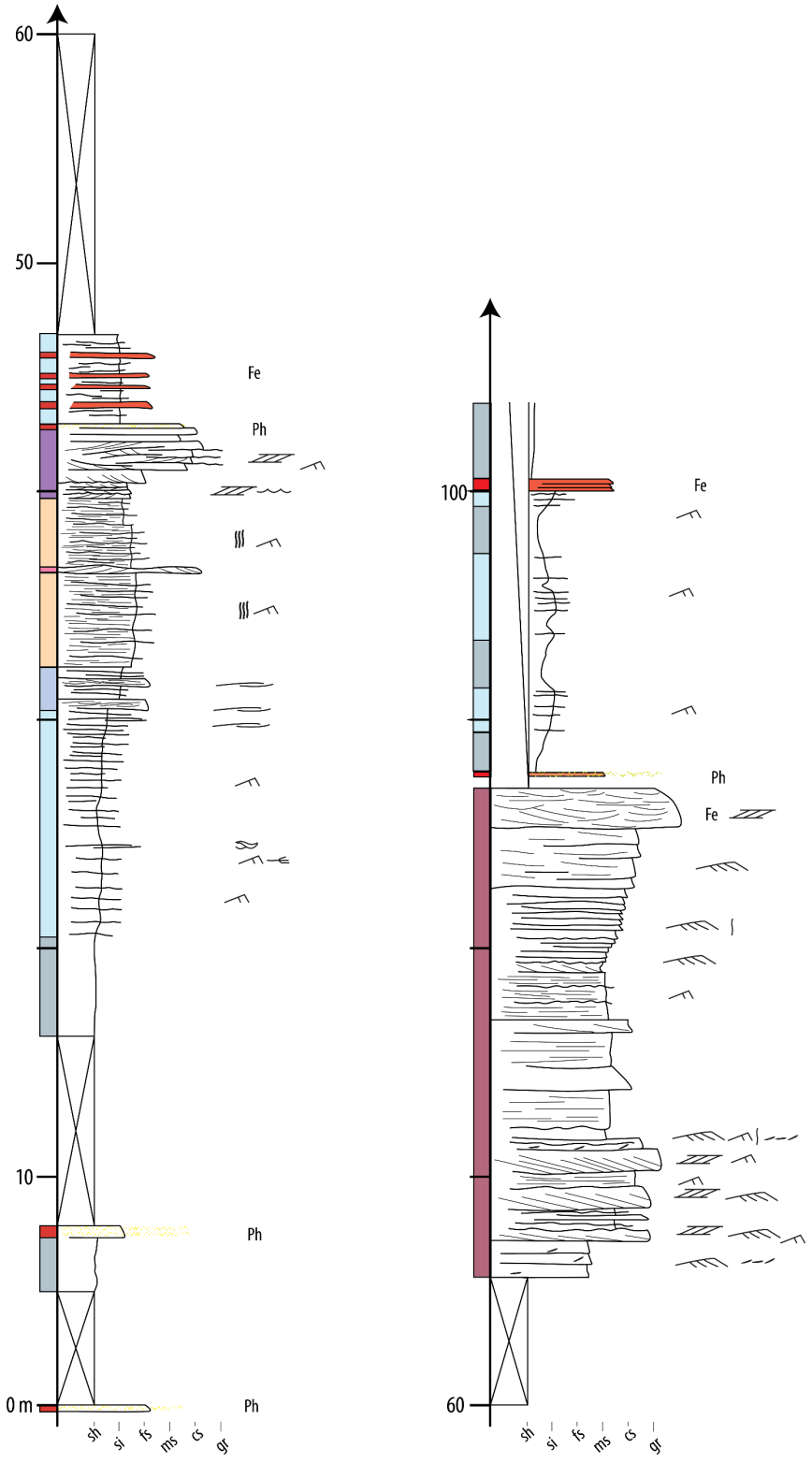

***Supplementary figure A.25**: Detailed stratigraphic profile of log 36. For location, see Fig. 2.3. For legend, see Fig. 2.14.*

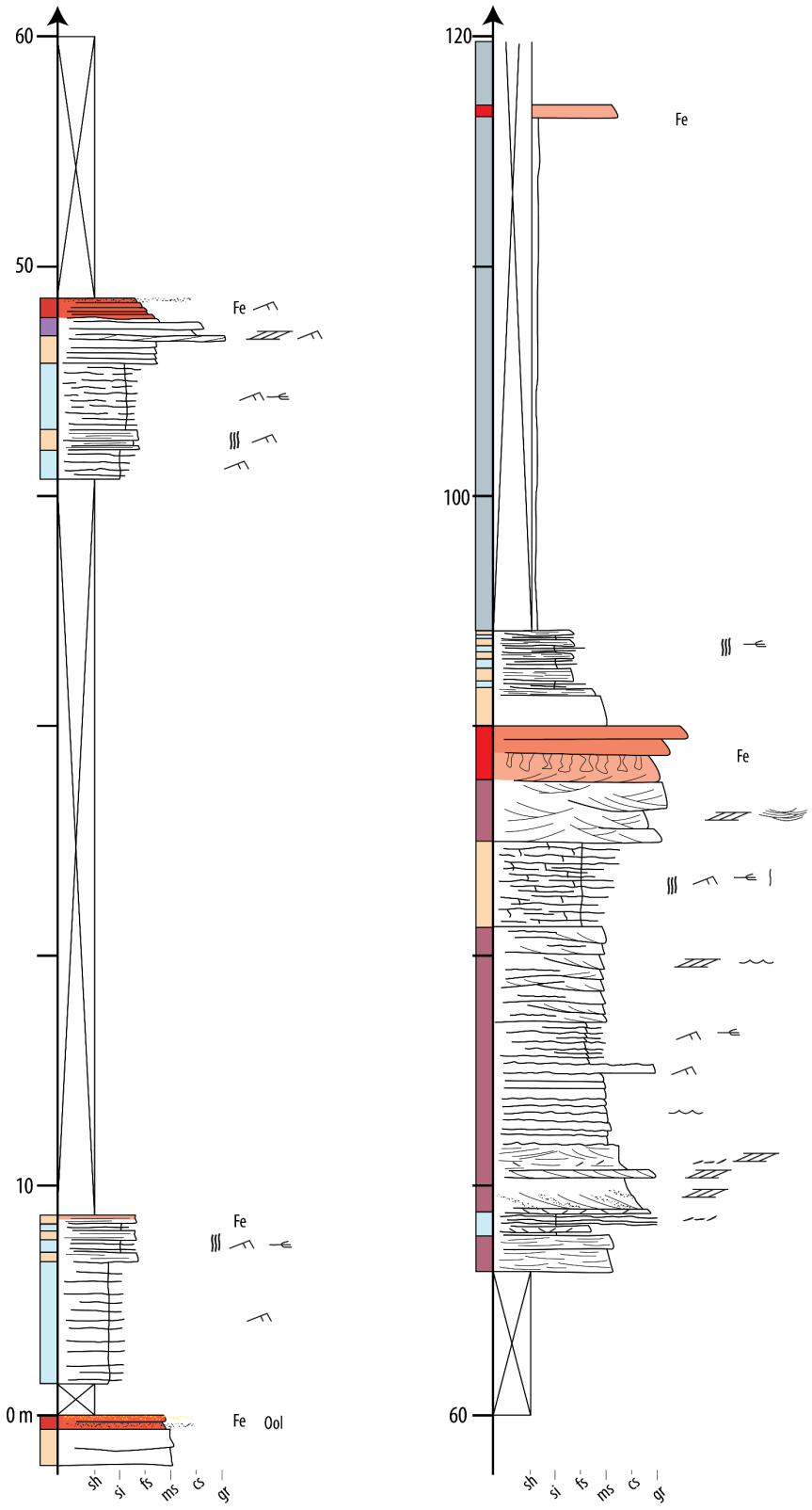

***Supplementary figure A.26**: Detailed stratigraphic profile of log 37. For location, see Fig. 2.3. For legend, see Fig. 2.14.*

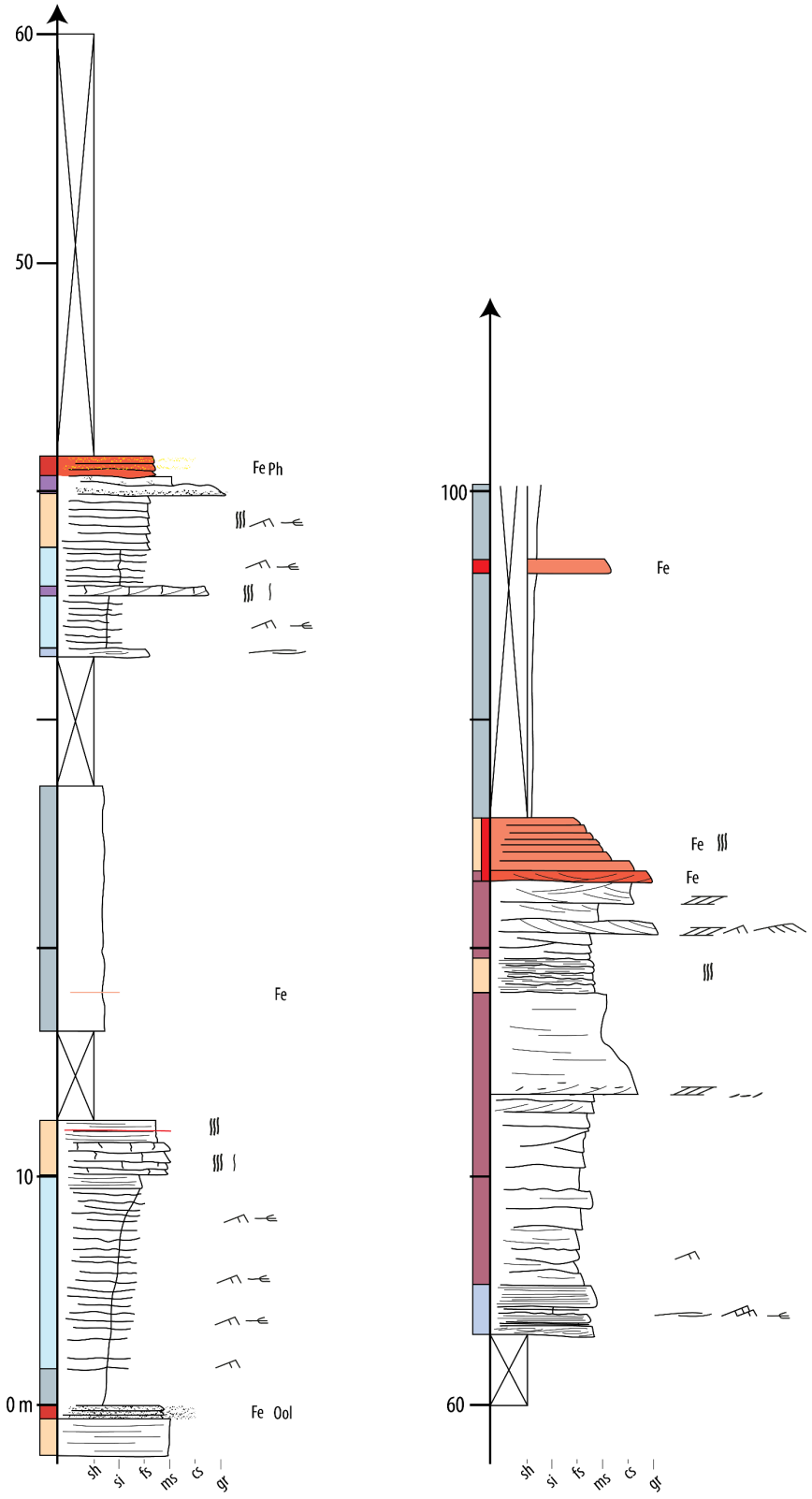

***Supplementary figure A.27**: Detailed stratigraphic profile of log 38. For location, see Fig. 2.3. For legend, see Fig. 2.14.*

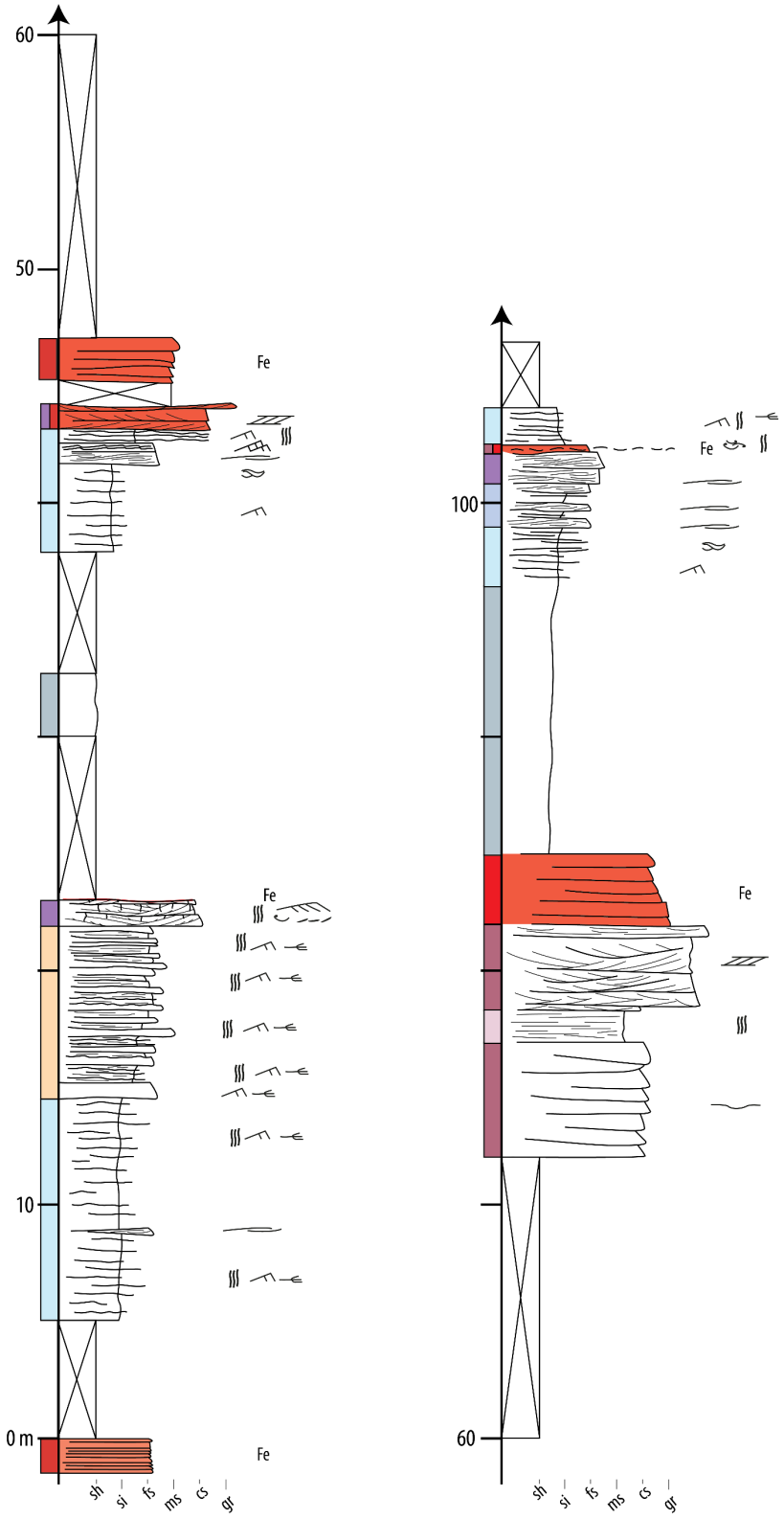

***Supplementary figure A.28**: Detailed stratigraphic profile of log 39. For location, see Fig. 2.3. For legend, see Fig. 2.14.*

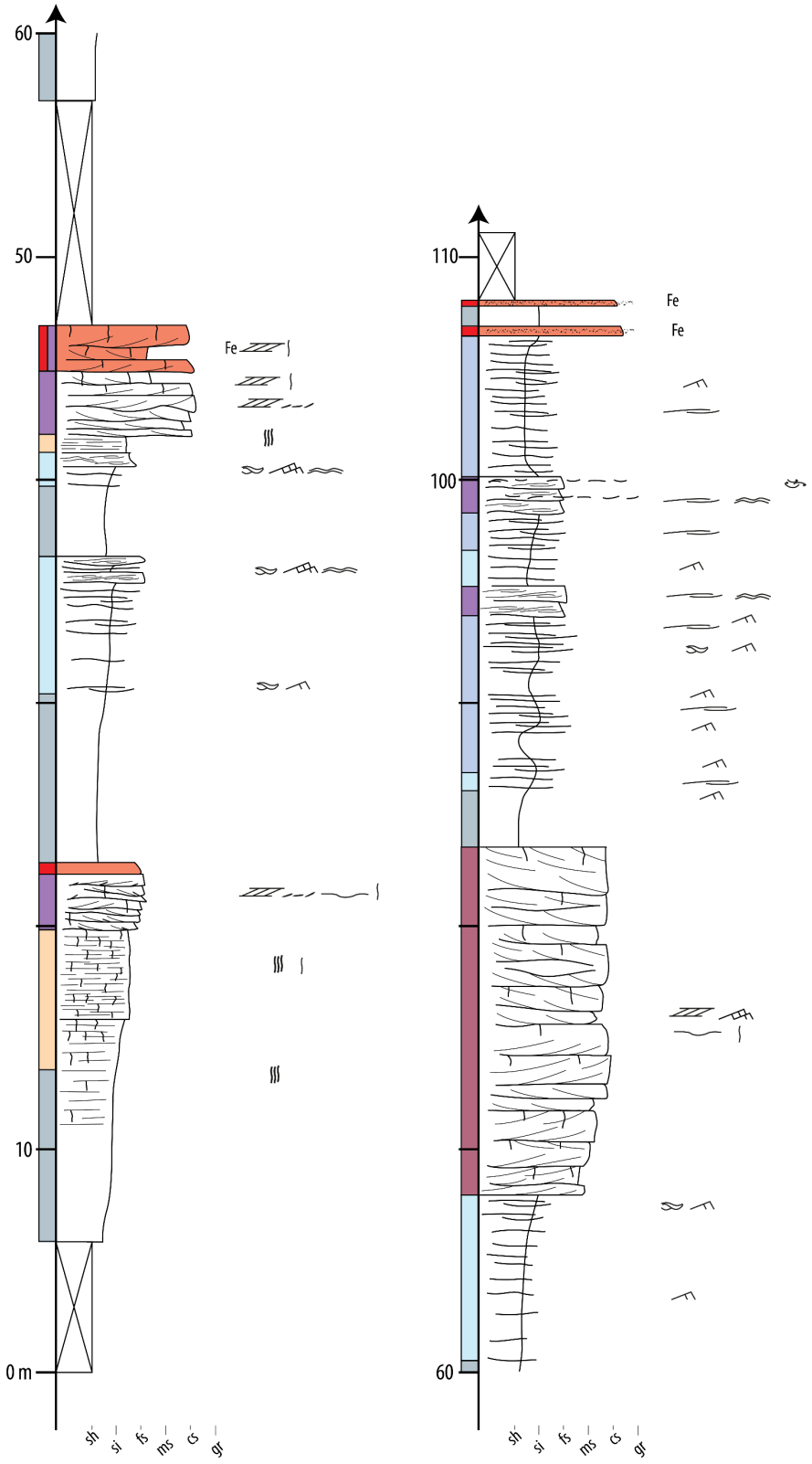

***Supplementary figure A.29**: Detailed stratigraphic profile of log 40. For location, see Fig. 2.3. For legend, see Fig. 2.14.*

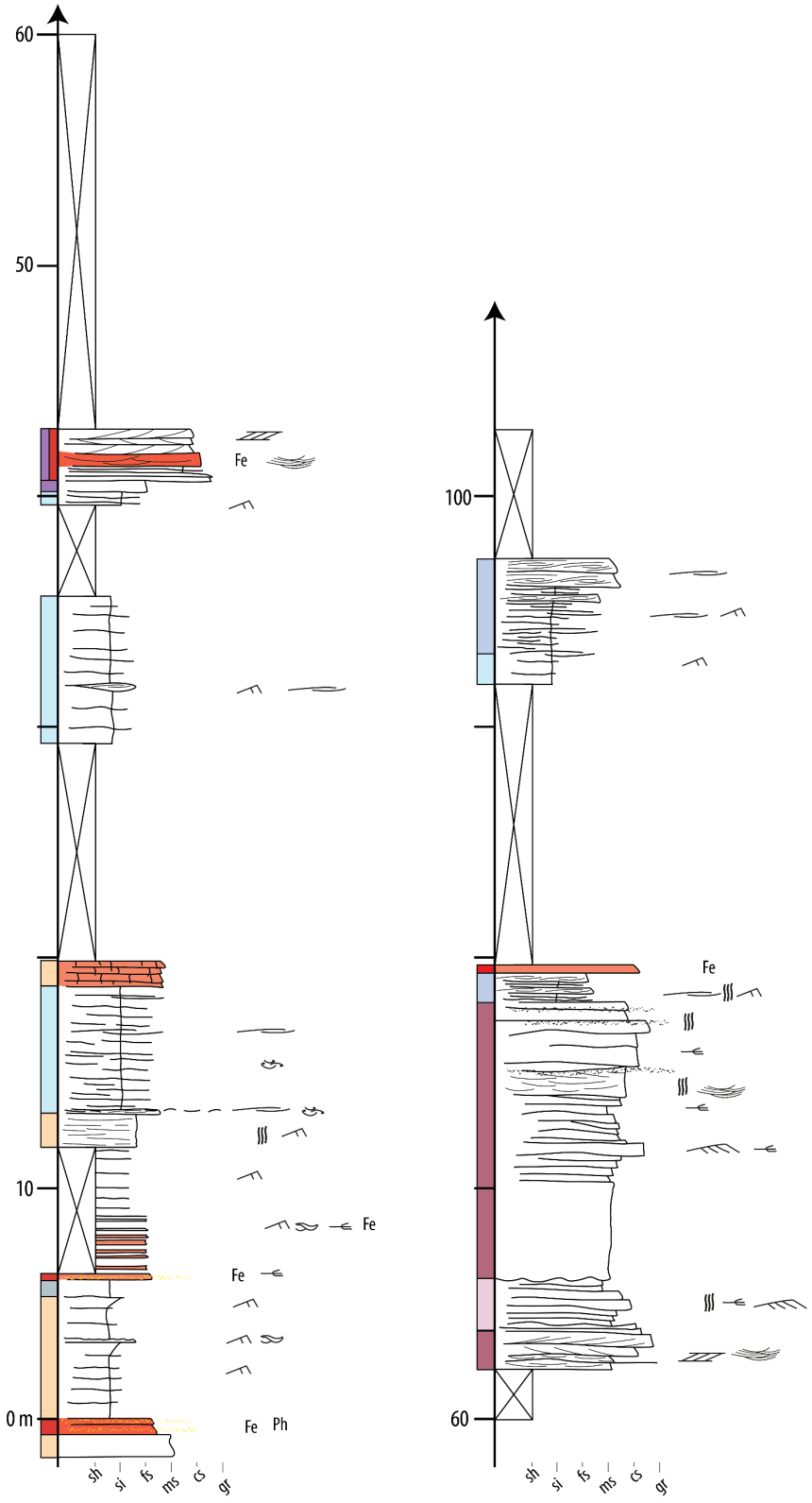

***Supplementary figure A.30**: Detailed stratigraphic profile of log 41. For location, see Fig. 2.3. For legend, see Fig. 2.14.*

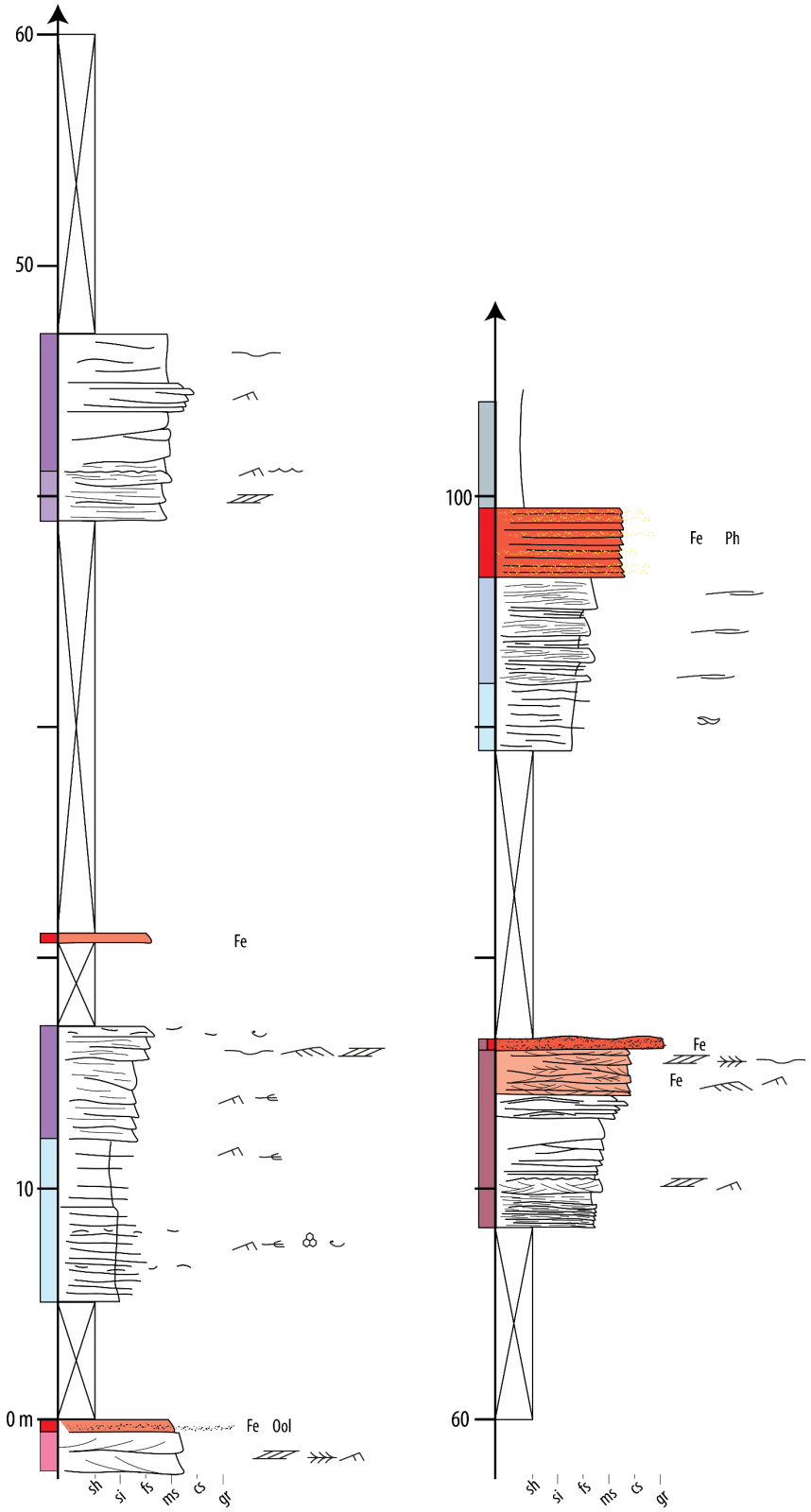

***Supplementary figure A.31**: Detailed stratigraphic profile of log 42. For location, see Fig. 2.3. For legend, see Fig. 2.14.*

Appendix B

Supplementary materials for Chapter 2

3D photogrammetric reconstruction of stratigraphic profiles

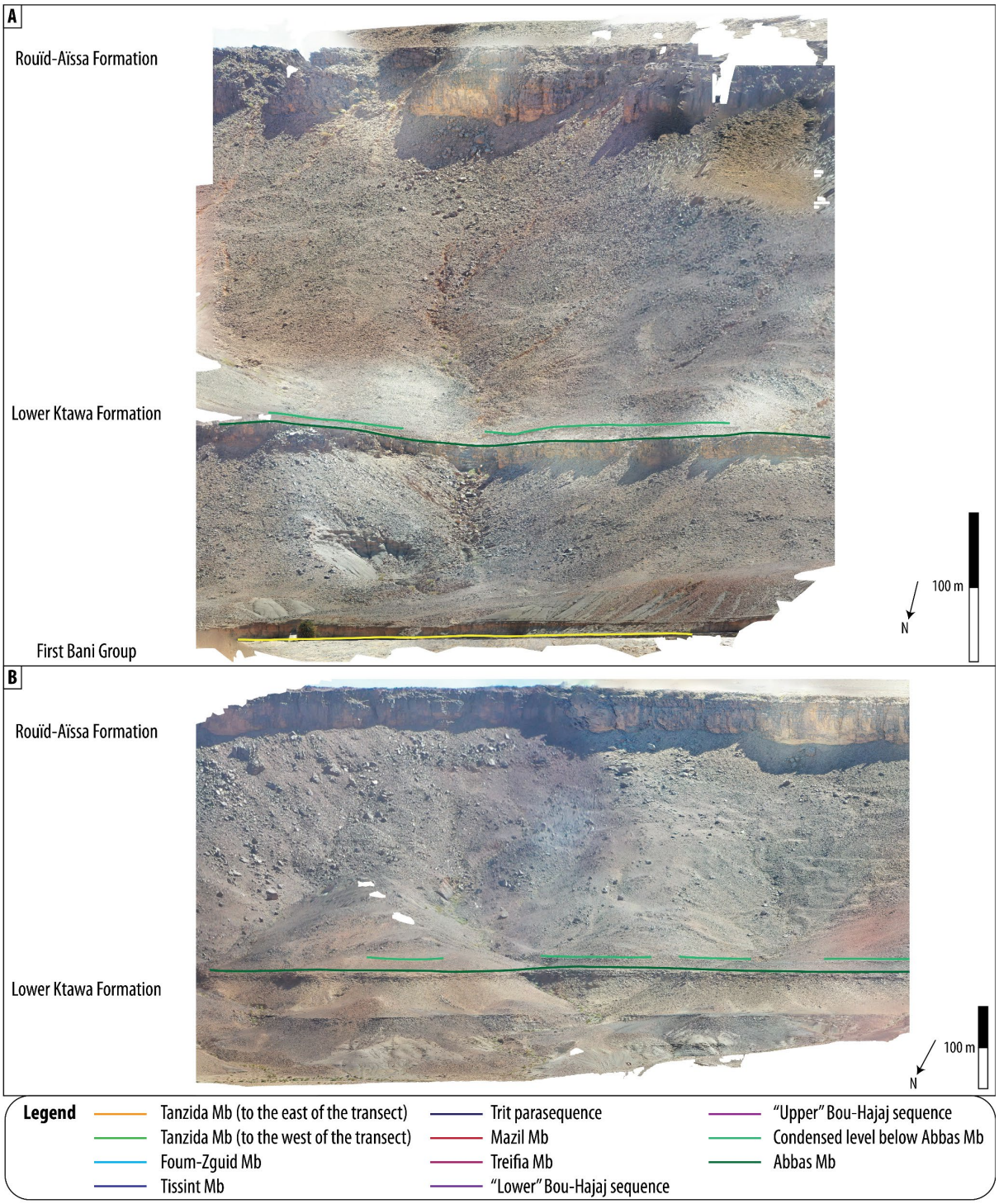

***Figure B.1**: 3D photogrammetric reconstructions from Unmanned Aerial Vehicle (UAV) images of logs 13 and 14. For location, see Fig. 2.3. Colored lines represent the top of a member, sequence, parasequence or characteristic condensel level.*

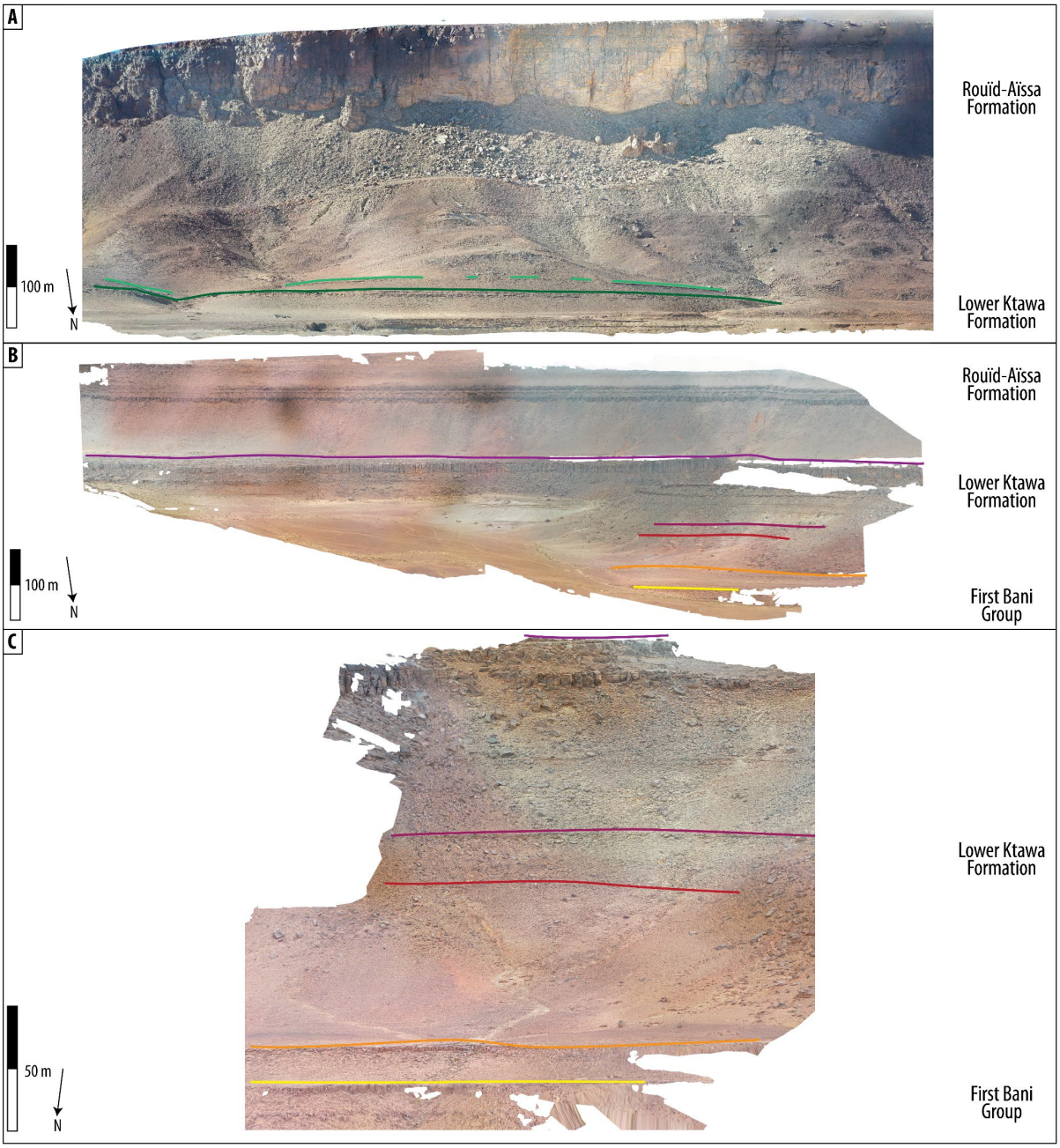

***Figure B.2**: 3D photogrammetric reconstructions from UAV images of logs 15, 21 and 22, respectively to (A), (B), and (C). For location, see Fig. 2.3. For legend, see Fig. B.1.*

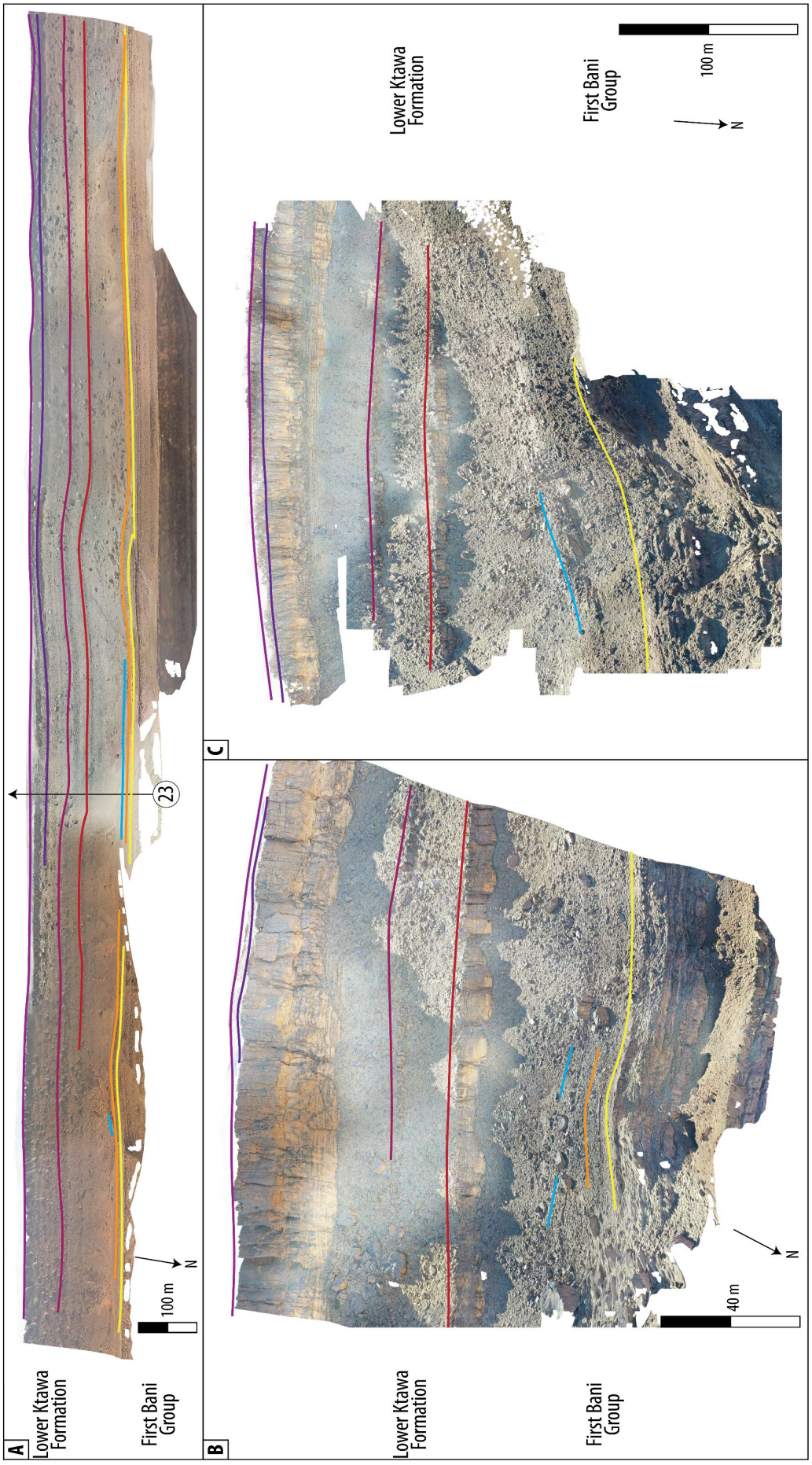

***Figure B.3**: 3D photogrammetric reconstructions from UAV images of logs 23 to 25, respectively to (A), (B), and (C). For location, see Fig. 2.3. For legend, see Fig. B.1.*

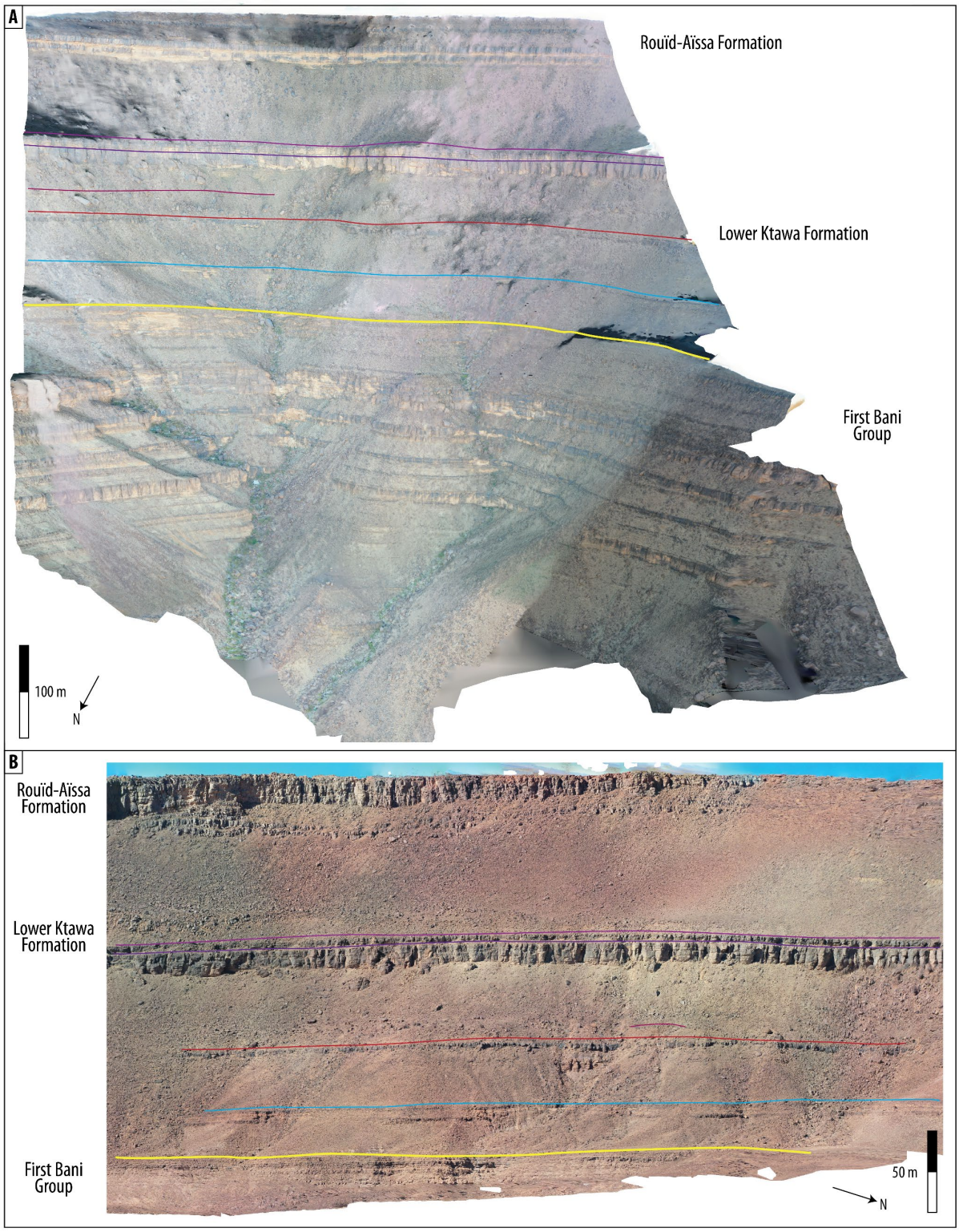

***Figure B.4**: 3D photogrammetric reconstructions from UAV images of logs 26 and 27, respectively to (A) and (B). For location, see Fig. 2.3. For legend, see Fig. B.1.*

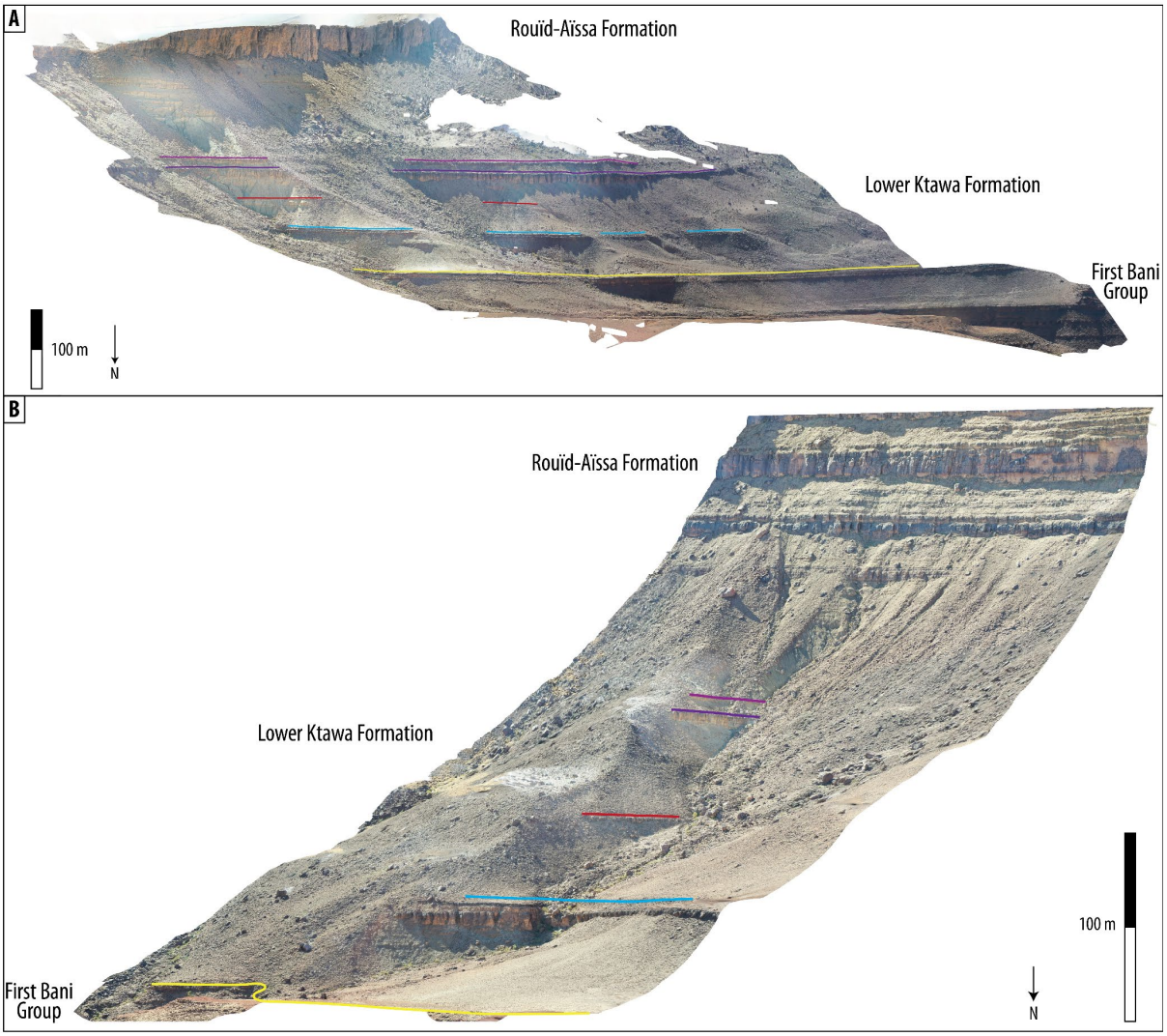

***Figure B.5**: 3D photogrammetric reconstructions from UAV images of logs 28 and 29, respectively to (A) and (B). For location, see Fig. 2.3. For legend, see Fig. B.1.*

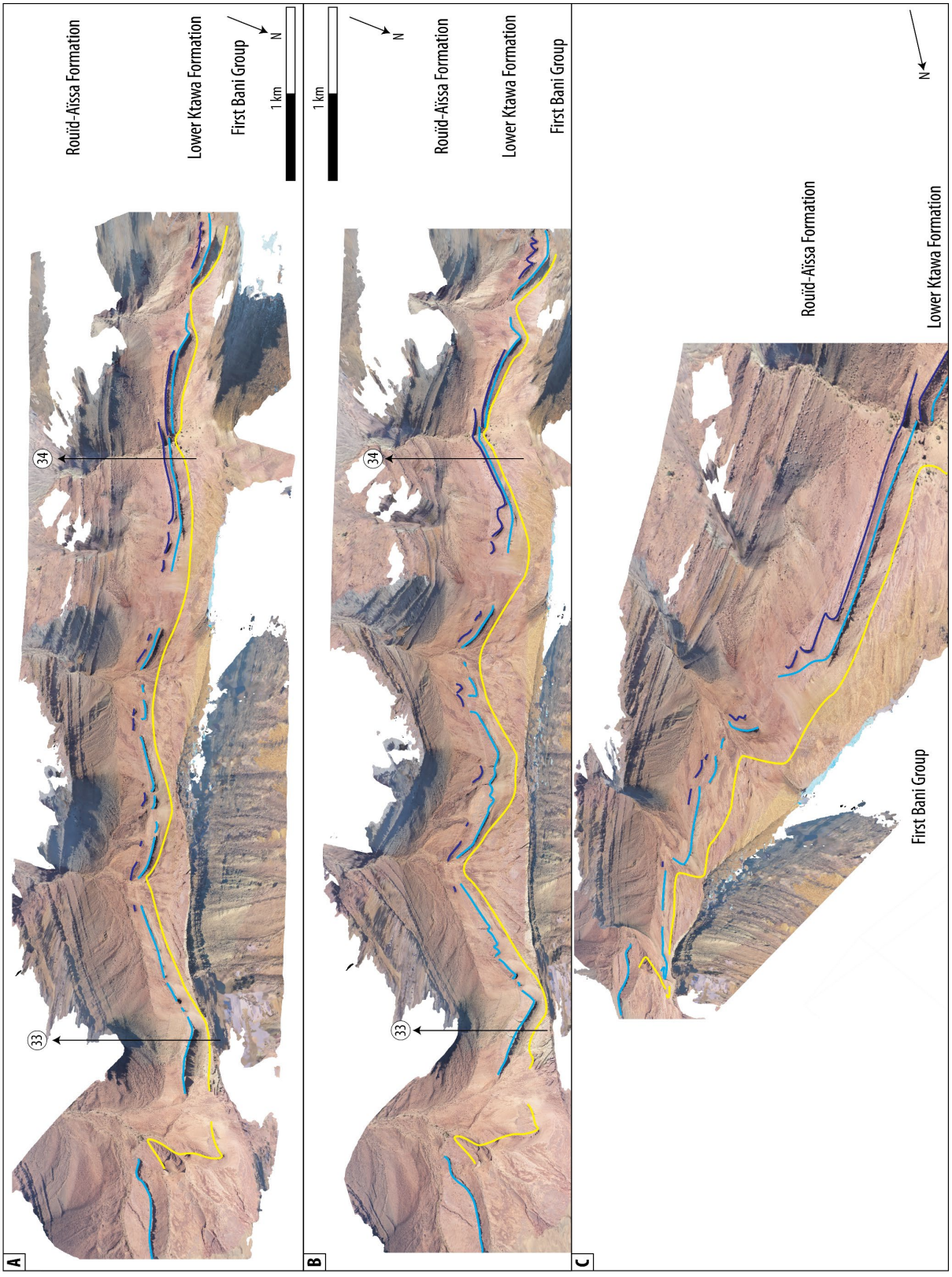

***Figure B.6**: 3D photogrammetric reconstructions from UAV images of the disappearance of Tissint toward the NE. (A) View facing the outcrop. (B) Planar view. (C) Oblique view. For location, see Fig. 2.3. For legend, see Fig. B.1.*

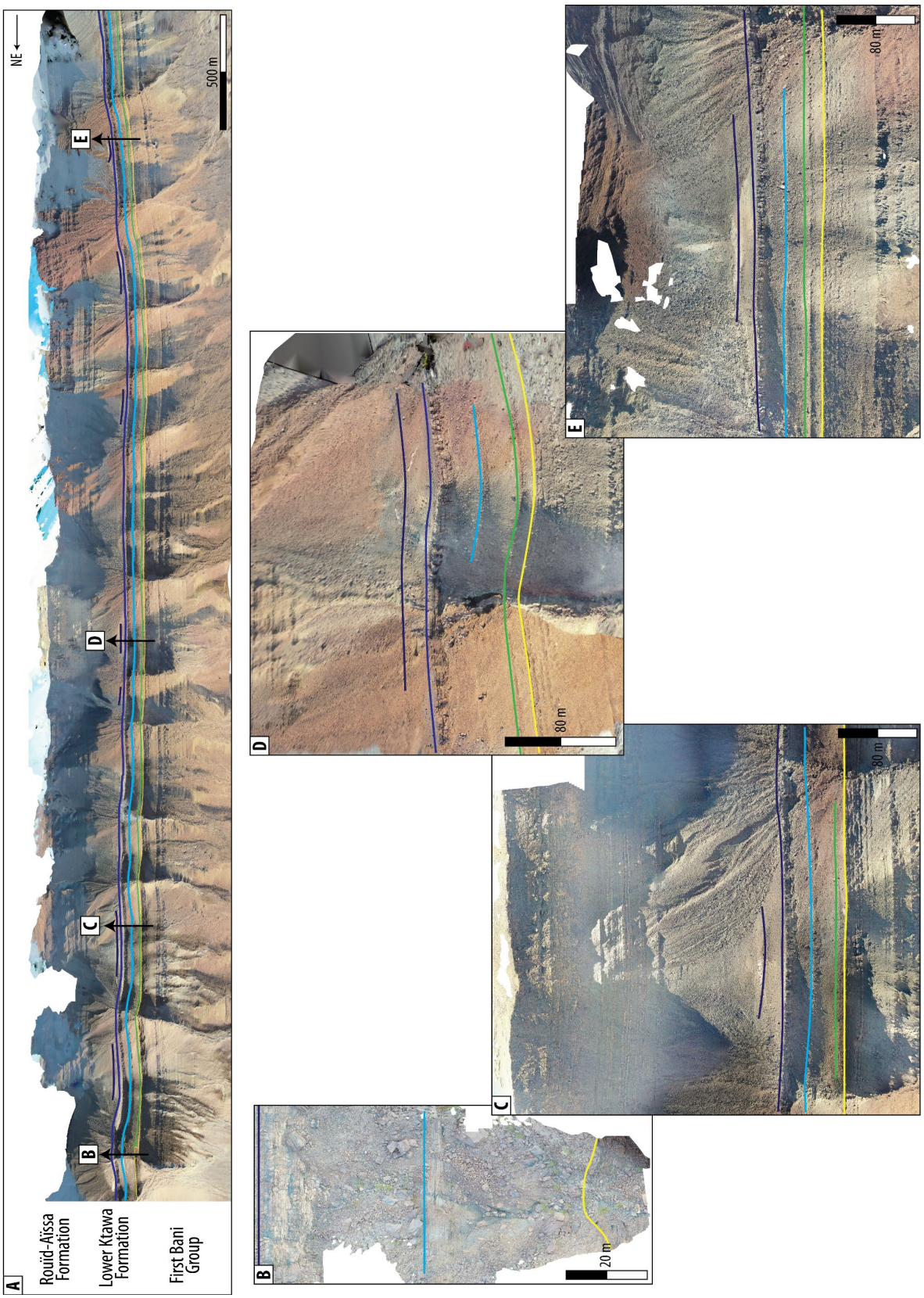

***Figure B.7**: 3D photogrammetric reconstruction from UAV images. (A) Disappearance of the Tanzida Mb toward the NE. Note how the member is getting close to the top of the First Bani Group. (B to E) Reconstructions of logs 36 to 39 respectively. For location, see Fig. 2.3. For legend, see Fig. B.1.*

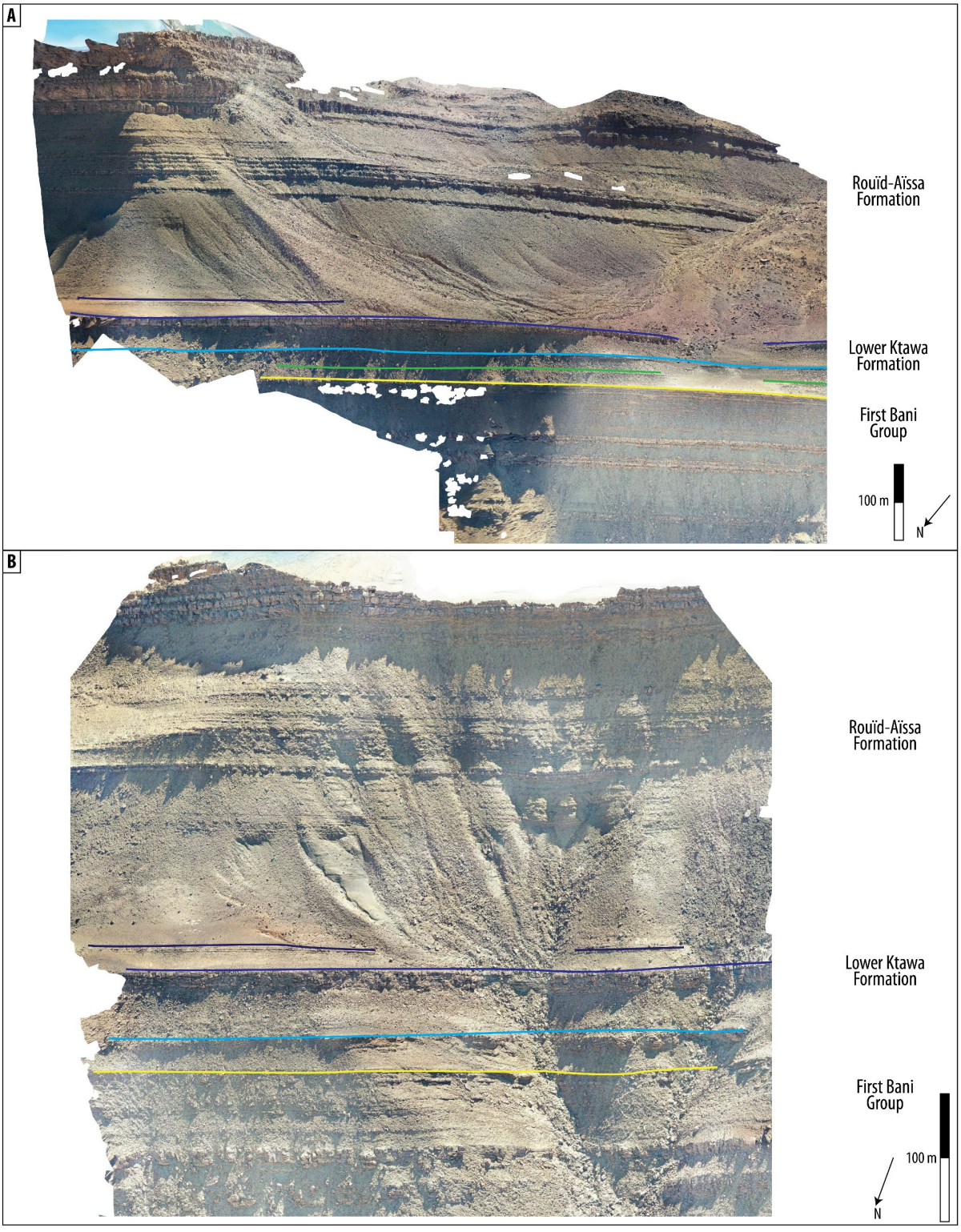

***Figure B.8**: 3D photogrammetric reconstructions from UAV images of logs 41 and 42, respectively to (A) and (B). For location, see Fig. 2.3. For legend, see Fig. B.1.*

Appendix C

Supplementary materials for Chapter 3

Detailed stratigraphic profiles of the Rouïd-Aïssa Formation in the western Central Anti-Atlas

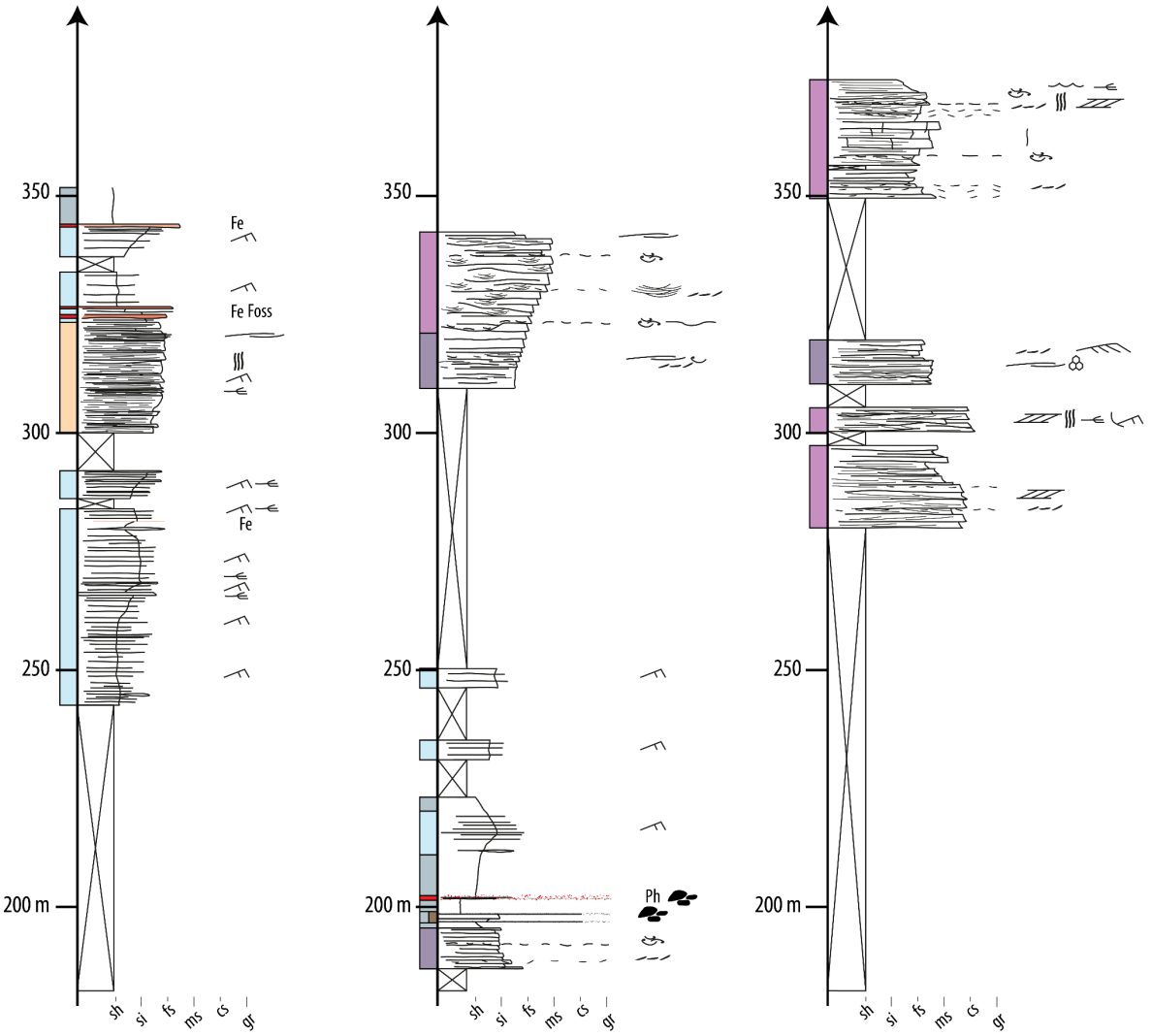

Supplementary figure B.1*: Detailed stratigraphic profiles of the Rouïd-Aïssa Fm and part of the underlying Lower Ktawa Fm of logs 1 to 3 (left to right respectively). Height scales start at 0 m at the top surface of the First Bani Group. For location, see Fig. 3.1. For legend, see Fig. 3.10. Panorama views of logs 2 and 3 in Fig. 11B and C respectively.*

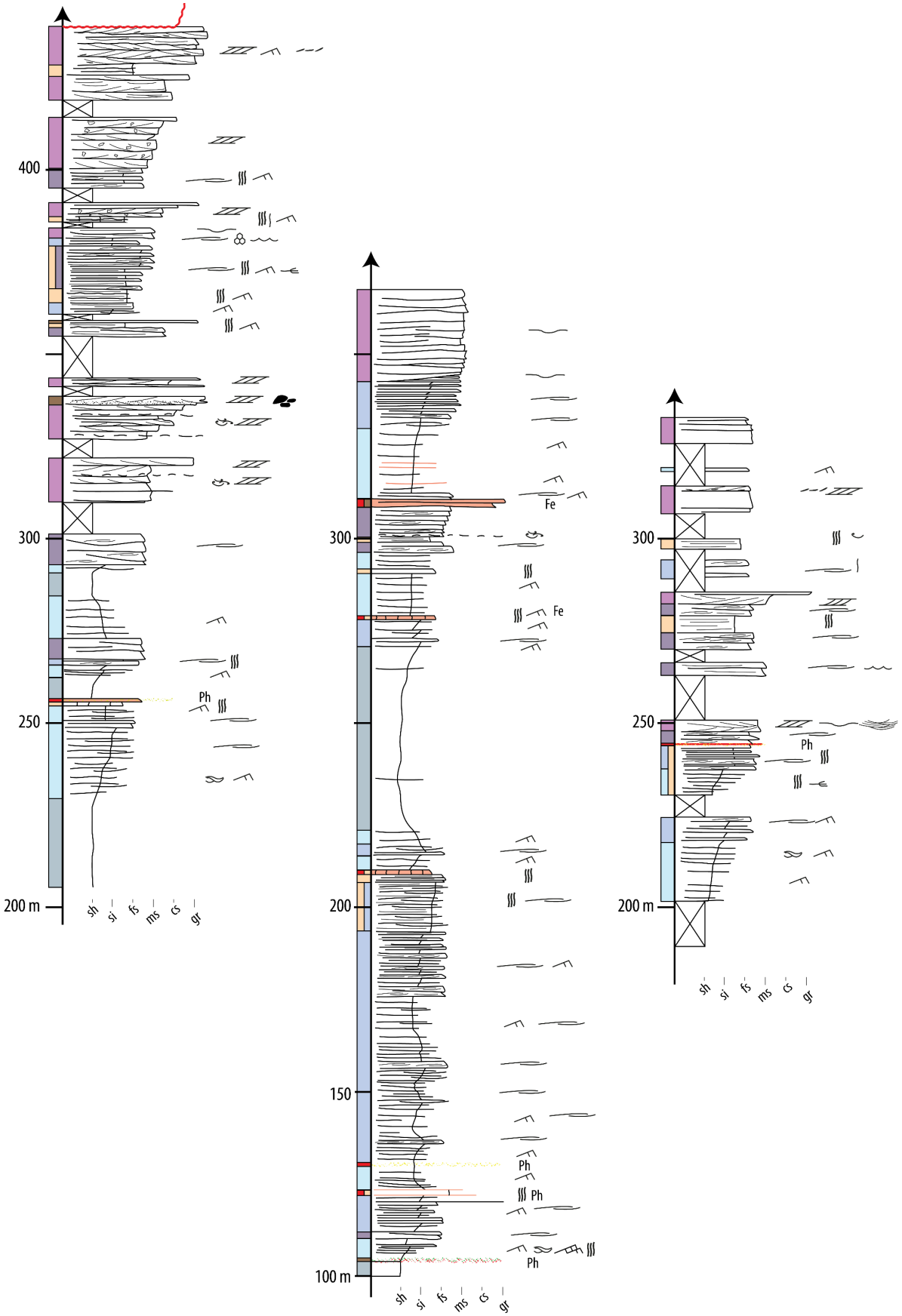

***Supplementary figure B.2**: Detailed stratigraphic profiles of the Rouïd-Aïssa Fm (up to the glacial incision of the lower part of the formation) and part of the underlying Lower Ktawa Fm of logs 4 to 6 (left to right respectively). Height scales start at 0 m at the top surface of the First Bani Group. For location, see Fig. 3.1. For legend, see Fig. 3.10.*

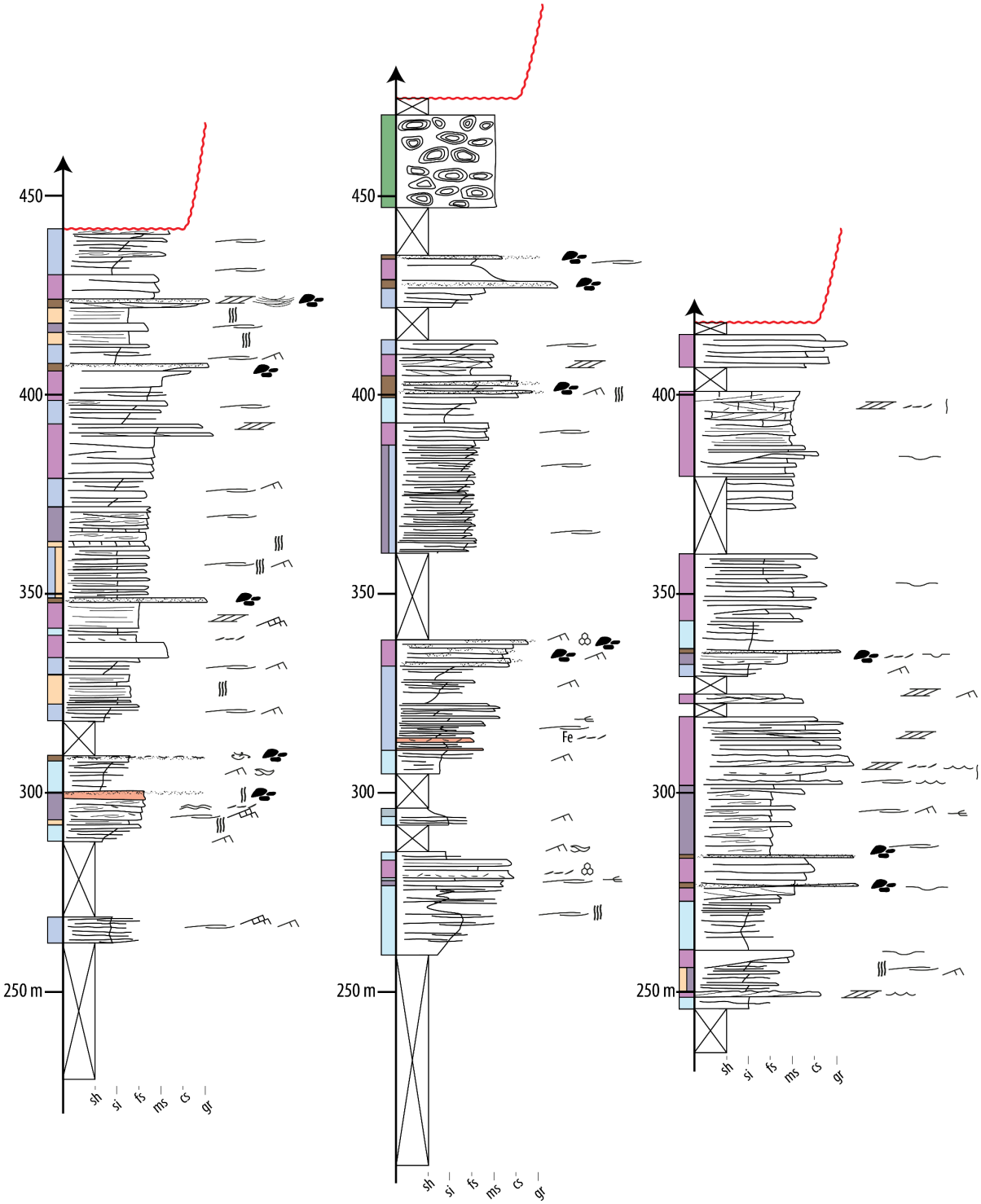

***Supplementary figure B.3**: Detailed stratigraphic profiles of the Rouïd-Aïssa Fm up to the glacial incision and part of the underlying Lower Ktawa Fm of logs 7 to 9 (left to right respectively). Height scales start at 0 m at the top surface of the First Bani Group. For location, see Fig. 3.1. For legend, see Fig. 3.10. Panorama views between logs 7 and 8 in Fig. 11E.*

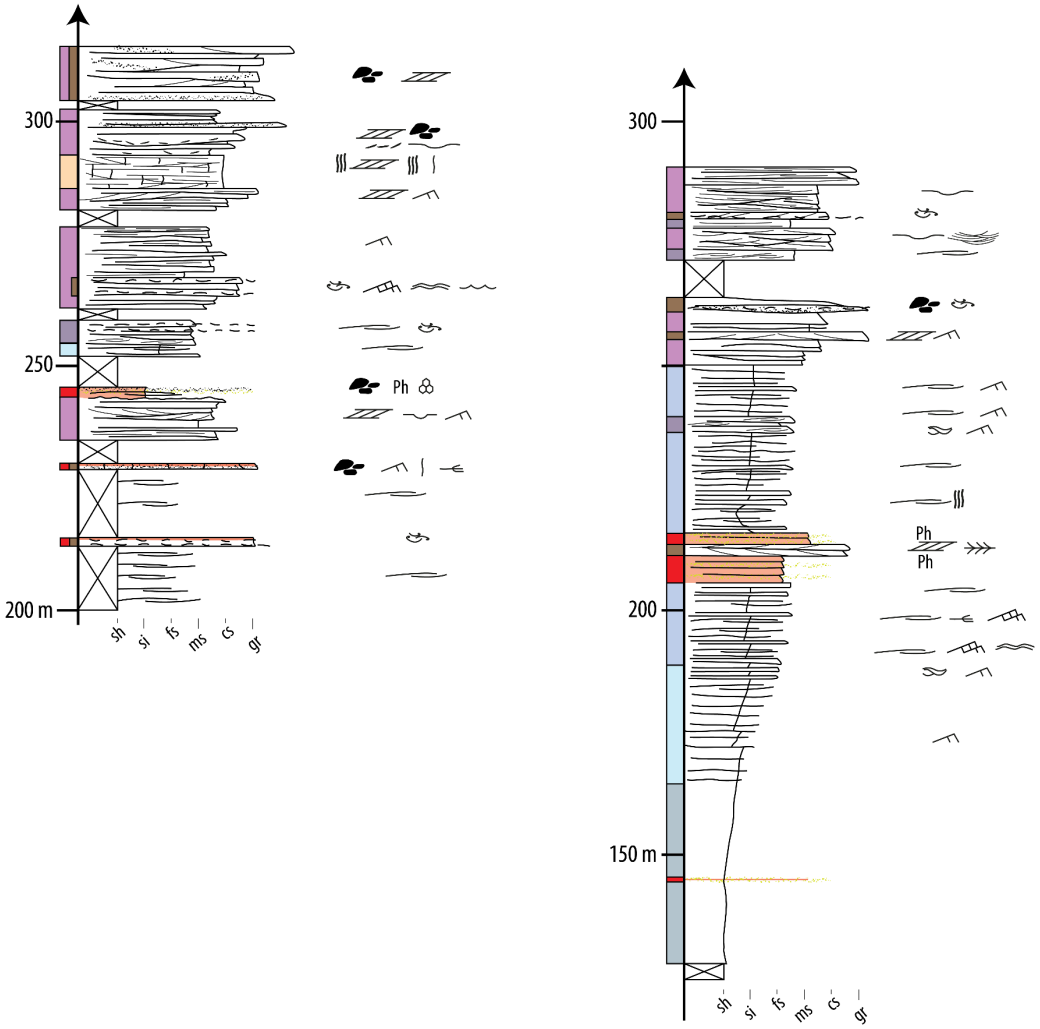

***Supplementary figure B.4**: Detailed stratigraphic profiles of lower part of the Rouïd-Aïssa Fm and part of the underlying Lower Ktawa Fm of logs 10 and 11 (left to right respectively). Height scales start at 0 m at the top surface of the First Bani Group. For location, see Fig. 3.1. For legend, see Fig. 3.10. Panorama views of log 11 in Fig. 11F.*

List of figures

***Figure 1.1**: Geological context of the Ktawa Group in the Anti-Atlas, South Morocco……17*

***Figure 2.1**: Location of the studied area.……..28*

***Figure 2.2**: Nomenclature……30*

***Figure 2.3**: Overview of the entire investigated transect……33*

***Figure 2.4**: Offshore facies associations ……..36*

***Figure 2.5**: Silts and sandstone ripples facies association……38*

***Figure 2.6**: Silts and isolated HCS facies association……39*

***Figure 2.7**: Stacked HCS sandstones facies association……41*

***Figure 2.8**: Quartzose amalgamated HCS sandstones facies association……43*

***Figure 2.9**: Coarse-grained cross-bedded sandstones facies association. ……44*

***Figure 2.10**: Coarse-grained cross-bedded sandstones facies association. ……45*

***Figure 2.11**: Coarse-grained cross-bedded sandstones facies association. ……46*

***Figure 2.12**: Intensely bioturbated muddy-sandstones facies association. ……48*

***Figure 2.13**: Three typical stacking patterns of facies associations ……50*

***Figure 2.14**: Semi-3D transect with precise logs and correlations, Tanzida and Foum-Zguid Members.……52*

***Figure 2.15**: Semi-3D transect with logs correlations, Tissint Member……53*

***Figure 2.16**: Semi-3D transect with logs correlations, Mazil and Treifia Members……54*

***Figure 2.17**: Semi-3D transect with logs correlations, Bou-Hajaj Member……55*

***Figure 2.18**: Semi-3D transect with logs correlations, Abbas Member……56*

***Figure 2.19**: Depositional models……61*

***Figure 3.1**: Context and paleogeographic location of the study area……85*

***Figure 3.2**: Isolated sandstones bearing HCS sandstones (and shell concentrations) with silts and rippled-marked sandstones interbeds facies association……90*

***Figure 3.3**: Shell imprints concentrations……91*

***Figure 3.4**: Stacked to amalgamated HCS sandstones (bearing shell concentrations) facies association……92*

***Figure 3.5**: Coarse cross-bedded sandstones bearing rip-up and shell clasts in concentrations facies association……94*

***Figure 3.6**: Detail on grain-size and clasts composing the coarse cross-bedded sandstones bearing rip-up and shell clasts in concentrations facies association……96*

***Figure 3.7**: Silty very-fine and medium-grained intensely bioturbated sandstones facies association……..97*

***Figure 3.8**: Lag deposits bearing pebble and shell clasts facies association……..98*

***Figure 3.9**: Highly deformed sandstones facies association……100*

***Figure 3.10**: 2D transect with precise stratigraphic profiles and facies associations of the Rouïd-Aïssa Formation……..100*

***Figure 3.11**: Panorama of the Rouïd-Aïssa Formation at different localities……103*

***Figure 3.12**: Correlations of selected stratigraphic profiles of the Rouïd-Aïssa Formation ..103*

***Figure 4.1**: Context and location of the study area……119*

***Figure 4.2**: Sandstone bodies as identified in the Central to Oriental Anti-Atlas.……123*

***Figure 4.3**: Correlations of the Lower Ktawa Formation members……127*

***Figure 4.4**: Detailed stratigraphic profiles of the Rouïd-Aïssa Formation……129*

***Figure 4.5**: Time constraint on the Ktawa Group and members with interpreted composite relative sea level curve for the studied region, and comparison to global scale data, including global relative sea level curve $\delta^{18}O$ and $\delta^{13}C$ curve as well as known climatic events……139*

***Figure 4.6**: Comparison of sedimentary successions across the northern Gondwana platform……141*

***Figure 4.7**: Correlations of sections from the Ktawa Group in the Anti-Atlas……146*

***Figure 5.1**: Context and location of the Lower Ktawa Formation in the Anti-Atlas, South Morocco. ……162*

***Figure 5.2**: 3D reconstructions of the hypothesized proximal-to-distal trend recorded in the Anti-Atlas. ……164*

***Figure 5.3**: Semi-3D transect of the study area with simplified depositional environments, detailed in Chapter 2……165*

***Figure 5.4**: 3D model of members thicknesses. ……166*

***Figure 5.5**: Paleocurrents measured along 2D outcrops for each sequence……167*

***Figure 5.6**: Megalobe shapes and channel-complexes extrapolated from thicknesses of each member. (A) Maximum extension of megalobes (i.e. isopach of 0 m). (B) Maximum thickness of megalobes……169*

***Figure 5.7**: Extrapolation and isostatic adjustment after deposition of the Foum-Zguid Mb……/……173*

***Figure 5.8**: Extrapolation and isostatic adjustment after deposition of the Tissint Mb. ……174*

***Figure 5.9**: Extrapolation and isostatic adjustment after deposition of the Mazil Mb……176*

***Figure 5.10**: Extrapolation and isostatic adjustment after deposition of the Treifia Mb. ……178*

***Figure 5.11**: Extrapolation and isostatic adjustment after deposition of the "lower" Bou-Hajaj sequence and Abbas Mb……179*

***Figure 5.12**: Extrapolation and isostatic adjustment after deposition of the "upper" Bou-Hajaj sequence……181*

***Figure 5.13**: Comparison between the output from BasinVis using a backstripping method, and Flex3D using flexural isostasy, for the Foum-Zguid sequence……188*

List of tables

***Table 3.1**: Summary of facies associations in the studied interval for the Rouïd-Aïssa Formation. ……87*

***Table 4.1**: Summary of facies associations in the studied interval for the Ktawa Group……124*

***Table 4.2**: Correlations from the western Central Anti-Atlas (this study) to the Bou Ingarf section and the eastern Central/Oriental Anti-Atlas…… ……148*

***Table 5.1**: Input parameters……171*

DÉBORAH HARLET

Institut für Geologie, University of Bern, Baltzerstrasse 1+3, 3012 Bern, Switzerland
iCRAG, University College Dublin, O'Brien Centre for Science (East), Belfield, Dublin 4, Ireland
+33 6 45 71 57 69, deborah.harlet@unibe.ch / deborah.harlet@icrag-centre.org

EDUCATION

School of Earth Sciences and iCRAG, University College Dublin (Ireland)
February 2024 – January 2025

Research Assistant Pending Viva – Supervisor: Dr. Koen Torremans

- *Project:* Lithostratigraphic architecture of the Ghanzi Group, Kalahari Copperbelt, Botswana, and its influence on deformation and mineralisation.

Institut für Geologie, University of Bern (Switzerland) *2020 - Present*

Ph.D. - Supervisor: Dr. Guilhem A. Douillet

- Sedimentary facies and depositional environments of a storm-dominated platform: implications for the platform morphology (Ktawa Group, Late Ordovician, Morocco) (in prep.)
- Stratigraphic architecture of a storm-wave-dominated platform: the Lower Ktawa Formation (Late Ordovician, Morocco) (in prep.)
- Depositional facies and stratigraphic architecture recording sea-level variations (Ktawa Group, Morocco): the onset of the Early Palaeozoic glaciation (in prep.)

Grenoble-Alpes University (France) *2017 - 2019*

M.Sc. Earth Sciences, Planets, and Environment, Geodynamics specialty

- *Master 2 project:* Basin analysis (source-to-sink, petrography and geodynamics) of the Tornillo Basin (Texas, U.S.A.) – Supervisor: Prof. Kenneth Ridgway, EAPS Laboratory, Purdue University, U.S.A.
- *Master 1 project:* Structural study of the Pianamen-Duwa fold (Tarim Basin, Occidental Kunlun) – Supervisor: Ass. Prof. CNRS Martine Simoes, Tectonic Laboratory, mechanics of the lithosphere, Institut de Physique du Globe de Paris.

Sorbonne University, Paris (France) *2014 - 2017*

B.Sc. Earth Sciences

- *Project:* Influence of pH on trace elements dynamics in high latitude: monitoring climate change on extreme environments (Abisko, Sweden) – Scientific station of Abisko, Sweden and METIS Laboratory, Paris.

RESEARCH/FIELD WORK EXPERIENCE

Research Assistant Pending Viva Project – Supervisor: Dr. Koen Torremans
February 2024 – January 2025

Basin analysis of the Kalahari Copperbelt focusing in Botswana

- Extensive fieldwork in Botswana. Core logging

Ph.D. Project - Supervisor: Dr. Guilhem A. Douillet *2020 - Present*

Basin analysis of Late Ordovician deposits of the northern Rim of the Tindouf Basin (Southern Morocco)

- Extensive fieldwork in the Anti-Atlas, southern Morocco. Logging of 42 stratigraphic sections with detailed facies analysis along a ca. 150 km long transect. Reconstruction of the outcrops using an UAV images and Agisoft Metashape 1.6 processing. Subsidence and flexural analysis and platform morphology modelling using Flex3D and BasinVis 2.0 (and basics of PaleoStrip1.0).

Master 2 Project - Supervisor: Prof. Kenneth Ridgway *2019*

Basin analysis (source-to-sink, petrography and geodynamics) of the Tornillo Basin (Texas, U.S.A.)

- Field in the Tornillo Basin and in Texas on fluvial siliciclastic deposits and carbonates. Oil and gas study of Texas (U.S.A.). Petrography of thin sections. Flexural (finite-element method) and subsidence analysis (backstripping) of the basin with BasinVis 1.0. Source-to-sink study using U/Pb detrital zircon geochronology.
- Scholarship from the Région Auvergne-Rhône-Alpes for International Mobility.

Master 1 Project - Supervisor: Ass. Prof. CNRS Martine Simoes *2019*

Structural study of the Pianamen-Duwa fold (Tarim Basin, Occidental Kunlun)

- Interpretation of several seismic lines/dataset of a fold. Restoration of balanced geological transects prior to deformation in order to quantify the amount of shortening, shortening rate, and timing of deformation. Type of deformation and fold to fault systems highlighted.

Bachelor Project – METIS Laboratory *2016 - 2017*

Influence of pH on trace elements dynamics in high latitude (Abisko, Sweden)

- Field in Abisko (Sweden). Soils sampling in different environments. Measurements of pH, weight in situ and trace elements concentrations in the METIS laboratory.

Other Relevant Geological Field Experience *2014 - present*

Field studies in the Romanian Carpathian, French Alps including Briançonnais Nappe, Vercors, Digne window, Normandy, Chaîne des Puys, the Italian and Swiss Alps and Swiss Alps foreland, Morocco, Florida Keys, Kalahari Copperbelt focusing on the sedimentology, sequence stratigraphy, petrology, and geomorphology, geodynamics, tectonics, volcanology.

CONFERENCE PRESENTATIONS

Association des Sédimentologistes Français – Oral *2022*

"Stratigraphic architecture of a siliciclastic shallow-marine giant platform of the Ktawa Group, Late Ordovician (Anti-Atlas, Morocco)"

International Sedimentological Congress – Invited talk (online)

"How to orientate a shallow-marine platform in 3D? A stratigraphic study from the Ktawa Group, Morocco (Late Ordovician, Gondwana)"

European Geosciences Union – Oral
"Semi-3D stratigraphic architecture of a siliciclastic shallow-marine platform: Insights from the Ktawa Group (Late Ordovician), Morocco"

Earth Surface Processes and Paleobiosphere Day (Doctoral School) 2022 – Oral
"Stratigraphic architecture of a siliciclastic shallow-marine giant platform of the Ktawa Group, Late Ordovician (Anti-Atlas, Morocco)"

Swiss Geoscience Meeting (online) – Oral *2021*
"Stratigraphic architecture of a siliciclastic shallow-marine platform: Insights from the Late Ordovician of the Anti-Atlas (Morocco)"

Earth Surface Processes and Paleobiosphere Day (Doctoral School) – Oral
"Stratigraphic architecture of a siliciclastic shallow-marine platform: Insights from the Late Ordovician of the Anti-Atlas (Morocco)"

European Geosciences Union (online) – vPICO
"Sedimentology, stratigraphy and clinoform architectures of a siliciclastic shallow-marine platform: Insights from the Late Ordovician of the Anti-Atlas (Morocco)"

Swiss Geoscience Meeting (online) – Poster *2020*
"Stratigraphic architecture and depositional processes across lower Paleozoic siliciclastic shallow-marine platforms: Insights from the Late Ordovician of the Anti-Atlas (Southern Morocco)"

DIVERSITY, EQUALITY, INCLUSION

Womentoring a Master student – Mentoring a first year female Master student from abroad, include her in the institute, give her advices on her career (2021-2023)

OTHER EXPERIENCE AND INTERESTS

ESPP Representative – Representative of Bern University in the Conference Universitaire de Suisse Occidentale of the Earth Surface Processes & Paleobiology (ESPP) doctoral program (January 2023 – December 2023)

Doctoral School – Internal Earth @les Houches – Thermochronology and plate tectonics conference, les Houches, France (2018)

Climate and Environment Internship – Label L-IPSL, Ecole Polytechnique, France (2017)

Archaeology Internship – L'Ilot Cygne, Saint-Denis, France (2016)

Declaration of consent

on the basis of Article 18 of the PromR Phil.-nat. 19

Name/First Name:	Harlet Déborah
Registration Number:	19-124-262
Study program:	Doctorate, Phil. Nat., University of Bern

Bachelor ☐ Master ☐ Dissertation ☑

Title of the thesis:	Sedimentology and stratigraphy of the Ktawa Group: the record of a shallow marine siliciclastic platform of Late Ordovician age in the Anti-Atlas, Morocco.
Supervisors:	Dr. Guilhem Amin Douillet, University of Bern (Switzerland) Prof. Dr. Fritz Schlunegger, University of Bern (Switzerland) Dr. Jean-François Ghienne, University of Strasbourg (France)

I declare herewith that this thesis is my own work and that I have not used any sources other than those stated. I have indicated the adoption of quotations as well as thoughts taken from other authors as such in the thesis. I am aware that the Senate pursuant to Article 36 paragraph 1 litera r of the University Act of September 5th, 1996 and Article 69 of the University Statute of June 7th, 2011 is authorized to revoke the doctoral degree awarded on the basis of this thesis.
For the purposes of evaluation and verification of compliance with the declaration of originality and the regulations governing plagiarism, I hereby grant the University of Bern the right to process my personal data and to perform the acts of use this requires, in particular, to reproduce the written thesis and to store it permanently in a database, and to use said database, or to make said database available, to enable comparison with theses submitted by others.

Place/Date

Dublin, Ireland, 22/05/2024

Signature

Déborah Harlet

“Bad girls do it right”